



Centro Brasileiro de Pesquisas Físicas
Coordenação de Matéria Condensada, Física Aplicada e Nanociência

**High-field relaxation and diffusion NMR studies
applied to the characterization of confined fluids.**

Bruno Chencarek

Supervisor: Prof. Ivan S. Oliveira

Submitted in part fulfilment of the requirements
for the degree of Doctor of Philosophy in Physics
of the Brazilian Center for Research in Physics.

January 2021

“HIGH-FIELD RELAXATION AND DIFFUSION NMR STUDIES
APPLIED TO THE CHARACTERIZATION OF CONFINED
FLUIDS”

BRUNO CHENCAREK

Tese de Doutorado em Física apresentada no
Centro Brasileiro de Pesquisas Físicas do
Ministério da Ciência Tecnologia e
Inovação. Fazendo parte da banca
examinadora os seguintes professores:



Ivan dos Santos Oliveira Junior – Presidente/Orientador/CBPF



Tito José Bonagamba – IFSC/USP



Jorge Luís Gonzalez Alfonso - UFES



Alexandre Mello de Paula Silva - CBPF



Eduardo Matzenbacher Bittar- CBPF

Rio de Janeiro, 03 de março de 2021.

Centro Brasileiro de Pesquisas Físicas

Rua Doutor Xavier Sigaud, 150, URCA, Rio de Janeiro, Brasil

Tel.: +55 21 2141-7100 CEP:22290-180

<http://www.cbpf.br>

Abstract

Relaxation and diffusion nuclear magnetic resonance (NMR) studies of confined fluids performed in high-field conditions are presented and discussed within the framework of time-domain (TD) NMR. Particularly, an emphasis was given to the foundation of suitable theoretical frameworks for the analysis of relaxation times and time-dependent diffusion coefficients extracted from NMR data sets and the establishment of proper relations between these parameters and physical properties of fluids and confining spaces. A retrospect on relaxation and diffusion NMR studies in porous media and the fundamentals of NMR are presented, respectively. A systematic study of high- (500 MHz) and low-field (15 MHz) NMR T_2 relaxation times performed on artificial sintered sand glass samples saturated with water is presented. Sample's pore structure was analyzed by scanning electron microscopy and microtomography techniques, the latter used for the determination of pore size distributions through image processing techniques. NMR data sets were analyzed using three different approaches: (i) Laplace inversion with optimized regularization based on measured noise level, (ii) bi-exponential and (iii) q -exponential nonlinear least-squares. Upon a careful measurement protocol, the assumption of a fast diffusion regime and the relation between the observed relaxation rates and pore size distribution is addressed. It is presented a characterization of phase configuration in water-saturated synthetic porous samples after oil injection, through the analysis of time-dependent diffusion coefficients obtained from sets of pulsed field gradient nuclear magnetic resonance (PFG NMR) measurements, pre and post drainage. Short-time analysis of diffusion coefficients extracted from PFG measurements was used for estimates of samples surface-to-volume ratio and permeability from pre drainage PFG measurements, and to quantify the increase in surface-to-volume ratio probed by the wetting phase after drainage. Analysis of water and oil diffusion coefficients from post drainage PFG experiments were carried out using a bi-Gaussian model, and two distinct scenarios were considered to describe fluids conformation within pores. The application of the singlet-assisted NMR technique to the study of restricted diffusion in the long-time regime is also discussed, and initial experimental developments are presented.

Keywords: NMR; relaxation; diffusion; porous media; confined systems.

Resumo

Estudos de relaxação e difusão de ressonância magnética nuclear (RMN) de fluidos confinados realizados em condições de alto campo são apresentados e discutidos dentro do arcabouço teórico de RMN no domínio do tempo (TD). Em particular, foi dada ênfase à fundação de arcabouços teóricos adequados para a análise de tempos de relaxação e coeficientes de difusão dependentes do tempo extraídos de conjuntos de dados de RMN e o estabelecimento de relações adequadas entre esses parâmetros e propriedades físicas de fluidos e espaços confinantes. Uma retrospectiva sobre os estudos de relaxação e difusão de RMN em meios porosos e os fundamentos de RMN são apresentados, respectivamente. É apresentado um estudo sistemático de tempos de relaxação T_2 de RMN de alto (500 MHz) e de baixo campo (15 MHz) realizado em amostras artificiais de areia de vidro sinterizada saturadas com água. A estrutura dos poros das amostras foi analisada por técnicas de microscopia eletrônica de varredura e microtomografia, esta última utilizada para a determinação da distribuição de tamanhos de poros por meio de técnicas de processamento de imagens. Os conjuntos de dados de RMN foram analisados utilizando-se três abordagens distintas: (i) inversão de Laplace com regularização otimizada com base no nível de ruído medido, mínimos quadrados não lineares por modelo (ii) bi-exponencial e (iii) q -exponencial. Mediante um protocolo de medição cuidadoso, a suposição de um regime de difusão rápida e a relação entre as taxas de relaxação observadas e a distribuição do tamanho dos poros é abordada. É apresentada uma caracterização da configuração de fases em amostras porosas sintéticas saturadas com água após a injeção de óleo, através da análise dos coeficientes de difusão dependentes do tempo obtidos a partir de conjuntos de medidas de ressonância magnética nuclear de gradiente de campo pulsado (PFG), pré e pós-drenagem. A análise de tempos curtos dos coeficientes de difusão extraídos das medidas de PFG foi utilizada para estimativas da razão superfície-volume e permeabilidade em amostras pré-drenagem, e para quantificar o aumento na razão de superfície-volume sondado pela fase molhante após a drenagem. A análise dos coeficientes de difusão de água e óleo de experimentos PFG pós-drenagem foram realizados usando um modelo bi-Gaussiano, e dois cenários distintos foram considerados para descrever a conformação de fluidos dentro dos poros. A aplicação da técnica de RMN assistida por estados singletons ao estudo da difusão restrita no regime de tempos longos também é discutida e os

desenvolvimentos experimentais iniciais são apresentados.

Palavras-chave: RMN; relaxação; difusão; meios porosos; sistemas confinados.

Acknowledgements

I would like to express my sincere gratitude to:

- My supervisor, and may a say close friend, Prof. Ivan S. Oliveira, from whom I received not only the strong and solid guidance that allowed me to develop the works presented in this thesis, but also the carrying and support of a great human being and the trust of an admirable chief and supervisor.
- My old friend Dr. Maury Duarte Correia, the responsible for the establishment of a fundamental bridge between academical and industrial research, materialized as a set of R&D Projects between the Brazilian Center for Research in Physics and PETROBRAS, which made possible the development of this and several other works.
- Dr. Moacyr do Nascimento, my close friend and main research colleague. I can certainly find myself privileged in sharing most of my Ph.D. time with him, and sincerely hope our friendship and research partnership to be long-lived.
- Prof. Alexandre Martins Souza for the mentorship, the long hours and countless experiments shared inside the NMR lab at CBPF.
- To the colleagues in R&D Projects, and members of the NMR research group Prof. Roberto Sarthour, Filipe, Arthur, Linneu, Léo, Josie, Nayara, Renan, Eldues and Bernardo.
- My mother and father, Marice and Mário Chencarek, who have always went to great lengths for me and my siblings to have an exceptional education. To my sister Fernanda and my brother Renato, my greatest friends.
- My wife Greta, with whom I always shared my dreams and goals. Thank you for all the support during one the most important years of our life together. I also would

like to thank Cátia and Rogério, Greta's parents, for the long-distance yet always strong support.

- To the Queda Livre Blues Band friends: Prof. Ivan Oliveira, Prof. João Paulo Sinner, Prof. Itzhak Roditi, Prof. Marcello Neto and Anna Chataignier. Thank you for all the amazing moments shared, specially the virtual ones during the unforgettable year of 2020.

Preface

I started working with NMR during the second half of 2015, when I re-encountered in Rio de Janeiro an old friend, Dr. Maury Duarte Correia, a former physics Ph.D. candidate from the Brazilian Center for Research in Physics (CBPF) and currently a geophysicist at the research center in PETROBRAS (CENPES). At the time Dr. Correia introduced me to Prof. Ivan S. Oliveira, leader of the NMR and quantum computing research group in CBPF, who was also his former and my soon-to-be supervisor. The establishment of a cooperation term between CBPF and CENPES was been discussed at the time and a research team was about to be assembled.

From 2016 to 2018 I had the opportunity to compose this team of five researchers on the first R&D Project between the NMR groups from CBPF and CENPES, particularly as in charge of the enhancement and development of NMR relaxation techniques for application in porous media petrophysics. During this period I concluded my Master's in Physics, also under the supervision of Prof. Oliveira and further the results obtained during the M.Sc. developed the work presented in the Chapter 3 of this thesis.

In 2018 a second, and this time four year-long cooperation term was signed, with new goals and a larger research team, a group of 7 other scientists working in numerical simulations, theoretical models, mathematical approaches for data analysis, nanofabrication and the development of NMR instrumentation. The new experimental developments in NMR were expected to have an emphasis in flow and transport properties of confined fluids. Hence, still in 2018 I became a Ph.D. candidate at CBPF and started my studies in diffusion NMR while working as a NMR scientist in this new R&D project. During this period I shared most of my Ph.D. time and developments with Dr. Moacyr do Nascimento, a former Ph.D. candidate in CBPF and currently a geophysicist at CENPES research center, who also worked with NMR of confined systems.

The works presented in Chapter 3, 4 and 5 of this thesis were developed from the second half of 2017 to the first half of 2020, in the context of these R&D projects funded by PETROBRAS. Naturally, the petrophysical application of models and techniques investigated has always been the north of our research. Nevertheless, the results presented in this thesis are applicable to the study of confined systems and porous materials, in general.

Contents

Abstract	i
Resumo	ii
Acknowledgements	v
Preface	vii
List of Tables	xiii
List of Figures	xv
I Introduction	1
1 A Retrospect on Relaxation and Diffusion NMR in Porous Media	2
2 Nuclear Magnetic Resonance (NMR)	16
2.1 Fundamentals of NMR	16
2.1.1 Magnetic Moments in a Magnetic Field	16
2.1.2 Larmor Precession and the Spin Equation of Motion	20
2.2 NMR Relaxation	22
2.2.1 Longitudinal and Transverse Relaxation	22
2.2.2 The Rotating Frame of Reference	25

2.2.3	Radiofrequency Pulses and Rotations	27
2.2.4	Free Induction Decay (FID) and NMR Spectroscopy	30
2.2.5	Spin Echoes	32
2.2.6	Common Protocols for Relaxation Measurements	37
2.2.7	2D NMR	44
2.3	NMR in Petrophysics	46
2.3.1	Fast Diffusion Regime and Relaxation Rates	49
2.3.2	A Microscopic Note on Surface Relaxation Processes	52
2.3.3	Inversion of Multiexponential Decays and Relaxation Time Distributions	54
	Publications	60
	II Results	61
3	Multi-exponential Analysis of Water NMR Spin–Spin Relaxation in Porosity/Permeability - Controlled Sintered Glass	62
3.1	Motivation and Background	62
3.2	Sample Fabrication and Characterization	65
3.2.1	Sintering and Chemical Analysis	65
3.2.2	Porosity and Permeability Measurements	67
3.3	Calculation of Pore Size Distribution from 2D Micro-Tomography Images .	68
3.4	NMR Relaxation Measurements and Data Analysis	75
3.5	Concluding Remarks	84
4	PFG NMR Time-Dependent Diffusion Coefficient Analysis of Confined Emulsion: Post Drainage Phase Conformation.	86
4.1	Diffusion NMR	86

4.1.1	Self-Diffusion and the Diffusion Equation	86
4.1.2	The Averaged Propagator	87
4.1.3	Pulsed-Field Gradient (PFG) NMR	88
4.1.4	Narrow Pulse and Gaussian Phase Approximations	91
4.1.5	The Bloch-Torrey Equation	94
4.1.6	Spin Echo PFG Sequence	95
4.1.7	Stimulated Spin Echo PFG Sequence	97
4.1.8	13-Interval PFG Sequence by Cotts	97
4.1.9	Restricted Diffusion and Short-Time Analysis	100
4.2	Motivation: The Characterization of Multiphase Saturation in the Framework of Restricted Diffusion	101
4.3	Fluid Conformation After Drainage	102
4.4	Experimental Description	104
4.4.1	Samples and Preparation	104
4.4.2	Measurements	106
4.5	Results and Discussion	106
4.5.1	Fluids Characterization	106
4.5.2	Pre Drainage PFG Analysis	106
4.5.3	Post Drainage PFG Analysis	111
4.6	Concluding Remarks	118
5	Applications in Progress and Future Works: Singlet States as a Tool for the Determination of Diffusive Tortuosity	120
5.1	Singlet States and Long-Lived Spin Order	120
5.1.1	Coupled Spin-1/2 Systems: Singlets and Triplets	121
5.1.2	Singlets in Magnetically Equivalent Environments	122
5.1.3	Singlets in Magnetically Inequivalent Environments	123

5.1.4	High-Field Radiofrequency Spin-Locking	126
5.1.5	Sample Preparation and Experimental Setup	133
5.1.6	Preliminary Results and Discussion	134
5.2	Singlet-Assisted Diffusion NMR (SAD-NMR)	138
5.2.1	Diffusive Tortuosity and The Long-Time Diffusion Regime	138
5.2.2	Time-Dependent Diffusion Coefficients in Packed Glass Beads	141
5.2.3	SAD-NMR Pulse Sequences	145
6	Conclusion	147
	Bibliography	149

List of Tables

1.1	Timeline of NMR Logging. Adapted from ref. [17]. Copyright © 2001 John Wiley & Sons, Inc.	6
2.1	Gyromagnetic ratio of some nuclei and their natural abundance. Adapted from ref. [2]. Copyright © Cambridge University Press.	19
3.1	High-field NMR (500 MHz) T_2 exponential and q-exponential fitting pa- rameters	82
3.2	Low-field NMR (15 MHz) T_2 exponential and q-exponential fitting parameters	83

List of Figures

Credit authorship statement: All figures in this thesis were drawn by the author.

2.1	Zeeman energy levels for a nuclear spin $I = 3/2$ in the presence of an applied magnetic field $\vec{B} = (0, 0, B_0)$. The magnetic quantum number m can assume four different values $(2I + 1)$, and the energy difference between two adjacent levels is proportional the applied magnetic field and the nucleus gyromagnetic ratio γ	18
2.2	Rotation of the magnetization vector \vec{M} by a static magnetic field B_0	21
2.3	Illustration of longitudinal and transverse relaxation of the magnetization components M_z and M_x with time.	25
2.4	Illustration of the effective magnetic field \vec{B}_{eff} as summation of a static magnetic field \vec{B}_0 and a transverse rotational field \vec{B}_1 , as seen in a stationary and in a rotating frame of reference.	28
2.5	Illustration of the $\pi/2$ and the π rotations of the magnetization vector in the $y - z$ plane by a transverse RF pulse \vec{B}_1 applied in the positive x -direction, as seen in a rotating frame of reference.	29
2.6	Illustration of the Lorentzian lineshape in the frequency domain (Equation 2.56). The left plot shows the real, or absorption, lineshape and the dispersion, or imaginary, lineshape is shown in the right plot. The linewidth at half-height in the left plot is inversely proportional to T_2^* . The greater the magnetic field inhomogeneity is, the smaller (shorter) T_2^* is and the broader the linewidth.	32

2.7	Illustration of the loss of precession phase coherence by the magnetic moments after a $\pi/2$ pulse applied in the positive x -direction, from the point of view of an observer standing at the rotating frame of reference. Immediately after the $\pi/2$ pulse the magnitude of the transverse magnetization equals the equilibrium value $M_{xy} = M_0$	33
2.8	Illustration of the effect of a π pulse, applied on the positive x -direction, on the recovering of the precession phase coherence and the formation of a spin echo at $t = 2\tau$	36
2.9	Illustration of the protocol suggested by Carr and Purcell for the measurement of the T_2 relaxation time. Each refocusing π pulse induces the formation of a new spin echo, which is the complex conjugate of the previous one. In this protocol the π pulses are applied in the same direction as the $\pi/2$ pulse. The amplitude of the echoes decrease due to relaxation and is modulated by the exponential decay expressed in Equation 2.89.	41
2.10	Illustration of the Carr-Purcell-Meiboom-Gill (CPMG) method for the measurement of the T_2 relaxation time. In this protocol the π pulses are applied perpendicular to the $\pi/2$ pulse and all echoes are formed at the same direction. The amplitude of the echoes decrease due to relaxation and is modulated by the exponential decay expressed in Equation 2.89.	42
2.11	Illustration of the saturation-recovery (a) and the inversion-recovery (b) protocols for the measurement of the T_1 relaxation time. The upper graphs illustrate the pulse sequence schemes and the lower graphs show the evolution of the observed $M_z(t)$ signal as the pulse separation delay is increased in each repetition of the pulse sequence.	43
2.12	Illustration of the pulse sequence for the T_1 - T_2 correlation map combining an inversion recovery and a CPMG experiment, during which the spin system experiences longitudinal and transverse relaxations, respectively. The parameter t_e denotes the separation between the $\pi/2$ and the π pulses, or the echo time. Data is obtained varying the parameters τ_1 and τ_2 . For each τ_1 value the echo train in the CPMG is measured, wherein $\tau_2 = 2nt_e$ and n is the number of echoes acquired. The data matrix $M(\tau_1, \tau_2)$ is constructed over the two independent variables τ_1 and τ_2	45

- 2.13 Illustration of the pulse sequence for the T_2 - T_2 self-correlation map, combining two CPMG experiments, during which the spin system experiences transverse relaxation, separated by a time interval Δ , wherein the longitudinal relaxation acts. After the first segment the second $\pi/2$ pulse stores the signal as longitudinal magnetization. After the interval Δ the CPMG in the second segment acquires the echo train. The variable parameters are $\tau_1 = n_1 t_{e1}$ and $\tau_2 = n_2 t_{e2}$, wherein $n_i t_{ei}$ denotes the number of pulses and the echo time adopted in each segment. 46
- 2.14 Illustration of an idealized log interpretation from a reservoir containing brine and a medium viscosity oil. Adapted from reference [103]. A series of T_2 distributions are stacked in the left column, as a function of the well depth. The vertical red line in the T_2 distributions represent the T_2 cutoff, a value determined experimentally as a reference to separate relaxation times associated with oil (shorter T_2) and brine (longer T_2). The black and blue areas in the central column stands for the producible volumes of oil and water, respectively. The dashed line represents the total porosity ϕ . The right column presents a permeability estimate, calculated using the logarithmic mean of the relaxation time distribution and an empirical function [104]. Three distinct regions are marked on the left. Region I correspond to a cap rock, a highly impermeable rock, usually shale, anhydrite or salt, which seal the reservoir rock so that fluids cannot escape. Region II correspond to a low-permeability oil reservoir. Region III denotes a moderate-permeability water saturated rock. 48
- 2.15 Illustration of the slow (left) and fast (right) diffusion regimes of confined fluid molecules. In the slow diffusion regime molecules do not experience an expressive number of encounters with pore walls and the relaxation process is diffusion-limited. In the fast diffusion regime molecules experience surface relaxation several times, and the relaxation process is referred to as surface-limited. 51
- 2.16 Illustration of the 3-step surface relaxation process considering, for an example, the interaction of the ^1H proton nuclear spin with free electrons or paramagnetic ions at the pore surface. (I) The excited proton spin diffuses from the bulk phase to the surface bound layer. (II) Relaxation mechanisms take place during the residence time of molecules at the surface bound layer, during which molecules may diffuse along adsorbing sites. (III) The relaxed proton spin diffuses back to the bulk phase. 54

2.17	Inverse Laplace transform of a synthetic data composed by the summation of three exponential decays (left plot) with distinct weights and relaxation rates (Equation 2.115), using a Tikhonov regularized algorithm with positivity constraint, for three different values of the regularization parameter α (right plot). The amplitudes of the inverted solutions were normalized by their maximum height for a clear visualization. The behavior of the inverted data depends on the balance between the exact and the smoothed solutions, determined by the value of α	57
3.1	Ceramic crucibles (left) and synthetic porous samples from size range D after sintering (right), for application in high- and low-field equipment. . . .	65
3.2	Energy dispersive spectroscopy analysis in sintered synthetic samples from size ranges A to D. The presented graphs denote the average signal obtained from several acquisitions performed in different regions of a sample, showing no significant variation in composition among the observed samples.	66
3.3	(Left) Porosity values estimated by saturated mass (triangles) versus the values obtained using the free-gas expansion method (squares). (Right) Permeability values obtained using the steady-state method. A significant increase of permeability is observed, in opposition to porosity, which remains nearly constant. Here, the average grain diameter represents simply the mathematical average between the lower and upper microspheres' diameters within each chosen grain (sample) size range.	68
3.4	SEM images (left) and micro-tomography slices (right) artificial samples examples for each size range of grains. In spite the clear variation of porous sizes, the porosity remains nearly the same in all samples.	69
3.5	Scheme illustrating the acquisition of 2D transverse micro-tomography images from cylindrical samples. Each sample is scanned along the z axis for a full set 2D images.	70
3.6	Example of segmentation of pore space and grains from a 2D micro-tomography image in a synthetic sample from size range C. After the calibration of an appropriate threshold the original image is processed to be converted in a binary map. In the original image, the light gray pixels represent the grains and the dark gray pixels denote the porous space. Segmentation was performed using the Image Processing toolbox (MATLAB 2019b).	70

3.7	Example of a watershed segmentation process. An Euclidean distance map (central image) is calculated from the original image (left image), composed by two overlapping spheres. In the Euclidean distance map the intensity of each pixel represents the distance between that pixel and the first non-zero pixel in the original binary image. Regional minimum points are determined through the location of high or low intensity pixels. After the flooding by each one of the sources distinct regions are then separated by a watershed (right image).	71
3.8	Porosity values obtained by the free-gas expansion method (blue squares), saturated mass (red triangles) and by 2D micro-tomography image processing (green circles) as a function of the average range diameter. The vertical bars in the green circles denotes the standard deviation of values obtained along the set of micro-tomography images.	72
3.9	Synthetic sample A (53-106 μm): (Left) Porosity values obtained from segmented 2D transverse micro-tomography images versus the slice number along the z axis. (Right) Sample's pore size distribution obtained from the analysis of 2D micro-tomography images using the algorithm proposed by Rabbani et al. [123]. The green bar represents the average pore size of the obtained distribution and the red bar denotes an estimate of the pore radius considering the relation proposed by Rémond et al. [126].	73
3.10	Synthetic sample B (150-212 μm): (Left) Porosity values obtained from segmented 2D transverse micro-tomography images versus the slice number along the z axis. (Right) Sample's pore size distribution obtained from the analysis of 2D micro-tomography images using the algorithm proposed by Rabbani et al. [123]. The green bar represents the average pore size of the obtained distribution and the red bar denotes an estimate of the pore radius considering the relation proposed by Rémond et al. [126].	73
3.11	Synthetic sample C (250-300 μm): (Left) Porosity values obtained from segmented 2D transverse micro-tomography images versus the slice number along the z axis. (Right) Sample's pore size distribution obtained from the analysis of 2D micro-tomography images using the algorithm proposed by Rabbani et al. [123]. The green bar represents the average pore size of the obtained distribution and the red bar denotes an estimate of the pore radius considering the relation proposed by Rémond et al. [126].	74

3.12	Synthetic sample D (350-500 μm): (Left) Porosity values obtained from segmented 2D transverse micro-tomography images versus the slice number along the z axis. (Right) Sample's pore size distribution obtained from the analysis of 2D micro-tomography images using the algorithm proposed by Rabbani et al. [123]. The green bar represents the average pore size of the obtained distribution and the red bar denotes an estimate of the pore radius considering the relation proposed by Rémond et al. [126].	74
3.13	High field NMR spectra and respective line width values obtained for each sample. As the porous sizes decreases the NMR line becomes broader. . . .	76
3.14	High and low-field transverse magnetization decay. Relaxation of water nuclear spin magnetization is faster in samples with smaller porous sizes. The systematic is the same on both, high and low-fields, but relaxation times are shorter in high-field. The continuous lines are bi-exponential fits (see text).	77
3.15	Comparison between the three methods of numerical analysis for high-field decay data. On top, it is shown the χ^2 distributions obtained from q -exponentials least-squares. In the middle, Laplace inversion with optimized regularization, and in the bottom bi-exponential nonlinear least-squares. The distributions fall in the same region of relaxation times and the weights of the modes are similar to each other. The relaxation times of the bi-exponential modes approximately meet the corresponding ones in the other distributions.	79
3.16	The same analysis made in Figure 3.15 but for low-field decay data. One can observe that the general behavior is similar for high and low-fields. The corresponding areas under the curves agree to each other within 10%. . . .	80
4.1	Simplified pulsed field gradient sequence. The upper schematic diagram illustrates the free induction decay of the magnetization after a $\pi/2$ pulse with (red line) and without (blue line) the pair of gradient pulses ($-G$ and $+G$) applied during the encoding and decoding periods, illustrated in the central schematic. Both gradient pulses are matched in amplitude and length, but with opposite directions. The lower schematic illustrates the helix-like effect of the encoding gradient pulse on the magnetization and the phase evolution of the spins due to random thermal motion during the diffusion interval.	89

4.2	Spin echo PFG sequence (PGSE) proposed by Stejskal and Tanner [33] in the presence of a constant background gradient g . The refocusing π pulse inverts the phase imposed by the first gradient pulse during the encoding period. After the second gradient pulse a spin echo will be formed at $t_e = 2\tau$.	96
4.3	Stimulated echo PFG sequence (PGSTE) in the presence of a constant background gradient g . After the first gradient pulse a $\pi/2$ pulse rotates the magnetization to the z -axis. After the storage (diffusion) interval a third $\pi/2$ pulse rotates the magnetization back to the transverse plane. The phases of the two $\pi/2$ pulses can be set to have the same refocusing effect of the π pulse in the spin echo sequence. After the second gradient pulse a spin echo will be formed at $t_e = \Delta' + 2\tau$.	98
4.4	13-Interval stimulated echo APFG sequence proposed by Cotts et al. [133] in the presence of a constant background gradient g . The encoding and decoding intervals are both composed by a pair of gradient pulses with opposed polarities separated by a π RF pulse. Similarly to the stimulated echo sequence, after the encoding interval the magnetization is stored in the z -axis. A spin echo will be formed at $t_e = \Delta' + 4\tau$ after the decoding period.	99
4.5	Illustration of simplified conformation scenarios for the non-wetting phase after drainage. (a) Oil is located only in the innermost region of pores, with pore throats still filled with water. In this scenario the non-wetting phase exhibits limited or no connectivity. (b) Non-wetting phase fills both inner regions of pores and throats, in a highly-connected configuration.	103
4.6	2D micro-tomography image of microspheres after the sintering process employed in the fabrication of the synthetic porous samples. The sintering protocol was designed to preserve most of the porosity from the original package [147].	105
4.7	Illustration of the experimental setup employed for the drainage of water-saturated samples. An oil volume equal to the sample's total volume was forced into the water-saturated samples using a manually controlled piston at an average rate of 1 ml/s.	105
4.8	Bulk water (a) and oil (b) normalized spin echo attenuation Ψ as a function of squared gradient G^2 . Diffusion time (Δ) value was 40 ms for water and 100 ms for oil measurements. Black lines denote fittings using Equation (4.36). Self-diffusion coefficients obtained were $D_0^w = 2.29 \times 10^{-9}$ m ² /s for water and $D_0^o = 0.79 \times 10^{-9}$ m ² /s for oil.	107

4.9	Signal attenuation Ψ as a function of squared gradient G^2 for different diffusion times, on the water-saturated porous sample, for Δ values between 3 and 8 ms. The black lines represent linear fittings considering the initial slope of each data set. Loss of linear behavior for different Δ values can be used to validate the Gaussian propagator approximation, and the short-time regime definition.	108
4.10	Signal attenuation Ψ as a function of squared gradient G^2 for different diffusion times, on the water-saturated porous sample, for Δ values between 9 and 16 ms. The black lines represent linear fittings considering the initial slope of each data set. Loss of linear behavior for different Δ values can be used to validate the Gaussian propagator approximation, and the short-time regime definition.	108
4.11	Signal attenuation Ψ as a function of squared gradient G^2 for different diffusion times, on the water-saturated porous sample, for Δ values between 18 and 60 ms. The black lines represent linear fittings considering the initial slope of each data set. Loss of linear behavior for different Δ values can be used to validate the Gaussian propagator approximation, and the short-time regime definition.	109
4.12	Analysis of the normalized time-dependent diffusion coefficients as a function of diffusion length $\sqrt{D_0\Delta}$, extracted from the decay curves presented in Figures 4.9 to 4.11, performed using the short-time approximation proposed by Mitra et al. In order to assure the validity of the short-time regime only the diffusion coefficients extracted from data sets with Δ values up to 20ms were considered. The black line represents a linear fitting considering only the term of order $\mathcal{O}[(D_0t)^{1/2}]$ in Equation (4.35).	109
4.13	^1H spectra of oil-saturated sample (red dotted line), water-saturated sample before (blue dashed line) and after (solid black line) drainage. Even though line are particularly broad it is possible to roughly identify the presences of oil and water peaks in the post drainage spectrum.	112

- 4.14 Estimate of water and oil quantities obtained from weighed mass, spectroscopy (Figure 4.13), longitudinal relaxation (T_1) and PFG measurements after drainage. The estimate error (vertical black bars) was 6% for the weighed mass method and not greater than 4% for the NMR-based techniques. The errors for the spectrum and the T_1 methods were determined as the relative fitting error considering a bi-Lorentzian and a bi-exponential model, respectively. The error for the PFG method was determined as the standard deviation for the saturation values (s_w and s_o) obtained from fittings considering the data sets for different Δ values, using for each one of them the bi-Gaussian model expressed in Equation 4.39. 113
- 4.15 [Upper plot] Signal attenuation Ψ as a function of squared gradient G^2 for different diffusion times, on the water-saturated porous sample after drainage. Acquisitions were performed for 18 different Δ values between 3 and 60 ms. Representative signal decays for Δ values 3, 7, 12, 20 and 30 ms are shown. [Lower plot] Time-dependent diffusion coefficients obtained for water (blue squares) and oil (red triangles) extracted using the bi-Gaussian model in Equation (4.39) from PFG experiments in water-saturated sample after drainage. Fitting error bars are shown for both fluids, however for the oil points error is smaller than marker size. Dashed blue line and dotted red line represent bulk values of water and oil diffusion coefficients (D_0^w and D_0^o), respectively. The black line on the lower plot represents the analysis of post drainage water time-dependent diffusion coefficients as a function of diffusion length $\sqrt{D_0\Delta}$, performed using the short-time approximation (Eq. (4.35)) considering only the term of order $\mathcal{O}[(D_0t)^{1/2}]$ 114
- 4.16 Signal attenuation $\ln[\Psi(\delta, G, r_0, \sigma)/\Psi_0]$ as a function of β^2 for oil diffusion after drainage. Blue solid line denotes the fitting performed with Equation (4.40) considering the formation of oil-in-water droplets within pores. Validity of the carried approximations can be observed through the agreement between data and the proposed model (red triangles) for small β^2 values. Cross markers represent large β^2 values that were excluded from fit. The extracted values for the average radius and the standard deviation assuming a Gaussian distribution of oil droplets radii were $r_0 \approx 20 \mu\text{m}$ and $\sigma \approx 4 \mu\text{m}$, respectively. The relative error in the estimate of r_0 was less than 1 %. 116
- 5.1 Representation of the energy levels for the singlet and triplet states, which in this case compose the base that diagonalizes the Hamiltonian in Equation 5.4. This representation considers a system of coupled spins in a magnetically equivalent environment, assuming the case wherein $\gamma > 0$ and $J > 0$. 123

5.2	Illustration of the exchange mechanisms relating to transitions between two exchange symmetric spin states (upper scheme) and between an exchange antisymmetric and an exchange symmetric state (lower scheme).	124
5.3	Representation of the 2,3-dibromothiophene molecule showing the two protons considered for the singlet-assisted NMR experiments to fulfill the homonuclear weak coupling condition of a spin-1/2 pair in a magnetically inequivalent environment.	133
5.4	Illustration of the singlet-assisted NMR pulse sequence using the (a) WALTZ-16 and the (b) XY-16 spin-locking scheme. The conversion of Zeeman states into singlet states and back are illustrated in the M2S and S2M blocks, respectively. The storage interval, during which the T_s relaxation takes place, is denoted as the spin-locking interval.	134
5.5	Illustration of the WALTZ-16 (a) and the XY-16 (b) spin-locking scheme. In the WALTZ-16 pulse sequence the pulse phases are denoted by x , y , $-x$ and $-y$. The lower case q denotes the same pulse block as in Q , but with the inverted pulse phases. In the XY16 sequence all the pulses have a 180° flip angle (π), with the respective phases also denoted by x , y , $-x$ and $-y$	135
5.6	^1H singlet-assisted NMR spectra of the 2,3-dibromothiophene solution (20mM in DMSO-d^6). The characteristic anti-phase peak can be seen at the site of the chemical shift $\delta_2 \approx 7.72\text{ppm}$	136
5.7	Inversion-recovery T_1 measurement of the 2,3-dibromothiophene solution (20mM in DMSO-d^6). The values obtained for each chemical shift were $T_1(\delta_1) = 8.1 \pm 0.2$ s and $T_1(\delta_2) = 8.9 \pm 0.2$ s.	136
5.8	Singlet relaxation T_s of the 2,3-dibromothiophene solution (20mM in DMSO-d^6) obtained with the sequence illustrated in Figure 5.4, using the XY16 spin-locking protocol. The singlet relaxation time-constant T_s values obtained for each peak of the anti-phase spectra were $T_s = 8.1 \pm 0.5$ s and $T_s = 8.6 \pm 0.5$ s for the positive and the negative peaks, respectively. The cross markers denote the peaks which were excluded from the fit procedure (see text).	137
5.9	Signal attenuation due to diffusion Ψ as a function of gradient field strength G^2 for the water-saturated microsphere packing A: $45\text{-}53\mu\text{m}$, using the 13-interval APFG sequence (Figure 4.4). Diffusion was measured for 18 different diffusion time Δ values, ranging from 4ms up to 1s.	142

5.10	Signal attenuation due to diffusion Ψ as a function of gradient field strength G^2 for the water-saturated microsphere packing B: 106-125 μm using the 13-interval APFG sequence (Figure 4.4). Diffusion was measured for 18 different diffusion time Δ values, ranging from 4ms up to 1s.	142
5.11	Signal attenuation due to diffusion Ψ as a function of gradient field strength G^2 for the water-saturated microsphere packing C: 212-250 μm using the 13-interval APFG sequence (Figure 4.4). Diffusion was measured for 18 different diffusion time Δ values, ranging from 4ms up to 1s.	143
5.12	Signal attenuation due to diffusion Ψ as a function of gradient field strength G^2 for the water-saturated microsphere packing D: 425-500 μm using the 13-interval APFG sequence (Figure 4.4). Diffusion was measured for 18 different diffusion time Δ values, ranging from 4ms up to 1s.	143
5.13	Signal attenuation due to diffusion Ψ as a function of gradient field strength G^2 for the water-saturated microsphere packing E: 710-850 μm using the 13-interval APFG sequence (Figure 4.4). Diffusion was measured for 18 different diffusion time Δ values, ranging from 4ms up to 1s.	144
5.14	Effective diffusion coefficients extracted from the data sets in Figures from 5.9 to 5.13 using a standard 13-interval PGSTE sequence. Only the data sets with diffusion times Δ wherein the Gaussian approximation for the diffusion propagator was taken as valid were considered for the analysis. The error bar for the determination of D_{eff} values increases with the diffusion time as an effect of signal loss due to relaxation.	144
5.15	Singlet-assisted pulsed-field gradient stimulated echo (Singlet-PGSTE) sequence proposed by Yadav et al. [167, 174]. The upper scheme (RF) represents the radio-frequency pulses and the lower scheme (G) the pulsed gradients. At the lower scheme the encoding and decoding pulsed-gradient pairs are illustrated in blue and the spoiler gradients g_1 and g_2 are illustrated in red. The phase cycling schemes are: $\phi_1 = x$; $\phi_2 = x$; $\phi_3 = x, y, x, y, -x, y, x, y$; $\phi_4 = x, y, x, y, x, y, x, y$ and $\varphi_R = x, x, x, x, -x, -x, -x, -x$.	145

Part I

Introduction

Chapter 1

A Retrospect on Relaxation and Diffusion NMR in Porous Media

Nuclear magnetic resonance (NMR) has been widely applied in several segments of both industrial and academic research since its simultaneous discovery in 1946 by Edward Purcell and Felix Bloch [1], at Harvard and Stanford University, respectively. The reason upholding NMR rapid dissemination is also one of its main advantages up to present days: NMR is a high-sensitivity technique able to provide information in a non-invasive manner reaching internally occurring processes and phenomena in samples, without affecting them. Fluid molecules diffusing within porous geometries have become accessible through the interaction between magnetic fields and magnetic moments associated with proton spin. As theoretical and empirical models were proposed to explain the effects of confinement in nuclear magnetic relaxation, a wide range of NMR applications in the condensed matter physics quickly emerged. In this Chapter we present a retrospect on important historical and theoretical aspects regarding the development and the application of relaxation and diffusion NMR techniques to confined systems.

In 1946 Bloch phenomenologically added relaxation terms into the equations that described the Larmor precession of the angular momentum \vec{L} (or the magnetic moment $\vec{\mu}$ associated with nuclear spin) experienced in the presence of a magnetic field \vec{B} [2, 3]. Even though a theoretical background for relaxation processes was not presented at the time, the relaxation terms introduced by Bloch would become a milestone in NMR, especially on what regards its applications in porous media [4–6]. These equations will be addressed again in Section 1.2, in which the fundamentals of NMR are presented.

A theory relating the dependence of relaxation times in liquids on parameters associated with molecular motion, such as temperature and viscosity, was proposed by Bloembergen, Purcell and Pound (BPP theory), in 1948, two years after the discovery of NMR [7]. The work already presented notions related to the “saturation” behavior of spin systems absorbing energy from applied radio-frequencies, and the use of such effect on the observation of spin-lattice relaxation times. The idea that fluid molecules could be adsorbed near solid surfaces and have their movement restricted was also presented, despite the fact that confinement influence on nuclear magnetic relaxation times had not been experimentally observed yet. Bloch, in 1951, also addressed the role of confinement as a mechanism to promote an increase in relaxation rates [8].

In 1950 the seminal work by Hahn entitled “*Spin Echoes*” [9] would establish the grounds for the vast development of pulsed-NMR techniques on the following decades, both in relaxation and diffusion studies. An ensemble of spins under the action of a static magnetic field B_0 can be driven to a non-equilibrium state through the application of radiofrequency (RF) pulses perpendicular to the polarizing magnetic field and tuned at the nuclei’s Larmor frequency (see Section 1.2). The direction of the macroscopic magnetization vector can be changed in proportion to the time during which the RF pulse is held on, inducing a time-controlled rotation in spins’ magnetic moments. Once the RF is removed the ensemble will once again precess freely under the action of the static magnetic field, and a distribution of precession frequencies will be imposed upon the ensemble by inhomogeneities in B_0 . Hahn observed that after two successive 90° (or $\pi/2$) radiofrequency-induced rotations (pulses), separated by a short time interval, such distribution of precession frequencies inflicted some sort of constructive interference as the precessing ensemble recovered phase coherence, giving rise to what Hahn called in his work “spontaneous nuclear induction signals”, or spin echoes.

Herman Y. Carr and Edward Purcell would present in 1954 the advantages of a π pulse for the refocusing effect on precession phase coherence and the formation of a spin echo [10]. The observed phenomenon provided an opportunity for the wide development of pulsed-field NMR techniques. Among a huge set of echo-based protocols, renowned pulse sequences can be cited as an example, such as the CPMG (Carr-Purcell-Meiboom-Gill) protocol [10, 11] for transverse relaxation measurements, the pulsed-field gradient (PFG) sequence proposed by John Tanner in 1965 [12], that would become the foundation for NMR-based diffusion protocols, and also the spin-warp technique that was to be applied a few decades later on the development of magnetic resonance imaging (MRI).

Ten years after the discovery of NMR, in 1956, confinement effects and the influence of pore surface on relaxation rates were observed experimentally. Brown and Fatt [13] studied the influence of wettability on relaxation rates and proposed the use of NMR as a

tool to characterize porous rocks with different wettabilities. Also in 1956 two vital works were published by Torrey. The first one brought the inclusion of diffusion terms (and the self-diffusion¹ coefficient D) into Bloch equations [14], giving rise to the so-called Bloch-Torrey equation of motion for the magnetization. The second work presented by Torrey in 1956 was entitled “*Theory of nuclear spin relaxation of liquids for large surface-to-volume ratios*” [15], and brought in two fundamental notions for the application and interpretation of relaxation measurements of liquids under confinement: the establishment of a diffusion regime and an expression accounting for the surface influence on relaxation rates. Torrey introduced the idea that, if molecules diffuse fast enough, nuclear magnetization inside a single pore can be held uniform, and the interaction of molecules with pore surface would inflict an increase in the overall relaxation rate. As a consequence of such regime it was proposed that the observed relaxation rate inside a pore could be modeled as:

$$\frac{1}{T} = \frac{1}{T_b} + \frac{V_s}{V} \frac{1}{(T_s + \tau)}, \quad (1.1)$$

wherein T_b stands for the bulk relaxation time, V_s is the volume of a surface layer of the liquid, V is the pore volume, T_s is the relaxation time associated with pore surface, and τ represents the residence time of molecules in the surface layer. The hypothesis of fast diffusion regime would support, for years to come, one of the most common models used in petrophysics, relating pore sizes and multiexponential relaxation profiles, that will be addressed in the following sections.

Here, the author would like to remark some important features regarding the application of relaxation measurements to confined fluids that will compose the main motivation for the work presented in the Chapter 3 of this thesis. Almost all the information extracted from relaxation profiles of liquids in porous media is model-dependent [16]. Molecules under thermal motion are constantly diffusing within (and sometimes among) pores and interacting with pore walls. Confinement scale, pore network connectivity, surface physico-chemical properties and diffusion regimes are a few examples of features that will influence observed relaxation rates, and must be considered for the application of models and interpretation of the results. This is especially relevant for the case of porous rocks, and the development of NMR in Petrophysics. A macroscopic rock sample can represent a complex system of pores, in which the previously mentioned features are not necessarily homogeneous. Hence, in these systems, relaxation is expected to be multi-exponential, and the extraction of relaxation rates from raw data and the establishment of a relation between these rates and confinement geometry features depends on a set of *a priori* hypothesis.

¹Two approximations will be considered in the upcoming developments presented in this thesis. The first one is that the diffusion tensor \mathbf{D} is space-independent. The second one is that the diffusion process of nuclei is isotropic. Considering these two approximations, the diffusion tensor can be reduced to a scalar diffusion coefficient D [4]. Here the term self-diffusion was also employed. A proper distinction between diffusion and self-diffusion processes will be addressed in the first section of Chapter 4.

Notwithstanding, the application of NMR to petrophysical studies was closely related to the development of the technique itself.

As the relation between relaxation rates of confined fluids and confinement features was being investigated, the research on logging projects was actively promoted by oil industry. Table 1.1, adapted from the work of Kleinberg and Jackson [17], presents a timeline with the development highlights of nuclear magnetic resonance for well logging (NML), from the discovery of NMR in 1946 up to the year 2000. In 1948 results obtained by Russell Varian, observing the proton NMR free precession using the Earth's magnetic field, led to several studies focused on the building of a tool capable of detecting NMR signals from water and oil in porous rocks, inside the wells at thousands of meters below the sea level. Varian itself filed a patent in 1952 for the construction of a NMR tool for well logging using Earth's magnetic field [18].

The investments from oil industry on NML research were an important part of the expansion of NMR since its early days. The potential application of relaxation and diffusion measurements to the characterization of water and oil in porous rocks motivated the development of new NMR techniques. Up to recent years several prominent authors with a solid work on the application of NMR techniques to the characterization of porous media, such as Yi-Qiao Song, Martin D. Hürlimann, Lalitha Venkataramanan, Robert L. Kleinberg and Lawrence M. Schwartz, were also part of oil companies research staff.

The initial steps on NML were focused on the development of a tool capable of detecting separated NMR signals from water and oil. This idea was based on the notion that bulk samples of both fluids present distinct relaxation rates (almost one order of magnitude higher for oil compared to water). However, not much later than this first initiative researchers would realize that under confinement, and mostly in a configuration where water is the wetting phase and oil occupies the innermost part of pore space, both fluids could exhibit similar relaxation rates. Although this behavior could frustrate the efforts invested in NML, still in the 1950's the relationship between relaxation rates and confinement geometrical features such as specific surface, porosity and permeability was being investigated, which motivated further developments. A U.S. patent entitled "*Methods for investigating the properties of fluid (materials) within porous media*" [19] was filed in 1956 by Henry Torrey, Jan Korringa and Bob Brown, summarizing NMR relaxation techniques applied in well logging for observation of water and oil in porous rocks.

The development of NML in the 1960's included initial experimental tryouts and the availability of the first commercial NML service for field applications. Seevers [20] proposed in 1966 a method to estimate the specific permeability of sandstones using the free fluid index (FFI) - a parameter created to quantify the movable portion of a confined fluid -

Table 1.1: Timeline of NMR Logging. Adapted from ref. [17].

Copyright © 2001 John Wiley & Sons, Inc.

1946	Discovery of NMR by Bloch (Stanford) and Purcell (Harvard)
1948	Russell Varian files patent for Earth's-field NMR magnetometer
1950	Spin echo, Hahn (U. of Illinois)
1952	Russell Varian files patent for Earth's-field NMR well logging
1953	Nobel Prize in Physics awarded to Bloch and Purcell
1954	Carr and Purcell devise spin-echo pulse train
	Harold Schwede (Schlumberger) files patent application for permanent magnet well logging tool
1956	Discovery of reduced fluid relaxation time in porous media by Brown, Fatt, and others
1960	First Earth's-field NML tool—Chevron Research Lab and collaborators
1960's	Laboratory and theoretical studies in various universities and petroleum laboratories of the effect of restricted diffusion on T_1 , and relationship of T_1 and permeability
1960's	Several companies offer NML commercial logging service
	NML fails to live up to advance billing; NML gains bad reputation in petroleum industry
1978	Schlumberger introduces new, improved NML tool
1978	Jackson at Los Alamos, invents first "inside-out" pulsed RF NMR logging technique
1980	Laboratory demonstration of Los Alamos technique
1983	Proof-of-principle demonstration of Los Alamos logging technique at Houston API test pit
1984	NUMAR formed to commercialize advances in medical NMR technology
	Schlumberger begins development of permanent magnet/pulsed NMR technique
1985	NUMAR obtains license for Los Alamos inside-out NMR patent
1985	NUMALOG demonstrates increased S/N for new magnet/RF scheme in laboratory scale model
1989	First field test of full scale NUMAR logging tool in Conoco test hole, Ponca City, OK
1990	NUMAR announces commercial availability of MRIL logging service based on Series B single frequency tool
1992	Schlumberger starts field test of skid-type pulsed NMR tool
1993	Numar and Western Atlas sign cooperative agreement for MRIL services
1994	NUMAR introduces dual frequency MRIL Series C tool
	Western Atlas logs MRIL in combination with conventional tools
1995	Schlumberger announces commercial introduction of CMR tool
	Peoples Republic of China purchases two logging systems from Western Atlas, including MRIL
1996	NUMAR and Halliburton sign cooperative agreement for MRIL services
1997	Halliburton buys NUMAR
1990's	Laboratory and theoretical studies of the effect of restricted diffusion on T_2 (most NMR logging data use T_2)
2000	NMR logging-while-drilling prototype

and T_1 relaxation times. In the late 1960's the notion of a "cutoff" T_1 relaxation time was introduced by Timur [21], and applied to distinguish a movable water phase, associated with longer relaxation times, from an irreducible one, exhibiting faster relaxation.

In the 1970's significant biological applications of NMR were developed alongside the research in petrophysics. The employment of increased relaxation times to the detection of tumors was proposed in 1971 by Raymond Damadian [22]. Chang et al. [23] conducted a study on the influence of confinement on the NMR spectral line width of water in rat muscle cells. Nonetheless, possibly one of the most important works of that decade was published by Kenneth R. Brownstein and Charles E. Tarr in 1979, entitled "*Importance of classical diffusion in NMR studies of water in biological cells*" [24]. In this seminal work the authors proposed a theory based on classical diffusion and the Bloch-Torrey equation to explain the multi-exponential behavior of NMR signals obtained from fluid molecules diffusing under confinement, without the need to consider the existence of different fluid phases.

The main presented idea was to separate the relaxation associated with the volumetric part of the confinement environment, or "bulk sink", from the relaxation associated with the confining surface, or "surface sink". According to the proposed model the diffusion equation for the magnetization density $m(\vec{r}, t)$ inside a volume V , and the boundary condition² on the confining surface S can be written, respectively:

$$\frac{\partial m(\vec{r}, t)}{\partial t} = D\nabla^2 m - \lambda m, \quad (1.2)$$

$$\left[D \frac{\partial m(\vec{r}, t)}{\partial \hat{n}} + \rho m \right] \Big|_S = 0, \quad (1.3)$$

wherein λ [s^{-1}] accounts for the relaxation rate associated with the bulk sink, \hat{n} is the unity vector normal to the surface, ρ [m/s] is the parameter associated with the relaxation on the surface S (or surface relaxivity [25]) and the magnetization density $m(\vec{r}, t)$ satisfy the initial condition $m(\vec{r}, 0) = M(0)/V$. The general solution for these equations can be written as a summation over a set of normal modes:

$$m(\vec{r}, t) = \sum_{n=0}^{\infty} A_n F_n(\vec{r}) e^{-\frac{t}{T_n}}, \quad (1.4)$$

in which A_n are constants, and $F_n(\vec{r})$ and $1/T_n$ [s^{-1}] are the eigenfunctions and eigenvalues, respectively, that satisfy the eigenvalue problem described by Equations 1.2 and 1.3.

²The boundary condition expressed in Equation 1.3 is called *Robin* boundary condition, used to portray an impermeable surface on which nuclei can partly lose their magnetization. Here, this loss is expressed by the parameter ρ [25]. The case of an impermeable wall that does not affect nuclei magnetization ($\partial m(\vec{r}, t)/\partial n = 0$) is referred to as a *Neumann* boundary condition [4].

The observed macroscopic magnetization $M(t)$, defined as the integral of $m(\vec{r}, t)$ over the volume V , will now be expressed as a summation of magnetization modes, each one associated with your respective eigenvalue (relaxation rate):

$$M(t) = M(0) \sum_{n=0}^{\infty} I_n e^{\frac{-t}{T_{1n}}}, \quad (1.5)$$

wherein I_n represents the weight of the n th eigenfunction (with its associated eigenvalue $1/T_n$) on the observed signal, satisfying the normalization condition:

$$\sum_{n=0}^{\infty} I_n = 1. \quad (1.6)$$

In their original work, Brownstein and Tarr presented the solution for these equations for regular confining geometries (planar, cylindrical and spherical), and also successfully applied the model to adjust NMR data obtained from spin-spin relaxation measurements in rat gastronemius muscle cells. The proposed model showed that a multi-exponential NMR signal, depending on the diffusion regime, could be observed even from fluid molecules confined into a single pore, as no more than a consequence of the mathematical structure of an eigenvalue problem with boundary conditions.

Although they were considered for applications in biological systems, the results obtained by Brownstein and Tarr could be applied for any kind of porous media, including rocks [26]. Another important feature of this work was the distinction between different diffusion regimes for the analysis of the overall relaxation rates observed. Supposing a fluid with a self-diffusion coefficient D [m^2/s] confined within a simple geometry with a characteristic dimension a [m] and a surface relaxivity ρ [m/s], the dimensionless parameter $\rho a/D$ can be used to define a diffusion regime, wherein:

$$\frac{\rho a}{D} \gg 1, \quad (1.7)$$

characterizes a *slow diffusion* regime, and:

$$\frac{\rho a}{D} \ll 1, \quad (1.8)$$

defines a *fast diffusion* regime. In the former case, diffusion limits the signal decay and the observed relaxation rate will be, in a fair approximation, proportional to a^2/D [24, 26]. For the latter case, molecules will, on average, experience the relaxation at pore surface several times, and the observed decay will be dominated by surface effects, and proportional to a/ρ .

Once again, it is important to draw attention to the tricky effort on interpreting

observed NMR relaxation rates, or even to directly associate such rates to geometrical parameters. Although it may seem straightforward to employ this theoretical framework and its approximations on complex porous materials, such as rocks, one can not perform this task without the assumption of a set of *a priori* information on confinement features, especially the ones regarding pore network connectivity. To set a proper definition for the concept of a “pore” itself is non-trivial when porous space is well connected. Most of the approximations employed above can be successfully applied in systems where the diffusion of fluid molecules will occur predominantly inside a single pore, rather than among pores, in a way that the observed set of relaxation rates will reflect the individual contribution of each “isolated” pore to the total signal decay, and most importantly, that the assumed pore scale heterogeneity do not implicates the presence of different diffusion regimes in the investigated system. Elliot Grunewald and Rosemary Knight [27] presented a systematic study on the influence of pore coupling, referring to the process where nuclei diffusing within a well connected porous systems probe two different pores before relaxing completely. Their results are discussed considering the role of surface relaxivity on such process and the observed distribution of relaxation rates in systems with a heterogeneous and well connected pore scale.

Another common assumption relates to the surface relaxivity parameter ρ and regards its homogeneity along the investigated system. While this approximation can be held valid for some specific biological samples, or even for some particular types of rocks, it can not be applied for systems that exhibit significant heterogeneities in its chemical composition, such as carbonate rocks, for an example. A thorough investigation on the microscopic details of surface relaxation is not necessary here for one to intuitively relate the chemical composition of pore walls to the overall effect of ρ in surface relaxation and, consequently, to assume the existence of a distribution of ρ values in systems with mineralogenic heterogeneity. An enlightening discussion on the microscopic mechanisms of surface relaxation, along with a theoretical framework for nuclear magnetic relaxation in the presence of surface paramagnetic sites, is presented in the PhD thesis of Moacyr do Nascimento [28, 29]. Despite those specifics, the model proposed by Brownstein and Tarr had a largely positive impact on NMR Petrophysics, and numerous works and techniques were (and still are) dedicated to comprehend and characterize the parameter associated with surface relaxivity and its influence on the nuclear magnetic relaxation of confined fluids [26, 30–32].

Crucial developments on diffusion studies were also achieved in the 1960’s and the 1970’s after the seminal work by Stejskal and Tanner [33] in 1965, presenting the pulsed-field gradient nuclear magnetic resonance (PFG-NMR) technique for diffusion measurements. Nonetheless, the first steps in NMR diffusometry were given long before. The effect of molecular self-diffusion in NMR had already being addressed in the work of Hahn [9] in

1950, in which he observed that the measured NMR signal was attenuated by the self-diffusion of molecules carrying nuclear spins. Hahn noticed that this process depended on the homogeneity of the applied magnetic field, and used the known value of water self-diffusion coefficient to estimate the field gradient of his own magnet. Carr and Purcell [10] also proposed in 1954 an arrangement of wires carrying electrical currents to produce a magnetic field gradient that could be used to estimate the water self-diffusion coefficient.

Initial developments in NMR diffusometry took place between the late 1950's and the earliest 1960's, and were based in the application of constant magnetic field gradients [34–36]. The development of coil technologies and the opportunity for rapidly switching and reversing magnetic field gradients provided the grounds for the fundamental PFG technique proposed by Stjeskal and Tanner. In this new NMR-based diffusion measurement protocol a pair of strong magnetic field gradient pulses of reversed polarity were employed to “label” and “read” molecules carrying nuclear spins according to a space-dependent precession phase, introduced by the field gradient pulses. The diffusion coefficient of molecules could then be determined associating the remaining phase of the spin ensemble with the displacement of molecules between labeling and reading steps. The theoretical background for the PFG-NMR technique will be addressed in details in Chapter 4.

The non-invasive ability of relaxation and diffusion NMR to monitor processes in molecular level was one of the main reasons for its application in different research fields, other than porous media petrophysics, such as food science [37], molecular dynamics [38], polymer systems [39], crude oils [38, 40] and also material science [41]. All these fields also benefit from the capabilities of the high-field NMR spectroscopy. The chemical shift resolution of protons with different molecular environments, in the presence of high-homogeneity magnetic field strengths up to 28 T, produced by superconducting magnets [42], allows a detailed investigation of molecular structure and dynamics. On the other hand, low-field NMR, usually performed with benchtop equipment, based on permanent magnets with relatively low homogeneity, does not possess such ability, and the search to improve its resolving power motivated the development of 2-dimensional techniques, or 2D NMR.

The idea was to combine different experiments into one protocol, varying two distinct parameters simultaneously, in order to access more information on molecular level. Since relaxation and diffusion of fluids were shown to be sensitive to features like pore confinement scale, fluid viscosity or concentration of ions, both techniques could be combined into one protocol able to produce two-dimensional correlation maps, with significantly increased resolving power. Relaxation-relaxation protocols (T_1 - T_2) [43], (T_2 - T_2) [44, 45], or even diffusion-relaxation (D - T_2) [46] and diffusion-diffusion (D - D) [47] are a few examples of techniques that can be performed in low-field equipment, and are capable to produce two-

dimensional correlation maps that can be interpreted to distinguish different components of a sample, and also to monitor molecular dynamics (see Section 1.2.3).

Concurrently, data processing of 2D NMR measurements emphasized another important aspect of relaxation studies, also relevant for one-dimensional experiments: the extraction of relaxation rates from multiexponential data sets. The determination of time constants in multiexponential decay phenomena is a subject of interest in many areas of knowledge, especially in relaxation NMR. The inherent difficulties related to the mathematical structure of the problem can cause data analysis to be a considerably burdensome, and most often, an ambiguous task.

A multiexponential signal $f(t)$ (as the one commonly observed in NMR relaxation measurements of liquids in porous materials, for an example) can be represented by a sum of exponential decays, each one characterized by a decay amplitude A and a decay rate λ , expressed by:

$$f(t) = \sum_{i=0}^n A_i \exp(-\lambda_i t), \quad (1.9)$$

for the discrete case, and

$$f(t) = \int_0^{\infty} g(\lambda) \exp(-\lambda t) d\lambda, \quad (1.10)$$

for the continuous case, wherein the spectral function $g(\lambda)$ represents a continuous distribution of decay rates.

Assuming a context where one holds a model based on *a priori* information, regarding the behavior of total signal as a function of its exponential components, a simple fit procedure can be applied to the measured data for one to extract such distribution of rates. Nonetheless, the general method for solving the multiexponential analysis problem expressed in Equation 1.10, known as the Laplace integral equation, can be achieved performing the inverse Laplace transform of $f(t)$ in order to determine $g(\lambda)$ [48]. Notwithstanding, equations such as 1.10 belong to a class of differential equations known as Fredholm integral equations of the first kind, which are known to be ill posed, or poorly conditioned from the mathematical standpoint, meaning that to this end, the obtained solution $g(\lambda)$ may not be unique, not exist, or even may not depend continuously on the data set [49].

Therefore, in order for one to minimize uncertainties, and extract a mathematical solution with physical meaning, a set of *a priori* information must be incorporated into the inversion method. These imposed constraints are known as regularization tools. The positivity constraint regarding the solution $g(\lambda)$, based on the assumption that the investigated system possess no relaxation rates associated with negative amplitudes, or even the principle of parsimony, applied for one to choose the simplest solution among

all possible ones, are important examples of common regularization tools. The necessity of extracting time constants from real data sets, which are discrete and also commonly noisy, motivated the development of inverse Laplace transform algorithms, with different regularization methods, which could be applied to the analysis of one- and two-dimensional NMR experiments [43, 50–52].

The ill-posed character of multi-exponential analysis inflicts here another barrier on the onerous task of interpreting relaxation rates obtained from NMR experiments, which in this case, relates only to the mathematical structure of the problem. Different mathematical solutions, in some cases with equally valid but distinct physical meanings, can be obtained from the same data set depending on noise level, or on the chosen regularization method and the criteria adopted to determine the value of the applied regularization parameter [49]. Once more, one will be required to evaluate the available information on the investigated system, in order to choose, among the set of possible solutions, the most suitable one according to the phenomena investigated. The mathematical problem of multiexponential analysis, as well as the other previously mentioned barriers of interpreting relaxation rates obtained from liquids under confinement, are discussed on the work presented in Chapter 3.

The 1980's brought another milestone in the history of NMR, made possible mostly by improvements in pulsed-field gradient technology: the development of magnetic resonance imaging (MRI), one of the greatest achievements of NMR comprising both relaxation and diffusion techniques. The combination of selective (narrow band) radio-frequency and field gradient pulses allows the excitation of spins in a limited region of the sample's space, such as a specific plane or volume, as well as the labeling of the observed magnetization by a space-dependent precession phase. The recorded NMR signal intensities are spatially resolved and can be associated with representations in a reciprocal-space, also known as k -space, or the domain of spacial frequencies [53–56]. These reciprocal-space variables (“wavenumbers”) can be converted into real-space images by two- or three-dimensional Fourier transformations of the signal as a function of the respective wave-vector components. The technique proposed by Edelstein in 1980, known as the “spin-warp” method, set the ground for the development of several MRI techniques, employing different contrast mechanisms and covering a wide range of applications.

Advances in relaxation and diffusion NMR techniques for the characterization of fluids confined in porous media were mostly motivated by the abundant information that could be retrieved from nuclear spins diffusing across the pore network, their interactions with the confining surfaces and the overall effect of confinement in measured relaxation rates and diffusion coefficients. The extraction and interpretation of such information relies on the accompanying development of proper theoretical frameworks to provide a physical

description on the internally occurring processes. Particularly, the substantial increase in the observed relaxation rates of fluids under confinement was a subject of great interest.

Initially, it was believed that diffusing molecules were somehow locked up at pore surface under the action of binding forces, during a time interval wherein relaxation mechanisms took place, such as homonuclear dipole-dipole coupling, or the interaction between nuclei and paramagnetic centers or free electrons at the pore surface [4, 29]. Notwithstanding, field-gradient NMR diffusivity measurements of aqueous protein systems, and also polar and non-polar fluids adsorbed in porous silica glass, presented by Kimmich et al. [57, 58], demonstrated that the observed attenuation in measured diffusion coefficients was mainly associated with geometric restrictions rather than to interactions of adsorbates with solid surfaces, which means that the residence time of molecules diffusing across the surface was actually not as long as it was expected, and adsorbate molecules exhibited translational diffusivities close to bulk values. Despite those findings, it was known that the characteristic time scale of molecular reorientation process³ of confined fluid molecules could be increased by up to eight orders of magnitude in comparison with bulk conditions [4]. The explanation for the discrepancy between the two observed phenomena was provided by the theory called bulk mediated surface diffusion (BMSD) [63, 64]. It was proposed that adsorbate molecules move from one adsorbing site to another, performing a kind of Lévy walk along pore surface. That being the case, the reorientation process of adsorbate molecules was indeed correlated with surface topology, or its orientations, and was mediated by these translational displacements.

A two-dimensional theory was proposed by Korb et al. to correlate adsorbate diffusion and the role of paramagnetic sites in relaxation of molecules at pore surface [65, 66]. The model was successfully applied in field-cycling NMR experiments (*i.e.*, measurement of relaxation rates at different magnetic field strengths) of hydrated cement-based materials containing paramagnetic contaminants (*e.g.*, iron ions), and the observed dispersion of relaxation rates was used to extract the surface to volume ratio of the confining geometry. [67, 68].

The presence of paramagnetic sites in pore walls acting as relaxation “sinks” was shown to be a crucial mechanism to explain enhanced relaxation of liquid molecules at pore surface. Nascimento et al. [29] also proposed a theory for the NMR relaxation of polar fluids (*e.g.*, water) confined to porous structures exhibiting a scarce surface distribution of paramagnetic centers, referring to any molecular configuration able to bear unpaired electrons, such as adsorbed paramagnetic ions or even superficial crystallographic defects.

³An important feature of liquid water is the presence of directional hydrogen-bond interactions. These bonds can assume different configurations with distinct bond lengths and angles, associated with liquid water capacity in rearranging its molecules to enable, for example, the solvation of reactants. This rearrangement is characterized by the molecular reorientation of the water molecules. Experimental techniques like NMR [59] and light scattering [60] can be used to investigate this process [61, 62].

One of the main results accomplished by the proposed model was to show that the local anisotropy introduced by the dominant dipolar coupling in the relaxation rates of active surface elements can be measured by the dependence on sample orientation in the overall relaxation rates of the saturating fluid.

The overall effect of confinement in the diffusion of liquids in porous media was also observed. The diffusivity of fluid molecules within porous materials was attenuated with respect to its bulk value, and diffusion itself could be used to extract information from the interaction between the fluid and the porous matrix, along with geometric properties of the pore space (see Chapter 4). The behavior of spin-echo attenuation due to diffusion of molecules in restricted geometries, such as in a set of isolated pores, in the presence of steady gradients, was investigated by Neuman [69], and adapted for the case of pulsed-field gradients by Murday et al. [70] and Callaghan et al. [71].

In materials with interconnected pores, molecules are allowed to probe the pore space depending on pore connectivity and the diffusion length, a quantity proportional to the bulk diffusivity of the fluid and the diffusion time. Accordingly, the analysis of the effect of confinement in diffusion must be carried out considering the observed diffusion regime. Mitra [72] analyzed the diffusion of confined fluids in the so called short-time regime, which can be assumed under the validity of the condition:

$$\Delta \ll \frac{R_p^2}{D_0}, \quad (1.11)$$

wherein Δ [s] represents the diffusion time, R_p [m] denotes the characteristic pore radius and the fluid bulk diffusivity is expressed by D_0 [m²/s]. Mitra derived an expression relating the observed diffusivity of confined fluids with geometry parameters, such as specific surface (or surface-to-volume ratio), grain average curvature and surface relaxativity. The application of short-time regime analysis on diffusion measurements became a powerful tool for the characterization of porous materials, including porous rocks [30]. The ability of diffusion measurements to distinguish fluids with distinct diffusivities and the framework of short-time regime diffusion analysis were applied to the investigation of water-oil geometrical conformation in drainage experiments. This work, and a detailed theoretical background on diffusion NMR are presented in Chapter 4.

Restricted diffusion of fluid molecules in interconnected pore spaces could also be analyzed in the long-time regime, in which the diffusion length can be considered much larger than the characteristic confinement scale:

$$\Delta \gg \frac{R_p^2}{D_0}. \quad (1.12)$$

In such regime, molecules diffuse within and across pores, probing, on average, not only the confinement scale but also the connectivity of the pore network. Both properties relate to an important geometrical characteristic of pore spaces: the tortuosity (see Section 5.2.1). Depending on the physical quantity investigated, different types of tortuosities can be defined, including the so-called diffusive tortuosity (τ_d) [73], related to the ratio between the diffusion coefficient of diffusing species in free fluid (D_0) and its value measured in a porous medium ($D(\Delta)$) in the long-time diffusion regime [30, 73]:

$$\lim_{\Delta \rightarrow \infty} \frac{D_0}{D(\Delta)} = \tau_d. \quad (1.13)$$

The major barrier regarding long-time measurements in NMR is relaxation, since as diffusion time is increased, longitudinal and transverse relaxation attenuate the observed signal. If one considers the diffusion of water molecules at room temperature ($D_0 \approx 2.3 \times 10^{-9} \text{ m}^2/\text{s}$) in a porous sample with characteristic pore scale of tens of nanometers, the condition expressed by Equation 1.12 can be fulfilled for diffusion times as large as a few milliseconds, which are accessible by usual NMR techniques. Notwithstanding, for samples exhibiting pore sizes with characteristic lengths as large as hundreds of micrometers, a long-time regime condition for diffusion may only be reached with diffusion times as large as tens of seconds, a time range during which almost all NMR signal can be lost due to relaxation effects.

In 2004 Carravetta et al. [74, 75] presented a new technique wherein special molecules containing pairs of coupled spins-1/2 displayed long-lived nuclear spin order, exhibiting relaxation times of orders of magnitude above their usual longitudinal relaxation time. The two nuclear spins can be combined to create a non-magnetic singlet state with total spin $I = 0$, and such long-lived states could be exploited in a variety of NMR experiments [76–78]. Tourell et al. [79] presented the application of long-lived singlet order in diffusion NMR experiments to measure the tortuosity in samples of randomly packed spheres, reaching diffusion times of up to 240s. The technique comprises complex pulse sequences combining the steps for the preparation and maintenance of singlet states, as well as the encoding and decoding stages for PFG-NMR measurements. The theoretical background and initial experimental developments in singlet-assisted NMR are presented in Chapter 5.

Chapter 2

Nuclear Magnetic Resonance (NMR)

2.1 Fundamentals of NMR

In this Section a theoretical background for nuclear magnetic resonance will be presented. Notions from both, the semi-classic and the quantum descriptions of NMR, will be resorted in order to clarify important aspects of the phenomenon and the techniques presented in the following Chapters. A more detailed parallel on the classical and the quantum descriptions of NMR and their equivalences can be found in references [2] and [3].

2.1.1 Magnetic Moments in a Magnetic Field

In the electromagnetism theory the Ampère's law quantitatively relates a magnetic field to the electric current or varying electric field that produces it. Therefrom, the phenomenon of magnetism on matter was similarly associated with the existence of microscopic current loops [2].

For an example, the orbital magnetic moment $\vec{\mu}_L$ associated with the orbit of an electron with charge e and an orbital angular momentum \vec{L} , has its magnitude expressed¹ as:

$$\mu_L = \left(\frac{e}{2m_e}\right)L, \quad (2.1)$$

¹Equation 2.1 can be easily deduced assuming the magnetic moment associated with a current loop $\mu = IA$, where A denotes the area of a circular loop. The current I can be expressed in terms of the charge e and the orbital period, T , wherein $I = e/T$ and $T = 2\pi r/v$, being v the velocity of the electron on its trajectory. Using the expression for the magnitude of the angular momentum in a circular trajectory $L = rmv$, the relation in Equation 2.1 is obtained.

wherein m_e is the electron mass. Electrons also exhibit an intrinsic angular momentum associated with their spin $1/2$. The experiment of Stern and Gerlach proved the existence of a magnetic moment $\vec{\mu}_S$ associated with the electronic spin momentum \vec{S} , whose magnitude could be expressed similarly to the result obtained in Equation 2.1:

$$\mu_S = \left(\frac{e}{2m_e}\right)gS, \quad (2.2)$$

in which g is the Landé splitting factor, or g factor, whose value is approximately 2 for a free electron.

Nuclei also exhibit a magnetic moment associated with the total nuclear spin angular momentum, \vec{I} , a quantity represented by an integer or half-integer number. The nuclear magnetic moment associated with the spin momentum was also measured in the experiments of Stern and Gerlach [80], and its magnitude can be similarly expressed:

$$\mu_I = \left(\frac{e}{2m_p}\right)g_I I, \quad (2.3)$$

wherein m_p stands for the proton mass and g_I is the corresponding g factor. Considering that the proton mass m_p is a few thousand times greater than the electron mass m_e , and that both S and I are of the order of unity, the spin magnetic moments of nuclei are in fact one thousandth of the electron spin magnetic moment.

Particles such as electrons, protons and neutrons can be imagined as spinning on their axes. In many atoms the nucleus, containing a certain number of protons and neutrons, exhibits no overall spin (such as ^{12}C), since these spins are paired against each other. Nevertheless, in some atoms such as ^1H and ^{13}C the nucleus does possess an overall spin. According to the quantum mechanics theory, a nucleus of spin I will have $2I + 1$ possible orientations, or quantum states. A nucleus with spin $I = 3/2$ will exhibit four possible orientations, $+3/2$, $+1/2$, $-1/2$ and $-3/2$. In the absence of an external magnetic field, these orientations are of equal energy. In the presence of a magnetic field these energy levels split, and for each orientation, the component parallel to the direction of the applied magnetic field will assume values of $\hbar m$ (see Figure 2.1), wherein m is the magnetic quantum number [81], running from $-I$ to I in steps of unity. This split in the energy levels in the presence of a static magnetic field is known as the Zeeman effect (named after Dutch physicist Pieter Zeeman) and the splitted energy levels are also referred to as Zeeman levels.

The energy of a magnetic moment $\vec{\mu}$ under the action of a magnetic field \vec{B} is described by classical magnetism as the inner product:

$$E = -\vec{\mu} \cdot \vec{B}, \quad (2.4)$$

and the energy associated with the m_{th} state, considering a magnetic field with the form $\vec{B} = (0, 0, B_0)$, is given by:

$$E = -\left(\frac{g_I e}{2m_p}\right)m\hbar B_0. \quad (2.5)$$

The factor $g_I e/2m_p$ is defined as the nuclear gyromagnetic ratio γ , a property (or a signature) of the observed nuclei, and also an important quantity in NMR. Table 2.1, adapted from reference [2], shows the value of the gyromagnetic ratio for nuclei commonly used in NMR, as well as their natural abundance. Hence, following Equation 2.5, the energy difference between two adjacent levels can be written as:

$$\Delta E = \hbar\gamma B_0. \quad (2.6)$$

According to the Planck-Einstein relation ($E = \hbar\omega$), the expression in Equation 2.6

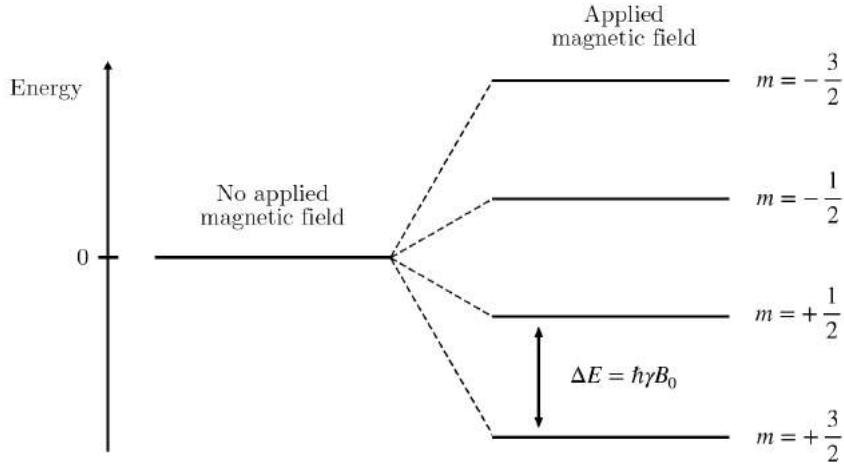


Figure 2.1: Zeeman energy levels for a nuclear spin $I = 3/2$ in the presence of an applied magnetic field $\vec{B} = (0, 0, B_0)$. The magnetic quantum number m can assume four different values $(2I + 1)$, and the energy difference between two adjacent levels is proportional the applied magnetic field and the nucleus gyromagnetic ratio γ .

implies that transitions between two energy levels (or resonance) can be induced through an applied radiation with angular frequency ω , wherein:

$$\omega = \gamma B_0. \quad (2.7)$$

The angular frequency ω , also known as the resonance frequency, had its first applications after the development of NMR for the determination of magnetic field intensities, using the known value of the proton gyromagnetic ratio. Since the magnetic field experienced by a certain atomic nucleus is affected by local field fluctuations, related to the nucleus

Table 2.1: Gyromagnetic ratio of some nuclei and their natural abundance. Adapted from ref. [2].

Copyright © Cambridge University Press.

Isotope	Spin [I]	Natural Abundance [%]	Gyromagnetic Ratio $\gamma/2\pi$ [MHz/Tesla]
¹ H	1/2	100	42.58
² H	1	0.02	6.54
³ He	1/2	0.0001	32.44
⁷ Li	3/2	92	16.55
¹³ C	1/2	1.1	10.71
¹⁹ F	1/2	100	40.06
²³ Na	3/2	100	11.26
²⁹ Si	1/2	4.7	8.46
³⁵ Cl	3/2	75	4.17

chemical environment and diamagnetic screening effects from electrons and interactions with other nuclei, the resonance frequency ω became the foundation for the elucidation of chemical structures, one of the most prosperous applications of NMR.

Let us consider, for an example, the case of a system composed by N spin-1/2 nuclei in the presence of a magnetic field $\vec{B} = (0, 0, B_0)$. Following the Boltzmann statistics, in the thermodynamical equilibrium at a fixed temperature T , a number N_m of nuclei will occupy an energy level E_m , according to:

$$N_m = \frac{N e^{-E_m/kT}}{\sum_{m'} e^{-E_{m'}/kT}} = \frac{N e^{-\gamma \hbar m B_0/kT}}{\sum_{m'} e^{-\gamma \hbar m' B_0/kT}}, \quad (2.8)$$

wherein k is the Boltzmann constant, T denotes the temperature, $m' = \{-1/2, +1/2\}$ and the occupation numbers N_m satisfy the condition $N = \sum_m N_m$. The macroscopic equilibrium magnetization M_0 can be obtained by the summation over magnetic moments in each population:

$$M_0 = \sum_m N_m \mu_z = \gamma \hbar \sum_m m N_m = \gamma \hbar \left(\frac{N^+}{2} - \frac{N^-}{2} \right), \quad (2.9)$$

in which N^+ and N^- denote the populations occupying, respectively, the lower energy level, representing the spin up or parallel to the applied field, and the higher energy level, representing the spin down or anti-parallel to the applied field. Therefore, the nuclear polarization will depend on the difference between both populations, and from Equation 2.8 it follows that:

$$\frac{N^-}{N^+} = e^{-\gamma \hbar B_0/kT}. \quad (2.10)$$

A quick estimate can be carried out: the thermal energy at room temperature kT is of the order of 4×10^{-21} J, while the magnetic energy $\gamma\hbar B_0$, considering a magnetic field capable of producing a resonance frequency of 2 MHz for the proton ($B_0 \approx 0.04$ T), is approximately 12×10^{-14} J. Therefore, the factor $e^{-\gamma\hbar B_0/kT} \approx 1 - 3 \times 10^{-7}$, which means that the number of spins occupying the lower energy level N^+ will exceed the number of spins occupying the higher energy level N^- by only three parts per ten million. The nuclear polarization, or the net magnetization, is in fact extremely low and also depends on the value of the applied magnetic field. This represents one of the challenges in performing NMR techniques using nuclei with low natural abundance (see Table 2.1), and also one of the advantages of high-field NMR equipment, since superconducting magnets are capable of producing magnetic field strengths from a few Tesla up to tens of Tesla, increasing significantly the nuclear polarization.

2.1.2 Larmor Precession and the Spin Equation of Motion

Here, we shall address the classical description of a magnetic moment under the action of a magnetic field, as a simple framework for one to investigate the dynamics of a collection of such moments and the relation between magnetic resonance and relaxation.

A magnetic moment $\vec{\mu}$ in the presence of a magnetic field \vec{B} will experience a torque Γ expressed as:

$$\Gamma = \vec{\mu} \times \vec{B}. \quad (2.11)$$

According to the rotational analogue to Newton's Second Law, the torque equals the rate of change of the angular momentum. For the spin angular momentum I , we have:

$$\vec{\mu} \times \vec{B} = \frac{\partial \vec{I}}{\partial t}, \quad (2.12)$$

and since the magnetic moment and the spin angular momentum are parallel and proportional ($\vec{\mu} = \gamma \vec{I}$) we can write for the magnetic moment $\vec{\mu}$:

$$\frac{\partial \vec{\mu}}{\partial t} = \gamma \vec{\mu} \times \vec{B}. \quad (2.13)$$

The summation of magnetic moments for a system with an assembly of nuclear spins from the same kind gives rise to a macroscopic magnetization. Hence, Equation 2.13 holds for the magnetization vector \vec{M} :

$$\frac{\partial \vec{M}}{\partial t} = \gamma \vec{M} \times \vec{B}. \quad (2.14)$$

The static magnetic field is commonly assumed parallel to the z axis ($\vec{B} = B_0 \hat{k}$). Hence,

following Equation 2.14, the equations of motion for the magnetization components are:

$$\frac{\partial M_x}{\partial t} = \gamma B_0 M_y, \quad (2.15)$$

$$\frac{\partial M_y}{\partial t} = -\gamma B_0 M_x, \quad (2.16)$$

$$\frac{\partial M_z}{\partial t} = 0. \quad (2.17)$$

Assuming that the magnetization direction forms an angle θ with the z axis (Figure 2.2), the respective solutions, as a function of the magnitude M , can be written as:

$$M_x(t) = M \sin(\theta) \cos(\gamma B_0 t), \quad (2.18)$$

$$M_y(t) = -M \sin(\theta) \sin(\gamma B_0 t), \quad (2.19)$$

$$M_z(t) = M \cos(\theta). \quad (2.20)$$

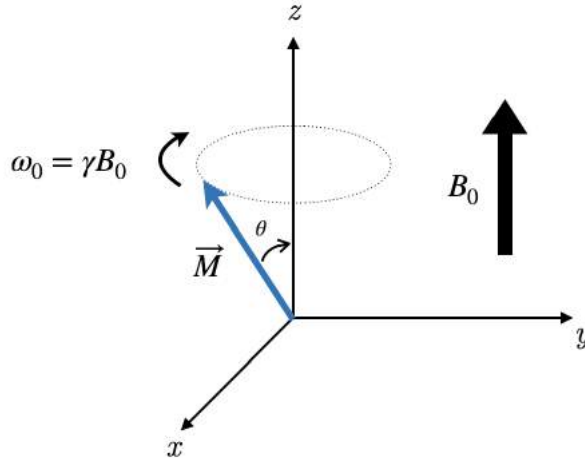


Figure 2.2: Rotation of the magnetization vector \vec{M} by a static magnetic field B_0 .

The solutions expressed in Equations 2.18, 2.19 and 2.20 mean that the magnetization component in the transverse plane ($x - y$) has a constant magnitude and it rotates in the clockwise direction with angular velocity $\omega_0 = \gamma B_0$, which is exactly the angular frequency expressed in Equation 2.7. The longitudinal component of the magnetization (z axis) has also a constant magnitude. The movement of the magnetization vector in the presence of a magnetic field is called Larmor precession (named after Joseph Larmor) and the angular frequency ω_0 is referred as the precession frequency, or Larmor frequency. According to

these equations, the precession of the transverse component of the magnetization vector by B_0 develops indefinitely and the longitudinal component exhibits a constant value. Notwithstanding, real systems tend to evolve to equilibrium states like the one expressed by Equation 2.8, obtained in the framework of Boltzmann statistics. In practice, not only the longitudinal component of the magnetization achieves such equilibrium along the B_0 direction during a certain time range, but also the transverse component of the magnetization vanishes with time. The explanation for these discrepancies relies in the concept of relaxation.

2.2 NMR Relaxation

2.2.1 Longitudinal and Transverse Relaxation

The obtained equations for the motion of the magnetization components assumed that nuclei experience the exact same magnetic field \vec{B} . Nonetheless, each nuclei probes a local magnetic field, as a summation of the applied field and local interactions, that can vary spatially and also fluctuate in time. Among several sources for the existence of such local fields, two can be said of major importance. The first one is associated with the fact that the applied magnetic field \vec{B} will not be perfectly homogeneous spatially, even in magnets from high-end equipment, and consequently a distribution of field values will always be imposed along the sample. This spatial distribution of the magnetic field is especially relevant for the case of fluids confined in porous media.

Here, it is necessary to recall the distinction on the magnetic fields \vec{B} and \vec{H} . Strictly, \vec{H} is defined as the magnetic field intensity, or the magnetizing force, while \vec{B} is the magnetic flux density. The practical difference is that \vec{H} is a quantity induced in the space around moving charges, while \vec{B} is a response of the medium to the applied excitation \vec{H} . When \vec{H} is impressed through a magnetic permeable material, the flux density \vec{B} is increased proportional to the relative permeability of the material. The relation between \vec{B} and \vec{H} is defined as:

$$\vec{B} = \mu_0(\vec{H} + \vec{M}), \quad (2.21)$$

wherein μ_0 , here, denotes the magnetic permeability of vacuum and \vec{M} is the resultant magnetization. The relation between \vec{M} and \vec{H} is defined as a function of the magnetic susceptibility χ , a dimensionless quantity representing a property of the medium:

$$\chi = \frac{\vec{M}}{\vec{H}}, \quad (2.22)$$

and Equation 2.21 can be rewritten as:

$$\vec{M} = \frac{\chi}{1 + \chi \mu_0} \vec{B}. \quad (2.23)$$

As magnetic susceptibility values in nuclear paramagnetic systems can be of the order of 10^{-9} , the expression in Equation 2.23 is sometimes approximated by:

$$\vec{M} = \frac{\chi}{\mu_0} \vec{B}. \quad (2.24)$$

Fluids (*e.g.*, air or water) and the material of confining porous samples (*e.g.*, rocks) exhibit distinct susceptibility values, thus, as a result of this difference (contrast) the applied \vec{B} field distribution is distorted and will exhibit different values along the porous space, *i.e.*, magnetic field gradients will be formed within pores. This is a very important aspect regarding the NMR of confined fluids, since diffusing nuclei will experience such gradients and this will affect both relaxation and diffusion measurements [82–84]. The influence of internal magnetic field gradients in relaxation measurements will be addressed again in the following Sections, and in the discussion of the results presented in Chapter 3 and 4. Some modern NMR techniques, denominated magnetization decay due to diffusion in the internal magnetic field (DDIF), proposed by Song [85], successfully employed the diffusion of fluid molecules through internal field gradients as tool to probe the characteristic confinement scale of porous samples.

The second and most important source of varying local magnetic fields relies on the principle that nuclear magnetic moments not only produce magnetic fields, but also respond to them. Interactions of the nuclear magnetic moment with fields created by the electronic cloud, or even the direct dipole-dipole coupling between nuclei, result in different local magnetic fields, which in the case of fluid molecules, will also fluctuate in time as nuclei are moving (diffusing). The overall effect, according to Equation 2.7, is that a distribution of field values, actually imposes on the system a distribution of precession frequencies. Therefore, such incoherence of precessing motion results in dephasing and consequently relaxation of the magnetization. Thus, we shall distinguish the mechanisms that promote relaxation and their effect on the magnetization components.

The evolution of the magnetization to the equilibrium state, during which spins shift between lower or higher energy configurations (in order to the occupation numbers in Equation 2.8 to take place), is a process that implicates energy exchange between the spins and the degrees of freedom of the environment, also referred to as the “lattice”. Therefore, since the value of the longitudinal component (z) of the magnetization varies depending on the population of each level, this process is also referred to as spin-lattice, or longitudinal relaxation. The transverse, or spin-spin relaxation process involves no

energy exchange and is a simple consequence of a loss of precession coherence between rotating magnetic moments, as spins experiencing different local fields will exhibit distinct precession frequencies. As a consequence, the transverse magnetization, a summation over the components of the precessing magnetic moments in the $x-y$ plane, vanishes as a result of destructive interference.

Relaxation processes may be parametrized by time constants. As mentioned in Chapter 1, Bloch [1] phenomenologically included relaxation times to the equations describing the dynamics of the magnetization components M_x , M_y and M_z in the presence of a static (or polarizing) magnetic field \vec{B} , known as Bloch Equations:

$$\frac{dM_x}{dt} = \gamma(\vec{M} \times \vec{B})_x - \frac{M_x}{T_2}, \quad (2.25)$$

$$\frac{dM_y}{dt} = \gamma(\vec{M} \times \vec{B})_y - \frac{M_y}{T_2}, \quad (2.26)$$

$$\frac{dM_z}{dt} = \gamma(\vec{M} \times \vec{B})_z - \frac{M_z - M_0}{T_1}, \quad (2.27)$$

wherein M_0 denotes the equilibrium magnetization directed at the z axis ($\vec{M}_{eq} = (0, 0, M_0)$), since M_x and M_y relax to zero and M_z relax to M_0 in the presence of a magnetic field $\vec{B} = (0, 0, B_0)$. T_1 and T_2 represent the spin-lattice (or longitudinal) and the spin-spin (or transverse) relaxation times, respectively. Assuming once more that the initial condition for $M_y(0) = 0$, the solution for M_x and M_z components, now including the effects of T_1 and T_2 relaxation (Figure 2.3), can be expressed as:

$$M_x(t) = M_x(0) \cos(\omega_0 t) e^{-t/T_2}, \quad (2.28)$$

$$M_z(t) = M_0 - [M_0 - M_z(0)] e^{-t/T_1}, \quad (2.29)$$

wherein $M_z(0)$ denotes the initial condition for the longitudinal magnetization and M_0 is the equilibrium value.

The exponential behavior associated with the decay of magnetization and relaxation times is commonly observed in fluids, although relaxation can exhibit a non-exponential behavior. Non-exponential NMR relaxation behaviors are mainly related to two different situations. The first one regards dynamically heterogeneous systems with distinguishable populations characterized by individual, yet exponential, relaxation decays [27]. A suitable example in the context of this thesis is the multiexponential behavior of the NMR relaxation of liquids confined in porous rocks. In these systems, under a proper set of approximations (see Section 1.4) the total magnetization decay can be modeled as a summation of exponential decays arising from fluids confined within pores with distinct characteristics. Each population contributes to the total signal with a single relaxation rate, and the distribution

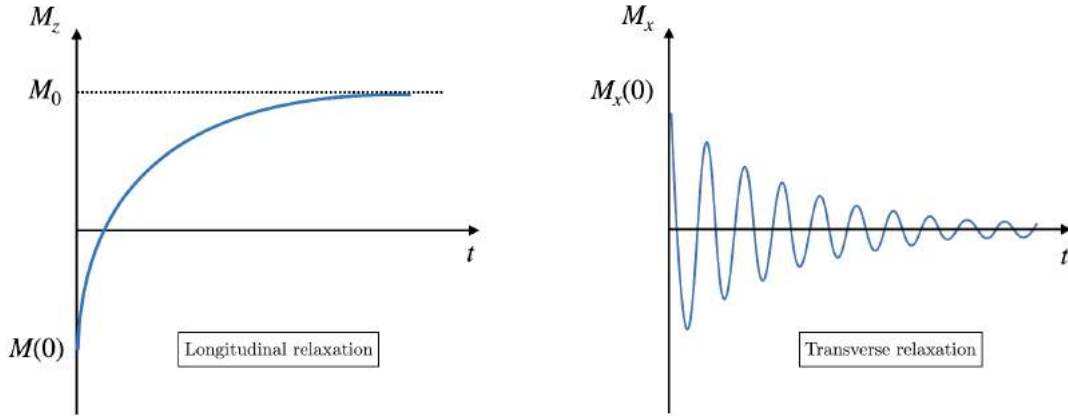


Figure 2.3: Illustration of longitudinal and transverse relaxation of the magnetization components M_z and M_x with time.

of such rates can be related with the heterogeneity of confinement features [5]. Nevertheless, some homogeneous systems can exhibit intrinsic non-exponential relaxations [86, 87], which require distinct modeling approaches from the ones assumed as part of the scope of this thesis.

Regardless of its exponential or non-exponential behavior, one should draw attention to the fact that relaxation is the reason why the observation of NMR is possible. What is being monitored is indeed the evolution (relaxation) of the system from non-equilibrium states back to the equilibrium.

2.2.2 The Rotating Frame of Reference

A common feature regarding both continuous-wave² and pulsed NMR techniques is the application of oscillating magnetic fields in order to conduct the system to the required non-equilibrium state, in which relaxation is then observed. The Larmor precession and the dynamics of the magnetization in the presence of a large static field and transverse oscillating fields can be more easily comprehended from the point of view of a frame of reference that rotates with the same precession frequency ($\omega_0 = \gamma B_0$) as the magnetic

²An NMR signal can be observed by two distinct experimental approaches, known as pulsed-field (PF) and continuous-wave (CW) NMR. At the simultaneous development of NMR by Edward Purcell and Felix Bloch in 1946, the continuous-wave spectroscopy was the technique employed. In CW-NMR the transverse spin magnetization is generated by a continuous oscillating magnetic field of low intensity and its signal is recorded as a function of the oscillation frequency or the static field strength B_0 . The transverse magnetization signal is maximized and a peak is observed in the spectrum when the oscillation frequency matches the nuclear resonance frequency [2, 3, 88]. The development of pulsed NMR, wherein short-duration and strong magnetic field bursts (pulses) are employed (see Section 1.3.3), was accomplished by Hahn, in 1950.

moments. Over the perspective of an observer rotating at the same ω_0 frequency, the effect of the static field B_0 on the magnetic moments actually disappears. Let us write the equations for the new frame of reference in order to visualize the effect of such transformation into the equation of motion for the magnetic moment (Equation 2.13).

The derivative with respect to the time of the magnetic moment vector $\vec{\mu}$ is written as a function of the derivatives of each component. For a stationary frame of reference we have:

$$\frac{d\vec{\mu}}{dt} = \frac{\partial}{\partial t}(\mu_x \hat{i}) + \frac{\partial}{\partial t}(\mu_y \hat{j}) + \frac{\partial}{\partial t}(\mu_z \hat{k}) = \frac{\partial \mu_x}{\partial t} \hat{i} + \frac{\partial \mu_y}{\partial t} \hat{j} + \frac{\partial \mu_z}{\partial t} \hat{k}, \quad (2.30)$$

wherein \hat{i} , \hat{j} and \hat{k} represent the orthogonal unit vectors from the stationary frame of reference. Considering a non-stationary frame of reference the derivative of $\vec{\mu}$ must also include the derivatives of \hat{i} , \hat{j} and \hat{k} :

$$\frac{d\vec{\mu}}{dt} = \left(\frac{\partial \mu_x}{\partial t} \hat{i} + \frac{\partial \mu_y}{\partial t} \hat{j} + \frac{\partial \mu_z}{\partial t} \hat{k} \right) + \mu_x \frac{\partial \hat{i}}{\partial t} + \mu_y \frac{\partial \hat{j}}{\partial t} + \mu_z \frac{\partial \hat{k}}{\partial t}, \quad (2.31)$$

in which the three terms in brackets represent the rate of change of $\vec{\mu}$ according to the stationary frame of reference, denoted by the partial derivative $\partial \vec{\mu} / \partial t$.

We shall consider a frame rotating about the z axis with angular frequency ω . The new unit vectors \hat{i}' , \hat{j}' and \hat{k}' , as seen from the stationary frame of reference, will vary according to:

$$\hat{i}' = \hat{i} \cos(\omega t) + \hat{j} \sin(\omega t), \quad (2.32)$$

$$\hat{j}' = -\hat{i} \sin(\omega t) + \hat{j} \cos(\omega t), \quad (2.33)$$

$$\hat{k}' = \hat{k}. \quad (2.34)$$

Hence, the time derivatives in Equation 2.31 can be written as:

$$\frac{\partial \hat{i}'}{\partial t} = -\hat{i} \sin(\omega t) \omega + \hat{j} \cos(\omega t) \omega = \omega \hat{j}', \quad (2.35)$$

$$\frac{\partial \hat{j}'}{\partial t} = -\hat{i} \cos(\omega t) \omega - \hat{j} \sin(\omega t) \omega = -\omega \hat{i}', \quad (2.36)$$

$$\frac{\partial \hat{k}'}{\partial t} = 0. \quad (2.37)$$

Thus, according to the new frame of reference, Equation 2.31 can be rewritten as:

$$\frac{d\vec{\mu}}{dt} = \frac{\partial \vec{\mu}}{\partial t} + \omega(\mu_x \hat{j}' - \mu_y \hat{i}') = \omega \hat{k}' \times \vec{\mu}, \quad (2.38)$$

and since the angular velocity is expressed as $\vec{\omega} = \omega \hat{k}$ we have:

$$\frac{d\vec{\mu}}{dt} = \frac{\partial \vec{\mu}}{\partial t} + \vec{\omega} \times \vec{\mu}. \quad (2.39)$$

We can finally visualize the effect of such transformation into the equation of motion for the magnetic moment in the presence of a magnetic field \vec{B} (Equation 2.13). Considering the result obtained in Equation 2.39, according to the new frame of reference the rate of change of the magnetic moment $\partial \vec{\mu} / \partial t$ can be written as:

$$\frac{\partial \vec{\mu}}{\partial t} = \frac{d\vec{\mu}}{dt} - \vec{\omega} \times \vec{\mu} = \gamma \vec{\mu} \times \vec{B} - \vec{\omega} \times \vec{\mu}, \quad (2.40)$$

or rearranging:

$$\frac{\partial \vec{\mu}}{\partial t} = \gamma \vec{\mu} \times (\vec{B} + \vec{\omega} / \gamma). \quad (2.41)$$

The important result expressed in Equation 2.41 is the presence of an effective magnetic field ($\vec{B}_{eff} = \vec{B} + \vec{\omega} / \gamma$), experienced by the magnetic moment in the rotating frame of reference. This means that the Larmor precession of a magnetic moment in the presence of a magnetic field $\vec{B} = B_0 \hat{k} = (\omega_0 / \gamma) \hat{k}$, as seen in a frame of reference that rotates with an angular frequency $\omega_0 = -\gamma / B_0$, will appear stationary.

2.2.3 Radiofrequency Pulses and Rotations

The behavior of the Larmor precession of magnetic moments in a rotating frame of reference is particularly useful when one considers the presence of transverse oscillating or rotating fields, along with an static magnetic field. Strictly, a linearly polarized rotating magnetic field \vec{B}_1 is expressed as a summation of a rotating and a counter-rotating part:

$$2B_1 \cos(\omega t) \hat{i} = B_1 [\cos(\omega t) \hat{i} + \sin(\omega t) \hat{j}] + B_1 [\cos(\omega t) \hat{i} - \sin(\omega t) \hat{j}]. \quad (2.42)$$

In practice, the contribution of the component rotating in the opposite sense with respect to the Larmor precession is negligible in comparison with the effect of the component moving with the precession [2]. Therefore, let us consider the case of magnetic moments in the presence of two magnetic fields, one static field $\vec{B}_0 = B_0 \hat{k}$ and a second oscillating field \vec{B}_1 rotating in the plane transverse to \vec{B}_0 with frequency ω . The total magnetic field can then be expressed as:

$$\vec{B}_{total} = B_1 [\cos(\omega t) \hat{i} + \sin(\omega t) \hat{j}] + B_0 \hat{k}. \quad (2.43)$$

According to the transformations obtained, in a frame of reference rotating with angular frequency $\vec{\omega}' = \omega' \hat{k}$, the effective magnetic field experienced by a magnetic moment can be expressed as:

$$\vec{B}_{\text{eff}} = \vec{B}_{\text{total}} + \vec{\omega}'/\gamma = B_1 \{ \cos[(\omega - \omega')t] \hat{i} + \sin[(\omega - \omega')t] \hat{j} \} + (B_0 + \omega/\gamma) \hat{k}. \quad (2.44)$$

Considering the case where the field \vec{B}_1 and the rotating frame have the same angular frequency, the transverse field appear to be stationary (Figure 2.4), and the effective magnetic field is simplified to:

$$\vec{B}_{\text{eff}} = B_1 \hat{i} + (B_0 + \omega/\gamma) \hat{k}. \quad (2.45)$$

The most interesting case regarding the effective magnetic field as seen in a rotating frame is obviously the resonance condition, when $\omega = \omega_0$. In this case, since $B_0 = -\omega_0/\gamma$, the effective magnetic field reduces to:

$$\vec{B}_{\text{eff}} = B_1 \hat{i}, \quad (2.46)$$

which means that, as seen from the rotating frame of reference, the effective field is static and rests in the transverse plane. The result expressed in Equation 2.46 is especially useful

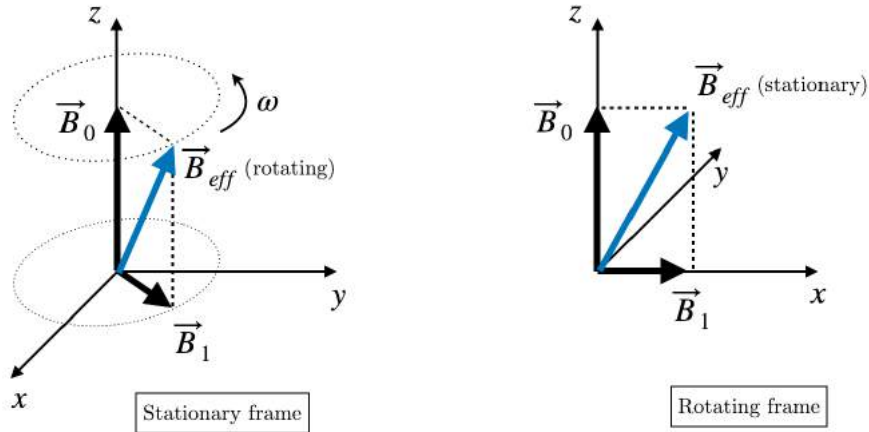


Figure 2.4: Illustration of the effective magnetic field \vec{B}_{eff} as summation of a static magnetic field \vec{B}_0 and a transverse rotational field \vec{B}_1 , as seen in a stationary and in a rotating frame of reference.

in the context of pulsed-field NMR. Once the field \vec{B}_1 is applied, the nuclear magnetic moments will experience a torque and precess in the plane transverse to \vec{B}_1 about its direction. Hence, defining the time during which \vec{B}_1 is applied, it is possible to induce controlled rotations on the magnetic moments, and consequently on the macroscopic

magnetization vector \vec{M} (Figure 2.5).

These transverse field pulses are known as radio-frequency (RF) pulses, since considering the proton gyromagnetic ratio $\gamma = 42.58 \text{ MHz/T}$, for field strengths ranging from tenths of a Tesla up to a few Tesla, the pulse frequency ($\omega/2\pi$) values will be in the range of mega Hertz, or radio frequencies. In NMR, RF pulses are also referred to by their resulting rotation angles. The most common ones are the $\pi/2$ and the π pulses. Considering the magnitude of the angular velocity $\omega_1 = \gamma B_1$, we have:

$$\gamma B_1 t_{90^\circ} = \pi/2, \quad (2.47)$$

$$t_{90^\circ} = \frac{\pi}{2\gamma B_1}, \quad (2.48)$$

wherein t_{90° represents the time duration of the applied \vec{B}_1 field that results in a $\pi/2$ RF pulse, which rotates the equilibrium magnetization pointing at the z -direction ($\vec{M} = M_0\hat{k}$) to the transverse plane, and:

$$\gamma B_1 t_{180^\circ} = \pi, \quad (2.49)$$

$$t_{180^\circ} = \frac{\pi}{\gamma B_1}, \quad (2.50)$$

in which t_{180° represents the time duration of the applied \vec{B}_1 field that results in a π RF pulse, which inverts the equilibrium magnetization sense \vec{M} to $-\vec{M}$ (Figure 2.5). These pulses are used to manipulate the magnetization vector and to conduct the system to non-equilibrium states, in which relaxation processes will take place.

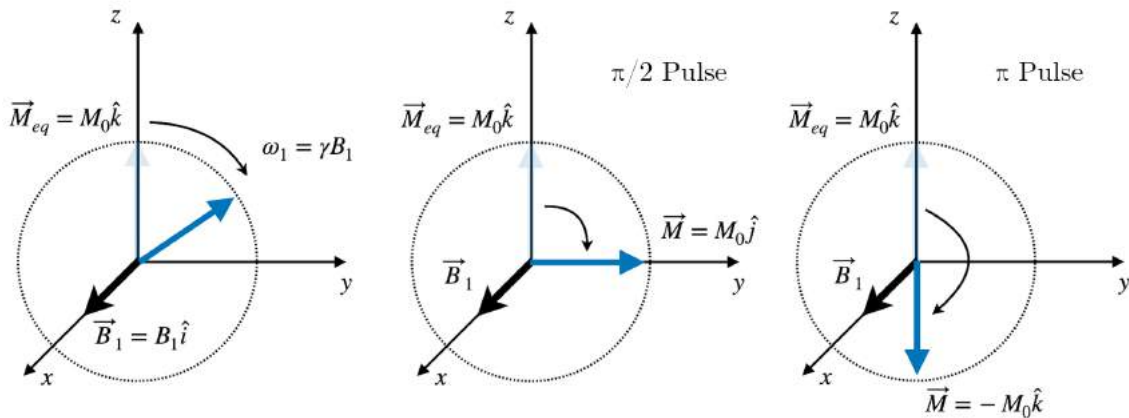


Figure 2.5: Illustration of the $\pi/2$ and the π rotations of the magnetization vector in the $y - z$ plane by a transverse RF pulse \vec{B}_1 applied in the positive x -direction, as seen in a rotating frame of reference.

2.2.4 Free Induction Decay (FID) and NMR Spectroscopy

We will now take a closer look at the behavior of the magnetization at the transverse plane after the application of a $\pi/2$ RF pulse. Once in the transverse plane, the ensemble of magnetic moments will precess about the static magnetic field directed at the z axis, and immediately after the $\pi/2$ pulse the magnitude of the transverse magnetization M_{xy} equals the equilibrium magnetization M_0 . Notwithstanding, a distribution of precession frequencies is imposed on the ensemble due to a distribution of local fields experienced by the nuclei. Thus, the magnetic moments start losing precession coherence, and the macroscopic magnetization signal starts to decay due to destructive interference. This process is known as free induction decay (FID), and is the most simple experiment that can be performed in pulsed NMR.

As formerly discussed, two physically distinct reasons contribute to create a spatial distribution of local magnetic fields: the inhomogeneities in the static magnetic field as the result of intrinsic imperfections in the magnet itself or from susceptibility-induced field distortions, and the interactions of diffusing magnetic moments with their chemical environment. The time constant associated with the free induction decay of the magnetization, considering a summation of all these effects, is referred to as T_2^* (reads “ T_2 -star”), which is different from the relaxation time T_2 in the sense that the latter is considered as arising only from intrinsic interactions at the atomic or molecular levels, and does not account for inhomogeneities in the static magnetic field. For this reason T_2 is often referred to as the “real” or “true” T_2 , while T_2^* is the “observed” or “effective” T_2 .

Let us consider the example of a real system composed by a collection of magnetic moments (*e.g.*, same specie nuclei in a liquid sample) in the presence of a static magnetic field $\vec{B} = B_0\hat{k}$ after the application of a $\pi/2$ RF pulse in the positive x -direction. The initial conditions, describing the magnetization immediately after the RF pulse are $M_x(0) = 0$ and $M_y(0) = M_0$, wherein M_0 denotes the magnitude of the equilibrium magnetization. The equation of motion for the magnetization components M_x and M_y , considering the observed transverse relaxation time T_2^* , can be written as (Equations 2.25 and 2.26):

$$\frac{dM_x}{dt} = -\omega_0 M_y - \frac{M_x}{T_2^*}, \quad (2.51)$$

$$\frac{dM_y}{dt} = \omega_0 M_x - \frac{M_y}{T_2^*}. \quad (2.52)$$

Defining the magnitude of the transverse magnetization as $M_{xy} = M_x + iM_y$, Equations 2.51 and 2.52 can be combined into:

$$\frac{dM_{xy}}{dt} = (i\omega_0 - \frac{1}{T_2^*})M_{xy}. \quad (2.53)$$

Considering the initial conditions, the solution can be expressed as:

$$s(t) = \frac{M_{xy}(t)}{M_0} = e^{i\omega_0 t} e^{-t/T_2^*}, \quad (2.54)$$

wherein $s(t)$ denotes the normalized recorded signal in the time domain. We can obtain the signal in the frequency domain performing the Fourier Transform of the time domain signal. Considering the case wherein the time domain signal is a decaying exponential $f(t) = e^{-at}$, the Fourier Transform can be defined³ as:

$$\mathcal{F}\{f(t)\} = F(\omega) = \int_0^\infty e^{-at} e^{-i\omega t} dt = \frac{e^{-(a+i\omega t)}}{-(a+i\omega t)} \Big|_0^\infty = \frac{1}{(a+i\omega)} = \frac{a+i\omega}{(a^2+\omega^2)}. \quad (2.55)$$

Hence, Fourier transforming the result in Equation 2.54 we obtain:

$$S(\omega) = \mathcal{F}\{s(t)\} = \frac{T_2^*}{1+(T_2^*)^2(\omega_0-\omega)^2} + \frac{i(\omega_0-\omega)}{1+(T_2^*)^2(\omega_0-\omega)^2}. \quad (2.56)$$

The expression in Equation 2.56 denotes a complex Lorentzian function, or a Lorentzian lineshape, with a real (or absorption) and an imaginary (or dispersion) component (Figure 2.6). As the NMR spectrum can be record in complex form, it is possible to observe both of these components. Strictly, the a raw spectra is a linear combination of the real and imaginary parts, and phase correction procedures are used to convert this mixed form into a pure lineshape. Nevertheless, since the real part is associated with a narrower linewidth, it is usually the component that is plotted as the NMR spectra (left plot from Figure 2.6).

The real part in Equation 2.56 is the expression of a Lorentzian function centered in ω_0 with a linewidth at half-height given by:

$$\Delta\nu = \frac{\Delta\omega}{2\pi} = \frac{1}{\pi T_2^*}, \quad (2.57)$$

wherein ν denotes the linear frequency [1/s].

In a bulk liquid sample the effect of field inhomogeneities in the overall relaxation rate $1/T_2^*$ is actually much greater than the one associated with the relaxation time T_2 . For this reason the spectrum linewidth at half-height of liquids is commonly used as a measurement of the static field inhomogeneity. Note that, the greater the magnetic field inhomogeneity is, the smaller (shorter) T_2^* is and the broader the linewidth. Finally, for the case of complex molecules, in which same specie nuclei experience different magnetic fields as a consequence of distinct chemical environments, the signal expressed in Equation 2.54 will be a composition of signals with different resonance frequencies. Hence, the Fourier

³One should notice that although the Fourier Transform integration must be performed from $-\infty$ to $+\infty$, here, the observed signal is only different from zero, or defined, for $t > 0$.

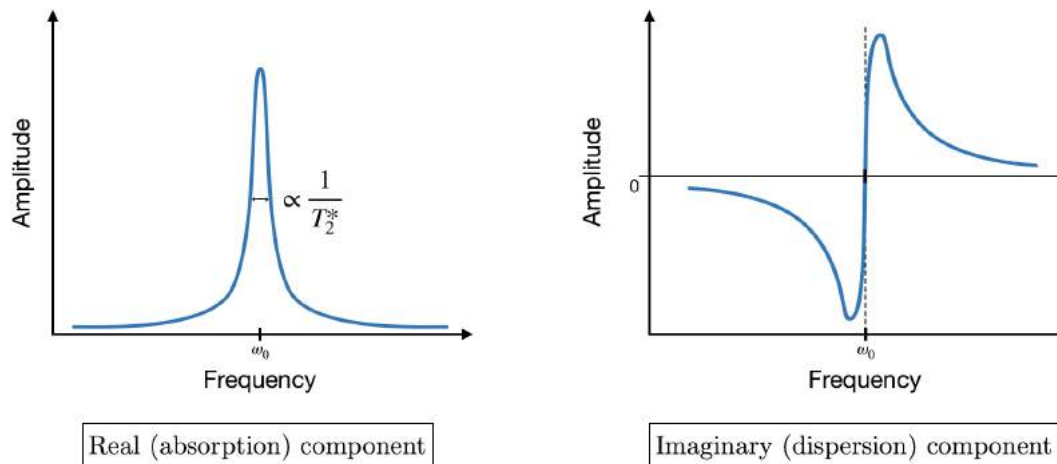


Figure 2.6: Illustration of the Lorentzian lineshape in the frequency domain (Equation 2.56). The left plot shows the real, or absorption, lineshape and the dispersion, or imaginary, lineshape is shown in the right plot. The linewidth at half-height in the left plot is inversely proportional to T_2^* . The greater the magnetic field inhomogeneity is, the smaller (shorter) T_2^* is and the broader the linewidth.

Transform of the recorded NMR signal will exhibit a composition of peaks distributed along the frequency axis with their respective amplitudes (areas) representing the nuclei population associated with a particular chemical environment, or chemical group. This is the foundation of the NMR spectroscopy technique.

2.2.5 Spin Echoes

Let us consider the behavior of the magnetization at the transverse plane after the application of a $\pi/2$ pulse. Once in the transverse plane, magnetic moments start losing phase coherence due to inhomogeneities in the static field and the presence of local fields produced by interactions with the chemical environment. From the point of view of an observer standing at the rotating frame of reference, the magnetic moments with precession frequencies smaller than ω_0 will appear to rotate clockwise (Figure 2.7), and the magnetic moments with precession frequencies greater than ω_0 will appear to rotate counterclockwise (see also Figure 2.4). Intuitively, one can assume that after a short period of time, the most effective way to recovering precession coherence would be to invert the rotation direction of magnetic moments. As we will see in the following steps such refocusing effect can be achieved by a π pulse.

It is possible to build a simple model in order for one to visualize the effects of local fields experienced by spins in the loss of precession coherence, and also the formation of a

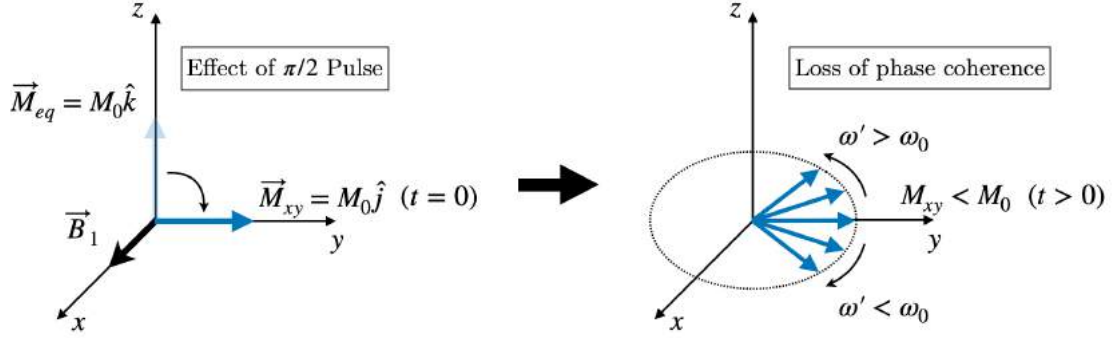


Figure 2.7: Illustration of the loss of precession phase coherence by the magnetic moments after a $\pi/2$ pulse applied in the positive x -direction, from the point of view of an observer standing at the rotating frame of reference. Immediately after the $\pi/2$ pulse the magnitude of the transverse magnetization equals the equilibrium value $M_{xy} = M_0$.

spin echo. First, we are going to assume that the magnetic field experienced at a certain i th spin site can be written as the summation of an static field \vec{B}_0 and the local magnetic field deviation at the i th spin site \vec{b}_i . Two important approximations are being considered in this simplified model. The first one relates to the interaction between spins, as for this purpose solely, spins are being regarded as independent. This means that each spin experiences a field which is a composition of the contribution from all of its neighbours and the static field, in an approach similar to mean field, or single particle approximations.

The second important approximation relates to the effect of the deviation field \vec{b}_i . It will be assumed that only the component of \vec{b}_i which is parallel to the static field will cause changes in the precession frequency about \vec{B}_0 , and consequently only the local fields parallel to the static field will be taken in to account. Anderson and Weiss [89] first considered these simplifications in order to investigate the spectral lineshape of a spin system taking into account their interactions with local dipolar fields.

Under the light of these two approximations, and considering the static magnetic field pointing at z -direction, the local field experienced at the i th spin site can be written as:

$$\vec{B}_i = (B_0 + b_i)\hat{k}, \quad (2.58)$$

and the equation of motion for the magnetic moment is:

$$\frac{d\vec{\mu}_i}{dt} = \gamma\vec{\mu}_i \times \vec{B}_i = \gamma\vec{\mu}_i \times (B_0 + b_i)\hat{k}. \quad (2.59)$$

As the local field transverse components were neglected, the longitudinal component $d\mu_z/dt$ resulting from the cross product in Equation 2.59 vanishes, which means that

this simplified model is not capable to approach longitudinal relaxation. Similarly to the transverse magnetization, we can define the complex transverse magnetic moment as $\mu_{xy} = \mu_x + i\mu_y$. Here, as we intend in this model to approach only the transverse relaxation effect, the notation μ_{xy} will be simplified to only μ , and the subscripts will be used to denote different spins. Assuming the complex magnetic moment form, the equation of motion following from the cross product can be written as:

$$\frac{d\mu_i(t)}{dt} = -i\gamma(B_0 + b_i)\mu_i(t). \quad (2.60)$$

It must be noticed that the deviation field \vec{b}_i was defined as the spatial variation of the applied static field \vec{B}_0 , and especially for liquid samples, since spins are moving (diffusing), these fields change with time. Assuming that the motion is sufficiently slow so that the time variation of \vec{b}_i can be neglected, the solution of Equation 2.60 can be written as:

$$\mu_i(t) = e^{-i\gamma(B_0 + b_i)t}\mu_i(0), \quad (2.61)$$

wherein one can observe that each spin i will precess with an “effective” angular frequency $\omega_i = \gamma(B_0 + b_i)$. The macroscopic magnetization considering a system with N spins is defined as the summation over magnetic moments per unit volume:

$$\vec{M} = \frac{1}{V} \sum_{i=1}^N \vec{\mu}_i, \quad (2.62)$$

and assuming once more the complex form for the transverse components, and the same simplified notation used in Equation (2.60) we have:

$$M(t) = \frac{1}{V} \sum_{i=1}^N \mu_i = \frac{1}{V} \sum_{i=1}^N e^{-i\gamma(B_0 + b_i)t}\mu_i(0). \quad (2.63)$$

Considering that the initial value of the transverse magnetic moment of the i th spin $\mu_i(0)$ is independent from its associated local field \vec{b}_i , the initial magnetization may be factorized:

$$M(0) = \frac{1}{V} \sum_{i=1}^N \mu_i(0), \quad (2.64)$$

hence, the magnetization expression becomes:

$$M(t) = e^{-i\gamma B_0 t} \frac{1}{N} \sum_{i=1}^N e^{-i\gamma b_i t} M(0), \quad (2.65)$$

wherein the term $\exp[-i\gamma B_0 t]$ represents the precession of the magnetization at the Larmor

frequency, and the summation term denotes the distribution of precession frequencies which gives rise to the loss of phase coherence illustrated in Figure 2.7, and consequently the decay of the transverse magnetization signal.

As seen in Section 1.3.2, from the point standpoint of a rotating frame of reference with angular frequency $\omega_0 = \gamma B_0$, the magnetization vector appears to be stationary, which means that the term $\exp[-i\gamma B_0 t]$ can be removed from Equation 2.65, and the expression for the transverse magnetization at a time t is given by:

$$M(t) = \frac{1}{N} \sum_{i=1}^N e^{-i\gamma b_i t} M(0). \quad (2.66)$$

Let us now consider the effect of a π pulse, applied at the positive x -direction, on the magnetization components. After a rotation of π about the x axis the magnetization components will be transformed the following way: $M_x \rightarrow M_x$, $M_y \rightarrow -M_y$ and $M_z \rightarrow -M_z$. Effectively, a π pulse will transform the transverse magnetization M into its complex conjugate M^* . Considering that the spin ensemble evolved during a time τ after the initial $\pi/2$ pulse, and that at $t = \tau$ a π pulse was applied, immediately after the second pulse the expression of the magnetization can be written as:

$$M(\tau) = \frac{1}{N} \sum_{i=1}^N e^{+i\gamma b_i \tau} M^*(0). \quad (2.67)$$

The subsequent time evolution of the magnetization after the π pulse can be obtained multiplying the term in the summation by $\exp[-i\gamma B_0 t]$:

$$M(t + \tau) = \frac{1}{N} \sum_{i=1}^N e^{-i\gamma b_i t} e^{+i\gamma b_i \tau} M^*(0), \quad (2.68)$$

$$M(t + \tau) = \frac{1}{N} \sum_{i=1}^N e^{-i\gamma b_i (t - \tau)} M^*(0). \quad (2.69)$$

According to the expression in Equation 2.69, when $t = \tau$ the magnetization recovers its full value:

$$M(2\tau) = M^*(0). \quad (2.70)$$

Notwithstanding, this fully-recovered behavior is not observed in real systems, and this occurs by two reasons. The first relates to the fact that in this simple model we took an approximation to neglect the effect of motion on the local deviation fields. Although for small values of τ this could be considered valid, strictly, the \vec{b}_i fields will vary with time.

The second and most important reason for the partial refocusing effect of a π pulse regards the effect of the pulse on local dipolar fields, which arise from the interaction of spins with its “neighbours”. A π pulse reverts the spin orientation and also the source of dipolar fields. The cross product between the magnetic moment $\vec{\mu}$ and the local fields \vec{b} in the equations of motions will thus remain unchanged, and consequently the pulse has no effect on such mechanism.

In practice a π pulse will recover the precession phase coherence loss due to inhomogeneities in the static field, but it does not avoid the magnetization loss associated with local dipolar fields, which means that the transverse relaxation process related to atomic and molecular interactions (associated with the T_2 time constant) will proceed as before, and Equation 2.70 becomes:

$$M(2\tau) = M^*(0)e^{-2\tau/T_2}. \quad (2.71)$$

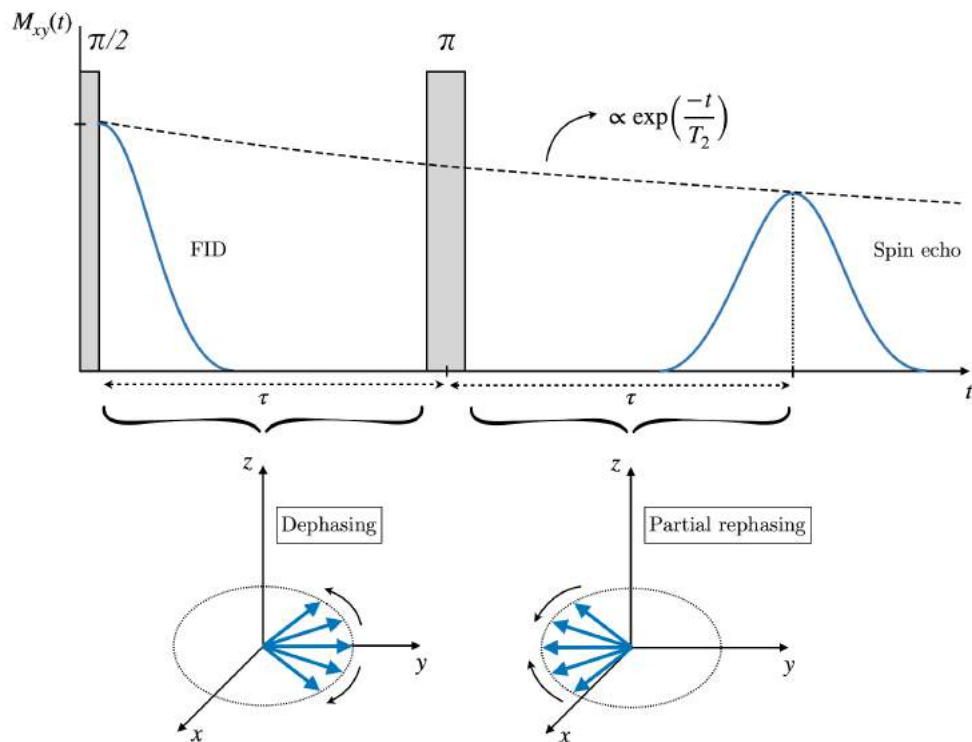


Figure 2.8: Illustration of the effect of a π pulse, applied on the positive x -direction, on the recovering of the precession phase coherence and the formation of a spin echo at $t = 2\tau$.

2.2.6 Common Protocols for Relaxation Measurements

*Free Induction Decay (FID) - T_2^**

As we saw in Section 1.3.4, the most simple experiment for the determination of the T_2^* time constant is to apply a $\pi/2$ pulse and immediately after to observe the free decay of the magnetization. Also, the spin echo mentioned in the previous section has the exact shape of two back-to-back FIDs, and the experiment $\pi/2 - \tau - \pi - \tau$ - echo can be used to the determination of T_2^* . In fact, this protocol, known as a Hahn echo sequence, is very useful considering electronic-related detection effects, since signal observation will take place far away from the high-voltage RF pulse, which can affect the reception of the induced signal.

Distinct effects contribute to the free decay of the magnetization after a $\pi/2$ pulse; spatial inhomogeneities in the static field along the sample, local interactions in atomic and molecular levels and also the diffusion of spins through internal field gradients, in the sense that, generally, there is no reason for the observed field (or frequency) distribution to be exactly a Lorentzian. Hence, the relaxation will not be exponential, and T_2^* was for a long time only used as a rough measurement of the relaxation time-scale.

Nevertheless, the analysis of NMR signals in the time domain such as the FID, or other relaxation time constants (T_1 and T_2), as well as time-dependent diffusion coefficients, comprise an important NMR segment denominated Time-Domain (TD) NMR, which became especially useful in low-field situations wherein high-resolution spectroscopy is not available. A wide range of relaxometric and diffusometric techniques, such as the ones presented in this thesis, can be implemented on cost-effective benchtop NMR equipment, with applications in different research segments such as fuel [90], food [91] or polymer science [92].

Carr-Purcell-Meiboom-Gill (CPMG) - T_2

The formation of a spin echo after the $\pi/2$ - τ - π - τ is a powerful tool for one to recover the magnetization signal, and multiple π pulses can be used to monitor the echo amplitude decay in order for one to determinate the time constant T_2 . The method, proposed initially by Carr and Purcell in 1954 [10], consists in the observation of an echo-train obtained by a series of consecutive, and equally spaced π pulses, after the application of the initial $\pi/2$ pulse (Figure 2.9). It is important to observe that this approach is different from the one wherein multiple echoes are obtained in a series of $\pi/2$ - τ - π - τ -echo acquisitions for different τ values. The latter approach is often referred to as a Hahn echo protocol, and some practical and physical differences can be pointed out.

On what regards the acquisition process, the Carr-Purcell method is actually much faster, since the complete echo train can be observed in a single shot after multiple π pulses. Nevertheless, the most important difference between the two approaches relates to the diffusion of molecules during the interval between RF pulses. The echo amplitude is attenuated if one considers the movement of spins through internal field gradients (see Section 3.1.1), and the greater the diffusion time (or the separation between refocusing pulses) the less effective the refocusing effect will be. In essence, the method was developed with the purpose to reduce the influence of diffusion on relaxation. Performing such echo train acquisitions with short τ values minimizes the effect of spin diffusion through internal field gradients in signal attenuation and simultaneously increases the time scale of observation of the transverse magnetization decay.

For the case of a Hahn echo protocol as the time interval between the $\pi/2$ and the π pulse is increased in each step, so is the effect of spin diffusion through internal field gradients. The practical consequence is that in each step the echo amplitude will be affected differently by the distinct mechanisms promoting relaxation.

The effect of spin diffusion on the attenuation of the echo amplitude can be estimated. Considering that the local fields b_i are no longer constant due to diffusion of spins and the presence of magnetic field gradients, the expression obtained in Equation 2.66 can be written in a general form:

$$M(t) = \frac{1}{N} \sum_{i=1}^N \exp \left\{ -i\gamma \left[\int_0^t b_i(t') dt' \right] \right\} M(0), \quad (2.72)$$

and after a π pulse the magnetization is transformed to its complex conjugate:

$$M(t) = \frac{1}{N} \sum_{i=1}^N \exp \left\{ +i\gamma \left[\int_0^t b_i(t') dt' \right] \right\} M^*(0). \quad (2.73)$$

The normalized amplitude of the echo formed at $2t$ can then be expressed as:

$$E(2t) = \frac{1}{N} \sum_{i=1}^N \exp \left\{ -i\gamma \left[\int_t^{2t} b_i(t') dt' - \int_0^t b_i(t') dt' \right] \right\}, \quad (2.74)$$

and taking the average over the number of particles we have:

$$E(2t) = \left\langle \exp \left\{ -i\gamma \left[\int_t^{2t} b_i(t') dt' - \int_0^t b_i(t') dt' \right] \right\} \right\rangle. \quad (2.75)$$

The argument in Equation 2.75 denotes a phase angle $\phi_i(t)$ expressed as:

$$\phi_i(2t) = -\gamma \left[\int_t^{2t} b_i(t') dt' - \int_0^t b_i(t') dt' \right]. \quad (2.76)$$

Assuming that the acquired phase ϕ is a random variable with a Gaussian distribution (also known as the Gaussian Phase Approximation (GPA)) the expression for the relaxation function can be fairly approximated by $\exp(-\langle\phi^2\rangle/2)$ [2, 4, 53], hence the expression in Equation 2.75 becomes:

$$E(2t) = \exp \left\{ \frac{\gamma^2}{2} \left\langle \left[\int_0^t b_i(t') dt' - \int_t^{2t} b_i(t') dt' \right]^2 \right\rangle \right\}. \quad (2.77)$$

Using the transformation $(a-b)^2/2 = a^2 + b^2 - (a+b)^2/2$ the squared argument in Equation 2.77 can be rewritten. Let us take as an example the first term after the transformation (a^2):

$$a^2 = \frac{\gamma^2}{2} \left[\int_0^t b(t') dt' \right] \left[\int_0^t b(t') dt' \right] = \frac{\gamma^2}{2} \left[\int_0^t dt'_1 \int_0^t b(t'_1) b(t'_2) dt'_2 \right], \quad (2.78)$$

and applying the average bracket we have:

$$\langle a^2 \rangle = \frac{\gamma^2}{2} \left[\int_0^t dt'_1 \int_0^t \langle b(t'_1) b(t'_2) \rangle dt'_2 \right], \quad (2.79)$$

We may define the autocorrelation function of the variable $b(t')$ as the average $\langle b(t'_1) b(t'_2) \rangle$. The property of stationarity relating a random variable and its autocorrelation function ensure that, for systems in equilibrium, the dependence of b with t' can be determined only through the difference $t'_2 - t'_1$ [93]. This way, for a random stationary variable $b(t')$, such as the one in Equation 2.79, we may write:

$$\frac{\gamma^2}{2} \langle b(t'_1) b(t'_2) \rangle = G(t'_2 - t'_1), \quad (2.80)$$

wherein $G(t'_2 - t'_1)$ denotes the autocorrelation function, and the integration Equation 2.79 becomes:

$$\langle a^2 \rangle = \int_0^t dt'_1 \int_0^t G(t'_2 - t'_1) dt'_2. \quad (2.81)$$

With a change of variables, and considering that G only depends on t' , we may write:

$$\langle a^2 \rangle = 2 \int_0^t (t - t') G(t') dt'. \quad (2.82)$$

Applying the same procedure for all the terms resulting from the transformation $(a - b)^2/2 = a^2 + b^2 - (a + b)^2/2$ in the squared argument in Equation 2.77, we may rewrite

the echo amplitude using autocorrelation functions:

$$E(t) = \exp \left\{ - \int_0^t (t - t') [G(t'/2) - G(t')] dt' \right\}. \quad (2.83)$$

In order for one to apply the result obtained in Equation 2.83 to the problem of the diffusion influence on echo attenuation, the diffusion autocorrelation function must be determined considering the spatial dependence of the magnetic field gradient experienced by diffusing molecules. Assuming that the static field points at the z -direction, and considering a simple sinusoidal form for the field gradient $b(z)$ such as:

$$b(z) = A \sin(qz), \quad (2.84)$$

the diffusion correlation function $G(t)$ may be expressed as [2, 94]:

$$G(t) = \frac{\gamma^2 g^2}{q^2} \exp(-q^2 Dt), \quad (2.85)$$

wherein the diffusion parameter $q = q(\gamma, g, t)$ [m^{-1}] is known as the wavevector amplitude, g stands for the gradient strength and D [m^2/s] is the molecular self-diffusion coefficient. Using the diffusion correlation function described by Equation 2.85 in the expression of the echo attenuation (Equation 2.83) we have:

$$E(t) = \exp \left\{ - \int_0^t (t - t') \frac{\gamma^2 g^2}{q^2} [\exp(-q^2 Dt'/2) - \exp(-q^2 Dt')] dt' \right\}, \quad (2.86)$$

wherein solving the integration leads to:

$$E(t) = \exp \left\{ \frac{\gamma^2 g^2}{q^6 D^2} [4 \exp(-q^2 Dt/2) - \exp(-q^2 Dt) - 3 + q^2 Dt] \right\}. \quad (2.87)$$

In order to obtain the behavior of the echo attenuation in the presence of a constant field gradient, we must observe the limit when the wavelength ($1/q$) is large compared to the sample's dimensions, *i.e.*, the regime when the oscillations in the assumed sinusoidal gradient form can be neglected and the gradient can be considered linear. This can be achieved taking the limit $q \rightarrow 0$ in the expression in Equation 2.87. Expanding the exponentials in the argument and taking the limit we finally obtain:

$$E(t) = \exp(-\gamma^2 g^2 Dt^3/12). \quad (2.88)$$

The result obtained in Equation 2.88, regarding the echo signal decay due to diffusion of molecules through a field gradient g , can be included⁴ into the result obtained in Equation

⁴Strictly, the solution of the Bloch Equations including diffusion terms is only factorable into separate relaxation and diffusion parts under certain approximations, regarding the diffusion propagator and the

2.71. Hence, the echo amplitude at a given time t using the Carr-Purcell protocol may be expressed as:

$$M(t) = M(0)e^{-t/T_2}e^{(-\gamma^2 g^2 D t^3/12)}. \quad (2.89)$$

In a CPMG experiment with a sufficiently small τ value, the time molecules have to diffuse between two refocusing π pulses is short, and for weak field gradients g the diffusion term in Equation 2.89 may be neglected. It is important to recall that according to Equation 2.71 the magnetization recorded at the time $t = 2\tau$, after the first π pulse, is the complex conjugate of the equilibrium magnetization attenuated by the exponential relaxation factor $\exp(-2\tau/T_2)$. The next echo, formed at $t = 4\tau$, will be the complex conjugate of the previous one, and so on, in the sense that the echoes are not formed in the same direction. The effective shape of the recorded signal in the protocol proposed by Carr and Purcell is illustrated in Figure 2.9.

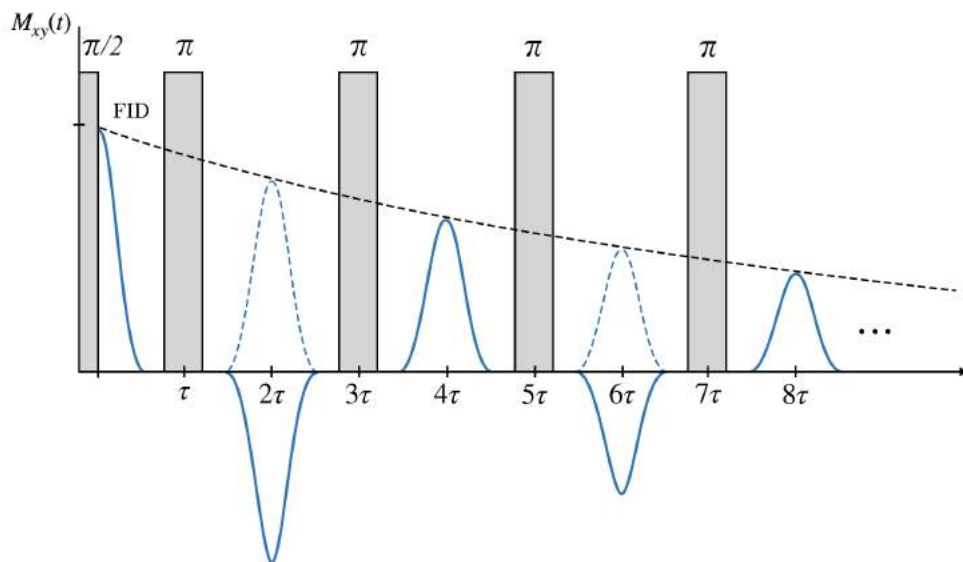


Figure 2.9: Illustration of the protocol suggested by Carr and Purcell for the measurement of the T_2 relaxation time. Each refocusing π pulse induces the formation of a new spin echo, which is the complex conjugate of the previous one. In this protocol the π pulses are applied in the same direction as the $\pi/2$ pulse. The amplitude of the echoes decrease due to relaxation and is modulated by the exponential decay expressed in Equation 2.89.

Nevertheless, when the π pulse is wrongly calibrated, a possible situation on real measurements, the refocusing of magnetization will be compromised in the sense that M_y will not be fully reversed and a small part of the magnetization may be placed in the z -direction. One should also notice that this error will accumulate along the π pulse

local field components. The result obtained in Equation (2.88) is only valid for bulk fluids undergoing unrestricted diffusion. These considerations will be addressed in Chapter 4.

train. An approach to correct this error was proposed by Meiboom and Gill in 1958 [11]. The authors proposed that the π pulse should be applied perpendicular to the $\pi/2$ pulse, *i.e.*, in the same direction as the magnetization points at after the first $\pi/2$ pulse ($+y$ direction in our example). As a consequence, the effect of the refocusing pulse will be just to reverse the sign of the dephased part. This way, a small error in the π pulse will not be cumulative, and the echoes will be formed in the same direction. This method is known as the Carr-Purcell-Meiboom-Gill (CPMG) sequence (Figure 2.10).

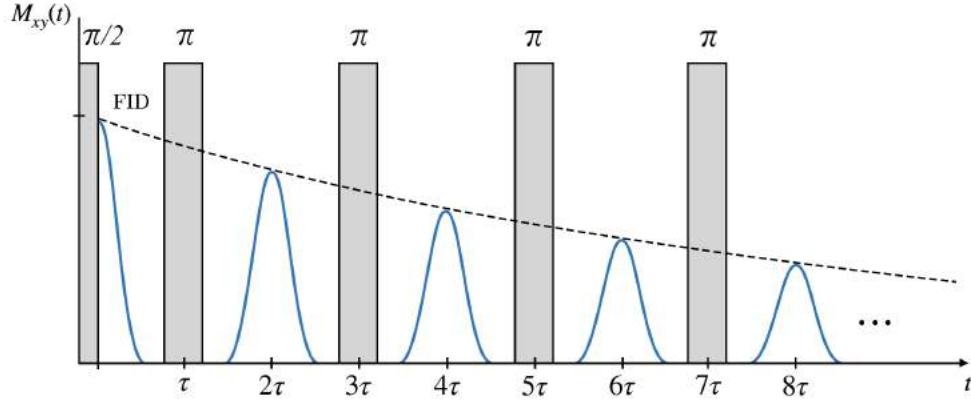


Figure 2.10: Illustration of the Carr-Purcell-Meiboom-Gill (CPMG) method for the measurement of the T_2 relaxation time. In this protocol the π pulses are applied perpendicular to the $\pi/2$ pulse and all echoes are formed at the same direction. The amplitude of the echoes decrease due to relaxation and is modulated by the exponential decay expressed in Equation 2.89.

Inversion- and Saturation-Recovery - T_1

For a measurement of T_1 the behavior of the longitudinal component of the magnetization M_z must be observed. The solution of the Bloch Equation for the dynamics of the z component of the magnetization was expressed in Equation 2.29:

$$M_z(t) = M_0 - [M_0 - M_z(0)]e^{-t/T_1}, \quad (2.90)$$

in which M_0 denotes the equilibrium magnetization directed at the z axis, considering a polarizing magnetic field $\vec{B} = (0, 0, B_0)$, and $M_z(0)$ is the initial condition.

The equilibrium magnetization can be driven to a non-equilibrium state by an initial $\pi/2$ or π RF pulse. In the former, the equilibrium magnetization is rotated to the transverse plane ($x - y$), and the initial condition will be $M_z(0) = 0$. For the latter, the equilibrium magnetization is reversed so that $M_z(0) = -M_0$. In both cases, given a certain time

after the initial pulse, a second $\pi/2$ pulse is applied to project the M_z component to the transverse plane for the detection of the signal. These methods for T_1 measurement are referred to as saturation-recovery and inversion-recovery, respectively (Figure 2.11).

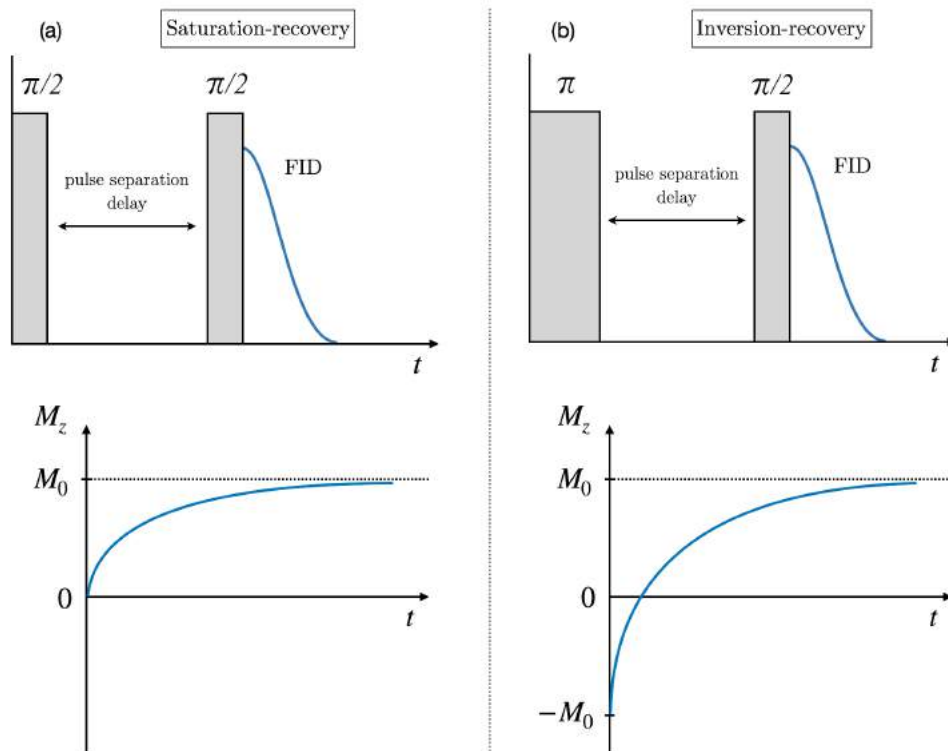


Figure 2.11: Illustration of the saturation-recovery (a) and the inversion-recovery (b) protocols for the measurement of the T_1 relaxation time. The upper graphs illustrate the pulse sequence schemes and the lower graphs show the evolution of the observed $M_z(t)$ signal as the pulse separation delay is increased in each repetition of the pulse sequence.

Considering the initial conditions for each method, the solution in Equation 2.90 can be expressed as:

$$M_z(t) = M_0[1 - \exp(-t/T_1)], \quad (2.91)$$

for the saturation-recovery protocol, and:

$$M_z(t) = M_0[1 - 2 \exp(-t/T_1)], \quad (2.92)$$

for the inversion-recovery protocol.

It should be recalled that the equations presented in this Section as the solution for the measurement of transverse and longitudinal relaxation times (T_2 and T_1) did not consider any boundary condition whatsoever, therefore being valid only for bulk samples, in the case

of fluids. The effect of confining geometries must be considered in the form of boundary conditions in order for one to properly solve the equations of motion for the magnetization components. Some of the most commonly used approaches developed with the purpose of accounting confinement effects into relaxation rates will be addressed in the following Sections.

2.2.7 2D NMR

In two-dimensional NMR different protocols can be combine into a single experiment, wherein two distinct parameters are varied simultaneously. The total magnetization signal in a 2D NMR experiment can be expressed in the following general form [4]:

$$M(x_1, x_2) = \iint k_1(x_1, R_1)k_2(x_2, R_2)\mathcal{F}(R_1, R_2) dR_1 dR_2, \quad (2.93)$$

wherein R_1 and R_2 represent the spectroscopic properties of the investigated sample (*e.g.*, the resonance frequency ω , or the spin-lattice relaxation time T_1), and x_1 and x_2 denote the pulse sequence parameters that will be varied (*e.g.*, RF pulses, evolution periods or magnetic field gradients). The functions $k(x, R)$, referred to as kernel functions, represent the response of the system to the NMR experiments that are being combined, depending on the spectroscopic properties R_1 and R_2 . The correlation function $\mathcal{F}(R_1, R_2)$ denotes the probability distribution, or the density map, of molecules with properties R_1 and R_2 , and it is the quantity to be measured.

For an example, if one of the experiments is a spectroscopy measurement the kernel $k(x, R)$ can be represented as $k(t, \omega) = \exp(-i\omega t)$, wherein $\omega \equiv R$ and $t \equiv x$. For the case of a CPMG experiment the kernel can be written as a simplified exponential form of Equation 2.89 $k(t, T_2) = \exp(-t/T_2)$, and so on. In 2D experiments the respective kernels are replaced in Equation 2.93 and the correlation function $\mathcal{F}(R_1, R_2)$ can be obtained by performing the 2D Inverse Laplace transform of the measured 2D signal [95].

Different correlation maps can be obtained depending on the two experiments involved. The most common ones are relaxation-relaxation, diffusion-relaxation and diffusion-diffusion correlation experiments. In a T_1 - T_2 experiment, for an example, the measured signal, considering the combination of an inversion-recovery and a CPMG protocol, can be expressed as:

$$M(\tau_1, \tau_2) = \iint (1 - 2e^{-\tau_1/T_1})(e^{-\tau_2/T_2})\mathcal{F}(T_1, T_2) dT_1 dT_2, \quad (2.94)$$

in which τ_1 and τ_2 represent the time parameters that are being varied in the inversion-recovery and in the CPMG experiment, respectively.

Figure 2.12 and 2.13 illustrate the pulse sequence scheme for the T_1 - T_2 and the T_2 - T_2 correlation experiments, respectively.

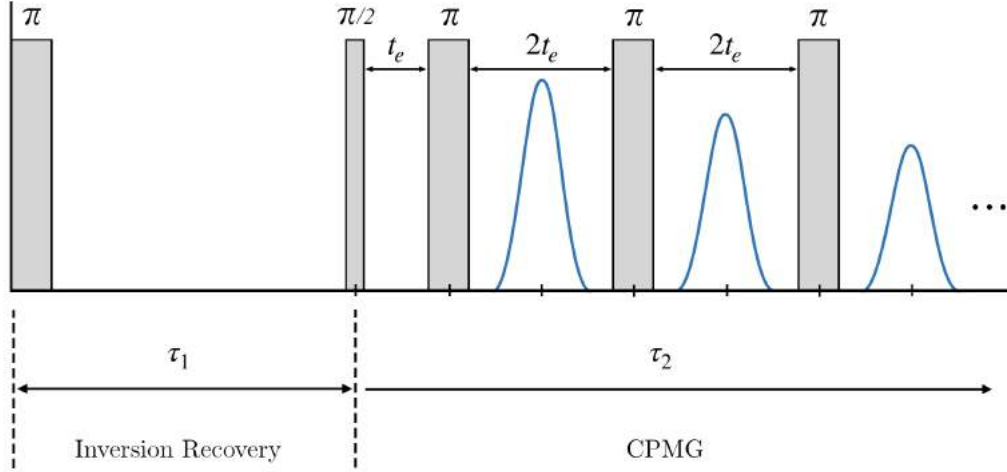


Figure 2.12: Illustration of the pulse sequence for the T_1 - T_2 correlation map combining an inversion recovery and a CPMG experiment, during which the spin system experiences longitudinal and transverse relaxations, respectively. The parameter t_e denotes the separation between the $\pi/2$ and the π pulses, or the echo time. Data is obtained varying the parameters τ_1 and τ_2 . For each τ_1 value the echo train in the CPMG is measured, wherein $\tau_2 = 2nt_e$ and n is the number of echoes acquired. The data matrix $M(\tau_1, \tau_2)$ is constructed over the two independent variables τ_1 and τ_2 .

In a T_2 - T_2 correlation map, both segments are CPMG experiments, commonly separated by a time interval Δ , during which the signal from the first CPMG protocol is stored as polarization (longitudinal magnetization), and the observed magnetization signal may be expressed as:

$$M(\tau_1, \tau_2) = \iint (e^{-\tau_1/T_{2a}})(e^{-\tau_2/T_{2b}})e^{-\Delta/T_1} \mathcal{F}(T_{2a}, T_{2b}) dT_{2a} dT_{2b}. \quad (2.95)$$

In a similar way, diffusion-relaxation maps can be obtained through the combination of some NMR-based diffusion protocol, such as a pulsed-field gradient (PFG) sequence, with a relaxation protocol, for an example, a CPMG. As it is shown in Chapter 4, the exact form of the kernel in the diffusion protocol, and which parameter will be varied, depends on the pulse sequence adopted. Differently from relaxation measurements, there is a large set of pulse sequences to be employed for the determination of self-diffusion coefficients, each one of them being best suited for a certain application depending on sample's characteristics. An enlightening review on PFG NMR diffusion sequences, including their exact expressions for the echo attenuation (*i.e.*, the respective kernels), was presented by Stallmach and Galvosas [96]. Two of those sequences, including a suitable one for the measurement of

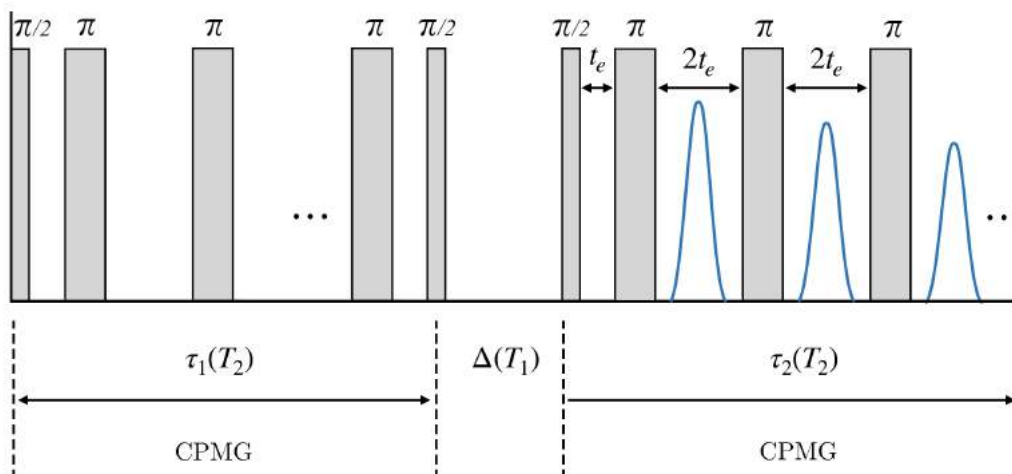


Figure 2.13: Illustration of the pulse sequence for the T_2 - T_2 self-correlation map, combining two CPMG experiments, during which the spin system experiences transverse relaxation, separated by a time interval Δ , wherein the longitudinal relaxation acts. After the first segment the second $\pi/2$ pulse stores the signal as longitudinal magnetization. After the interval Δ the CPMG in the second segment acquires the echo train. The variable parameters are $\tau_1 = n_1 t_{e1}$ and $\tau_2 = n_2 t_{e2}$, wherein $n_i t_{ei}$ denotes the number of pulses and the echo time adopted in each segment.

self-diffusion coefficients in confined fluids will be presented in Chapter 4.

Multidimensional experiments have been long applied in high-field NMR spectroscopy [97], and since the variable parameters are frequencies, a multidimensional inverse Fourier Transform must be applied to the data matrix in order for one to extract the corresponding correlation function [98]. On what regards diffusion and relaxation experiments, the signal decay is often associated with exponential profiles, and being that the case, an inverse Laplace Transform is employed instead of a Fourier one. The application of multidimensional inverse Laplace transform using conventional algorithms requires a great computational power [99, 100]. In 2000 a fast Laplace inversion (FLI) algorithm was developed [95, 101] enabling rapid inverse Laplace transform to be performed in regular desktop computers.

2.3 NMR in Petrophysics

The development of NMR instrumentation and techniques, especially the low-field ones, were mainly driven by the energy industry, particularly by oil research and its interest in accessing hydrocarbon reserves in subsurface conditions [5, 6, 102]. The NMR signals obtained from fluids under confinement can be interpreted in order to provide insightful

information on petrophysical properties of porous rocks, both in qualitative and quantitative manners. The need to perform such measurements *in situ* motivated the development of portable NMR devices to be integrated in the so-called well logging tools.

Well logging tools, as the name suggests, comprises a set of characterization techniques used to exploration (uncased reservoirs) and surveillance of subsurface reservoirs. Different techniques, such as acoustic, electromagnetic and chemical are employed to provide data that can be analyzed for the determination of subsurface physical properties and reservoir parameters, such as porosity, permeability or even fluid content (oil, water or gas). These measurements are collected versus depth along a well, and thus respond to variations in rock lithology and fluid composition. The profiles obtained by each technique are combined in a vertical data sheet for comparison and a petrophysical interpretation of the results, so that the commercial feasibility of the reservoir, as well as producible volumes of oil and gas, can be evaluated. Figure 2.14 shows an idealized log profile, including NMR T_2 distribution (to be addressed in this Section), porosity and permeability data, for a reservoir containing portions of oil and brine (salt-saturated water).

The first NMR logging tool was patented by Russell Varian in 1952 [18], proposing the use of the Earth's magnetic field to perform measurements of liquids confined in porous rocks at subsurface formations. In the 1970's new logging tools started to be developed and since then, companies like Schlumberger and Halliburton created and added sophisticated logging tools to routine analysis, that can be run along with different logging instruments such as resistivity, gamma ray, among others. Modern logging tools offer a set of useful resources which goes from logging while drilling (LWD) capabilities (a resource that represents a considerable cost reduction, since the drilling process does not need to be interrupted for the logging measurements), until magnetic resonance imaging logging (MRIL) systems [5].

Naturally, NMR measurements can also be performed in laboratory conditions using rock samples obtained from cored plugs extracted during the well drilling. Although in some cases the extracted samples may be maintained at reservoir pressures [4], commonly they are allowed to equilibrate with surface temperature and pressure conditions, a process during which the most volatile hydrocarbons are lost. The plugs are submitted to routine procedures of cleaning and drying, in order to be prepared for a large set laboratory measurements, denominated routine core analysis (RCAL). Routine measurements include porosity, permeability, mercury intrusion porosimetry, chemical analysis, microscopy imaging, among others [5].

A different group of techniques, denominated special core analysis (SCAL), relates to measurements such as wettability, relative permeability, and also NMR. Laboratory relaxation and diffusion NMR measurements are usually performed at low-field bench-

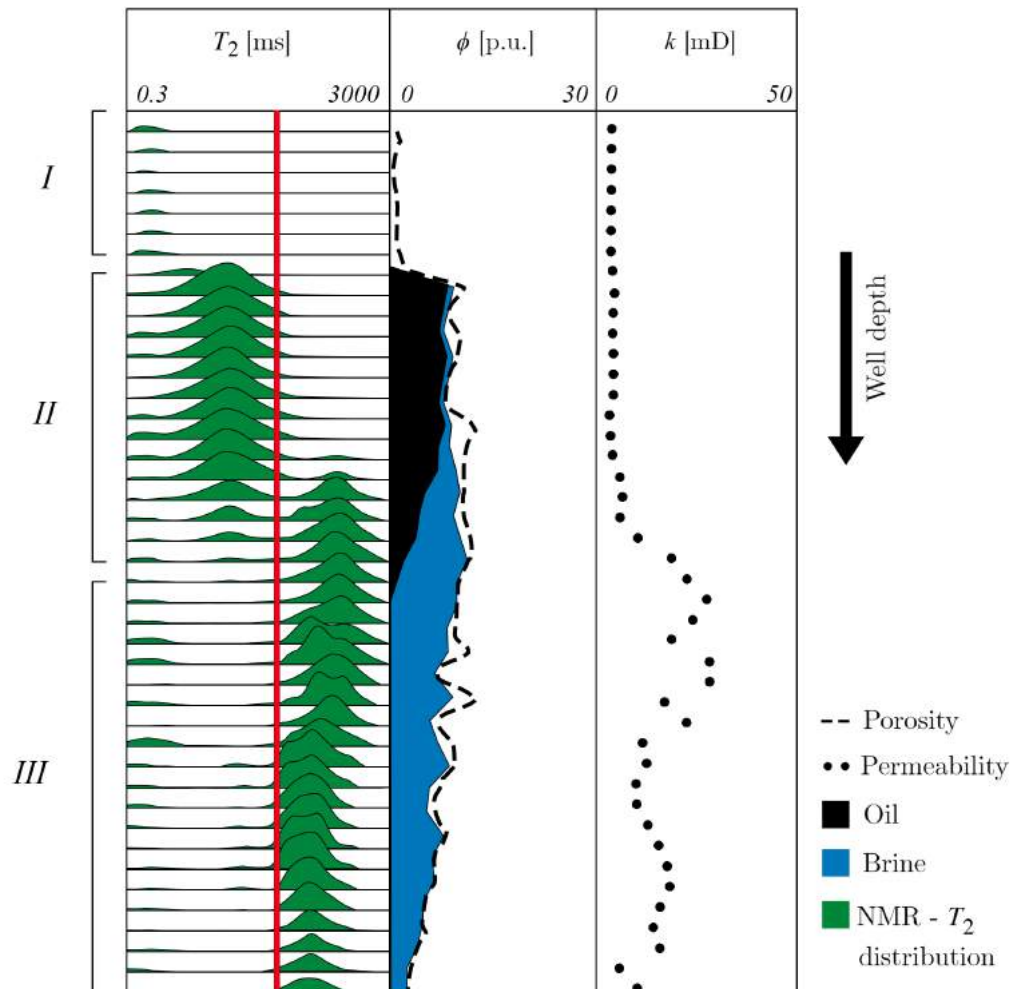


Figure 2.14: Illustration of an idealized log interpretation from a reservoir containing brine and a medium viscosity oil. Adapted from reference [103]. A series of T_2 distributions are stacked in the left column, as a function of the well depth. The vertical red line in the T_2 distributions represent the T_2 cutoff, a value determined experimentally as a reference to separate relaxation times associated with oil (shorter T_2) and brine (longer T_2). The black and blue areas in the central column stands for the producible volumes of oil and water, respectively. The dashed line represents the total porosity ϕ . The right column presents a permeability estimate, calculated using the logarithmic mean of the relaxation time distribution and an empirical function [104]. Three distinct regions are marked on the left. Region I correspond to a cap rock, a highly impermeable rock, usually shale, anhydrite or salt, which seal the reservoir rock so that fluids cannot escape. Region II correspond to a low-permeability oil reservoir. Region III denotes a moderate-permeability water saturated rock.

top equipment, so that the spin dynamics, and consequently the physical framework, can be consistent with the one from logging tool measurements. This is especially relevant considering the formerly discussed field distortions, induced by susceptibility contrast, and the influence of internal field gradients in the observed relaxation rates.

In this section we will discuss the theoretical framework required for one to comprehend how the interpretation of NMR measurements can be used to provide relevant information on petrophysical properties of porous rocks.

2.3.1 Fast Diffusion Regime and Relaxation Rates

The information provided by NMR logging profiles relates to relaxation time distributions, extracted from a series of longitudinal (T_1) or transverse (T_2) relaxation measurements (depending on the tool) versus the well depth. Before we discuss how such relaxation time distributions can be obtained, we shall recall some concepts regarding the behavior of fluids under confinement. The transverse magnetization signal obtained from a CPMG experiment in a bulk liquid sample, can be expressed by Equation 2.89, which can be rewritten as:

$$M(t) = M(0)e^{-t/T_2}, \quad (2.96)$$

wherein $1/T_2$ denotes the observed, or effective transverse relaxation rate, which considering our developments up to this point, can be expressed as:

$$\frac{1}{T_2} = \frac{1}{T_{2b}} + \frac{D(\gamma g \tau)^2}{12}, \quad (2.97)$$

in which $1/T_{2b}$ is the bulk value of the transverse relaxation rate and the second term on the right side accounts for the contribution associated with the diffusion through internal field gradients (Equation 2.88).

Notwithstanding, the influence of confinement was not yet considered in our calculations. For such task, the appropriate boundary conditions must be included to the solution of the Bloch-Torrey equations, which describe the dynamics of the magnetization components, including the diffusion terms [14]:

$$\frac{\partial M_x}{\partial t} = \gamma(\vec{M} \times \vec{B})_x - \frac{M_x}{T_2} + D\nabla^2 M_x, \quad (2.98)$$

$$\frac{\partial M_y}{\partial t} = \gamma(\vec{M} \times \vec{B})_y - \frac{M_y}{T_2} + D\nabla^2 M_y, \quad (2.99)$$

$$\frac{\partial M_z}{\partial t} = \gamma(\vec{M} \times \vec{B})_z - \frac{M_z - M_0}{T_1} + D\nabla^2 M_z, \quad (2.100)$$

wherein \vec{M} and \vec{B} are the local magnetization vector and the homogeneous polarizing magnetic field from the original Bloch equations, M_0 denotes the equilibrium magnetization directed at the z axis (considering a polarizing magnetic field $\vec{B} = (0, 0, B_0)$) and D is the molecular self-diffusion coefficient.

As proposed by Brownstein and Tarr [24], a general solution considering a Robin boundary condition, *i.e.*, portraying an impermeable surface on which nuclei can partly lose their magnetization, can be written as summation of normal magnetization modes (Equations 1.2 to 1.4). Considering the expressions obtained for the transverse and the longitudinal magnetization (Equations 2.89 and 2.90), and assuming that both calculations are also valid considering the case of fluids within a certain confining geometry, general solutions for the longitudinal and transverse magnetization densities in the presence of geometrical boundary conditions can be expressed as:

$$m_z(t) = m_0 - [m_0 - m_z(0)]e^{-t/T_{1b}} \sum_{n=0}^{\infty} A_n F_n(\vec{r}) e^{\frac{-t}{T_n}}, \quad (2.101)$$

$$m_{xy}(t) = m_{xy}(0)e^{-t/T_{2b}} e^{(-\gamma^2 g^2 D t^3/12)} \sum_{n=0}^{\infty} A_n F_n(\vec{r}) e^{\frac{-t}{T_n}}, \quad (2.102)$$

wherein T_{1b} and T_{2b} denote the longitudinal and the transverse bulk relaxation times, respectively, A_n are constants, and $F_n(\vec{r})$ and $1/T_n$ are the eigenfunctions and eigenvalues, respectively, that satisfy the eigenvalue problem described by Equations 1.2 and 1.3.

As discussed earlier, these equations show that multiexponential NMR signals, for both longitudinal and transverse magnetization, may emerge as a simple consequence of the mathematical structure of the problem regarding the solution of the Bloch-Torrey Equation with boundary conditions. Nevertheless, in order for one to give a proper interpretation for the observed relaxation rates it is important to analyze the role of diffusion in surface relaxation, and consequently in the solutions expressed above. The Robin boundary condition in Equation 1.3 means that diffusing molecules will partly lose their magnetization due to some sort of surface relaxation at the confining surface, a process associated with the parameter ρ . Notwithstanding, the total number of molecules that will encounter a confining surface will depend on the relation between the characteristic confining scale a and the molecular self-diffusivity D .

The relations expressed in Equations 1.7 and 1.8 can be used to determine which diffusion regime should be considered in the analysis of relaxation profiles. In the slow diffusion regime (*i.e.*, $\rho a/D \gg 1$), the relaxation process is referred to as being diffusion-limited, which means that depending on the relation between the characteristic confinement scale parameter a and the self-diffusion coefficient D , molecules may not, on average, experience an expressive number of encounters with pore walls, and consequently, surface

effects will not dominate over the measured relaxation rates. Nonetheless, in the fast diffusion regime (*i.e.*, $\rho a/D \ll 1$), the relaxation process is referred to as being surface-limited, as diffusing molecules will experience surface relaxation several times (Figure 2.15).

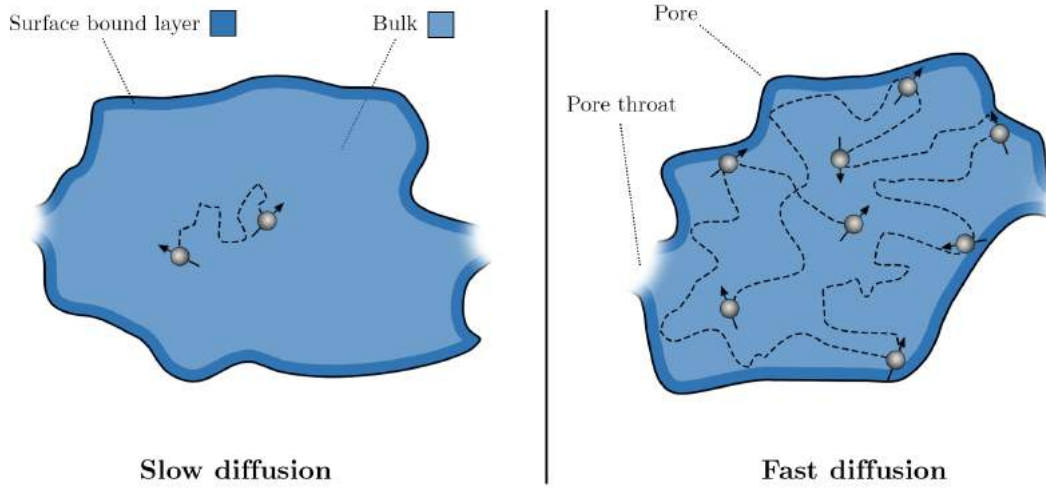


Figure 2.15: Illustration of the slow (left) and fast (right) diffusion regimes of confined fluid molecules. In the slow diffusion regime molecules do not experience an expressive number of encounters with pore walls and the relaxation process is diffusion-limited. In the fast diffusion regime molecules experience surface relaxation several times, and the relaxation process is referred to as surface-limited.

Particularly, the fast diffusion regime allows a more straightforward interpretation of multiexponential relaxation signals, and it became a very common approximation in NMR petrophysics. In the fast diffusion regime, diffusion of molecules will lead to a relative homogenization of the magnetization density, and the observed magnetization decay will be, in a fair approximation, ruled by a single relaxation rate, associated with surface effects. This means that the summation expressed in Equations 2.101 and 2.102 will be dominated by a single relaxation mode F , which in this case can be considered approximately constant. Integrating Equation 1.2 over the volume V and Equation 1.3 along the confining surface S , we have for the main magnetization mode F :

$$\int_V (D\nabla^2 F - \lambda F) dV = 0, \quad (2.103)$$

$$\oint_S (D\vec{\nabla}F \cdot \hat{n} + \rho F) da = 0. \quad (2.104)$$

Using the Gauss theorem, Equations 2.103 and 2.104 can be rearranged to:

$$\oint_S \rho F da = \lambda \int_V F dV, \quad (2.105)$$

and since F is approximately constant, we have for the governing relaxation rate λ the relation:

$$\lambda \approx \rho \frac{S}{V}. \quad (2.106)$$

The result expressed in Equation 2.106 is especially important for the interpretation of relaxation profiles obtained from fluids in porous rocks. Under the assumption of a fast diffusion regime, the magnetization decay obtained from fluid molecules inside a confining surface (pore) will be dominated by a single relaxation rate (*i.e.*, mono-exponential), which relates directly to pore's geometry (S/V) and chemical (ρ) features. If one considers that the diffusion of molecules within a single pore dominates over the diffusion along different pores, heterogeneous systems such as porous rocks with restricted pore connectivity, can be modeled by collection of "isolated" pores with different sizes, which can be thus characterized by a multiexponential relaxation profile. These assumptions, regarding the fast diffusion regime and the relation between the observed relaxation rates and pore features, are the foundation for the interpretation of relaxation time distributions obtained from NMR logging, which will be addressed in the following Sections.

In the fast diffusion regime, including the effect of confinement obtained in Equation 2.106, the observed longitudinal and transverse relaxation rates for a fluid within a confining surface (pore) may be approximated as:

$$\frac{1}{T_1} = \frac{1}{T_{1b}} + \rho_1 \frac{S}{V}, \quad (2.107)$$

$$\frac{1}{T_2} = \frac{1}{T_{2b}} + \rho_2 \frac{S}{V} + \frac{D(\gamma g \tau)^2}{12}, \quad (2.108)$$

wherein T_{1b} and T_{2b} denote the longitudinal and transverse bulk relaxation times, and ρ_1 and ρ_2 represent the surface relaxivity parameter associated with longitudinal and transverse relaxation processes, respectively.

2.3.2 A Microscopic Note on Surface Relaxation Processes

It is crucial to bear in mind that, in our previous developments the longitudinal and transverse surface relaxation processes of the nuclear spin are summarized, or represented, by the parameters ρ_1 and ρ_2 , relating to the surface relaxation "strength", or its overall effect. Microscopically, spin relaxation at the pore surface concerns complex processes involving the microdynamics of adsorbed molecules. Disregarding the choice of an exact

microscopic framework (one can find enlightening models and discussions in references [29] and [65]), generally, surface relaxation of nuclear spins can be understood as a 3-step process (Figure 2.16).

At first, the excited spin will diffuse through the bulk phase to encounter a pore wall and be adsorbed in the surface bound layer, a process which is bulk-mediated and whose time-scale depends initially on the balance between the confinement scale and the molecular self-diffusivity. Once at the surface, we enter the second phase, associated with the residence time of spins at the surface adsorbing sites, during which relaxation processes take place. Here, several mechanisms can be responsible for promoting spin relaxation [105].

Among the most common ones we may cite: the homonuclear dipole-dipole coupling, which can reduce the frequency of molecular motion; cross-relaxation processes by other nuclear spins, such as strong proton-proton interactions at the surface; relaxation promoted by paramagnetic ions, related to the large magnetic moment of electrons; and also relaxation promoted by free electrons, which occurs due to the presence of unpaired electron spins, usually populating crystallographic point defects at the surface. Furthermore, it was discovered that adsorbed molecules may diffuse along the surface, performing a sort of Lévy walk from one adsorbing site to another [63, 64, 106]. Hence, during the surface diffusion process any of those mechanisms, or even a combination of them, may cause nuclear spins to relax.

Surface relaxation processes were also found to be dependent on the magnetic field strength, a phenomenon known as relaxation rate dispersion. The first theory proposed to explain the dependence of relaxation rates on the magnetic field strength was the BPP theory (Bloembergen, Purcell and Pound [7]), in 1948, although the application of the model is considered more successful in homogeneous bulk systems than in heterogeneous complex ones. Late theories were also prosperous in explaining relaxation rate dispersion curves [29, 65, 107] with physical frameworks at a microscopical level. All of these model-predicted dispersions of relaxation rates can be experimentally verified by the use of field cycling NMR techniques - *i.e.*, variable field NMR - [108]. Finally, at the last phase, the relaxed spin leaves the surface and returns to the bulk phase.

The overall effect of surface relaxation and its effect into the observed relaxation rates in NMR experiments will depend, firstly, on the relation between molecular self-diffusivity and the confinement scale (or the surface-to-volume ratio), which defines, on average, the rate of encounters between excited diffusing spins and the pore surface. Nonetheless, the actual "strength" of surface relaxativity will rely on features regarding fluid's molecular properties, such as polarity, molecular shape and the nuclei chemical environment [76, 109], its affinity for the pore surface, as well as the surface topology [110]. Thereby, it should be emphasized that ρ_1 and ρ_2 quantities expressed in equations describing the role

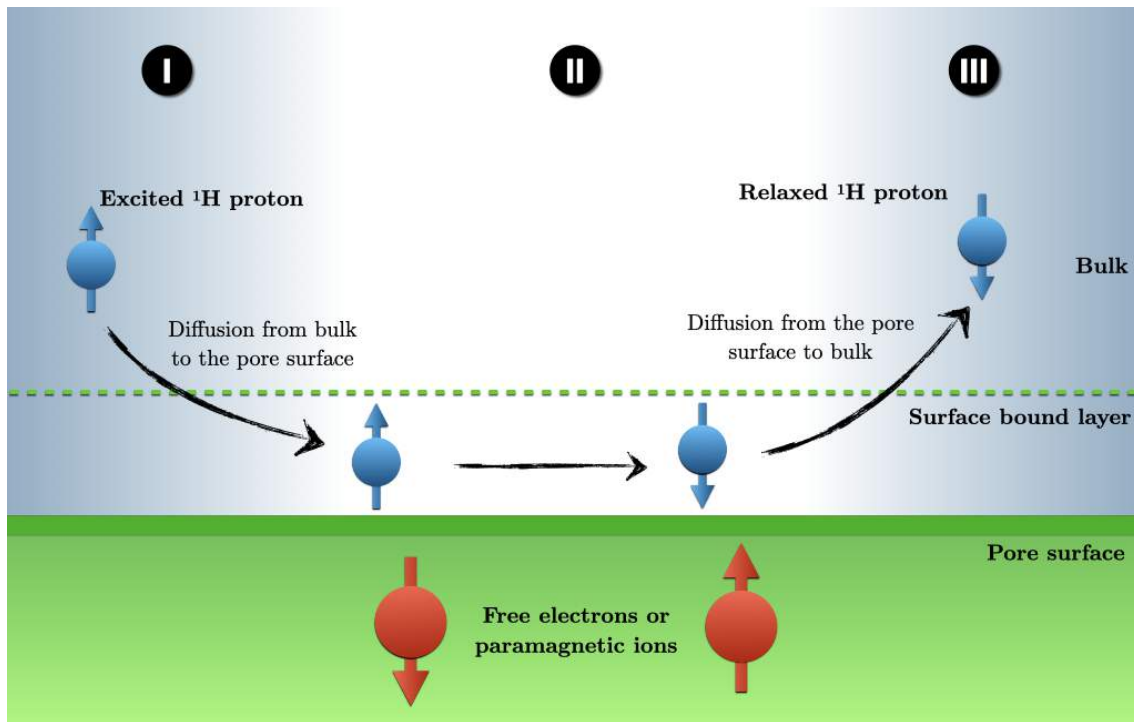


Figure 2.16: Illustration of the 3-step surface relaxation process considering, for an example, the interaction of the ^1H proton nuclear spin with free electrons or paramagnetic ions at the pore surface. (I) The excited proton spin diffuses from the bulk phase to the surface bound layer. (II) Relaxation mechanisms take place during the residence time of molecules at the surface bound layer, during which molecules may diffuse along adsorbing sites. (III) The relaxed proton spin diffuses back to the bulk phase.

of surface in the observed relaxation time of confined fluids synthesize the global effect resulting from an intricate network of microdynamical processes occurring at the pore surface, in a similar way as the parameters used to describe chemical reaction rates.

2.3.3 Inversion of Multiexponential Decays and Relaxation Time Distributions

Let us take once more, for an example, the measurement of the magnetization decay in a CPMG experiment, this time performed in a fluid-saturated porous rock. Assuming that the system is in fast diffusion regime, and that pore connectivity is such that the diffusion of molecules along different pores can be neglected, each pore will contribute to the total magnetization decay with its own relaxation rate $1/T_2$. Denoting by $f(T_2)$ the function representing the T_2 density, the total magnetization signal at a given time τ may

be expressed as:

$$M(\tau) = \int f(T_2) \exp(-\tau/T_2) dT_2. \quad (2.109)$$

Equation 2.109 express a multiexponential NMR signal associated with a distribution of relaxation times, which here, arises from a collection of fluid-saturated (and approximately isolated) pores in a rock sample, in the fast diffusion regime.

The T_2 density function $f(T_2)$ in Equation 2.109 may be obtained by the Inverse Laplace Transform of the acquired signal $M(\tau)$. In the case of a real measurement, the inversion process aims to find a set of T_2 amplitudes, or a discrete T_2 density function F , from a discrete data set of echo amplitudes M . Accordingly, the discretized version of Equation 2.109 may be expressed as:

$$M(\tau) = \sum_{i=1}^n F(T_2) \exp(-\tau/T_{2,i}). \quad (2.110)$$

Let us assume that the data set M is a m -dimensional vector, in which m represents the number of acquired echos. The discrete density function F , a unknown vector, is predetermined to be n -dimensional, which means that there will be a number n of T_2 values, commonly taken to be logarithmic distributed, whose amplitudes we want to determine. The relation between the matrices M and F is established by the new discrete kernel function $K = \exp(-\tau_m/T_{2,n})$, which is thus a $m \times n$ matrix:

$$M = KF + N, \quad (2.111)$$

wherein N represents the m -dimensional noise matrix. Solving for F may be achieved through a least squares fit performed to minimize the squared error sum functional defined by [52]:

$$\Phi[F(T_2)] = \|M - KF\|^2 \quad (2.112)$$

Generally, a valid solution for F should be determined in order to fulfill the condition:

$$\|M - KF\| < \sigma, \quad (2.113)$$

in which σ denotes the noise variance. Notwithstanding, the ill-posed character of the inverse Laplace problem inflicts that, for a finite signal-to-noise ratio, there is a set of mathematically valid solutions which satisfy the condition in Equation 2.113. In order to assist the solution choice process, a collection of *a priori* information, known as regularization tools, can be incorporated into the inversion procedure. Among several regularization techniques, the method proposed by Tikhonov [50, 51] became very popular as a general approach for one to solve Fredholm integral equations of the first kind, such as

Equation 2.109. Tikhonov proposed that an approximate solution could be found instead of an exact one. By performing such approximation, the new functional to be minimized can be generally expressed as:

$$\Phi_\alpha[F(T_2)] = \|M - KF\|^2 + \alpha\Omega[F(T_2)], \quad (2.114)$$

wherein $\Omega[F(T_2)]$ represents a regularizing (or smoothing) functional, and α is known as the regularization parameter.

In practice, the implementation of Tikhonov's method requires the choice of both, a smoothing functional form and the value of the corresponding regularization parameter. Different forms for the smoothing functional Ω may be employed depending on the problem investigated, relating to the zeroth, first and second derivatives of the density function F [52]. Once the smoothing functional is chosen, the value of the regularization parameter will determine the balance between the exact and the smoothed solutions. Taking the value of α as 0 to minimize the expression in Equation 2.114 usually leads to a solution which is unstable with respect to small fluctuations in F (*i.e.*, experimental noise) and may have no physical meaning. However, large α values may stabilize, but also overly smooth the solution, meaning that relevant physical information may be lost.

Several distinct criteria may be employed to assist a proper choice for the value of the regularization parameter, most of them being commonly related to the existence, or not, of some *a priori* information regarding the noise variance [111, 112], as well as problem features.

Although these criteria will not be detailed here, the effect of the regularization parameter value on the inversion process is illustrated in Figure 2.17. The decaying signal on the left plot is a normalized 2000-point synthetic data composed by the summation of three exponential decays with distinct weights, and relaxation rates which differ one from another by approximately one order of magnitude:

$$S(t) = 0.2e^{-t/T_{2,1}} + 0.3e^{-t/T_{2,2}} + 0.5e^{-t/T_{2,3}} + N, \quad (2.115)$$

wherein $T_{2,1}$, $T_{2,2}$ and $T_{2,3}$ were defined as 3, 30 and 150 ms, respectively, and N was added using a random noise function so that the final signal-to-noise ratio was $S/N = 5$, in order to simulate a real experimental data set. The inverse Laplace transform was performed using a Tikhonov regularization algorithm with a non-negativity constraint [113].

The results of the inversion for three different values of the regularization parameter α are shown in the right plot of Figure 2.17. For small values ($\alpha = 0.025$) the solution is actually unstable, and the inversion shows a relaxation distribution with several peaks, which in this case are only mathematical artifacts. For large alpha values ($\alpha = 25$) the

presented solution is overly smoothed, and part of the information on the three initial relaxation rates which compose $S(t)$ is lost. An intermediate behavior is seen for $\alpha = 2.5$, when the solution partially recovers a relaxation time distribution with three regions, relatively close to the initially proposed time constants. Noise plays an important role in the solution of inverted data, since it is usually the data signal-to-noise ratio that will dictate the weight of the smoothed solution over the exact one [114].

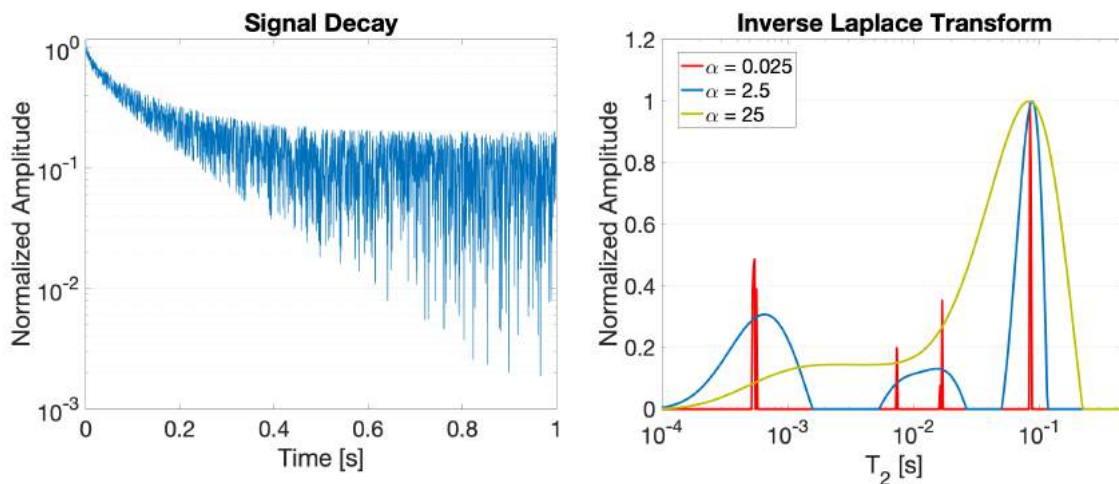


Figure 2.17: Inverse Laplace transform of a synthetic data composed by the summation of three exponential decays (left plot) with distinct weights and relaxation rates (Equation 2.115), using a Tikhonov regularized algorithm with positivity constraint, for three different values of the regularization parameter α (right plot). The amplitudes of the inverted solutions were normalized by their maximum height for a clear visualization. The behavior of the inverted data depends on the balance between the exact and the smoothed solutions, determined by the value of α .

The regularized inverse Laplace transform of data obtained from relaxation profiles inverts the signal in the time domain to a quasi-continuous distribution of relaxation times, and is the standard procedure for the analysis of NMR logging measurements (first column of Figure 2.14). The interpretation of the inverted data, assuming the condition of fast diffusion, is to associate a distribution of relaxation times with a pore size distribution, as a consequence of the relation expressed in Equation 2.108, assuming that the bulk relaxation rate and the effect of diffusion through internal field gradients may be neglected, and that the surface relaxivity ρ can be considered sufficiently homogeneous along the sample.

There are other advantages in visualizing NMR data as a distribution of relaxation times. The area underneath the inverted solution represents the total volume of fluid being measured and under a proper calibration the sample's porosity - the ratio between the

total porous volume (\approx fluid volume⁵) and the sample's total volume - can be determined. Besides, the association between pore sizes and relaxation rates allows one to relate smaller relaxation times to fluids under heavy confinement, or with low mobility, also referred to as bound fluids, and consequently, the ones with greater relaxation times are related to movable portions, or free fluid. Usually, a reference value known as T_2 cutoff is used to separate these two portions of fluid in the T_2 distribution, in order to provide a rough estimate of both volumes along the vertical NMR profile, *i.e.*, versus the well depth (Figure 2.14).

It must be noted that, the association between NMR relaxation rates and pore size distributions rely on a particular set of constraints regarding the diffusion regime (which depends itself on the self-diffusivity of the fluid and the relation between the value of the surface relaxivity parameter ρ and the confinement scale), the pore scale and connectivity (the latter determines if the diffusion within pores will dominate the over the diffusion along pores), and also the homogeneity of ρ along the porous sample. Furthermore, in the particular case of NMR logging profiles, each measurement will be sensitive to, and consequently averaged over a portion of the reservoir (depending on the tool design), which must be presumed to hold a certain degree of homogeneity in order for these approximations to be applied.

Chapters 3 and 4 present two works regarding the application of high-field NMR techniques to the characterization of confined fluids in porous media. Each of those works, developed in the context of a research project in NMR Petrophysics, was motivated by a careful evaluation of the respective framework employed for data analysis - including all the involved parameters, regimes and approximations - and the subsequent interpretation of the results, especially on what regards geometrical features of the investigated systems, and correlated properties.

In Chapter 3, we present a systematic study on T_2 relaxation times obtained from a set of water-saturated synthetic porous samples in high- and low-field NMR equipment. The choice for synthetic porous media was motivated by the possibility of achieving a better control on all the previously mentioned variables that influence the observed relaxation rates of confined fluids. Pre-selecting the material and customizing the fabrication process it was possible to produce a set of samples with distinct confinement scales, although maintaining the same mineralogy, in order to assure a homogeneous effect of surface relaxation along a single sample and also among different samples. All samples were carefully characterized for chemical composition, topology and also for petrophysical

⁵The total porous volume matches the fluid volume only in the case of full saturation, *i.e.*, when all the available pore space is filled with fluid. In practice this does not always happen. The ratio between the fluid volume and the sample's volume is referred to as the effective porosity, accounting for the saturable portion of the pore space. The ratio between the total pore space, saturable or not, and the sample's volume is referred to as the absolute porosity, often determined by micro imaging techniques.

properties such as porosity, permeability and pore size distribution, the latter performed by the processing of micro computed tomography images, in order to assure a proper analysis on the correlation between the measured relaxation rates and samples geometrical features. The influence of the magnetic field strength and the mathematical procedure for the processing of raw data on the observed relaxation rates were also addressed.

The work presented in Chapter 4 relates to the same paradigm: the analysis and interpretation of NMR data for the characterization of confined fluids, this time under the light of diffusion NMR. In this work, a set of time-dependent diffusion NMR experiments are carried out under the framework of restricted diffusion in order to provide information on conformation features of water-oil emulsions under confinement. The motivation relies on merging the capabilities of diffusion NMR techniques to identify distinct fluids, with the geometrical features that can be extracted through data analysis within the framework of restricted diffusion, in order to propose a methodology capable to provide valuable information not only on individual characteristics of both water and oil phases, but also on the conformation scenario of both fluids under confinement. Following an author's structure choice, the theoretical background for diffusion NMR, as well as the framework of restricted diffusion, were not presented in this Chapter, instead, both are discussed in Chapter 4, as a preparation to the referred work.

Chapter 5 presents a relatively new high-field NMR technique and its potential application to the characterization fluid-saturated porous media, which relate to future works and applications which are still under initial development. The application of long-lived singlet states is presented as a tool allowing the access to long-time regimes in diffusion NMR experiments with fluids under confinement. The behavior of molecular self-diffusion coefficients in the long-time regime can be associated with geometrical properties of porous media of great interest. The theoretical background, a potential application and initial developments are presented.

Publications

- B. Chencarek, M. Nascimento , A. M. Souza, R. S. Sarthour, B. Coutinho, M. D. Correia, and I. S. Oliveira. “Multi-exponential Analysis of Water NMR Spin–Spin Relaxation in Porosity/Permeability-Controlled Sintered Glass”. In: *Applied Magnetic Resonance* 50 (2019), pp. 211–225. doi: 10.1007/s00723-018-1050-x. url: <https://doi.org/10.1007/s00723-018-1050-x>.
- M. Nascimento, B. Chencarek, A. M. Souza, R. S. Sarthour, B. Coutinho, M. D. Correia, and I. S. Oliveira “Enhanced NMR relaxation of fluids confined to porous media: A proposed theory and experimental tests”. In: *Phys. Rev. E* 99 (4 2019), p. 042901. url: <https://link.aps.org/doi/10.1103/PhysRevE.99.042901>.
- B. Chencarek, M. Nascimento , A. M. Souza, R. S. Sarthour, B. Coutinho, M. D. Correia, and I. S. Oliveira. “PFG NMR time-dependent diffusion coefficient analysis of confined emulsion: post drainage phase conformation.” In: *Journal of Petroleum Science and Engineering* (2021), vol. 199, p. 108287. issn: 0920-4105. doi: <https://doi.org/10.1016/j.petrol.2020.108287>. url: <http://www.sciencedirect.com/science/article/pii/S0920410520313413>.

Part II

Results

Chapter 3

Multi-exponential Analysis of Water NMR Spin–Spin Relaxation in Porosity/Permeability - Controlled Sintered Glass

3.1 Motivation and Background

Nuclear magnetic resonance (NMR) experiments involving fluids confined in porous media are long used for the geometrical characterization of porous structures [4, 6]. Since the most common pore systems are filled with water, the technique often employed is proton NMR.

The association of nuclear magnetic decay and microstructure is based on the observed increased rate of relaxation generally promoted by confinement [6]. In ordinary sized samples, *e.g.*, fluids contained in probe tubes of NMR spectrometers, with dimensions in the order of millimeters - *i.e.*, bulk samples - the nuclear magnetic relaxation of water protons is well described by Bloch equations [2]. In practice, this means that single exponential curves fit the decay profiles obtained from typical NMR experiments. As the samples, however, become confined to dimensions in the order of tens of micrometers, a substantial increase in relaxation rates is observed, as surface relaxation effects become prominent. In this case, multiexponential NMR decays may arise as a consequence of a summation of magnetization modes, or from a system which is dynamically heterogeneous. In this case, the addition of more exponentials to fit the measured data is somewhat unrestricted since the number of exponentials needed to a good fit is generally not fixed

a priori. Notwithstanding, it is well known that two or three exponential terms suffice in describing a general decay behavior, which does not produce a conclusive information since entirely different multi-exponential fits can adjust to the same data with similar precision [52].

Assuming that the confined fluid molecules are in the fast diffusion regime (see Section 2.3.1), every pore in a porous system decays mono-exponentially and hence the overall relaxation corresponds to a sum of many exponential decays. In this particular case, data fitting by multiple exponentials is unfruitful in the sense that the exact number of signal components is unknown. In this case, a “guessed” interval for the values of T_2 is set, and numerical Laplace transform inversion techniques have become the usual approach for processing NMR relaxation data. Although the analytical inverse Laplace transform may be uniquely determined, the numerical procedure is highly sensitive to small fluctuations such as experimental noise, a problem commonly surpassed with regularization tools [49]. Inverted distributions are therefore not unique and the range of their distinction depends directly on the quality of the acquired data [114]. In any case, further conditions can always be assumed to ensure uniqueness or to pick a reasonable distribution among the available ones.

On the view of the most common interpretation, the inverted distribution of relaxation times corresponds to the distribution of pore sizes in the sample considered. As discussed in Chapter 2, there are clearly some problematic issues on establishing a direct relation between pore sizes and relaxation times. Whenever material heterogeneity is present, or even if the fast diffusion regime may not be assured, the relation cannot be imposed without concern and a model of how surface related parameters influence relaxation times needs to be introduced before any association with pore sizes is made.

Another issue relates to the fact that in general porous systems the pores are rarely disconnected. The impact of pore communication on relaxation however may be much more complex as it does not only depend on geometrical features of the pore space, since diffusion and intensity of surface activity also play important roles [27].

Evaluating surface activity in nuclear magnetic relaxation is then a fundamental step for a better interpretation of NMR decays and their relation with pore size distributions. From the mathematical perspective, the problem relates to include boundary conditions that account for surface effects in the Bloch-Torrey equations [14]. In the light of early heuristic attempts [8, 116] and formulations based on non-equilibrium thermodynamics principles [107, 117, 118], surface relaxation processes are taken to be well represented by the surface relaxivity parameter ρ , introduced in Chapter 2. Furthermore, the nuclear magnetization over a pore can be considered homogeneous in fast-diffusion regime, and so it is possible to associate to each pore a decay rate which is generally represented by

Equations 2.107 and 2.108.

Although the use of such approximations to the case of communicated porous structures should be carefully addressed, it is nevertheless the traditional interpretation for NMR relaxation data of saturated porous media. The relaxivity influence on the incremental pore relaxation rate is usually overlooked when applying Equations 2.107 and 2.108 to real pore systems on the grounds that specimens are sufficiently uniform in material composition or diffusion is fast enough to homogenize effectively surface heterogeneities.

While the latter argument may be considered valid on single pores, it most definitely cannot be true for the entire sample as a result of the relatively short distance traveled by most nuclear spins. Material homogeneity, on the other hand, may be safely assumed for synthetic structures, provided a controlled fabrication process, whereas for most natural ones, the assumption in fact only leads to a desirable approximation. In order for one to understand the exclusive effects of confinement on the NMR proton relaxation, one must assure an uniformity of surface activity along the sample, most easily obtained by employing artificial porous systems.

In spite of the vast literature on this subject, broadly motivated by the important applications in the oil industry, there is still room for systematic studies under controlled laboratory conditions on the roles that acquisition noise and the physical properties of the sample play on the observed NMR decay, as well on the conditions with which such data can be interpreted as corresponding to pore size distributions.

In this work a thorough study of T_2 water relaxation times is performed in artificially sintered sand-glass samples using high- (500 MHz) and low-field (15 MHz) NMR, under conditions of porosity and permeability control and low noise. Setting of material and geometric parameters is achieved by selecting different grain sizes and applying a specific thermal treatment. The pore size distribution of sintered samples is calculated through the analysis of 2D micro-tomography images using image processing tools and a proper segmentation algorithm.

The experimental NMR data is then analyzed by three distinct procedures: Laplace inversion with optimized regularization and nonlinear least-square curve fittings, first, with bi-exponential functions and, finally, q -exponentials. This last approach is based in the assumption of a chi-square distribution of relaxation times [119], as opposed to a Gaussian or half-Gaussian distribution in the case of a stretched exponential [120]. The results of the three methods are compared and it is discussed to what extent the distribution of relaxation times so obtained may be interpreted as pore size distributions.

3.2 Sample Fabrication and Characterization

3.2.1 Sintering and Chemical Analysis

Solid glass microspheres of four different size ranges (A: 53-106 μm ; B: 150-212 μm ; C: 250-300 μm ; D: 350-500 μm) were sintered to produce four types of porous samples. Microspheres from each range were placed in cylindrical ceramic crucibles (Al_2O_3 99.8%) and taken to a chamber furnace (Carbolite CWF 1200) for the following heat treatment: from room temperature to 560 C° at 140 C°/min, held for 20 minutes; from 560 to 700° C at 20° C /min, held for 1 hour; from 700 to 490° C at 14° C /min, 490 to 440° C at 28° C /min, and then cooled to room temperature. For each size range, two sizes of cylindrical crucibles were used to produce samples with $\varnothing 8 \times 40\text{mm}$ and $\varnothing 38 \times 28\text{mm}$ (Figure 3.1) for use in high- and low-field NMR equipment, respectively.

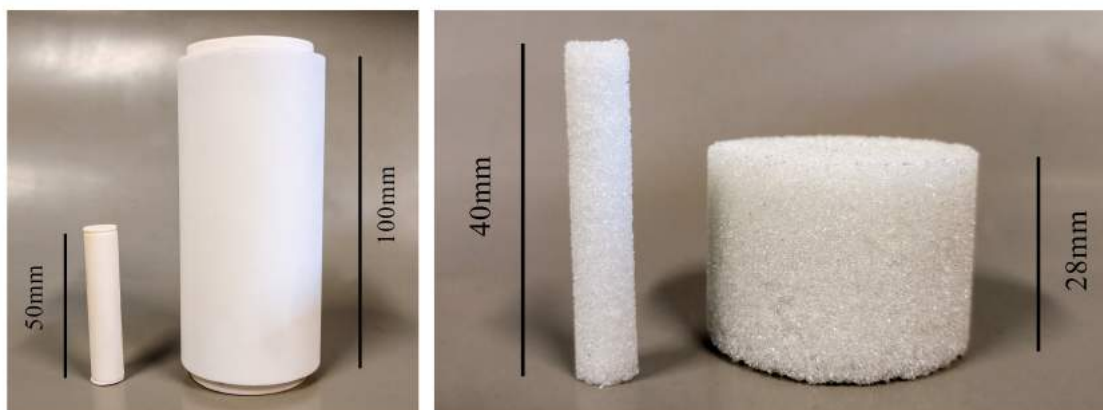


Figure 3.1: Ceramic crucibles (left) and synthetic porous samples from size range D after sintering (right), for application in high- and low-field equipment.

In order to assure the desired material homogeneity samples from all ranges were submitted to energy dispersive x-ray spectroscopy (EDS) in a scanning electron microscope (JEOL JSM-6490), in the LabNANO laboratory at CBPF. The EDS technique comprises a chemical microanalysis, usually performed in conjunction with scanning electron microscopy (SEM), wherein x-rays emitted from the sample during bombardment by an electron beam are detected to characterize the elemental composition of the analyzed volume. Results from the EDS analysis performed in samples of all size ranges are presented in Figure 3.2.

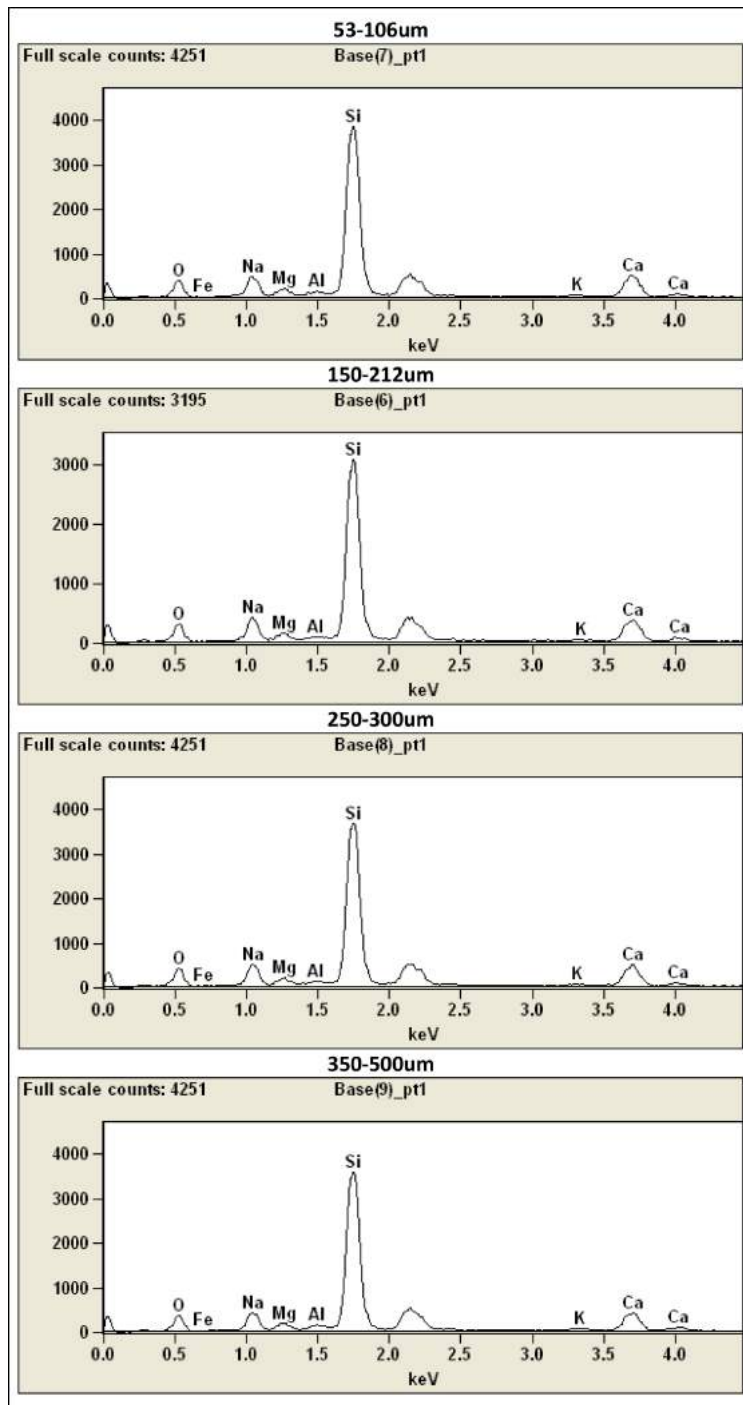


Figure 3.2: Energy dispersive spectroscopy analysis in sintered synthetic samples from size ranges A to D. The presented graphs denote the average signal obtained from several acquisitions performed in different regions of a sample, showing no significant variation in composition among the observed samples.

3.2.2 Porosity and Permeability Measurements

After the sintering process, samples were weighed, saturated with water and weighed again to a crude first mechanical estimation of porosity values. Saturation was performed using the method known as imbibition. The dry sample and the water recipient are placed in a desiccator connected to a vacuum pump. After the establishment of a low vacuum condition in the desiccator the sample is then dropped into the water recipient in order to minimize the formation of trapped air bubbles during saturation process.

Effective porosity and absolute permeability were respectively measured by the free-gas expansion [121] and steady-state method [122] using in-house equipments at the research center of Petrobras. Effective porosity accounts for the ratio between interconnected pore volume - or the saturable volume - and total sample volume, not considering the contribution of isolated pores:

$$\phi_e = \frac{\text{interconnected pore volume}}{\text{total sample volume}} \quad (3.1)$$

Absolute permeability, on the other hand, is related to the porous media ability to allow the flow of a single fluid, and can be defined by the relation:

$$v = -\frac{\kappa}{\mu} \frac{dP}{dL} \quad (3.2)$$

wherein v represents the apparent fluid velocity, κ is the sample permeability measured in units of Darcys¹, μ is the viscosity of the fluid, and dP/dL is the pressure drop per unit length. Whereas porosity values present no significant changes among the studied samples, permeability values, on the other hand, show a high dependence with average grain diameter, as it can be seen in Figure 3.3.

The sintering protocol was designed to preserve most of the porosity in the original unconsolidated sphere packing, which is nearly the same over all grain size ranges employed. This allows for the assumption of similar amounts of saturating fluid over samples that exhibit different pore sizes and, incidentally, with respect to NMR technique, a fair comparison between corresponding signals. Scanning Electron Microscopy (SEM) and micro-computed tomography techniques were used to evaluate the structure of porous spaces. Typical images are shown in Figure 3.4.

¹A porous sample with permeability equal to 1 Darcy allows a flow of $1\text{cm}^3/\text{s}$ of a fluid with viscosity of $1\text{mPa}\cdot\text{s}$ under a pressure gradient of $1\text{atm}/\text{cm}$ acting across an area of 1cm^2 .

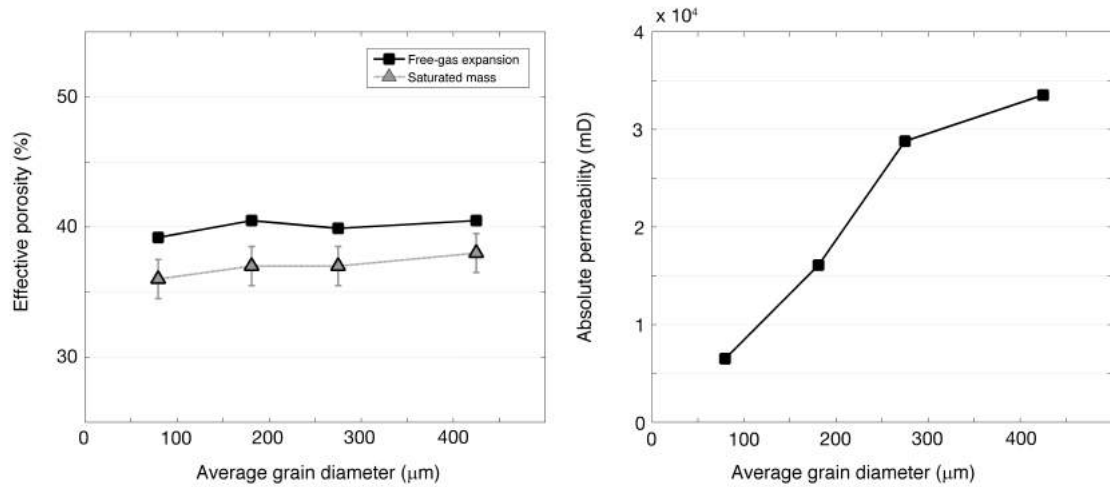


Figure 3.3: (Left) Porosity values estimated by saturated mass (triangles) versus the values obtained using the free-gas expansion method (squares). (Right) Permeability values obtained using the steady-state method. A significant increase of permeability is observed, in opposition to porosity, which remains nearly constant. Here, the average grain diameter represents simply the mathematical average between the lower and upper microspheres' diameters within each chosen grain (sample) size range.

3.3 Calculation of Pore Size Distribution from 2D Micro-Tomography Images

In order to investigate confinement features from the samples after the sintering process, 2D micro-tomography images with a resolution of $5 \mu\text{m}/\text{pixel}$ were processed for the determination of pore size distributions and two-dimensional porosity values. The first step regards the segmentation of pore spaces and grains in transverse ($x - y$ plane) 2D images obtained from cylindrical samples (Figure 3.5). Although this task can be considerably burdensome in the case of real rocks, mostly due to the mineralogical and geometrical heterogeneities of the porous space, it can be much simpler in the case of synthetic samples with a narrow grain size range and homogeneous mineralogical composition. Image segmentation was performed using the Image Processing toolbox (MATLAB 2019b). Figure 3.6 shows an example of a segmented micro-tomography image for a sample from size range C.

The crucial step for one to obtain a pore size distribution relates to the choice of a proper method to identify and characterize pore regions and sizes in the segmented image. For such task the algorithm proposed by Rabbani et al. [123] was adopted. One of the most positive aspects of the proposed method relates to the coupling of well-known distance functions and a watershed flooding segmentation algorithm [123–125], in order to directly

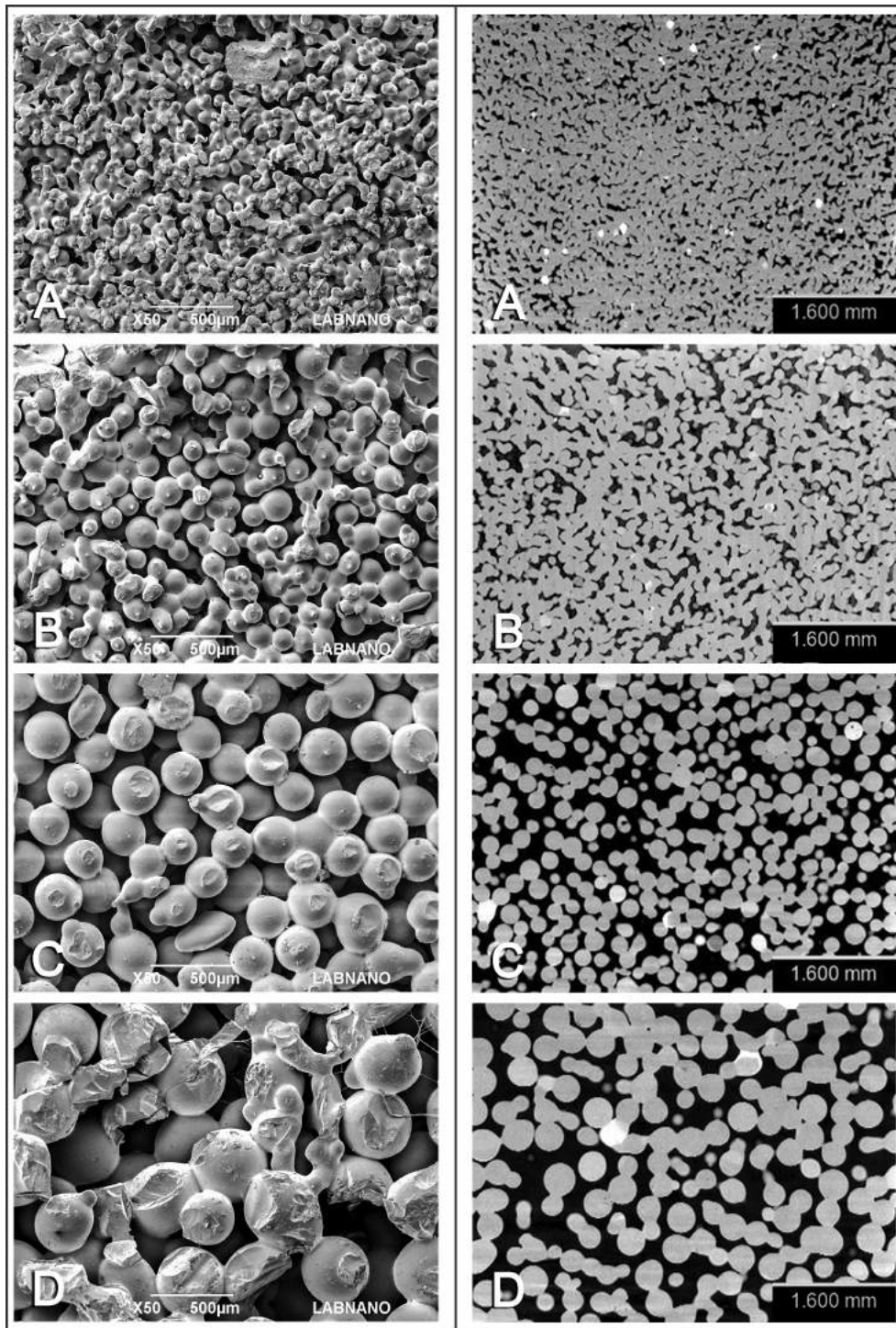


Figure 3.4: SEM images (left) and micro-tomography slices (right) artificial samples examples for each size range of grains. In spite the clear variation of porous sizes, the porosity remains nearly the same in all samples.

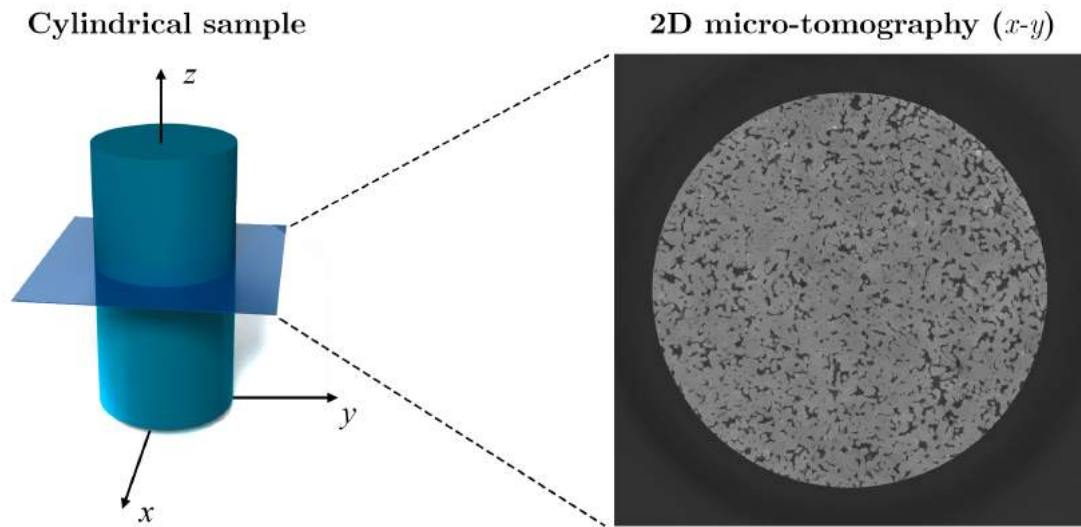


Figure 3.5: Scheme illustrating the acquisition of 2D transverse micro-tomography images from cylindrical samples. Each sample is scanned along the z axis for a full set 2D images.

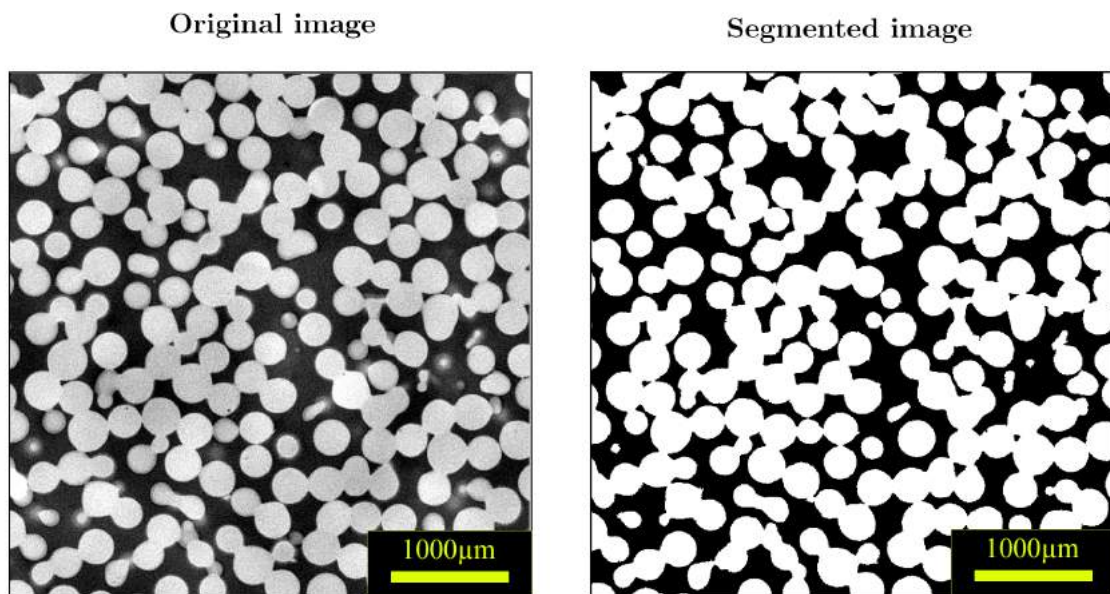


Figure 3.6: Example of segmentation of pore space and grains from a 2D micro-tomography image in a synthetic sample from size range C. After the calibration of an appropriate threshold the original image is processed to be converted in a binary map. In the original image, the light gray pixels represent the grains and the dark gray pixels denote the porous space. Segmentation was performed using the Image Processing toolbox (MATLAB 2019b).

identify and separate pore regions and throats.

The foundation of the watershed flooding algorithm can be understood considering the dynamics of a water drop once it is placed into a topographic relief, as it will flow to the nearest minimum. The method consist of identifying these regional minimum points and assuming each one of them as a water source, used to flood the entire relief. In points wherein floods by two distinct sources meet a watershed line (barrier) is created, and two distinct regions are defined.

A common procedure for the location of regional minimum points is to perform the calculation of the Euclidean distance distribution from the binary image (Figure 3.7). In the Euclidean distance map the intensity of each pixel represents the distance between that pixel and the first non-zero pixel in the original binary image. Through the distance map topographic regional minimum points can be found according to the location of high or low intensity pixels. Once the source points are defined, flooding by each one of the sources will result in distinct regions separated by a watershed.

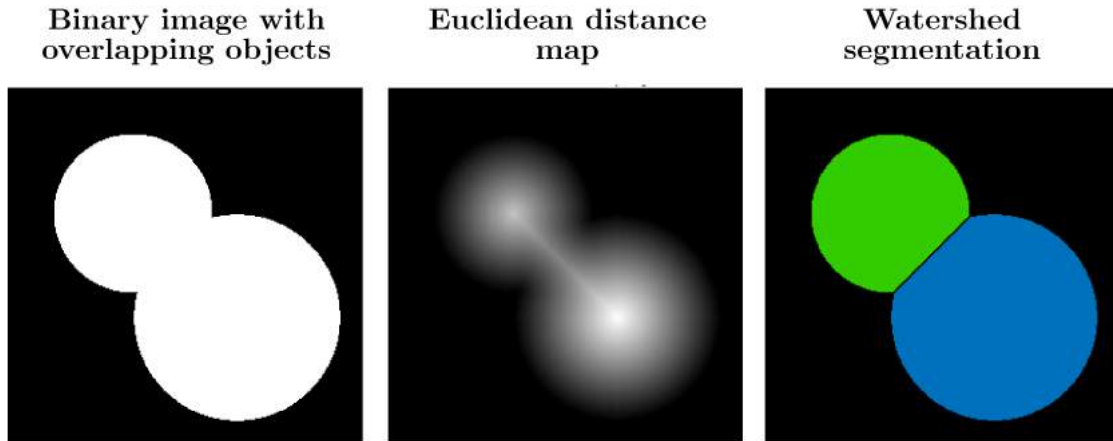


Figure 3.7: Example of a watershed segmentation process. An Euclidean distance map (central image) is calculated from the original image (left image), composed by two overlapping spheres. In the Euclidean distance map the intensity of each pixel represents the distance between that pixel and the first non-zero pixel in the original binary image. Regional minimum points are determined through the location of high or low intensity pixels. After the flooding by each one of the sources distinct regions are then separated by a watershed (right image).

The distribution of pore sizes in each 2D image was obtained assuming that the radius of realistic pores (regions) are equal to the radius of model circular pores with the same area. For each sample a set of 2D micro-tomography images of 864×864 pixels in size and a resolution of $5 \mu\text{m}/\text{pixel}$ were processed and the resulting pore size distribution was

represented by a 30-bin frequency histogram for a clear visualization of the results. The 2D porosity was calculated for each image simply as the ratio between the porous area and the total image area. Values of 2D porosity obtained from each transverse micro-tomography image were plotted against the slice number for an analysis of the porosity variation along the z axis. Pore size distributions and 2D porosity values obtained for samples from size range A to D are shown in Figures 3.9 to 3.12. In each pore size distribution histogram the green bar represents the average pore size of the obtained distribution and the red bar denotes an estimate of the pore radius considering the relation $d_{\text{pore}} \approx 0.45d_{\text{bead}}$, proposed by Rémond et al. [126] for a loose packing of mono-sized beads.

An interesting behavior can be noticed in the average 2D porosity values obtained by image processing in comparison with measured values (Figure 3.8). For the case of samples with smaller bead size range (samples A and B) a considerable discrepancy between image-processed and measured porosity values can be seen, due to the fact that the image resolution and pore size scale are the same order of magnitude. As the characteristic confinement scale increases in comparison with the image resolution (samples C and D) such discrepancy decreases, and image-processed porosities approximate the measured values. Another feature from 2D porosity curves is the noticeable dispersion of values along the z axis. Such behavior is believed to be a consequence of the expected tighter packing of smaller beads among each size range at the bottom of the ceramic crucible before sintering, and most importantly points out a fabrication feature to be improved.

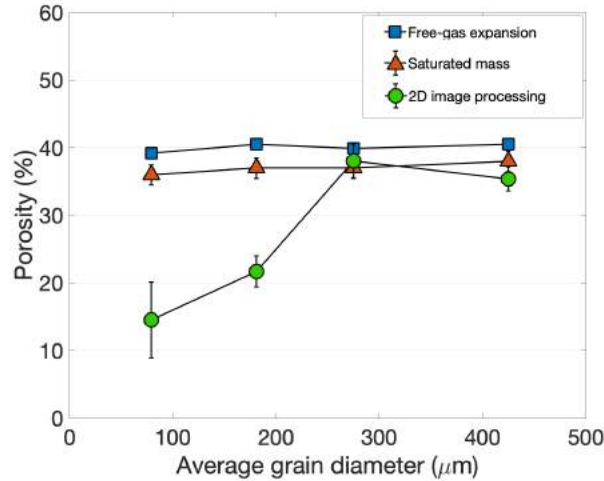


Figure 3.8: Porosity values obtained by the free-gas expansion method (blue squares), saturated mass (red triangles) and by 2D micro-tomography image processing (green circles) as a function of the average range diameter. The vertical bars in the green circles denotes the standard deviation of values obtained along the set of micro-tomography images.

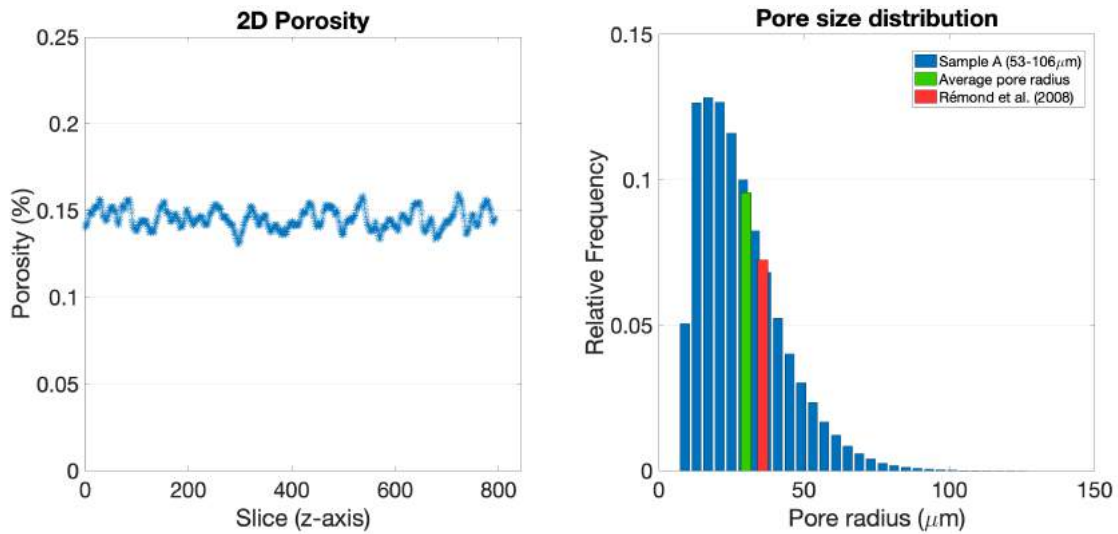


Figure 3.9: Synthetic sample A (53-106 μm): (Left) Porosity values obtained from segmented 2D transverse micro-tomography images versus the slice number along the z axis. (Right) Sample's pore size distribution obtained from the analysis of 2D micro-tomography images using the algorithm proposed by Rabbani et al. [123]. The green bar represents the average pore size of the obtained distribution and the red bar denotes an estimate of the pore radius considering the relation proposed by Rémond et al. [126].

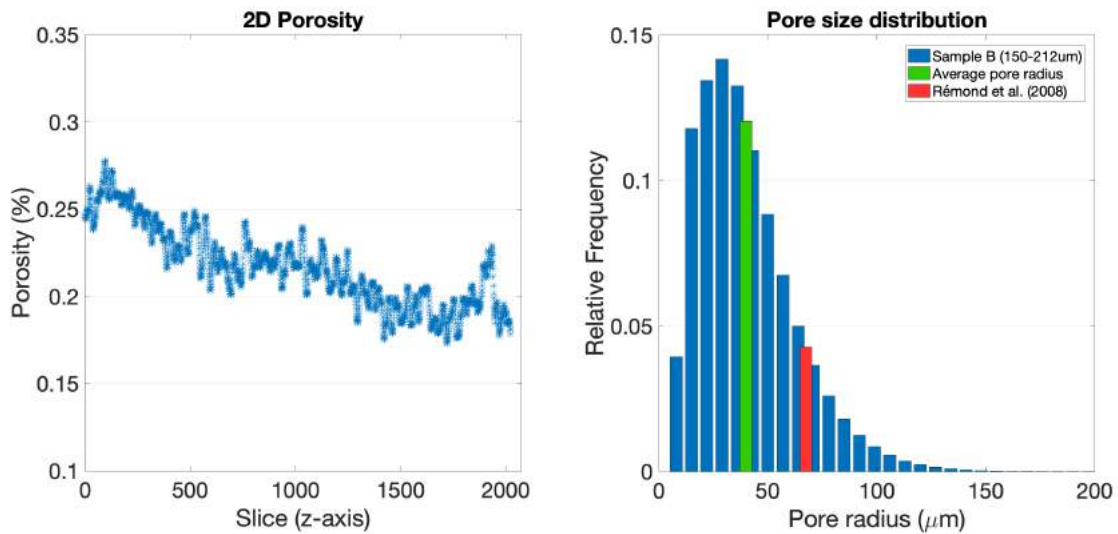


Figure 3.10: Synthetic sample B (150-212 μm): (Left) Porosity values obtained from segmented 2D transverse micro-tomography images versus the slice number along the z axis. (Right) Sample's pore size distribution obtained from the analysis of 2D micro-tomography images using the algorithm proposed by Rabbani et al. [123]. The green bar represents the average pore size of the obtained distribution and the red bar denotes an estimate of the pore radius considering the relation proposed by Rémond et al. [126].

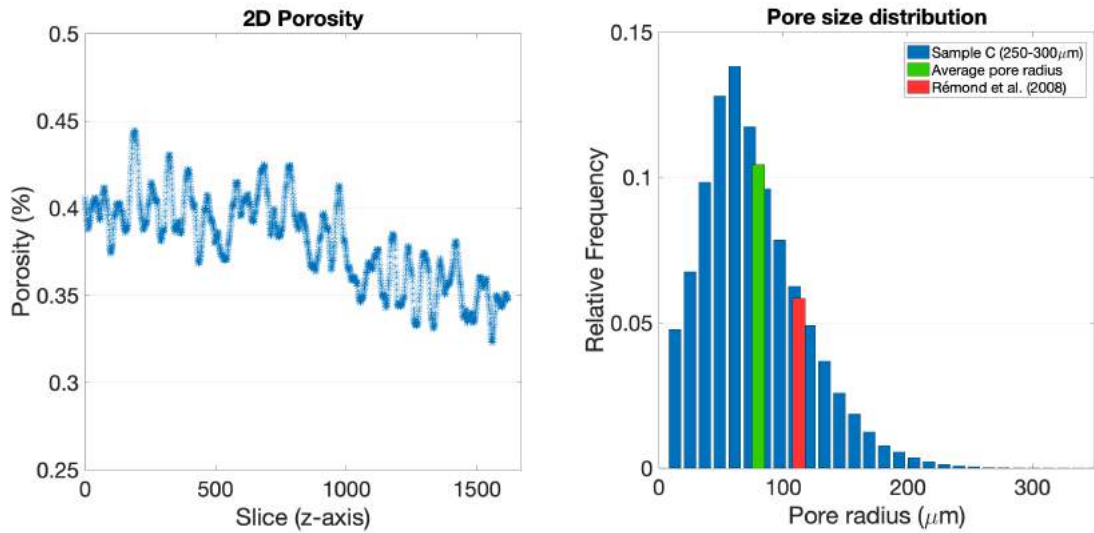


Figure 3.11: Synthetic sample C (250-300 μm): (Left) Porosity values obtained from segmented 2D transverse micro-tomography images versus the slice number along the z axis. (Right) Sample's pore size distribution obtained from the analysis of 2D micro-tomography images using the algorithm proposed by Rabbani et al. [123]. The green bar represents the average pore size of the obtained distribution and the red bar denotes an estimate of the pore radius considering the relation proposed by Rémond et al. [126].

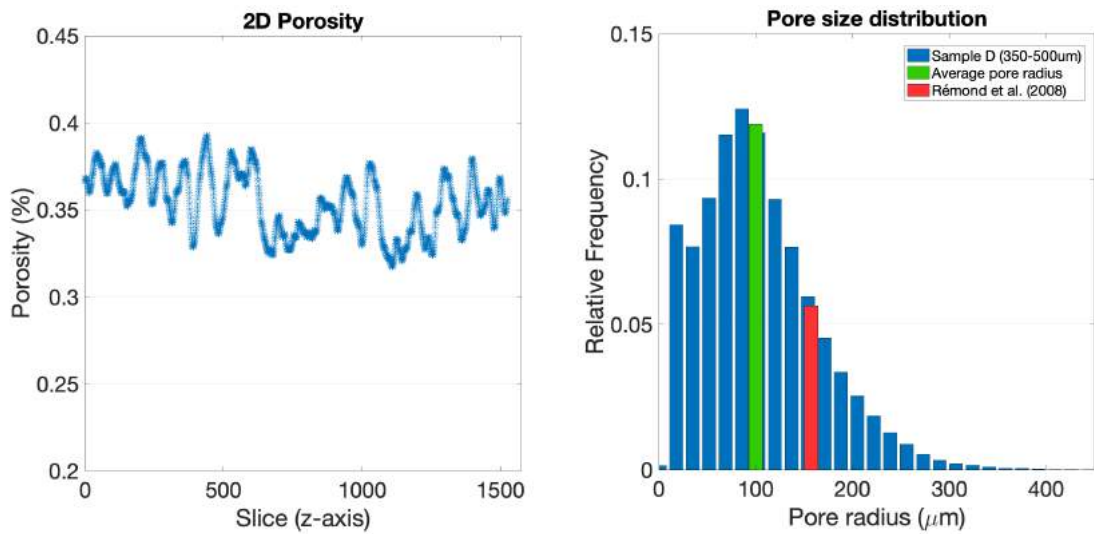


Figure 3.12: Synthetic sample D (350-500 μm): (Left) Porosity values obtained from segmented 2D transverse micro-tomography images versus the slice number along the z axis. (Right) Sample's pore size distribution obtained from the analysis of 2D micro-tomography images using the algorithm proposed by Rabbani et al. [123]. The green bar represents the average pore size of the obtained distribution and the red bar denotes an estimate of the pore radius considering the relation proposed by Rémond et al. [126].

Average pore radius values (green bars) were in fair agreement with predicted values (red bars) for all samples. One must notice that each sample was in fact fabricated with beads distributed over a size range, instead of mono-sized ones, and also that beads were sintered. Both factors implicate in a slight reduction of the average confinement scale, which can be noticed in the obtained data as distribution average values are always smaller than the estimated ones considering a loose packing. It is also worth noting that the image resolution also influences the observation of small sizes in pore size distributions, and hence the left side of each histogram is expected to be poorly represented as the image resolution became comparable with the confinement scale, an effect already evidenced on the processing of 2D porosity values.

3.4 NMR Relaxation Measurements and Data Analysis

NMR transverse relaxation (T_2) measurements were performed at 25°C using both a Varian (Agilent) 500 MHz (high-field) and a SpecFit (Fine Instrument Technology) 15 MHz (low-field) spectrometers, applying CPMG protocols with same echo-time spacing, 1 ms. All samples were saturated using the imbibition method with distilled water (100%). To minimize desaturation during the experiments, samples were coated with thread seal tape before insertion into the sample holder. This procedure was insufficient in the case of sample D due to its high permeability. Measurements with this sample were deemed inconclusive, therefore discarded from this discussion.

NMR spectra measured after a $\pi/2$ pulse obtained for samples A, B and C are shown in Figure 3.13. One can observe a systematic line-broadening with the decrease of grain sizes. This is consistent with the idea that magnetic field inhomogeneities due to susceptibility contrast are greater in more confined regions due to the fact that relatively larger portions of these regions are subjected to more intense field heterogeneities.

The results for high and low-field transverse relaxation are shown in Figure 3.14. A strong dependence of the decaying curves on grain size can be clearly seen, indicating that greater confinement yields faster relaxation. Notice that the effective relaxation rates found under high-field conditions are consistently higher than the low-field ones. This result is in sharp disagreement with the tendency reported in Ref. [107] in which the longitudinal relaxation rates of water protons decrease with increasing field, provided it can be assumed that the major mechanism of relaxation in the synthetic samples used in this work is the same reported in Ref. [107], namely, dipolar coupling with adsorbed paramagnetic ions.

Although only the field dependence of longitudinal relaxation rates is reported on that

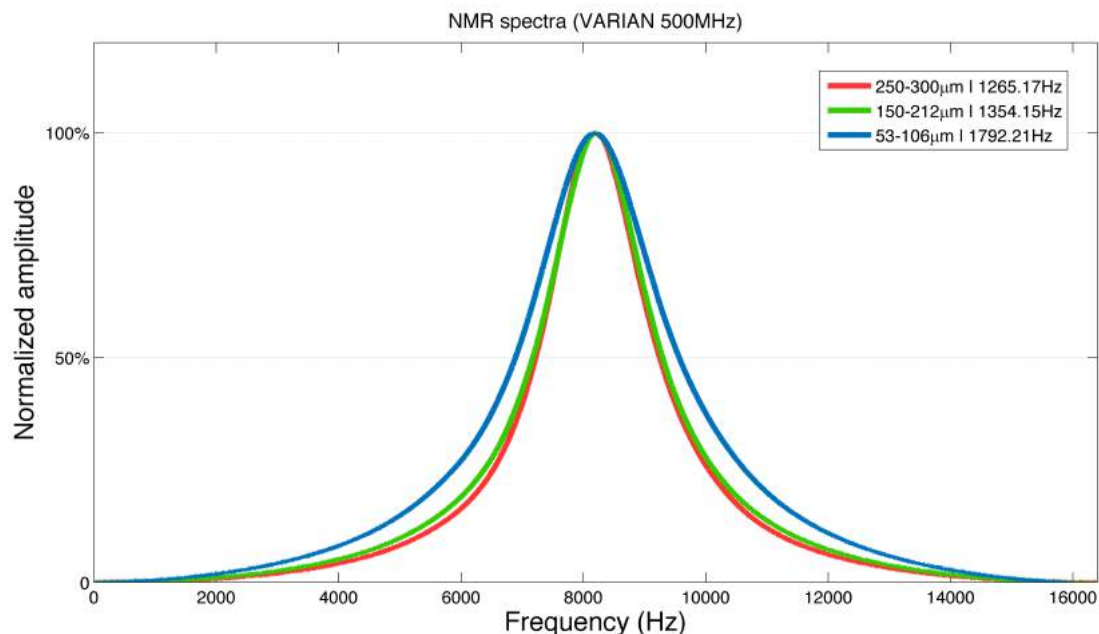


Figure 3.13: High field NMR spectra and respective line width values obtained for each sample. As the porous sizes decreases the NMR line becomes broader.

work, it could be anticipated that a similar trend should be observed in the case of transverse relaxation on the grounds that, essentially, longitudinal and transverse rates differ from one another by a field-independent contribution, the so-called adiabatic² T_2 [2, 3]. It is yet true that these authors only present experimental data points up to about 20MHz but they also propose a model that extrapolates the behavior as decreasing in higher field conditions. One possible reason that could lead to these differences would be the presence of paramagnetic impurities in the solid matrix, as well as the influence of magnetic susceptibility contrast between the fluid and the porous matrix on the measured relaxation rates, depending on the spin echo decay regime. These points will be addressed further in the discussion.

As none of the decay curves obtained can be satisfactorily fit with a mono-exponential function, it is unreasonable to associate a single relaxation time to the systems in spite of the fact that all studied samples are produced within relatively narrow grain size

²Considering the Heisenberg picture, a quantum mechanical description of longitudinal and transverse relaxation functions can be carried out through the definition of an appropriate Hamiltonian to account for the dynamics of the magnetization operator, especially on what regards its interaction part. The exact behavior of the relaxation functions will depend, among other features, on the relation between system's motion time scale and its Larmor frequency, according to the obtained correlation functions. Particularly, the adiabatic approximation comprises a system wherein particle motion can be considered much slower than its Larmor frequency. For such case it can be shown that the classical behavior of relaxation functions presented in Chapter 2 is recovered. A reader-friendly quantum mechanical approach on transverse and longitudinal relaxation functions in liquids is presented in Chapter 7 of Cowan's book [2].

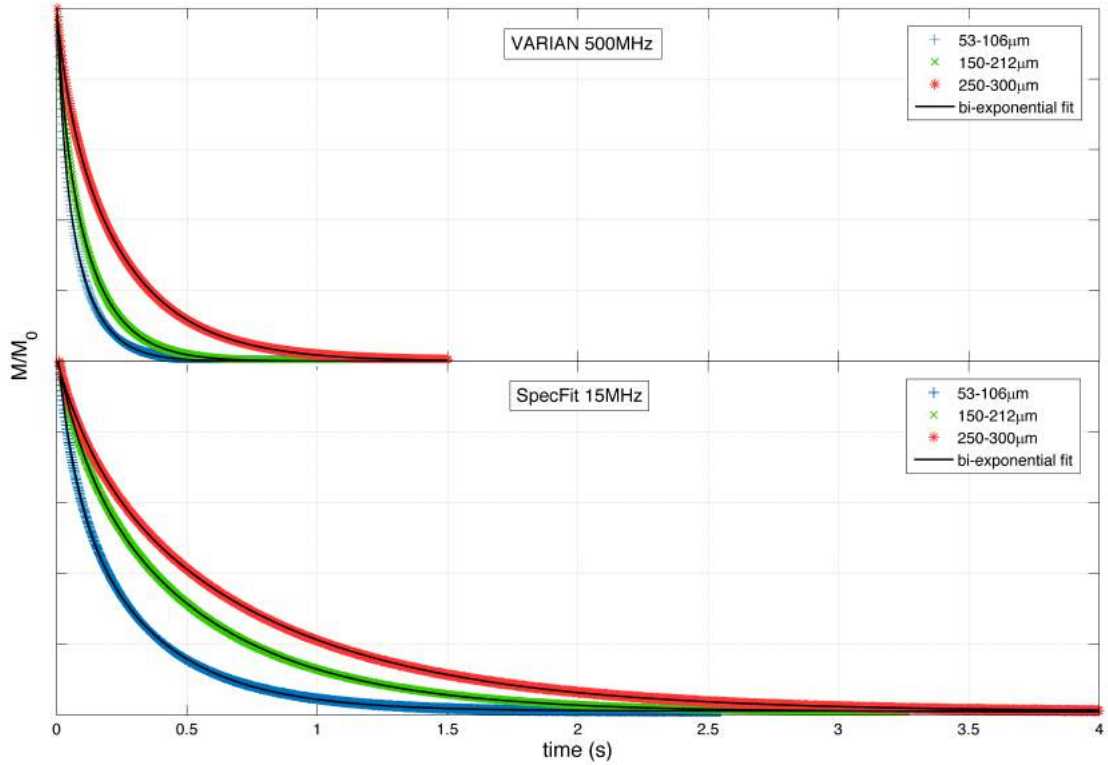


Figure 3.14: High and low-field transverse magnetization decay. Relaxation of water nuclear spin magnetization is faster in samples with smaller porous sizes. The systematic is the same on both, high and low-fields, but relaxation times are shorter in high-field. The continuous lines are bi-exponential fits (see text).

distributions. It becomes necessary therefore to introduce an alternative method for processing relaxation data.

There is a vast literature covering the issue of multi-exponential analysis, in particular, the comprehensive review by Istratov and Vyvenko [52], which describes the various existing methods, their limitations, the role played by noise, etc. The experiments presented here were designed to level the noise condition and, in some extent, to guarantee an uniform surface relaxativity among samples, whose porous structure can be characterized by three petrophysical parameters: porosity, granulometry and permeability. Nevertheless, as it was discussed in Chapter 2, some of the main difficulties of multi-exponential analysis remain, simply due to the fact that they are inherent to the mathematical structure of the problem.

The data analysis was performed using three different approaches: (i) Laplace inversion with optimized regularization, (ii) bi-exponential and (iii) generalized q -exponentials non-linear least-squares. Numerical Laplace inversion was carried through by a nonnegatively constrained Tikhonov regularized algorithm. The amount of regularization used was

determined by application of the *principle of discrepancy* [127], wherein the norm of data errors is the only knowledge required. It was used the fact that in quadrature detection, after a proper phase correction, the recorded signal on the 90° -shifted detection channel consists only of noise. Hence, it may be considered a sample of the random processes that contaminate the experimental data. The norm of the *quadrature* signal therefore is taken as the measure of errors on the *zero phase* signal. This identification allows a successful application of the principle and consequently an unique selection of regularization parameter based on the measured noise level.

For the nonlinear least-squares, two exponential functions were necessary and sufficient to achieve excellent fit in all samples' data. The quality of fit was verified by looking simultaneously at Sum of Squares due to Error (SSE) and the R-square coefficient which is about 0.9999 for all presented fits. Of course, the introduction of more exponential functions results in fits of comparable quality (effectively the SSE is reduced), but based in the *principle of simplicity* [52], the number of exponential functions was kept equal to two.

The use of the so-called q -exponentials was first applied to the problem of processing NMR relaxation data of fluid saturated porous media by Correia et al. [119]. These functions have the interesting feature of representing the exact Laplace transform of χ^2 distributions, which, consequently, leads to the assumption that, whenever they are a good fit, a χ^2 distribution of relaxation rates is a reasonable model. In motivation, the method is similar to the use of the stretched exponentials [120] in which a half-Gaussian or Gaussian distribution is implied. The fitting also yields directly the average relaxation time, $\langle T_2 \rangle$, and the average relaxation rate, $\langle 1/T_2 \rangle$, the former connected to the q parameter. Unfortunately, for the data considered, no reasonably good fit can be obtained with a single q -exponential function, so a composition of two is employed instead.

Figure 3.15 and Figure 3.16 compare the three methods of analysis respectively for high and low-field data. Table 3.1 and Table 3.2 refer to the relevant information obtained from bi-exponential and q -exponential least-squares in high and low-field measurements.

In all cases there are two very distinct modes, the second one exhibiting relaxation times a factor about 4 times larger than the first. In what concerns their weights, it was observed an approximate factor of 2 between them. It is clear that virtually the same information regarding the dominant relaxation times is retrieved from all methods. The agreement is in fact much better for slower modes although faster ones are seen in the same order of magnitude. As an analytical tool, the q -exponential method has the advantage of providing an explicit representation of the distributions, which is appealing from a physical point of view, as $\langle T_2 \rangle$ and $\langle 1/T_2 \rangle$ also result directly from the fit.

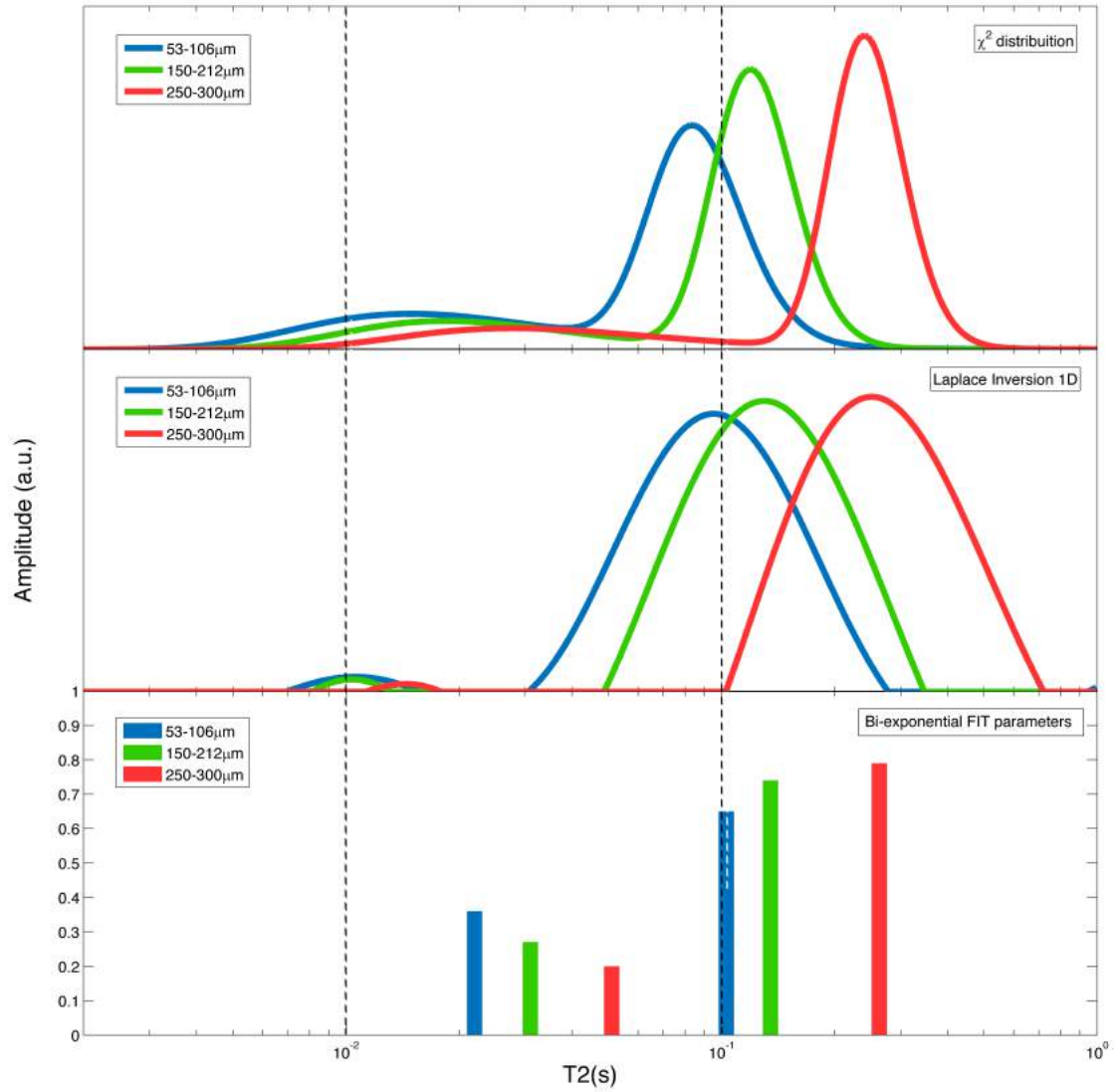


Figure 3.15: Comparison between the three methods of numerical analysis for high-field decay data. On top, it is shown the χ^2 distributions obtained from q -exponentials least-squares. In the middle, Laplace inversion with optimized regularization, and in the bottom bi-exponential nonlinear least-squares. The distributions fall in the same region of relaxation times and the weights of the modes are similar to each other. The relaxation times of the bi-exponential modes approximately meet the corresponding ones in the other distributions.

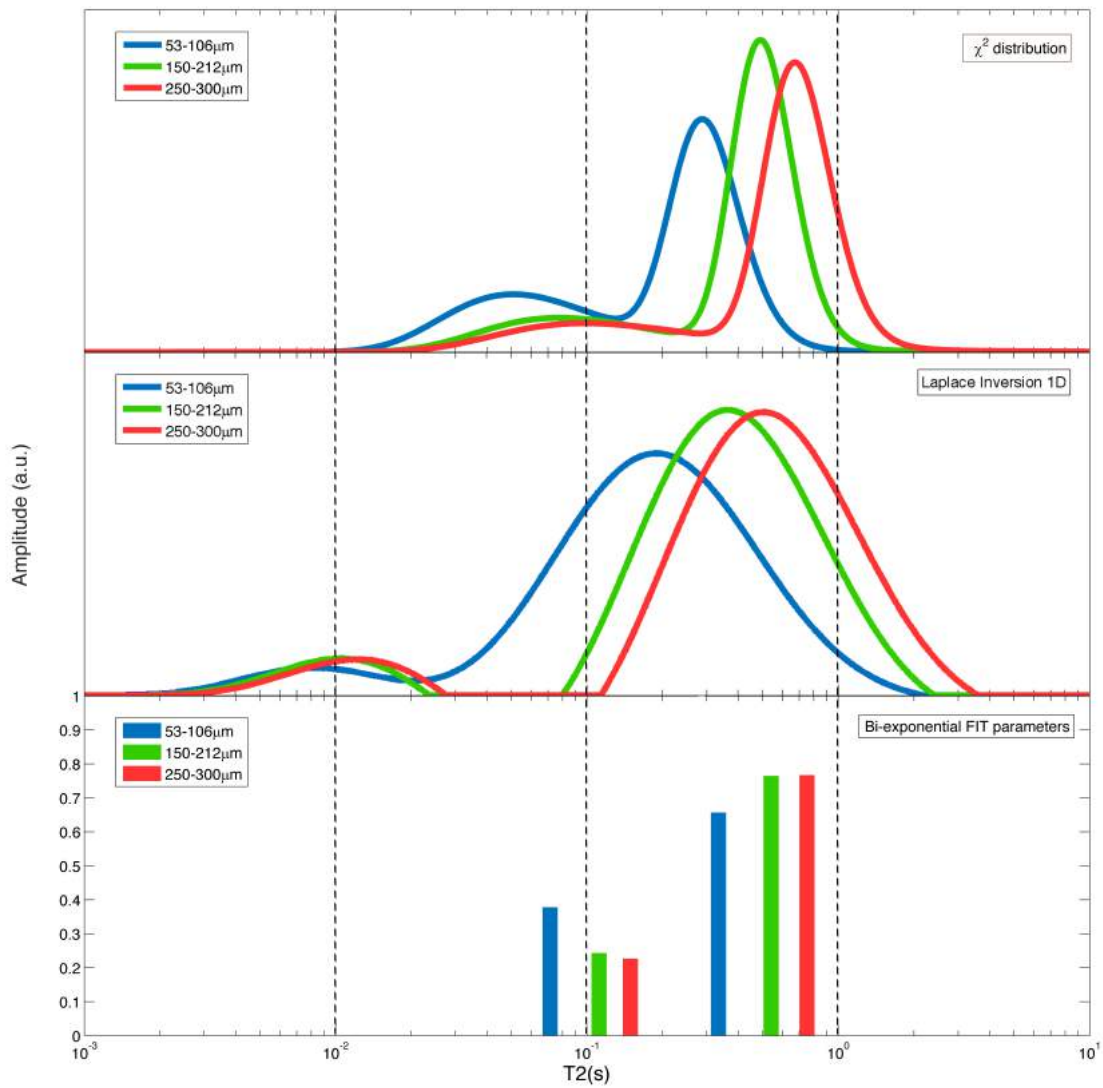


Figure 3.16: The same analysis made in Figure 3.15 but for low-field decay data. One can observe that the general behavior is similar for high and low-fields. The corresponding areas under the curves agree to each other within 10%.

In contrast, the bi-exponential fit, although parametrically simpler, seems to provide only the main tendencies of the signal decay. Any information whatsoever pertaining to a dispersion of relaxation times is revealed, an undesirable feature for an interpretation based on a direct relation of the latter with pore sizes. From the numerical standpoint, it is hard to assess the sensibility of fit parameters to the noise level [52]. The presented agreement may therefore indicate low noise conditions. Laplace inversion, on the other hand, does not rely on distribution models, since it is a numerical procedure performed directly on raw digitized relaxation data. The approach however introduces in the analysis an element of uncertainty on the form of the regularization parameter α which greatly influences shape, number and relative position of the distribution modes (see Figure 2.17). By a proper adjustment of NMR quadrature signals and a reasonable definition of noise level, an optimized choice of the regularization parameter can be made by choosing the largest value which yields a residue equal to the measured noise level³.

On the basis of the assumed relation between pore sizes and relaxation times, it is difficult to give a proper interpretation to the fastest modes due to the apparent homogeneity in porous structure revealed in the processing of micro-tomography scans. Although not noticed in the scanning microscopy images, these fast modes may be an indication of a secondary porosity in the microspheres, or even small crevices formed during manipulation and thermal treatment. The reappearance of essentially the same features in the derived distributions, as field conditions are varied, is taken as a reasonable indication that those distributions in fact correspond to samples geometry features.

It is well known that the presence of paramagnetic impurities on the solid matrix affects the relaxation rates in two different ways, first due to the appearance of internal field gradients induced by susceptibility contrast [82–84] and also by enhancing surface relaxation effects [27]. The overall influence can be seen as the result of a balance between paramagnetic impurities concentration, pore size scale and the diffusion length, being the latter proportional to the time during which molecules diffuse through internal field gradients, which in this case is the time interval between refocusing π pulses. Hence, the observed relaxation rates depend on the echo spacing used in transverse relaxation experiments, and for this reason measured T_2 values are often referred to as *apparent* relaxation times [128].

In order to investigate the influence of susceptibility contrast on the reported transverse relaxation rates samples were submitted to energy dispersive spectroscopy (EDS) for a compositional analysis. All the samples showed iron concentration no higher than 0.39% in weight, and no significant quantities of other paramagnetic impurities were found. Muncaci and Ardelean [129] investigated the influence of magnetic susceptibility difference

³The residue of regularized solutions as a function of the regularization coefficient, even for the nonnegatively constrained problem considered here, is usually non-decreasing.

on effective transverse relaxation rates as a function of echo spacing t_e for sintered porous ceramic samples, with grain sizes between 63 and 120 μm , each sample containing different iron concentrations. For low iron content ($< 1\%$), a decrease of approximately 50% in transverse relaxation rates was observed by reducing CPMG echo spacing in one order of magnitude (from 1 to 0.1ms), in a 20MHz field. Scanning electron microscopy images show that the final pore size scale of the sintered ceramic samples reported by Muncaci and Ardelean is in fact smaller than the one in the samples produced by glass beads sintering. This fact, added to the low concentration of magnetic impurities on the latter, suggests that a similar decrease could be expected in the low-field (15MHz) relaxation rates measured in this work.

Table 3.1: High-field NMR (500 MHz) T_2 exponential and q-exponential fitting parameters

Samples		Relaxation times		Weights		SSE
		(ms)		(%)		($\cdot 10^{-3}$)
		$T_2^{(1)}$	$T_2^{(2)}$	$A^{(1)}$	$A^{(2)}$	
Synthetic A	exp	24.7 (± 0.6)	102.3 (± 0.7)	35.4 (± 0.7)	64.6 (± 0.7)	3.256
	q-exp	14.9 (± 0.2)	83.8 (± 0.5)	31.5 (± 0.5)	68.5 (± 0.6)	0.108
Synthetic B	exp	30.7 (± 0.8)	135.3 (± 0.6)	25.9 (± 0.5)	74.1 (± 0.5)	2.321
	q-exp	18.4 (± 0.6)	119.5 (± 0.7)	22.7 (± 0.8)	77.3 (± 0.9)	0.167
Synthetic C	exp	51.1 (± 1.4)	262.8 (± 0.8)	20.4 (± 0.4)	79.6 (± 0.4)	3.828
	q-exp	27.8 (± 1.3)	239.9 (± 1.7)	19.2 (± 1.2)	80.8 (± 1.1)	0.320

Hurlimann [83] proposed an expression for a relevant length scale l^* that can be used to determine if spins are diffusing in the so-called “small” or “large” pore regime. A pore can be said “large” when the pore size scale is large compared to the local dephasing length ($l_g = \{D_0/(\gamma g_{\text{eff}})\}^{1/3}$), a function of the effective field gradient g_{eff} defined as the typical length scale over which a spin must diffuse to dephase by 2π radians. When molecules are diffusing in a “large” pore the echo dephasing is essentially governed by the free diffusion regime. In the “small pores”, the pore size is small compared to l_g and the internal field inhomogeneities are motionally averaged. Assuming that the variation in the local field is upper bounded [130] one can calculate the maximum value of the effective field gradient considering the echo attenuation due to diffusion in the susceptibility-induced field inhomogeneities [83], and the length l^* can be expressed as:

$$l^* = \left(\frac{D_0}{\gamma \Delta\chi B_0} \right)^{1/2}, \quad (3.3)$$

wherein D_0 is the molecular self-diffusion coefficient, γ is the gyromagnetic ratio, B_0 is the static field, and $\Delta\chi$ is the magnetic susceptibility difference between water and the porous matrix. All the samples were then submitted to magnetic susceptibility measures using a Vibrating Sample Magnetometer (Quantum Design PPMS) and the obtained susceptibility difference $\Delta\chi$ values were used to calculate the length scale l^* for low (15MHz) and high-field (500MHz). Calculated l^* values according to Equation 3.3 ranged from approximately 70 to 280 μm for high and low field respectively. Comparing pore size scale from sample's micro-tomography images with calculated l^* values showed that pores are in fact "large" and thus a significant dependence of relaxation rates on the echo spacing t_e should be expected in this case.

Table 3.2: Low-field NMR (15 MHz) T_2 exponential and q-exponential fitting parameters

Samples		Relaxation Times		Weights		SSE (.10 ⁻³)
		(ms)		(%)		
		$T_2^{(1)}$	$T_2^{(2)}$	$A^{(1)}$	$A^{(2)}$	
Synthetic A	exp	71.4 (± 1.1)	333.7 (± 1.5)	36.5 (± 0.4)	63.5 (± 0.4)	5.717
	q-exp	61.1 (± 2.2)	299.9 (± 3.8)	49.9 (± 1.2)	51.1 (± 1.1)	2.034
Synthetic B	exp	118.8 (± 1.7)	540.9 (± 1.5)	24.2 (± 0.3)	75.8 (± 0.3)	4.940
	q-exp	87.4 (± 2.7)	495 (± 2.6)	30.3 (± 0.6)	69.7 (± 0.7)	1.207
Synthetic C	exp	148.9 (± 2.2)	750.8 (± 2.1)	22.8 (± 0.4)	77.2 (± 0.6)	7.476
	q-exp	101.4 (± 3.3)	674.7 (± 3.3)	26.1 (± 0.5)	73.9 (± 0.6)	1.866

Finally, to evaluate the influence of this dependence on the results and analysis presented so far, the sample with smallest confinement scale (A: 53-106 μm) was submitted to complementary CPMG experiments in high-field (500MHz), with variable echo spacing from 1.1 to 0.3ms. The largest decrease observed in relaxation rates with lowering echo spacing in that range was approximately 45% for the fastest of the two relaxation rates observed on the decay curve. Still, the respective weights of the two modes showed a variation no larger than 5%. These results indicate that despite the fact that relaxation

rates obtained for these samples, for both low- and high-field measurements, exhibits an expected dependence on echo spacing, variations on the absolute values of those rates and their respective weights do not compromise the analysis presented comparing the results obtained by the three different approaches, in the author's opinion.

One remarkable aspect of the presented data is the relatively good agreement between mode weights when the same method of exponential analysis is applied to measurements acquired under distinct field conditions; the absolute deviation is less than 10% in all cases. It is important to remark that such a consistency reflects the reproducibility of the sintering protocol in yielding samples of completely different size standards without breaking the similarity of porous structures. At last, it can be said that all methods of analysis lead to the same picture.

3.5 Concluding Remarks

With a proper sintering protocol, artificial porous structures can be produced keeping constant porosities, which is important to establish an even noise level among samples with varied characteristic pore sizes, and uniform surface relaxativity. These attributes are essential in the reduction of ambiguities in assessment of how relaxation time distributions relate to pore size or, more appropriately, confinement characteristics.

Despite the effort in producing model porous media capable of maintaining close porosity values yet with distinct confinement scales, in order for one to establish a fair investigation of surface effects on relaxation rates, pore size scale and connectivity in all samples were nevertheless high, the former estimated considering a relevant diffusion length of molecules through internal field gradients and the latter confirmed by permeability measurements. The scenario wherein diffusion among pores is comparable with diffusion within pores, or even when internal field inhomogeneities are not motionally averaged, inhibit the application of the approximations deduced for the fast diffusion regime, and hence the establishment of a direct relation between relaxation time distributions and pore sizes.

The inherent problem of multi-exponential analysis has also been addressed and the results of three different approaches were compared, yielding essentially consistent features. The choice for either method seems therefore entirely conventional unless some *a priori* information is available to justify the adherence to some type of distribution. In such context, Laplace inversion may appear unbiased but it is important to recall the intrinsic difficulties and inevitable uncertainty associated with this method and regularization tools.

Natural next steps for this work are varying the porosity of samples, which can be achieved by mixing different grain sizes, and their mineral contents, which require new

sintering protocols or doping processes. Paramagnetic coating and cleaning off impurities are already under development, which can be used to extend the performed analysis to the appraisal of how surface activity affects relaxation.

Chapter 4

PFG NMR Time-Dependent Diffusion Coefficient Analysis of Confined Emulsion: Post Drainage Phase Conformation.

4.1 Diffusion NMR

4.1.1 Self-Diffusion and the Diffusion Equation

The first step to comprehend NMR-based diffusion techniques is in fact the proper distinction on two different physical processes, both described by the same term, diffusion. The mutual (or concentration) diffusion characterizes the dynamics of a system with distinct components inhomogeneously distributed in a non-equilibrium configuration, wherein the random motion of particles from each component, driven by a chemical potential gradient, leads to changes in the concentration differences. The dynamics of the concentration $c(\vec{r}, t)$ is described by the diffusion equation, a partial differential equation (Equation 4.1) also known as the Fick's second law [4].

The self- (or translational) diffusion regards the random thermal motion of particles in a system in equilibrium, which does not require a chemical potential gradient since it is driven by internal kinetic energy. The self-diffusion process may also be described by the diffusion equation if one considers the motion of labeled particles through an environment

of unlabeled yet identical particles [96]:

$$\frac{\partial c^*(\vec{r}, t)}{\partial t} = D \nabla^2 c^*(\vec{r}, t), \quad (4.1)$$

wherein D is the self-diffusion coefficient and $c^*(\vec{r}, t)$ denotes the concentration of labeled particles. Self-diffusion is actually the process which is observed by the pulsed-field gradient (PFG) NMR diffusion techniques presented in this Chapter, which from this point forward may be referred to only as diffusion.

Diffusion may be measured by several distinct techniques, all of them based on the same principle: an initial concentration of particles must be labeled - in preference by a non-invasive technique which does not influence the particles' motion - followed by the subsequent observation of the change in the concentration c^* of labeled particles. The measured concentration values are then used to fit the solution for the diffusion equation, using D as the adjustable parameter. The non-invasive character of NMR is once more the most important feature regarding NMR-based diffusion techniques. As it will be presented in the following sections the labeling and the motion observation steps in PFG NMR diffusion experiments are just two successive parts of a pulse sequence.

4.1.2 The Averaged Propagator

Solving the diffusion equation requires the establishment of an initial condition for the concentration c_0^* and also a proper boundary condition:

$$0 = D \hat{n} \vec{\nabla} c^* + \theta c^* \Big|_s, \quad (4.2)$$

in which $\vec{\nabla} c^*$ denotes the particle flux due to self-diffusion and the parameter θ accounts for interface properties wherein particles may be passed through, absorbed or even reflected. Among the usual mathematical approaches for one to solve partial differential equations, the concept of propagator can be said of particular interest in the case of diffusion processes considering its relation with the mean-squared displacement of labeled particles and the measured NMR signal in PFG experiments, as it will be discussed further in Section 4.1.4.

Considering a point source for the initial concentration $c_0^* = \delta(\vec{r}_2 - \vec{r}_1)$ and solving the diffusion equation with respect to the appropriate boundary condition (Equation 4.2) one obtains the propagator $P(\vec{r}_2, \vec{r}_1, t)$, a conditional probability of finding a particle, initially at a position \vec{r}_1 , in a position \vec{r}_2 after an interval of time t . The solution of the diffusion equation for a general initial condition $p_0(\vec{r}_1)$ may be obtained by integrating the product

of the propagator with the initial concentration for all possible starting positions \vec{r}_1 [4]:

$$\bar{P}(\vec{r}, t) = \int_V P(\vec{r}_1 + \vec{r}, \vec{r}_1, t) p_0(\vec{r}_1) d\vec{r}_1, \quad (4.3)$$

in which \vec{r} represents the displacement vector ($\vec{r} = \vec{r}_2 - \vec{r}_1$) and $\bar{P}(\vec{r}, t)$ is the so-called averaged propagator, representing the probability density of an arbitrary particle of being displaced by the distance r during a time t .

4.1.3 Pulsed-Field Gradient (PFG) NMR

Encoding Period

The pulsed-field gradient (PFG) NMR technique was proposed by Stejskal and Tanner [33] in 1965 and became the foundation for a large set of NMR-based protocols for diffusion measurement. A PFG NMR experiment may be separated into three distinct time intervals (Figure 4.1): encoding, the diffusion interval and decoding. During the encoding interval the molecules are labeled with a space-dependent precession frequency imposed upon the system by a magnetic field gradient pulse $G(t)$, commonly applied along the z -direction. For the upcoming developments regarding the description of each PFG interval it is thus necessary to define the one-dimensional magnetization density $m(z, t)$, in the sense that the total magnetization $M(t)$ at a given time t can be obtained by integrating over the magnetization density $m(z, t)$. It is worth noticing that $m(z, t)$ does not represent the longitudinal component of the magnetization $m_z(t)$. Instead, $m(z, t)$ represents solely a distribution of magnetization along the z axis.

After the initial $\pi/2$ pulse (for an example, applied in the $+y$ -direction) the magnetization density $m(z, t)$ is homogeneously distributed in space with a single component pointing in the positive x -direction. Neglecting for now the effects of transverse relaxation, in the rotating frame of reference during the first field gradient pulse $G(t)$ the precession frequency $\omega(z, t)$ of nuclear spins is dependent on the z -coordinate, which means that molecules will experience a frequency offset $\Delta\omega$ with respect to the static field Larmor frequency ω_0 , depending on their position:

$$\Delta\omega(z, t) = \omega_0 - \omega(z, t) = -\gamma G(t)z. \quad (4.4)$$

The magnetization density $m(z, t)$ is rotated from its initial x -direction during the first field gradient pulse $G(t)$, and the rotation phase $\phi(z, t)$ will also depend on the z -position:

$$\phi(z, t) = \int_0^t \Delta\omega(z, t') dt' = \int_0^t -\gamma G(t')z dt'. \quad (4.5)$$

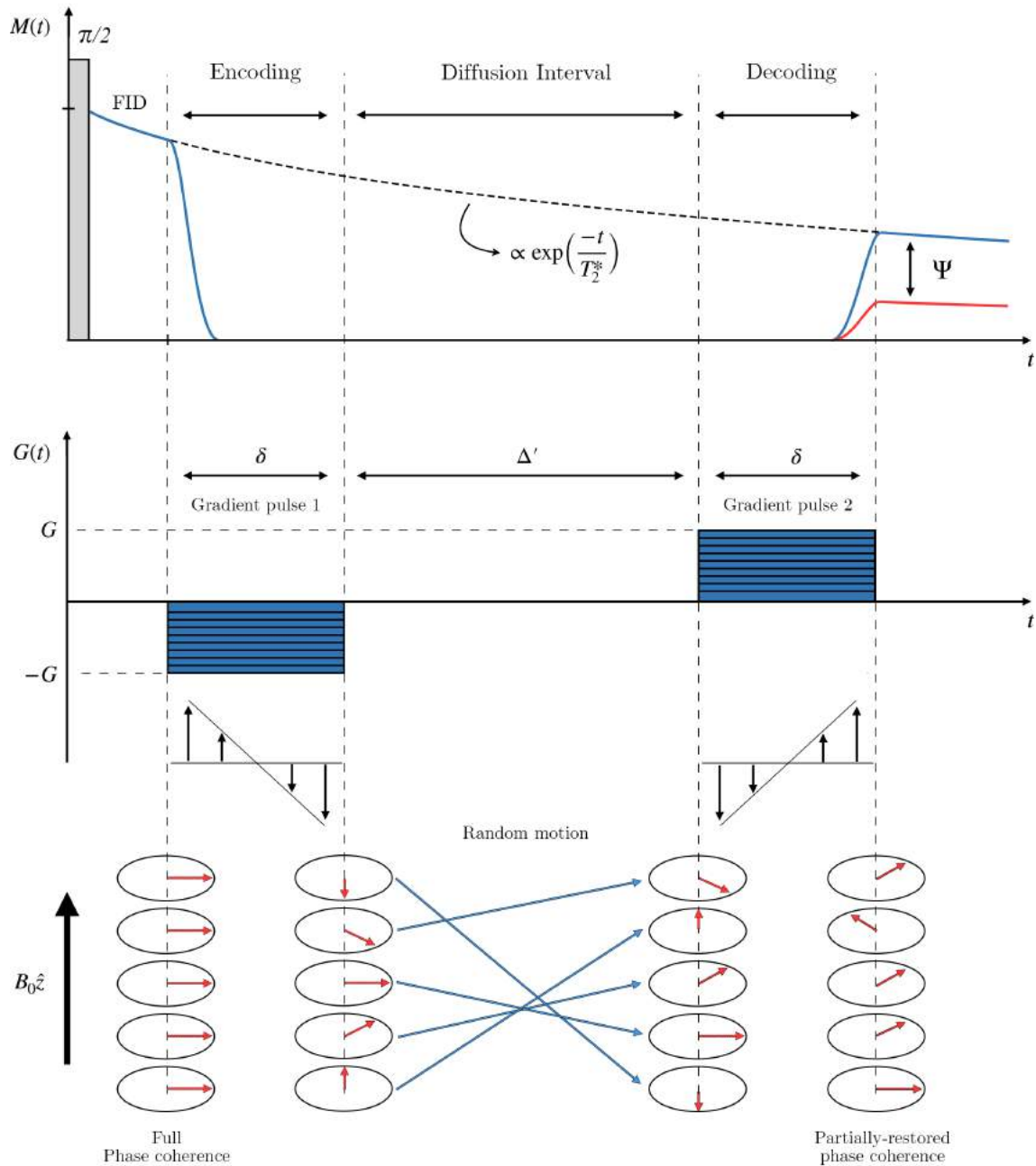


Figure 4.1: Simplified pulsed field gradient sequence. The upper schematic diagram illustrates the free induction decay of the magnetization after a $\pi/2$ pulse with (red line) and without (blue line) the pair of gradient pulses ($-G$ and $+G$) applied during the encoding and decoding periods, illustrated in the central schematic. Both gradient pulses are matched in amplitude and length, but with opposite directions. The lower schematic illustrates the helix-like effect of the encoding gradient pulse on the magnetization and the phase evolution of the spins due to random thermal motion during the diffusion interval.

Assuming that the gradient pulse has a time duration δ the total accumulated phase will be equal to $\gamma G\delta z$. Using the complex notation the magnetization density $m(z, t)$ right after the first gradient pulse may be expressed as a function of its x - and y -components:

$$m(z) = m_x + im_y = m_0[\cos(\gamma G\delta z) + i \sin(\gamma G\delta z)] = m_0 \exp(i\gamma G\delta z). \quad (4.6)$$

The effect of the field gradient pulse during the encoding period can be represented by a helix-like twist in the magnetization density $m(z, t)$ (Figure 4.1). The space-dependent precession phase imposed by the first gradient pulse on nuclear spins, which destroys the overall phase coherence in the transverse plane (and consequently the magnetization), is indeed the label applied in PFG NMR protocols which later will be used in the evaluation of molecules self-diffusion.

Diffusion Period

After the encoding period molecules carrying nuclear spins labeled by a precession (or magnetization) phase are allowed to diffuse during a time $\Delta = \Delta' + \delta$ (Figure 4.1), and it is in fact the molecular self-diffusion process that will determine the evolution of the space-dependent magnetization density. In that sense, the diffusion equation (Equation 4.1) represents the equation of motion for the space-dependent magnetization density, with the corresponding initial condition expressed by Equation 4.6. For one to obtain the magnetization density $m(G\delta, \Delta, z_2)$ after the diffusion interval during a time Δ the same procedure applied in Equation 4.3 may be repeated, but this time considering the initial condition expressed in Equation 4.6:

$$m(G\delta, \Delta, z_2) = \int P(z_2, z_1, \Delta) m_0 e^{i\gamma G\delta z_1} dz_1, \quad (4.7)$$

wherein $P(z_2, z_1, \Delta)$ represents the diffusion propagator. The random motion of molecules in a homogeneous infinitely extended liquid volume (unrestricted diffusion) is normally distributed, thus the propagator is a Gaussian function and m_0 is a constant. Hence, Equation 4.7 may be rewritten as:

$$m(G\delta, \Delta, z_2) = \frac{m_0}{\sqrt{4\pi D\Delta}} \int \exp\left[-\frac{(z_2 - z_1)^2}{4D\Delta}\right] e^{(i\gamma G\delta z_1)} dz_1, \quad (4.8)$$

which can be solved leading to:

$$m(G\delta, \Delta, z_2) = \Psi(G\delta, \Delta) m_0 e^{i\gamma G\delta z_2}, \quad (4.9)$$

wherein,

$$\Psi(G\delta, \Delta) = \exp[-(\gamma\delta G)^2 D\Delta] \quad (4.10)$$

represents the attenuation factor Ψ illustrated in Figure 4.1. The overall encoding phase $\exp(i\gamma G\delta z)$ is maintained after the diffusion interval.

Decoding Period

Following the diffusion period a second field gradient pulse of amplitude G' is applied in the opposite direction with respect to the first gradient pulse. The decoding period is responsible for removing the encoding phase in order to restore the precession phase coherence in the transverse plane and consequently the macroscopic magnetization signal.

The second gradient pulse superimposes an additional phase in the magnetization density after the diffusion interval expressed in Equation 4.9:

$$m(G\delta, \Delta, z_2) = \Psi(G\delta, \Delta)m_0 e^{i\gamma(G-G')\delta z_2}, \quad (4.11)$$

and the macroscopic magnetization $M(t)$ can be obtained by integration of the magnetization density expressed in Equation 4.11:

$$M(G\delta, \Delta) = \Psi(G\delta, \Delta) \int m_0 e^{i\gamma(G-G')\delta z_2} dz_2. \quad (4.12)$$

When $G = G'$ the overall phase is canceled and the resulting magnetization equals the initial value M_0 attenuated by the factor Ψ :

$$M(b) = \Psi(b)M_0 = e^{-bD}M_0, \quad (4.13)$$

in which the so-called b -factor is given by $b = (\gamma G\delta)^2 \Delta$. One should notice that only after the second gradient pulse the phase coherence is restored and the macroscopic magnetization arises. In practice, any mismatches between the amplitude of the encoding and the decoding gradient pulses inflicts a remaining precession phase leading to an additional loss in the NMR signal and consequently to erroneously determined diffusion coefficients. In that sense, the spin echo PFG sequences present important practical advantages which will be addressed further in Section 4.1.6.

4.1.4 Narrow Pulse and Gaussian Phase Approximations

The developments presented in Section 4.1.3 and consequently the expression obtained for the signal attenuation due to diffusion in Equation 4.13 do not take into account the

movement of molecules during the application of the encoding and decoding field gradient pulses. Strictly, these developments can be considered valid when the gradient pulse duration δ is very short ($\delta \rightarrow 0$). Although δ may be set for small values in the case wherein high gradient amplitudes are available, in real experiments gradient pulses have nevertheless a finite duration. For practical applications, as long as the diffusion time interval is much larger than the encoding and decoding periods ($\Delta \gg \delta$) the developments in Section 4.1.3 can be considered valid in a good approximation.

The above condition is known as *narrow gradient pulse approximation* (NPA). For the case wherein the NPA may not be considered valid the self-diffusion processes during encoding and decoding periods must be taken into account during the analysis of the observed spin echo attenuation. In Section 4.1.5 the Bloch–Torrey equation and the theoretical background for such considerations is presented.

Another important approximation relates to the signal attenuation expression in Equation 4.10 wherein diffusion was assumed to take place in a homogeneous infinitely extended volume, which allowed the assumption of a Gaussian propagator function. As one may expect, in real systems the diffusion propagator may deviate from a Gaussian function and a more general approach is recommended [4, 96].

The precession phase of a single spin after the decoding period depends directly on its displacement in gradient direction during the diffusion interval. Considering that the spin is displaced by a distance $z = z_2 - z_1$ during the diffusion period, its net phase after the decoding interval will be given by $\exp(i\phi)$, wherein $\phi = \gamma G\delta(z_2 - z_1) = \gamma G\delta z$. By integrating the phase factor over all possible displacements to account for the contribution of all spins one obtains the total signal. Each displacement must be weighted however by the proper conditional probability density regarding the movement of the spins, or, in this case, the averaged propagator in the gradient direction $\bar{P}(z, \Delta)$. The signal attenuation is thus expressed as:

$$\Psi(G\delta, \Delta) = \frac{M(G\delta, \Delta)}{M_0} = \int \bar{P}(z, \Delta) e^{i\gamma G\delta z} dz. \quad (4.14)$$

The expression in Equation 4.14 represents the Fourier transform of the averaged propagator with respect to the displacement z . Accordingly, the inverse Fourier transform of Equation 4.14 results in an expression for the averaged propagator as a function of the measured echo attenuation:

$$\bar{P}(z, \Delta) = \frac{1}{2\pi} \int \Psi(G\delta, \Delta) e^{-i\gamma G\delta z} d(\gamma G\delta). \quad (4.15)$$

The Fourier relationship expressed in Equations 4.14 and 4.15 is a fundamental advantage

of NMR-based diffusion studies since the measured echo attenuation and the averaged propagator are Fourier conjugates. This important result relates a solely theoretical description of the diffusion process, based on an approach for the solution of the diffusion Equation, with the resulting signal attenuation obtained from a real experiment. Naturally, assuming a Gaussian function for the averaged propagator leads to the results obtained in Section 4.1.3.

An useful approach for the analysis of diffusion measurements is to look at the series expansion of the signal attenuation in Equation 4.14 with respect to its exponential term:

$$\Psi(G\delta, \Delta) = \int \bar{P}(z, \Delta) dz + \sum_{n=1}^{\infty} \frac{(i\gamma G\delta)^n}{n!} \int z^n \bar{P}(z, \Delta) dz, \quad (4.16)$$

in which the first term on the right-side is equal to unity, as $\bar{P}(z, \Delta)$ represents a conditional probability integrated over all the possible displacements, and the summation term stands for the higher order moments of the averaged propagator for $n \geq 1$, which will define the shape of the signal attenuation. Considering that displacements in $+z$ and $-z$ directions are equally probable inflicts that averaged propagator is an even function. Under this assumption all the odd moments ($n \geq 2k + 1$ with $k \in N$) will vanish, and Equation 4.16 can be rewritten as:

$$\Psi(G\delta, \Delta) = 1 + \sum_{k=1}^{\infty} \frac{(-1)^k (\gamma G\delta)^{2k}}{(2k)!} \int z^{2k} \bar{P}(z, \Delta) dz. \quad (4.17)$$

Any PFG NMR data set may be fitted with a polynomial in $(\gamma G\delta)^2$ for the determination of the moments of the averaged propagator. For small field gradient values the terms in the summation expressed in Equation 4.16 for $n \geq 2$ may be neglected, and the signal attenuation due to diffusion may be expressed as:

$$\Psi_s(G\delta, \Delta) = 1 + i\gamma G\delta \int z(\Delta) \bar{P}(z, \Delta) dz - \frac{(\gamma G\delta)^2}{2} \int z^2(\Delta) \bar{P}(z, \Delta) dz, \quad (4.18)$$

which can be rewritten as:

$$\Psi_s(G\delta, \Delta) = 1 + i\gamma G\delta \langle z(\Delta) \rangle - \frac{(\gamma G\delta)^2}{2} \langle z^2(\Delta) \rangle, \quad (4.19)$$

wherein $\langle z(\Delta) \rangle$ and $\langle z^2(\Delta) \rangle$ represent the first and the second moments of the averaged propagator, respectively. This approximation, known as *Gaussian phase approximation* (GPA) it is extensively used in the analyses of PFG NMR data sets, including magnetic resonance imaging [131]. The first moment $\langle z(\Delta) \rangle$, associated with the imaginary part of the averaged propagator for small gradients, denotes the mean displacement in the gradient direction. For the case of unrestricted self-diffusion (random thermal motion)

the mean displacement is zero.

The second moment $\langle z^2(\Delta) \rangle$, associated with the real part of $\Psi_s(G\delta, \Delta)$, represents the mean squared displacement in gradient direction. The initial slope from the real part of the measured signal attenuation, associated with small gradient values, may be analyzed for the determination of the mean squared displacement, which may also be seen as a diffusion measurement:

$$\frac{d\Re\{\Psi_s(G\delta, \Delta)\}}{d(\gamma G\delta)^2} = \frac{\langle z^2(\Delta) \rangle}{2} = \Delta D_{\text{eff}}(\Delta), \quad (4.20)$$

wherein the symbol \Re stands for the real part of $\Psi_s(G\delta, \Delta)$ and $D_{\text{eff}}(\Delta)$ defines an effective diffusion coefficient - related with the mean squared displacement - which depends on the diffusion time. This approximation is especially useful on the analysis of diffusion measurements of confined fluids and will be addressed again on the discussion of the results presented in Section 4.5.

4.1.5 The Bloch-Torrey Equation

The transport of local magnetization components is described by the Bloch-Torrey equation of motion [14], which combines the Bloch equations for the magnetization (2.25, 2.26 and 2.27) with the diffusion equation (4.1):

$$\frac{\partial \vec{M}(\vec{r}, t)}{\partial t} = \gamma \vec{M} \times \vec{B} - \frac{M_x \hat{e}_x + M_y \hat{e}_y}{T_2} - \frac{M_z - M_0}{T_1} \hat{e}_z + D \nabla^2 \vec{M}, \quad (4.21)$$

wherein $\vec{M}(\vec{r}, t)$ is the local magnetization vector and $\vec{B} = (0, 0, B_0)$ is the homogeneous polarizing magnetic field in the \hat{z} direction. Under the commonly accepted approximation that off-resonance field components can be neglected, the presence of magnetic field gradients only affects field z-component [96]. In this case, considering that the diffusion propagator is a Gaussian function, Equation (4.21) can be solved using a variable separation *ansatz* [96, 132], and a general solution may be written as:

$$M(t) = \Psi(t)R(t)M_0, \quad (4.22)$$

in which M_0 is the equilibrium magnetization, $\Psi(t)$ denotes the signal attenuation due to diffusion processes and $R(t)$ represents signal attenuation due to relaxation effects.

The NMR signal attenuation due to molecules self-diffusion $\Psi(t)$ can be calculated

solving the double integral [96]:

$$\Psi(t) = \exp\left\{-D\gamma^2 \int_0^t dt' \left[\int_0^{t'} dt'' G^*(t'')\right]^2\right\}, \quad (4.23)$$

wherein D is the molecule self-diffusion coefficient, γ is the gyromagnetic ratio and $G^*(t)$ represents the effective magnetic field gradient. The solution of the double integral in Equation 4.23 depends specifically on the time profile of $G^*(t)$, which will change according to the PFG NMR pulse sequence adopted.

On what regards the signal loss due to relaxation, the term $R(t)$ may also be calculated (or measured) considering the exact form of the PFG sequence adopted. Notwithstanding, a particular type of data acquisition known as *time-independent acquisition* can be quite useful. In time-independent experiments the diffusion time is held fixed while the gradient pulse amplitudes are varied for the observation of the signal decay due to diffusion. As long as the diffusion time (and all the other sequence delays) are held equal for all points in the gradient strength array, the signal loss due to relaxation will be exactly the same along the decay points, becoming a normalization constant.

It is important to recall that the determination of transverse and longitudinal relaxation profiles, especially on the case of confined fluids, may be a burdensome task depending on the diffusion regime and the influence of the confining surface on relaxation. Hence, time-independent acquisitions are indeed advantageous for the determination of diffusion coefficients, as long as the approximations regarding the solution for the Bloch-Torrey expressed in Equation 4.22 can be considered valid.

4.1.6 Spin Echo PFG Sequence

One of the major downsides of the simple PFG sequence shown in Figure 4.1 is that the available time for the encoding, diffusion and decoding periods is limited by T_2^* , the FID time constant, which is affected by inhomogeneities on the static magnetic field B_0 . As discussed in Section 2.2.5 a π pulse can be employed to produce a spin echo and to minimize the signal loss due to inhomogeneities on B_0 .

The pulsed gradient spin echo (PGSE) sequence, proposed by Stejskal and Tanner [33], combines the simple PFG protocol with a refocusing π RF pulse resulting in a modified Hahn echo sequence (Figure 4.2), wherein the total available time is now T_2 , instead of T_2^* .

The spin echo PFG have another crucial advantage. Since the π refocusing pulse is applied after the first gradient pulse, it inverts not only the magnetization's precession

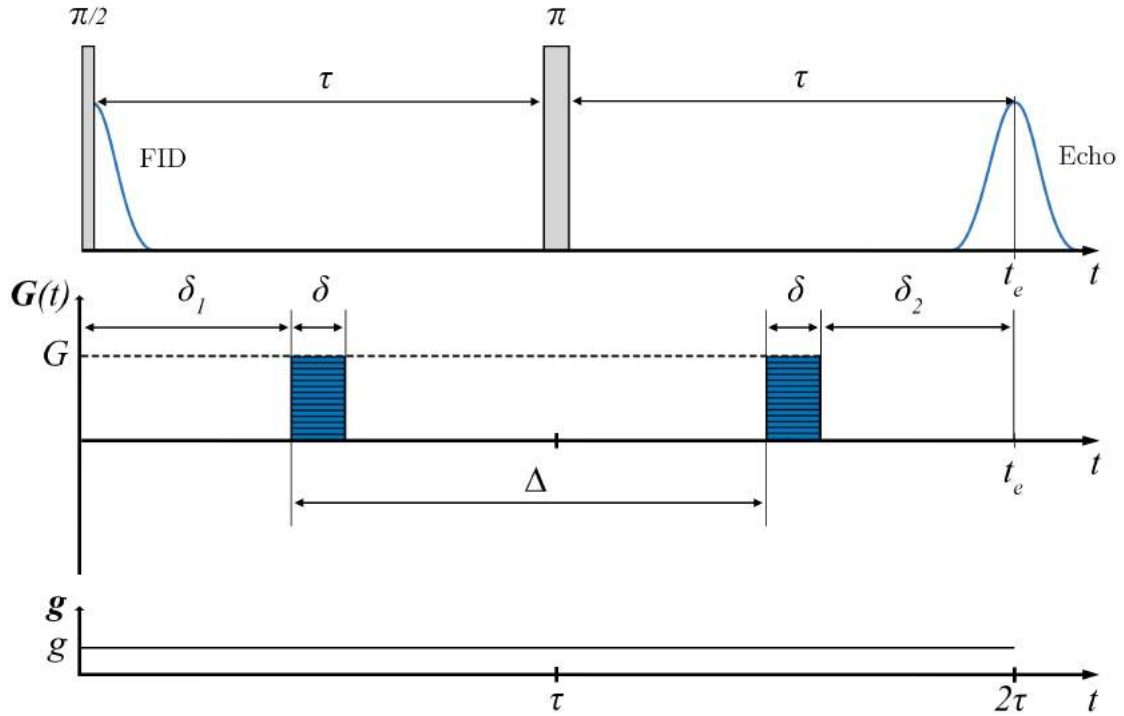


Figure 4.2: Spin echo PFG sequence (PGSE) proposed by Stejskal and Tanner [33] in the presence of a constant background gradient g . The refocusing π pulse inverts the phase imposed by the first gradient pulse during the encoding period. After the second gradient pulse a spin echo will be formed at $t_e = 2\tau$.

direction, but also the phase imposed by the encoding gradient pulse. Thus, the second gradient pulse applied during the decoding period does not need to be inverted with respect to the first gradient pulse. As discussed in Section 4.1.3 any mismatches between the amplitudes of the two gradient pulses may inflict in a remaining precession phase leading to an additional loss in the NMR signal. From the instrument stand point it is much easier to produce two gradient pulses of identical amplitudes in the same direction than in opposite ones.

The evaluation of the double integral expressed in Equation 4.23 must be carried on for each sequence interval considering that $G^*(t) = G(t) + g(t)$. For the case of the spin echo sequence illustrated in Figure 4.2 the evaluation of the double integral in Equation 4.23 leads to [96]:

$$\Psi(t_e) = \exp\{-D\gamma^2[A_p(t_e) + A_b(t_e) + A_c(t_e)]\}, \quad (4.24)$$

wherein, A_p , A_c and A_b denote the pulsed, cross and background gradient terms, respectively:

$$A_p(t_e) = \delta^2 \left(\Delta - \frac{1}{3} \delta \right) G^2, \quad (4.25)$$

$$A_c(t_e) = \delta \left[2\tau^2 - \frac{2}{3} \delta^2 - (\delta_1^2 + \delta_2^2) - \delta(\delta_1 + \delta_2) \right] Gg \quad (4.26)$$

and

$$A_b(t_e) = \frac{2}{3} \tau^3 g^2. \quad (4.27)$$

The pulsed term A_p depends only on the applied gradients ($+G$ and $-G$). The background term A_b depends, in this case, on the constant gradient g and the cross term A_c represents the coupling between the pulsed and the background gradients.

4.1.7 Stimulated Spin Echo PFG Sequence

During a spin echo PFG protocol the signal decay along the diffusion period is governed by the transverse relaxation (T_2). In systems where $T_1 > T_2$ it is useful to store the magnetization in the longitudinal axis. For such task the refocusing π RF pulse can be divided in two $\pi/2$ pulses, separated by the diffusion interval. This protocol, known as pulsed gradient stimulated echo (PGSTE), is illustrated in Figure 4.3.

The evaluation of the double integral in Equation 4.23 for the case of the stimulated echo sequence illustrated in Figure 4.3 leads to [96]:

$$A_p(t_e) = \delta^2 \left(\Delta - \frac{1}{3} \delta \right) G^2, \quad (4.28)$$

$$A_c(t_e) = \delta \left[2\tau(\Delta' + \tau) - \frac{2}{3} \delta^2 - (\delta_1^2 + \delta_2^2) - \delta(\delta_1 + \delta_2) \right] Gg \quad (4.29)$$

and

$$A_b(t_e) = \tau^2 \left(\Delta' + \frac{2}{3} \tau \right) g^2. \quad (4.30)$$

4.1.8 13-Interval PFG Sequence by Cotts

Cotts et al. [133] proposed a stimulated echo PFG sequence divided in 13 intervals, wherein both encoding and decoding periods contain a pair of gradient pulses of same amplitude but opposed polarities, separated by a π pulse (Figure 4.4). PFG sequences with gradient pulses of opposed polarities are also referred to as alternate pulsed field gradient (APFG). The evaluation of the double integral in Equation 4.23 for the case of

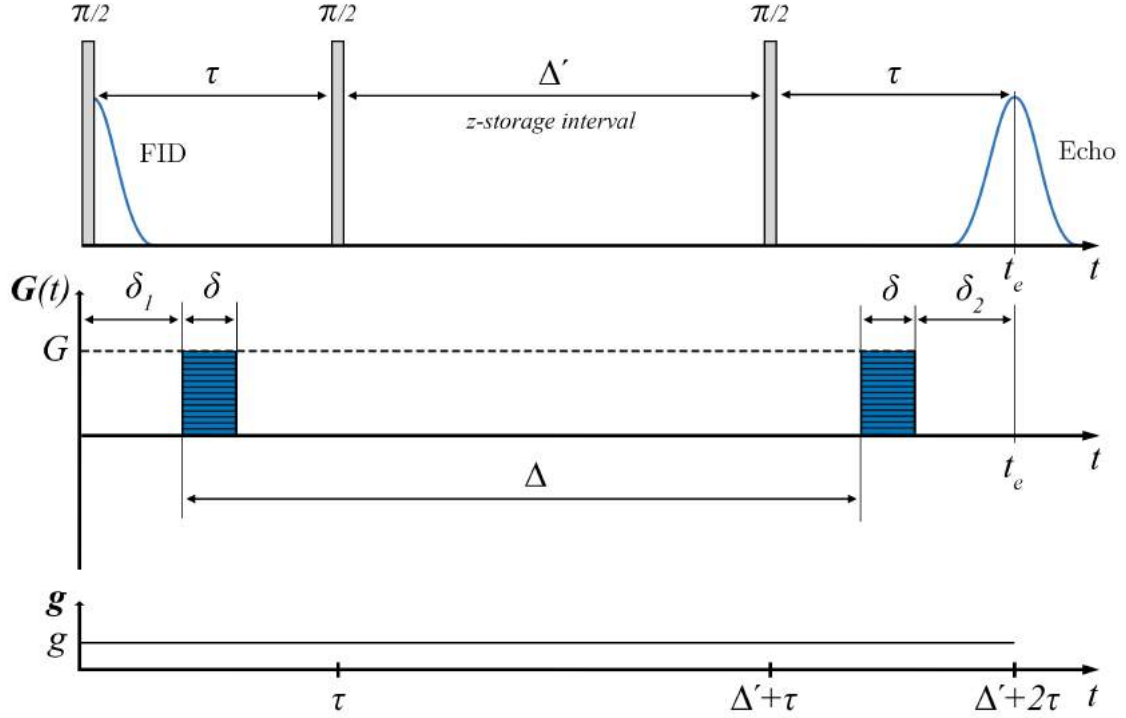


Figure 4.3: Stimulated echo PFG sequence (PGSTE) in the presence of a constant background gradient g . After the first gradient pulse a $\pi/2$ pulse rotates the magnetization to the z -axis. After the storage (diffusion) interval a third $\pi/2$ pulse rotates the magnetization back to the transverse plane. The phases of the two $\pi/2$ pulses can be set to have the same refocusing effect of the π pulse in the spin echo sequence. After the second gradient pulse a spin echo will be formed at $t_e = \Delta' + 2\tau$.

the 13-interval sequence illustrated in Figure 4.4 leads to:

$$A_p(t_e) = (2\delta)^2 \left[\Delta' + \frac{3}{2}\tau - \frac{1}{6}\delta \right] G^2, \quad (4.31)$$

$$A_c(t_e) = 2\delta\tau(\delta_1 - \delta_2)Gg \quad (4.32)$$

and

$$A_b(t_e) = \frac{4}{3}\tau^3 g^2. \quad (4.33)$$

There are several practical advantages in the 13-interval PFG sequence proposed by Cotts. The main one relates to the suppression of the background gradient influence on the signal decay due to diffusion. The cross attenuation term $A_c(t_e)$, which depends on both pulsed and background gradients, may be completely eliminated for $\delta_1 = \delta_2$, which can be easily achieved since both quantities are sequence delays. In this case, the pure background term $A_b(t_e)$ acts in much the same way as the relaxation term $R(t_e)$, in the

sense that if g may be considered constant during the time between encoding and decoding periods, $A_b(t_e)$ will represent just an additional global attenuation term, reducing the total signal amplitude, but not affecting the analysis of the observed echo attenuation [96].

The value of $A_b(t_e)$ can only be neglected for the cases wherein the magnitude of the background gradient is small in comparison with the pulsed gradients and the condition $g\tau \ll G\delta$ is fulfilled.

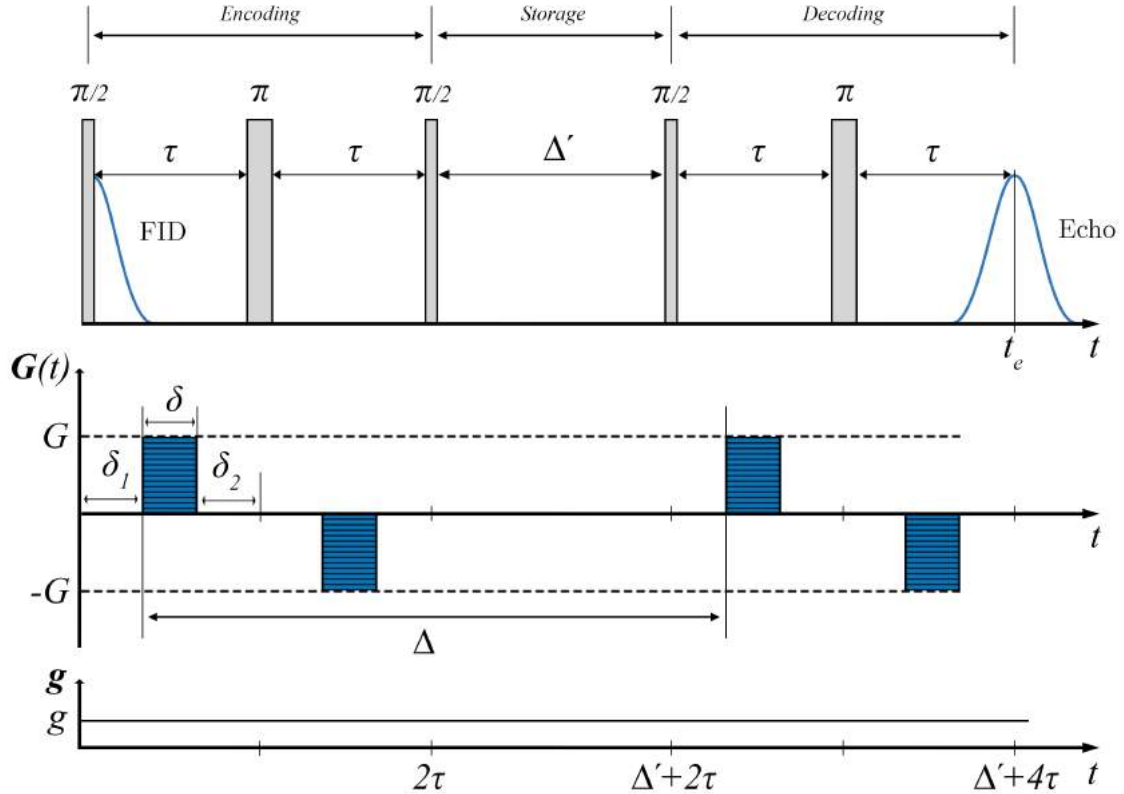


Figure 4.4: 13-Interval stimulated echo APFG sequence proposed by Cotts et al. [133] in the presence of a constant background gradient g . The encoding and decoding intervals are both composed by a pair of gradient pulses with opposed polarities separated by a π RF pulse. Similarly to the stimulated echo sequence, after the encoding interval the magnetization is stored in the z -axis. A spin echo will be formed at $t_e = \Delta' + 4\tau$ after the decoding period.

It is also worth noticing that, even though encoding and decoding intervals use each one a pair of gradient pulses with opposed polarities, the positive aspect of spin echo PFG sequences on what regards the matching between encoding and decoding gradient amplitudes is preserved, since from the instrument standpoint the same net phase is being applied in encoding and decoding stages. The π RF pulses between each pair of gradient pulses invert the phase imposed by the first gradient pulse, ensuring that the phase imposed

by the second is in fact added to the first one.

For the case of small δ_1 and δ_2 values this separation also allows the application of a larger net phase, although maintaining each pulse width small, an important feature for the validity of the narrow pulse approximation. The two $\pi/2$ RF pulses separated by the Δ' time interval act like a π pulse reverting the magnetization phase imposed at the end of the encoding interval, allowing both encoding and decoding gradient pulse pairs to be equal.

Provided that the background gradient $g(t)$ may not be considered constant, for an example, in the case of fluid molecules diffusing during large storage times through strong internal field gradients imposed by confinement, a more general approach should be considered assuming that $g(t)$ exhibits two different values during the encoding and decoding periods. Notwithstanding, the same evaluation for the double integral in Equation 4.23 can be carried out, although in this case the background and the cross gradient terms can not be easily neglected [96].

4.1.9 Restricted Diffusion and Short-Time Analysis

The assumption that the averaged propagator is a Gaussian function is valid considering the self-diffusion of fluid molecules due to random thermal motion in a homogeneous infinitely extended volume. For confined fluids the movement of molecules is now restricted by pore geometry, which consequently affects the probability density of finding a particle in a given position. In this case the diffusion propagator will not be a Gaussian function.

In restricted diffusion processes the influence of pore geometry on diffusive motion, however, will depend on the balance on how much time molecules have to diffuse and pore confinement scale. During short diffusion intervals, on average, only the molecules which are closer to the confining surface will have their movement restricted, while for the molecules which are far from pore walls diffusion will take place as in the unrestricted case. Therefore, for sufficiently short diffusion times the averaged propagator for restricted diffusion may be fairly approximated by a Gaussian function. This approximation, known as *short-time regime*, may be expressed by the condition:

$$\sqrt{D_0\Delta} \ll R_p, \quad (4.34)$$

in which D_0 is the bulk self-diffusion coefficient, Δ denotes the diffusion (or storage) time and R_p represents the characteristic confinement scale (or the average pore radius).

The diffusion coefficients obtained in measurements with confined fluids by PFG NMR reflect those geometry-imposed restrictions, and the observed values are in fact dependent

on the diffusion time. For this reason the diffusion coefficients of confined fluids are also commonly referred to as apparent or effective diffusion coefficients [131]. The idea that diffusion of confined fluid molecules would remain Gaussian, even though being slowed down by geometry obstacles, is one of the foundations for the application of the GPA mentioned in Section 4.1.4 (valid for small gradient values), on the analysis of apparent diffusion coefficients from confined fluids.

Mitra et al. [72] derived an analytical expression for the behavior of time-dependent diffusion coefficients in the short-time regime as a function of confinement geometrical parameters. In the short-time regime it may be assumed that only the molecules which started to diffuse within a surface layer of width $\sqrt{D_0 t}$ have their movement restricted by pore walls. This layer defines a portion of walkers proportional to $\sqrt{D_0 t}(S/V)$, wherein S represents the surface area and V is the volume of the considered domain. The measured apparent (or time-dependent) diffusion coefficient $D(t)$ will reflect the diffusion of both surface-affected and unaffected portions. Mitra showed that assuming a surface with smooth boundaries in the presence of surface relaxativity (partially absorbing boundary condition), the time-dependent diffusion coefficient $D(t)$ can be expressed by:

$$\frac{D(t)}{D_0} \simeq \frac{\langle |\vec{r}(t) - \vec{r}(0)|^2 \rangle}{6t} = 1 - \frac{4(D_0 t)^{1/2} S}{9\sqrt{\pi} V} + (D_0 t) \frac{S}{V} \left[-\frac{H}{12} + \frac{\rho}{6D_0} \right] + \mathcal{O}[(D_0 t)^{3/2}], \quad (4.35)$$

wherein (S/V) denotes the porous media surface-to-volume ratio, H is the pore mean curvature, ρ represents the surface relaxativity and the last term on the right side stands for the contributions of the order of $(D_0 t)^{3/2}$.

The analysis of short-time effective diffusion coefficients has being successfully applied to the characterization of geometrical parameters in model porous media such as glass sphere packs [134] and also natural rock samples [135].

4.2 Motivation: The Characterization of Multiphase Saturation in the Framework of Restricted Diffusion

Characterization of emulsions (immiscible fluid mixtures) is an essential part of research in different industry segments such as foods, chemicals, pharmaceuticals and also oil exploration [37, 136–139]. For the latter, due to the very own nature of oil formation and migration processes, reservoir rocks are commonly found saturated with water-oil mixtures, and some oil recovery strategies also utilize emulsions injection in underground reservoirs as a mechanism to increase oil extraction [139, 140]. Among several different tools employed to measure physical and chemical properties from fluids in saturated rocks, NMR relaxometry

techniques stand out as being non-invasive, and have been long used in porous media petrophysics [5, 102].

Although the application of one-dimensional relaxometry techniques and their theoretical framework on rocks saturated with a single fluid allows a relatively straightforward data interpretation, the analysis of relaxation profiles becomes problematic when porous space contains more than one phase. Water and oil subjected to different confinement conditions may exhibit similar relaxation rates, depending on pore features like geometry and surface physico-chemical properties [6, 115]. Moreover, as a result of magnetization transfer between present phases, exchange effects must now be accounted for into the Bloch equation formalism [141] and the behavior of solutions can become quite distinct from what it is generally expected from the single phase case.

A significant improvement in fluid identification can be achieved by combining molecular diffusion measurements, obtained from pulsed-field gradient (PFG) NMR, and relaxometry protocols into two-dimensional techniques such as diffusion-relaxation (D- T_2) and diffusion-diffusion (D-D) correlation maps [46, 47]. Despite the considerable increase in available information, these experiments can be very time-consuming and the extraction of correlation maps from raw data often relies on two-dimensional inverse Laplace Transform algorithms [95].

Restricted diffusion coefficients obtained from PFG NMR experiments in one dimension also provide valuable information on bulk emulsion [142, 143] and, for the case of molecules undergoing diffusion in the pore space, parameters pertaining to the confining geometry, such as porous media surface-to-volume ratio, become accessible under specific diffusion regimes [72, 135, 144].

In this Chapter we present the analysis of time-dependent diffusion coefficients, obtained from sets of one-dimensional PFG NMR measurements, to characterize the effects of drainage in phase conformation in water-saturated sintered glass beads, in order to identify and evaluate individual characteristics of water and oil phases, and mixture conformation features after drainage.

4.3 Fluid Conformation After Drainage

When oil is forced into a porous rock previously saturated with water, an emulsion can be formed inside the pore space. Conformation of fluids within pores depends on several factors such as physico-chemical properties of both phases, injection pressure, pore connectivity, and also on the relation between wetting and non-wetting phases [145]. Wettability is the property that intermediates the contact between a liquid and a solid

surface, determined by the interplay among attractive (adhesive) and repulsive (cohesive) forces. Although surface wettability can be altered by physico-chemical processes in the long-time presence of two fluids, reservoir rocks are commonly water-wet [139]. The process of forcing a non-wetting phase into a porous media previously saturated with a wetting phase is defined as drainage. Usually, oil migrates into most reservoirs as the non-wetting phase, which characterizes a drainage process [146].

The result of oil injection in a water-saturated porous sample, on what regards connectivity of wetting and non-wetting phases, may be illustrated by two simplified scenarios. In the first one (Fig. 4.5 - (a)) oil is distributed into several droplets, located in the innermost region of pores. In this case pore throats remain filled with water, and the non-wetting phase exhibits limited or no connectivity. In a second scenario oil fills both inner regions of pores and throats, in a highly-connected configuration (Fig. 4.5 - (b)). Naturally, scenarios (a) and (b) in Figure 4.5 only illustrate opposite cases related to the connectivity of the non-wetting phase. In complex porous media such as natural rocks, a combination of both scenarios is most likely to describe fluid conformation after drainage.

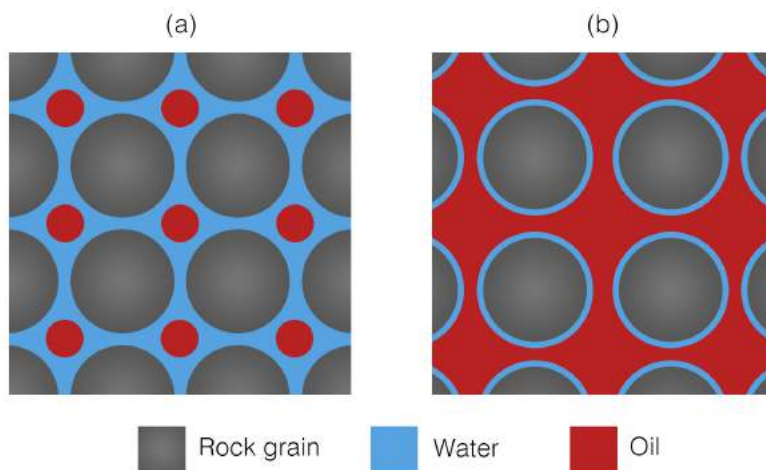


Figure 4.5: Illustration of simplified conformation scenarios for the non-wetting phase after drainage. (a) Oil is located only in the innermost region of pores, with pore throats still filled with water. In this scenario the non-wetting phase exhibits limited or no connectivity. (b) Non-wetting phase fills both inner regions of pores and throats, in a highly-connected configuration.

Conformation of water and oil phases after drainage and porous geometry features will determine how molecules of each fluid diffuse through the pore space. Molecular movement is now restricted and the time-dependent self-diffusion coefficients from each phase, measured through PFG NMR experiments, are expected to reflect these constraints.

In the following Sections a set of one-dimensional PFG NMR experiments performed

in water-saturated synthetic porous samples - pre and post drainage - is presented. The acquired data was analyzed under the framework of restricted diffusion and the short-time regime for an evaluation of the available information on individual phases and post drainage conformation features.

4.4 Experimental Description

4.4.1 Samples and Preparation

Samples of distilled water (100%) and isoparaffin (ISO FAR 17/21 100%) were used in the experiments. Synthetic porous samples were produced by glass microspheres sintering (diameter 250 – 300 μ m). The fabrication protocol is the same as described in Chapter 3 [147]. The microspheres were placed in a cylindrical ceramic crucible (Al_2O_3 99.8%) and taken to a chamber furnace (Carbolite CWF 1200) for the following heat treatment: from room temperature to 560° C at 140° C /min, held for 20 minutes; from 560 to 700° C at 20° C /min, held for 1 hour; from 700 to 490° C at 14° C /min, 490 to 440° C at 28° C /min, and then cooled to room temperature.

The effect of the thermal treatment in sample's pore structure, designed to lightly fuse the microspheres while preserving most of the porosity of the original sphere package before sintering, can be seen in the two-dimensional micro-tomography image presented in Figure 4.6.

Water saturation was performed by imbibition using a desiccator connected to a vacuum pump. The dry sample was placed inside a desiccator containing a recipient with distilled water. Only after the establishment of a low-vacuum condition the sample is then dropped into the water container in order to prevent the formation of trapped air bubbles within pores. Samples were left submerged in the water recipient in low-vacuum condition for approximately 30 minutes to remove residual air content.

For the drainage process the water-saturated samples were clothed in a rubber sleeve and placed into a cylindrical holder, illustrated in Figure 4.7. An oil volume equal to the sample's volume was manually forced into the sample using a piston at an average injection rate of 1 ml/s. Immediately after the drainage process samples were placed in the glass tubes for the NMR measurements.

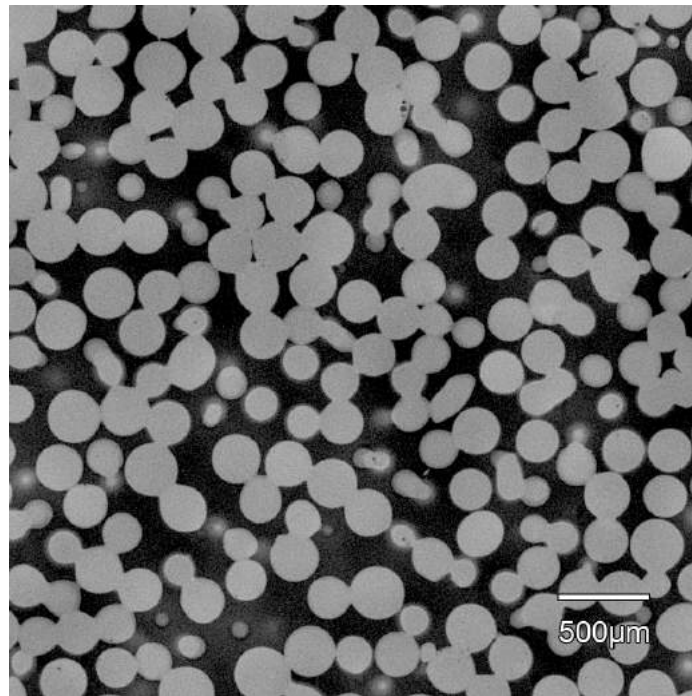


Figure 4.6: 2D micro-tomography image of microspheres after the sintering process employed in the fabrication of the synthetic porous samples. The sintering protocol was designed to preserve most of the porosity from the original package [147].

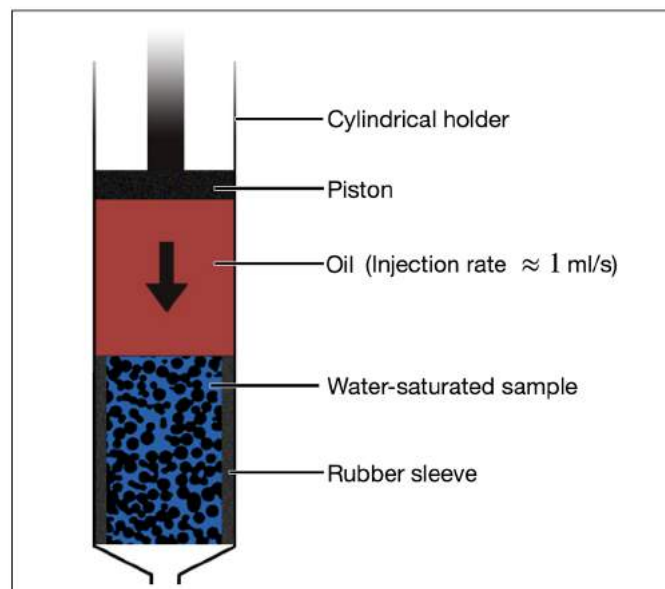


Figure 4.7: Illustration of the experimental setup employed for the drainage of water-saturated samples. An oil volume equal to the sample's total volume was forced into the water-saturated samples using a manually controlled piston at an average rate of 1 ml/s.

4.4.2 Measurements

^1H Spectroscopy, inversion recovery (T_1) and PFG NMR measurements were performed at room temperature (25° C) in bulk samples of both fluids, in an oil-saturated porous sample, and in a water-saturated porous sample before and after oil injection. Measurements were carried out in a Varian (Agilent) 500 MHz spectrometer using a 5 mm probe.

A 13-interval bipolar PFG NMR sequence (Fig. 4.4) was used for the PFG measurements. Several acquisitions were performed fixing the storage time Δ and varying the magnetic field gradient strength (time-independent acquisition) to monitor the signal attenuation due to diffusion. The PFG NMR experiments were performed using 18 different diffusion times Δ varying from 3 to 60 ms. The duration of magnetic field gradient pulses δ was set as 1 ms, and τ duration was set as 1.4 ms for all experiments.

4.5 Results and Discussion

4.5.1 Fluids Characterization

Individual phase self-diffusion coefficients were measured in bulk samples of each fluid. Figure 4.8 shows the signal attenuation Ψ as a function of squared gradient G^2 , and linear fittings performed with the Curve Fitting toolbox (MATLAB version R2019b). Obtained values were $D_0^w = 2.29 \times 10^{-9} \text{ m}^2/\text{s}$ for water (upper plot) and $D_0^o = 0.79 \times 10^{-9} \text{ m}^2/\text{s}$ for oil (lower plot). The fitting error was no greater than 1 % for both samples and the water diffusion coefficient value is in fair agreement with previously reported values [148]. No reference diffusion coefficient value was found in literature for this particular oil sample at 298.15 K.

4.5.2 Pre Drainage PFG Analysis

Figures 4.9 to 4.11 show signal attenuation Ψ as a function of squared gradient G^2 for different diffusion times ranging from 3 to 60 ms, obtained from PFG measurements in the water-saturated porous sample, before oil injection. Time-dependent diffusion coefficients (Figure 4.12) were extracted from the PFG decay curves by a linear fit combining the expressions in Equations (4.24) and (4.31) for the signal attenuation due to diffusion $\Psi(t_e)$:

$$\begin{aligned}\Psi(t_e) &= \exp\{-D\gamma^2[A_p(t_e) + A_b(t_e) + A_c(t_e)]\} \\ &= \exp\{-D\gamma^2[(2\delta)^2\left[\Delta' + \frac{3}{2}\tau - \frac{1}{6}\delta\right]G^2]\}\end{aligned}\tag{4.36}$$

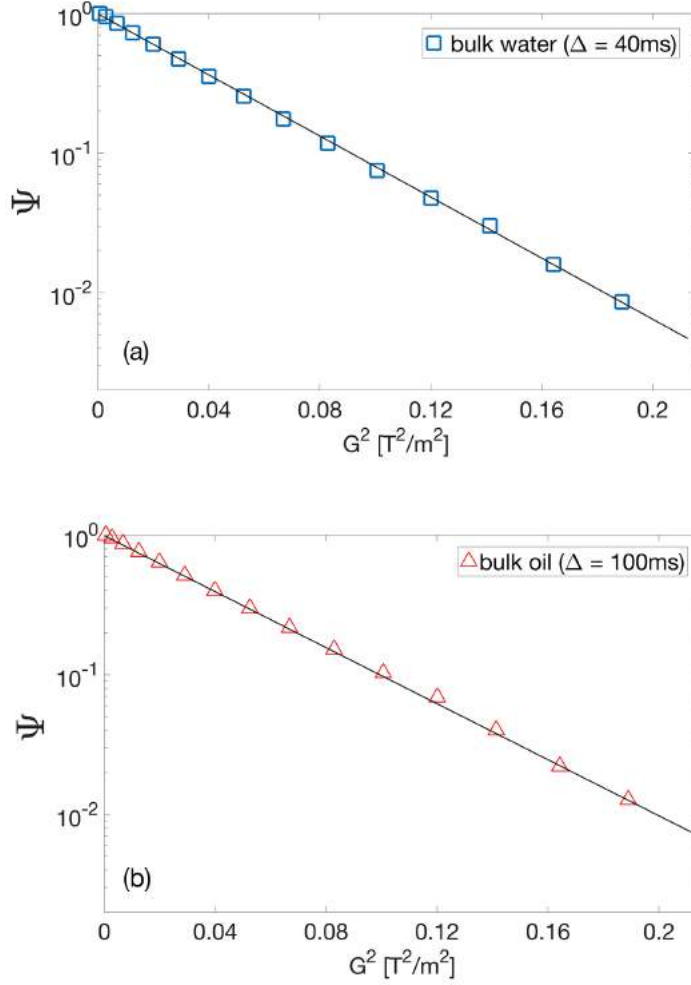


Figure 4.8: Bulk water (a) and oil (b) normalized spin echo attenuation Ψ as a function of squared gradient G^2 . Diffusion time (Δ) value was 40 ms for water and 100 ms for oil measurements. Black lines denote fittings using Equation (4.36). Self-diffusion coefficients obtained were $D_0^w = 2.29 \times 10^{-9}$ m²/s for water and $D_0^o = 0.79 \times 10^{-9}$ m²/s for oil.

The cross gradient term $A_c(t_e)$ (Equation (4.32)) was canceled making $\delta_1 = \delta_2$ in the PFG pulse sequence, and the background term $A_b(t_e)$ (Equation (4.33)) was neglected assuming that the background gradient $g(t)$ is, in a fair approximation, constant over the relatively short time scale of the experiments, which were designed to observe molecules self-diffusion during the short-time regime. Under such conditions $A_b(t_e)$ represents just a renormalizable attenuation term, not affecting the analysis of the observed echo attenuation [96].

Observing the signal attenuation in a vertical logarithmic scale it is possible to notice that the linear behavior, present in measurements with small Δ values (< 20 ms), is gradually lost as diffusion time is increased. This graphical approach is a useful tool to

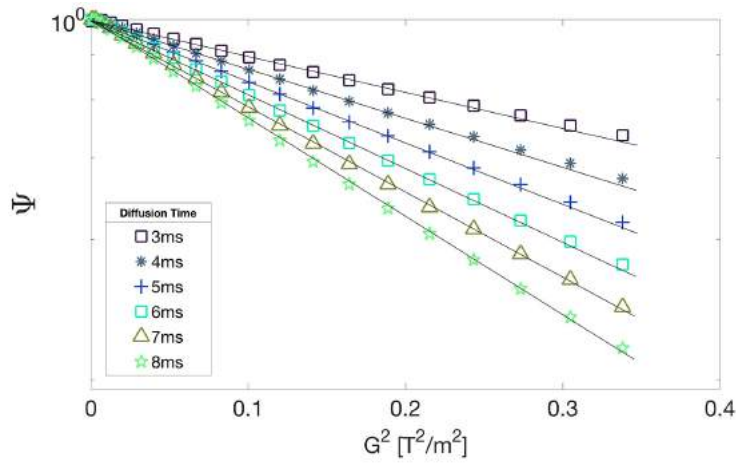


Figure 4.9: Signal attenuation Ψ as a function of squared gradient G^2 for different diffusion times, on the water-saturated porous sample, for Δ values between 3 and 8 ms. The black lines represent linear fittings considering the initial slope of each data set. Loss of linear behavior for different Δ values can be used to validate the Gaussian propagator approximation, and the short-time regime definition.

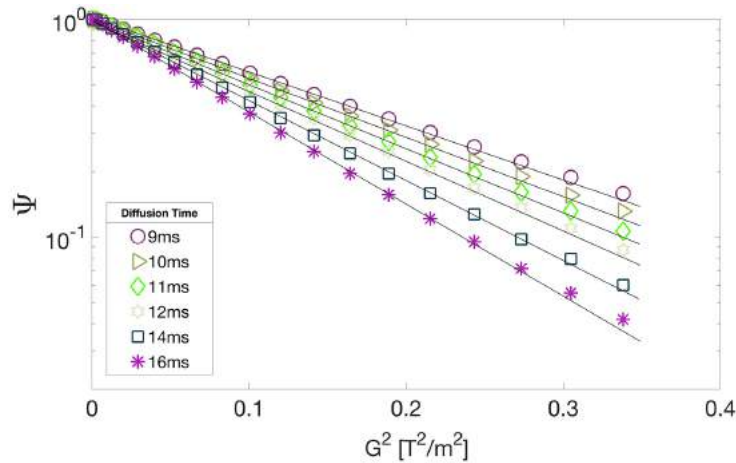


Figure 4.10: Signal attenuation Ψ as a function of squared gradient G^2 for different diffusion times, on the water-saturated porous sample, for Δ values between 9 and 16 ms. The black lines represent linear fittings considering the initial slope of each data set. Loss of linear behavior for different Δ values can be used to validate the Gaussian propagator approximation, and the short-time regime definition.

evaluate the validity of the Gaussian propagator approximation, and to properly define a short-time regime in the case of restricted diffusion. According to the behavior of signal decays showed in Figures 4.9 to 4.11, only the diffusion coefficients extracted from data sets with diffusion times up to 20 ms were considered for the analysis presented in Figure 4.12, in order to ensure the validity of the short-time regime and the Gaussian propagator

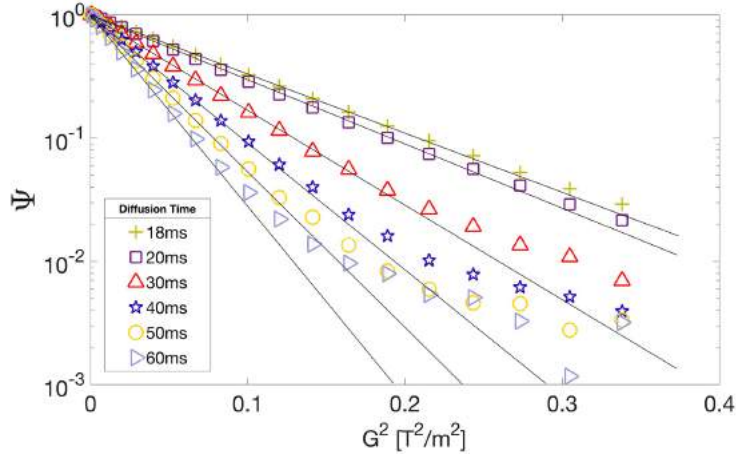


Figure 4.11: Signal attenuation Ψ as a function of squared gradient G^2 for different diffusion times, on the water-saturated porous sample, for Δ values between 18 and 60 ms. The black lines represent linear fittings considering the initial slope of each data set. Loss of linear behavior for different Δ values can be used to validate the Gaussian propagator approximation, and the short-time regime definition.

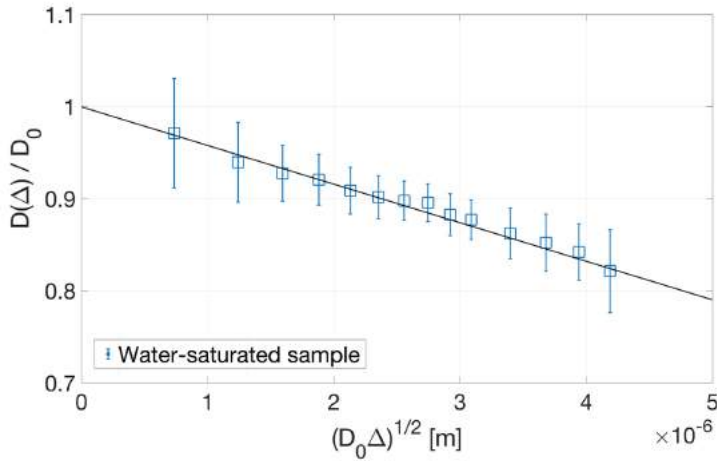


Figure 4.12: Analysis of the normalized time-dependent diffusion coefficients as a function of diffusion length $\sqrt{D_0\Delta}$, extracted from the decay curves presented in Figures 4.9 to 4.11, performed using the short-time approximation proposed by Mitra et al. In order to assure the validity of the short-time regime only the diffusion coefficients extracted from data sets with Δ values up to 20ms were considered. The black line represents a linear fitting considering only the term of order $\mathcal{O}[(D_0t)^{1/2}]$ in Equation (4.35).

approximation.

Figure 4.12 shows an analysis of the extracted time-dependent diffusion coefficients as a function of the storage time Δ , performed using the short-time approximation (Eq. (4.35))

proposed by Mitra et al. A linear fitting of the data was performed considering initially only the first order term in Equation (4.35). A sufficiently good adjustment was obtained with a surface-to-volume ratio value of $S/V = 9.22 \times 10^4 \text{ m}^{-1}$ with a relative error of 5 %. The quality of the fit was verified by looking at the Sum of Squares due to Error (SSE) and the R-square coefficients, which are about 6×10^{-4} and 0.9896, respectively.

The inclusion of the higher order term in the expansion for $D(t)$ adds two new parameters to the fit procedure, the surface relaxivity ρ and the pore mean curvature H . In this new fit the values obtained for the new parameters ρ and H exhibited associated errors which were larger than the parameters' values themselves, whereas no improvement was observed in the fit quality coefficients and also no significant change was verified in the value of the parameter S/V . Following the principle of simplicity, the first fit procedure, containing only the first order term in Equation (4.35), was considered.

An estimate of the surface-to-volume ratio for the porous space in a system composed by a random closed packing of mono-sized spheres can be performed using the relation $S/V = 6(1 - \phi)/(d_s\phi)$, wherein d_s stands for the spheres' diameter and ϕ represents the porosity of the package. Assuming $d_s = 250 \text{ }\mu\text{m}$ and the close random packing porosity as $\phi \approx 37 \%$ leads to a value of $S/V \approx 4.1 \times 10^4 \text{ m}^{-1}$.

Although the S/V value obtained by NMR data fitting with Equation (4.35) comes from an analytical expression, the estimated value on the other hand was obtained assuming an idealized system composed by a package of mono-sized spheres with perfect sphericity. The real measured system is the result of a sintering process performed in a random package of spheres with diameters varying within a size range, which are assumed to exhibit sphericities smaller than 1. A balance of all these factors is then expected to influence the resulting S/V of the fabricated samples. For these reasons the estimated S/V value was considered in fair agreement with the value extracted from PFG data using Equation (4.35).

The geometry of the samples used in this work can be approximated by a packing of overlapping spheres, considering the effect of the applied sintering protocol in glass microspheres, analyzed in scanning electron microscopy (SEM) images [147]. Weissberg [149] deduced an approximate expression for the geometric tortuosity τ of overlapping spheres as a function of geometry porosity ϕ :

$$\tau_g = 1 - \frac{1}{2} \ln \phi. \quad (4.37)$$

An estimate of samples permeability can be performed using the S/V value extracted from the PFG measurements and the Kozeny-Carmen relation [150]:

$$k_{perm} \approx \left(\frac{V}{S}\right)^2 \frac{\phi}{2\tau_g}, \quad (4.38)$$

wherein ϕ is the porosity and τ_g represents porous media geometric tortuosity.

A permeability estimate combining the S/V value extracted from data in Figure 4.12, and Equations (4.37) and (4.38), leads to a value of $k_{perm} \approx 16$ D with a relative error of 12 %, wherein in this case D stands for the permeability unit Darcy ($1 \text{ D} \approx 0.98 \mu\text{m}^2$). The permeability value reported in [147] for this sample, measured by the free gas expansion method, is $k_{perm} \approx 28$ D.

It is important to remark that Equation (4.38) represents simply a correlation between permeability and porous media geometrical properties, and not an exact dependency. It is noticeable that the permeability estimate performed with the surface-to-volume ratio value extracted from PFG data processing, and the tortuosity value obtained from Equation (4.37), recovered the high permeability value associated with this type of sample [147], and therefore, in the author's opinion, can be considered in fair agreement with the measured value.

4.5.3 Post Drainage PFG Analysis

^1H NMR spectra of an oil-saturated sample, and a water-saturated sample before and after drainage, are shown in Figure 4.13. Although lines are particularly broad, it is possible to identify water and oil phases in the post drainage spectrum. A bi-Lorentzian fit was performed to estimate fluids proportion after drainage. In general, this evaluation should not be considered an accurate one, since distinct effects contribute to the observed spectrum line shapes. Considering the case of confined fluids, a line broadening in spectrum is expected due to the presence of grossly inhomogeneous magnetic fields inside porous matrix. In addition, NMR spectrum of crude oils present multiple peaks, relating to the combined chemical-shift structure of various molecules. In this case, the former mentioned line-broadening effect due to confinement will affect all peaks, and the shape of the resulting spectrum is not necessarily a Lorentzian. Here, the intent of the presented spectra is not to determine quantities of both fluids, but mainly to confirm the presence of both phases after drainage.

Relative quantities of both phases were also evaluated by weighed mass, longitudinal relaxation (T_1) and PFG measurements (Figure 4.14). The model used to analyze the PFG data after drainage is discussed further. For the analysis of T_1 measurements after drainage both phases were assumed to be in the fast diffusion regime. Initial calibration experiments revealed that the fabricated samples saturated with a single fluid exhibit mono-exponential

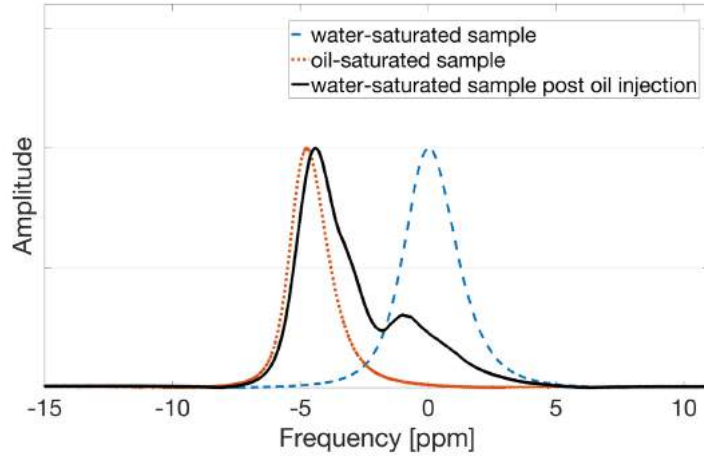


Figure 4.13: ^1H spectra of oil-saturated sample (red dotted line), water-saturated sample before (blue dashed line) and after (solid black line) drainage. Even though lines are particularly broad it is possible to roughly identify the presences of oil and water peaks in the post drainage spectrum.

T_1 decays. Assuming that both phases after drainage are in fast diffusion regime and considering that there is no spin exchange between the water and the oil phases allows a simpler estimate for the relative content of both fluids using a bi-exponential model for the T_1 relaxation.

For the case of water-saturated samples before drainage, Gaussian approximation for the diffusion propagator, and the extension of a short-time diffusion regime, can be evaluated through the analysis of signal attenuation linearity, in a semi-logarithmic $\Psi(t)$ versus squared gradient G^2 plot. However, after oil injection, in the presence of two fluids with different diffusion coefficients, PFG signal attenuation will no longer exhibit a single Gaussian behavior. Although a graphical validation for this approximation is no longer possible, the hypothesis that measurements may be carried in a short-time regime, where the Gaussian propagator approximation could be considered valid for both fluids, is quite reasonable, and is assumed in the presented analysis.

A two-fluid model was proposed by Stallmach and Thomann [151] to determine fluid fractions with different translational mobilities in porous media, by PFG NMR. The analysis of time-dependent diffusion coefficients from water-saturated samples after drainage was carried considering a similar bi-Gaussian model in the form:

$$\Psi(t_e) = s_w \exp[-D^w(t_e)\gamma^2(A_p(t_e))] + s_o \exp[-D^o(t_e)\gamma^2(A_p(t_e))], \quad (4.39)$$

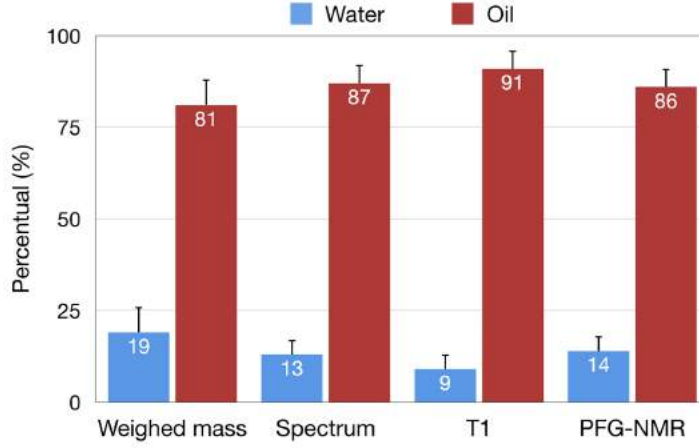


Figure 4.14: Estimate of water and oil quantities obtained from weighed mass, spectroscopy (Figure 4.13), longitudinal relaxation (T_1) and PFG measurements after drainage. The estimate error (vertical black bars) was 6% for the weighed mass method and not greater than 4% for the NMR-based techniques. The errors for the spectrum and the T_1 methods were determined as the relative fitting error considering a bi-Lorentzian and a bi-exponential model, respectively. The error for the PFG method was determined as the standard deviation for the saturation values (s_w and s_o) obtained from fittings considering the data sets for different Δ values, using for each one of them the bi-Gaussian model expressed in Equation 4.39.

in which $D^w(t_e)$, $D^o(t_e)$, s_w and s_o denotes the water and oil time-dependent diffusion coefficients and their respective saturations, with $s_w + s_o = 1$. The term $A_p(t_e)$ has the form expressed in Equation (4.31).

Representative signal decays obtained from post drainage PFG measurements for five different Δ values are shown in the upper plot of Figure 4.15. The lower plot in Figure 4.15 shows the time-dependent diffusion coefficients obtained from all the 18 performed measurements for water and oil, as a function of the diffusion length ($\sqrt{D_0\Delta}$), from PFG data analysis after drainage using Equation (4.39).

Throughout the Δ time interval investigated water diffusion coefficient values (blue squares) showed a clear attenuation while diffusion time is increased. As expected in both scenarios illustrated in Figure 4.5, wetting phase exhibits a good connectivity, as water molecules probe the new available porous space after drainage.

A new analysis of the short-time behavior of water time-dependent diffusion coefficients (black line in the lower plot) using Equation (4.35) reveals a new water-probed surface-to-volume ratio $S/V = 3.01 \times 10^5 \text{ m}^{-1}$; an increase of more than 300 % compared to its value before oil injection. This behavior is expected since not only the surface area of the water

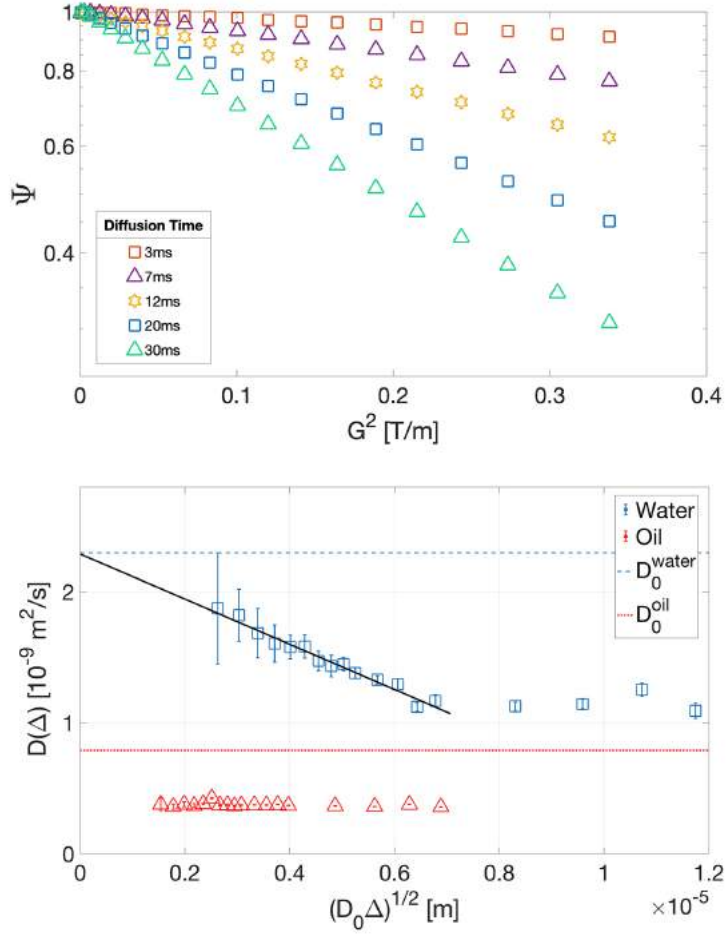


Figure 4.15: [Upper plot] Signal attenuation Ψ as a function of squared gradient G^2 for different diffusion times, on the water-saturated porous sample after drainage. Acquisitions were performed for 18 different Δ values between 3 and 60 ms. Representative signal decays for Δ values 3, 7, 12, 20 and 30 ms are shown. [Lower plot] Time-dependent diffusion coefficients obtained for water (blue squares) and oil (red triangles) extracted using the bi-Gaussian model in Equation (4.39) from PFG experiments in water-saturated sample after drainage. Fitting error bars are shown for both fluids, however for the oil points error is smaller than marker size. Dashed blue line and dotted red line represent bulk values of water and oil diffusion coefficients (D_0^w and D_0^o), respectively. The black line on the lower plot represents the analysis of post drainage water time-dependent diffusion coefficients as a function of diffusion length $\sqrt{D_0\Delta}$, performed using the short-time approximation (Eq. (4.35)) considering only the term of order $\mathcal{O}[(D_0t)^{1/2}]$.

phase is increased with the addition of a contact surface between wetting and non-wetting phases, but also a significant amount of wetting phase is drained in the injection to be occupied by the non-wetting phase (Figures 4.5 and 4.13).

Oil time-dependent diffusion coefficients (red triangles - Fig. 4.15) nevertheless showed

no significant variation with diffusion time. Such behavior can be analyzed over two different perspectives. In the first one, oil phase would also be distributed in a connected configuration, and considering that oil molecules bulk diffusivity is approximately three times smaller than water (Fig. 4.8), the diffusion time range investigated, from 3 to 60 ms, would not be long enough for one to measure an expressive attenuation in oil $D(\Delta)$ values, similar to the one observed in water during the same time range. Although a low diffusivity could be used to justify the small variation between oil $D(\Delta)$ values, the time-dependent diffusion coefficient of oil observed in a post drainage PFG experiment with the shortest available diffusion time ($\Delta = 3$ ms) corresponds to almost half of its bulk value (red dotted line - lower plot of Fig. 4.15). This considerable attenuation, observed during a small diffusion time, would not be expected assuming that oil is distributed in a connected configuration.

A different analysis can be done considering that oil diffusion coefficients have actually reached a stationary regime, which, in this case, indicates a highly-restricted diffusion process. Here, a scenario where non-wetting phase is poorly connected would be most likely to describe fluids conformation after drainage, and a distribution of oil-in-water droplets may have formed within pores.

An expression for the signal attenuation of molecules diffusing inside spherical cavities in PFG experiments was calculated by Murday and Cotts [70], and an approximation for it was later proposed by Callaghan et al. [71]. Assuming that oil droplets have spherical shape, and that a Gaussian distribution of droplets radii is to be found along the sample, PFG signal attenuation due to oil molecules diffusion can be approximated by [71, 152]:

$$\Psi(\delta, G, r_0, \sigma) = \Psi_0 \frac{1}{\sqrt{1 + 2\sigma^2\beta^2}} \exp\left(-\frac{\beta^2 r_0^2}{1 + 2\sigma^2\beta^2}\right), \quad (4.40)$$

wherein r_0 is the average radius of the droplets radii distribution, σ is the standard deviation and $\beta^2 = \gamma^2 \delta^2 G^2 / 5$. The validity of this expression is based on the assumption that the Gaussian phase approximation is valid, meaning that although short, gradient pulses have a finite duration δ , and spins, during this interval, accumulate a Gaussian distribution of phases. The correct corresponding between r_0 , σ and signal attenuation, using Equation (4.40), should be obtained only for small values of β^2 [71].

Once the diffusion time Δ was increased to the regime where signal attenuation does not depend on Δ , the initial slope in the plot of $\ln[\Psi(\delta, G, r_0, \sigma)/\Psi_0]$ versus β^2 can be adjusted with Equation (4.40) for small values of β^2 , and assuming a Gaussian distribution of droplets radii, r_0 and σ values can be estimated directly from data [71]. Figure 4.16 presents the signal attenuation $\ln[\Psi(\delta, G, r_0, \sigma)/\Psi_0]$ as a function of β^2 , and a fitting

performed with Equation (4.40) for oil diffusion after drainage. Validity of the carried approximations can be observed through the agreement between data and the assumed model for small β^2 values. Extracted values for the average oil droplet radius and the radii standard deviation were $r_0 \approx 20 \mu\text{m}$ and $\sigma \approx 4 \mu\text{m}$, respectively.

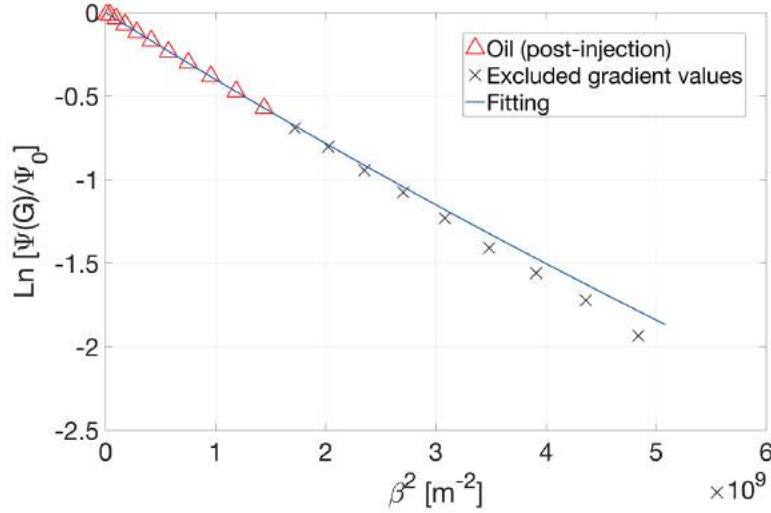


Figure 4.16: Signal attenuation $\ln[\Psi(\delta, G, r_0, \sigma)/\Psi_0]$ as a function of β^2 for oil diffusion after drainage. Blue solid line denotes the fitting performed with Equation (4.40) considering the formation of oil-in-water droplets within pores. Validity of the carried approximations can be observed through the agreement between data and the proposed model (red triangles) for small β^2 values. Cross markers represent large β^2 values that were excluded from fit. The extracted values for the average radius and the standard deviation assuming a Gaussian distribution of oil droplets radii were $r_0 \approx 20 \mu\text{m}$ and $\sigma \approx 4 \mu\text{m}$, respectively. The relative error in the estimate of r_0 was less than 1 %.

Although the bi-Gaussian model employed in the analysis of post drainage PFG data is based in a set of a priori information on the investigated system, which from the physical standpoint upholds the interpretation of the results, its application relies in a mathematical fit procedure. Grebenkov [131] addressed the mathematical limitations of the bi-exponential model on the analysis and interpretation of effective diffusion coefficients obtained from diffusion measurements in a two-phase system. On what regards the fit procedure, the analysis of PFG decays obtained for small diffusion times are the most challenging, as for these curves the signal attenuation is considerably smaller than the one obtained for larger diffusion times, as shown in Figure 4.15. It must be considered the possibility that oil diffusion coefficients obtained from bi-exponential fits performed in the data sets presented in this work may be misrepresented for the case of small diffusion times. The option of analyzing such data sets by inverse Laplace transform was initially considered but also discarded due to the fact that the procedure is also affected by nonzero baseline offsets [52], and without a proper baseline reference no reasonable regularization

criteria could be adopted for the choice of a regularization parameter. Nevertheless, water diffusion coefficients obtained from fit procedures performed in different data sets exhibited a very consistent behavior with respect to what was expected physically for the conformation of both fluids after drainage, reflecting the significant increase in the surface-to-volume ratio probed by the wetting phase.

The effect of the diffusion of fluid molecules through internal magnetic field gradients induced by susceptibility contrast, considering the use of a high magnetic field in the experiments (500MHz), should also be analyzed. The influence of diffusion through internal gradients on the NMR signal decay results from the interplay of pore confinement scale, molecular diffusion and the magnetic field strength (including the gradients induced by susceptibility contrast), and hence cannot be simply determined a priori. In this case, asymptotic limits can be used to investigate such effect, as proposed by Hürlimann [83]. According to Hürlimann's definition, three length scales are relevant in this analysis: the diffusion length l_D :

$$l_D = \sqrt{D_0\tau}, \quad (4.41)$$

wherein D_0 and τ stand for the molecular diffusion coefficient and the diffusion time scale, respectively; the length of the characteristic pore size scale, l_s ; and the dephasing length l_g :

$$l_g = \{D_0/(\gamma g)\}^{1/3}, \quad (4.42)$$

wherein γ is the gyromagnetic ratio and g denotes the internal magnetic field gradient.

The shortest among these three lengths, considering their order of magnitude, determines which asymptotic regime applies. In practice, due to diffusive coupling between pores and variations in local magnetic susceptibility contrast, it is common for two of these lengths to be of the same order. In this case, considering the relatively large pore size scale of the fabricated samples used in this work (see Figure 4.6), it is expected that l_D and l_g would be competing for the governing asymptotic regime.

The calculation of l_g , however, is not straightforward considering that internal gradients have a spatial profile and the dephasing length will, in fact, depend on the effective field gradient, which for the one-dimensional case can be expressed as $l_g(z) = \{D_0/(\gamma g_{\text{eff}}(z))\}^{1/3}$.

Assuming the hypothesis proposed by Brown and Fantazzini [130] that the total variation in the local field is effectively bounded by $\Delta\chi B_0$, wherein $\Delta\chi$ and B_0 represent the susceptibility contrast and the static magnetic field values, respectively, allows the estimate of an upper limit for the effective gradient (g_{max}) and consequently for the definition of the relevant length scale expressed in Equation (3.3) of Chapter 3:

$$l^* = \left(\frac{D_0}{\gamma \Delta\chi B_0} \right)^{1/2}. \quad (4.43)$$

The calculated value for l^* considering the result of the magnetic susceptibility measures performed in the fabricated samples using a Vibrating Sample Magnetometer (Quantum Design PPMS) is $l^* \approx 70\mu m$. Notwithstanding, during the diffusion time range investigated (from 3 to 60ms), l_D values are expected to range from about 1 and $8\mu m$, approximately, which is almost one order of magnitude smaller than l^* .

The case wherein l_D is the shortest length scale among the three defines the so-called short-time diffusion regime. In this regime the contribution of the background term $A_b(t_e)$ in the signal attenuation due to diffusion (Equation (4.33)), becomes a normalization constant, in the sense that it reduces the total signal amplitude in the same way for all the points in the gradient strength array (a positive feature of time-independent acquisition) and does not alter the analysis of the experimentally observed spin echo attenuation.

It is worth noticing that the validity of this approximation also relies on two assumptions: the first being the Gaussian behavior assumed for the diffusion propagator, which was investigated and discussed on the analysis of data in Figures 4.9 to 4.12. The second one regards the hypothesis that the probed background gradient g , associated in this case with internal field gradients originated due to susceptibility contrast, can be assumed constant during the experiment time scale, which in the authors opinion, given the short duration of the encoding, decoding and storage periods adopted, is also a reasonable approximation.

Hence, considering the estimates for the relevant length scales previously mentioned and the adopted experimental conditions, it is not believed that the analysis of the effective self-diffusion coefficients presented in this work was, in this case, compromised by virtue of being performed in high-field conditions. In fact, the use of bipolar PGSTE sequences in an electronically-robust high-field equipment permitted the application of sufficiently strong, yet short, gradient pulses allowing the observation of signal decays due to diffusion during considerably small diffusion times, without violating important conditions such as the narrow-pulse approximation (NPA).

4.6 Concluding Remarks

Time-dependent diffusion coefficients measured by PFG NMR can be used to characterize drainage experiments, providing valuable information on the individual phases and post drainage fluid conformation. Pre drainage PFG measurements in water-saturated samples were used to extract confinement features, and estimates of samples surface-to-volume ratio and permeability values, carried from PFG data analysis, were shown to be in fair agreement with analytical and reported results, respectively. The short-time analyses of time-dependent diffusion coefficients obtained from PFG measurements can be used to

characterize the increase in surface-to-volume ratio probed by the wetting phase after drainage.

Wetting and non-wetting phase time-dependent diffusion coefficients, extracted from PFG NMR experiments, can be analyzed to infer dynamics of single phases and to portray post drainage fluids conformation scenarios. The case where non-wetting phase was considered to exhibit a poorly connected geometry was analyzed assuming a restricted diffusion process and the formation of an oil-in-water distribution of droplets within pores, and PFG signal attenuation was used to determine a Gaussian distribution of oil-in-water droplets radii.

Analyses of post drainage PFG measurements were performed using simple bi-Gaussian models. Although the presented analysis required a particular set of approximations regarding self-diffusion regimes and diffusion propagators that are, nevertheless, common in the analysis of PFG NMR measurements in confined systems, data behavior itself can be used to check the regime in which said approximations become valid, so to ensure a proper interpretation of raw data and better estimations of the involved parameters.

Next steps for this work regard the application of the two dimensional D - T_2 NMR technique to the characterization of water- and oil-saturated porous samples under the framework of restricted diffusion and short-time analysis, in low-field conditions. In addition to the extra available information brought by the second (relaxation) kernel to the description of system's dynamics, data analysis is also greatly benefited from the mathematical standpoint. The inclusion of a CPMG protocol at the end of the initial PFG pulse sequence can be used to ensure that the measured signal decay will in fact reach the noise level, minimizing the influence of non-zero baseline offsets on data processing, especially for the case of short diffusion time data sets, wherein signal attenuation due to diffusion can be considerably small.

These new experiments are been designed to be performed on a bench-top low-field NMR equipment, allowing not only the use of larger samples on the experimental setup but also minimizing the influence of diffusion through magnetic field gradients induced by susceptibility contrast on signal decay.

Chapter 5

Applications in Progress and Future Works: Singlet States as a Tool for the Determination of Diffusive Tortuosity

5.1 Singlet States and Long-Lived Spin Order

As discussed in Chapter 2 relaxation relates to the establishment of a thermal equilibrium between a disturbed spin system and its environment. Roughly, these processes may be represented by the time constants T_1 and T_2 , and for most NMR experiments the accessible life time of a disturbed spins system is limited by a time of the order of $\sim 5T_1$, after which the spin-state populations recover their equilibrium configuration and the transverse magnetization coherence is completely lost. Spin systems wherein relaxation times can be substantially increased are known, such as spin-state isomers orthohydrogen and parahydrogen in dihydrogen gas samples [153], even though these experiments are considered an exception and are not regarded as usual NMR experiments performed in ordinary systems.

A new technique entitled “*Singlet-Assisted NMR*” was presented in 2004 [74, 75] wherein special molecules containing pairs of coupled spin-1/2 nuclei displayed long-lived nuclear spin order and relaxation times of orders of magnitude above their usual longitudinal relaxation time. Such long-lived states may be exploited in a variety of NMR experiments, including diffusion NMR [79].

In this Chapter we present the theoretical and experimental concepts regarding singlet-

assisted NMR experiments and discuss their applicability to diffusion studies of confined fluids under the framework of long-time diffusion regime, jointly to the presentation of initial experimental developments. In this Section the quantum mechanical description of NMR is necessary to present the technique's theoretical background, and it will be resorted accordingly. An enlightening presentation of the NMR quantum mechanical concepts, especially on what regards the theory of pairs of coupled spins, can be found in the book “*Spin Dynamics: Basics of Nuclear Magnetic Resonance*”, by Malcolm H. Levitt [76].

The bold notation \mathbf{A} will be resorted in this Chapter to denote the quantum operator related to the physical observable A , and the symbol ρ will be used to represent the density operator.

5.1.1 Coupled Spin-1/2 Systems: Singlets and Triplets

Initially, let us consider a homonuclear system composed by two coupled spin-1/2 nuclei, whose spin operators are denoted by \mathbf{I}_1 and \mathbf{I}_2 . Each isolated spin with quantum number I exhibits $2I + 1$ possible Zeeman states and any spin state may be represented as a superposition of these $2I + 1$ states, which for $I = 1/2$ spins can be denoted by the kets $|\alpha\rangle$ and $|\beta\rangle$, wherein α denotes a state with angular momentum of $+\frac{1}{2}\hbar$ along the direction of the applied magnetic field and β denotes a state with angular momentum of $-\frac{1}{2}\hbar$ in the opposite direction. Here the Dirac's bracket notation $|\psi\rangle$ is been used to denote the spin state ψ . For the case of a pair of two coupled spins-1/2 any spin state can be written as a combination of the four Zeeman product states $|\alpha\alpha\rangle$, $|\alpha\beta\rangle$, $|\beta\alpha\rangle$ and $|\beta\beta\rangle$ [76].

In particular, the Zeeman product states of the coupled spin pair may be combined to construct one singlet and three triplet states, defined as:

$$\begin{aligned} |S_0\rangle &= \frac{1}{\sqrt{2}}(|\alpha\beta\rangle - |\beta\alpha\rangle) \\ |T_{+1}\rangle &= |\alpha\alpha\rangle \\ |T_0\rangle &= \frac{1}{\sqrt{2}}(|\alpha\beta\rangle + |\beta\alpha\rangle) \\ |T_{-1}\rangle &= |\beta\beta\rangle, \end{aligned} \tag{5.1}$$

wherein $|S_0\rangle$ denotes the singlet state and $|T_{+1}\rangle$, $|T_0\rangle$ and $|T_{-1}\rangle$ represent the three states of the triplet manifold. The singlet state exhibits a total nuclear spin $I = 0$ according to the eigenequations [81]:

$$\begin{aligned} \mathbf{I}^2|S_0\rangle &= 0 \\ \mathbf{I}_z|S_0\rangle &= 0, \end{aligned} \tag{5.2}$$

wherein the spin operator \mathbf{I}^2 is defined as $\mathbf{I}^2 = \mathbf{I}_x^2 + \mathbf{I}_y^2 + \mathbf{I}_z^2$ and $\mathbf{I}_\mu = \mathbf{I}_{1\mu} + \mathbf{I}_{2\mu}$, with

$\mu \in \{x, y, z\}$. Thus, the singlet state is often referred to as a non-magnetic state. The same, however, does not occur to the triplet manifold states $|T_M\rangle$, which in this case behave as the three states of a spin-1 particle:

$$\begin{aligned} \mathbf{I}^2|T_M\rangle &= 2|T_M\rangle \\ \mathbf{I}_z|T_M\rangle &= M|T_M\rangle, \end{aligned} \tag{5.3}$$

in which $M \in \{-1, 0, +1\}$.

5.1.2 Singlets in Magnetically Equivalent Environments

Considering the case wherein the two coupled spins-1/2 are in a magnetically equivalent environment (as an example, the protons in a water molecule), the eigenstates of the nuclear spin Hamiltonian are given by the singlet and triplet states. Let us consider that the nuclear spin Hamiltonian is given by:

$$\mathcal{H} = \omega_0 \mathbf{I}_z + 2\pi J \mathbf{I}_1 \cdot \mathbf{I}_2, \tag{5.4}$$

wherein ω_0 is the imposed Larmor frequency ($\omega_0 = \gamma B_0$), J denotes the coupling constant and $\mathbf{I}_1 \cdot \mathbf{I}_2$ represents the inner product between \mathbf{I}_1 and \mathbf{I}_2 . Using the eigenstate basis composed by the singlet and the three triplet manifold states in Equation 5.1, the nuclear spin Hamiltonian may be written in its matrix form as:

$$\mathcal{H} = \begin{pmatrix} |S_0\rangle & |T_{+1}\rangle & |T_0\rangle & |T_{-1}\rangle \\ -\frac{3}{2}\pi J & 0 & 0 & 0 \\ 0 & \omega_0 + \frac{1}{2}\pi J & 0 & 0 \\ 0 & 0 & \frac{1}{2}\pi J & 0 \\ 0 & 0 & 0 & -\omega_0 + \frac{1}{2}\pi J \end{pmatrix}. \tag{5.5}$$

Singlet states act as non-magnetic particles (Equation (5.2)) and hence do not give rise to a NMR signal. In the case of a water molecule, as an example, the observable NMR signal arises exclusively from the transitions between the triplet manifold states (Figure 5.1), and a measurement of T_1 in this case reflects a property of triplet states only.

The transitions between populations of the singlet and the central triplet states are in fact the key for one to comprehend the practical advantage on the applicability of singlet states. Roughly these transitions depend on the exchange symmetry of both the involved spin states and the transition mechanism itself. The triplet manifold spin states

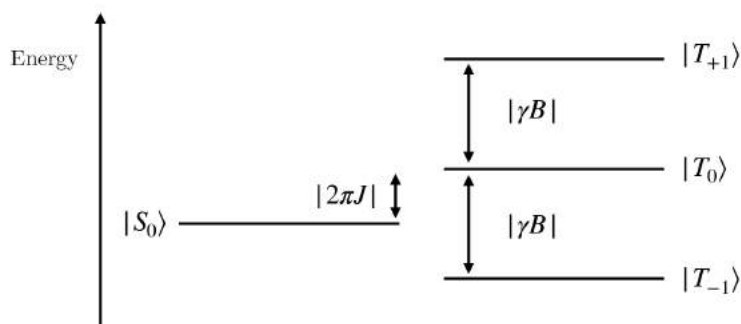


Figure 5.1: Representation of the energy levels for the singlet and triplet states, which in this case compose the base that diagonalizes the Hamiltonian in Equation 5.4. This representation considers a system of coupled spins in a magnetically equivalent environment, assuming the case wherein $\gamma > 0$ and $J > 0$.

are referred to as *exchange symmetric* states, in the sense that the exchange of spin 1 and 2 in Equation (5.1) does not alter the final triplet states. Under the same logic - or spin exchange - the singlet state is referred to as an *exchange antisymmetric* state. Transitions between spin populations of two symmetric states, such as the transitions between $|T_{+1}\rangle$ and $|T_{-1}\rangle$ states, characterized by the longitudinal relaxation time-scale T_1 , can only be mediated by an exchange symmetric mechanism (Figure 5.2). Notwithstanding, transitions between an antisymmetric and a symmetric state, as the one between populations of the singlet $|S_0\rangle$ and the $|T_0\rangle$ triplet states, in this case characterized by a time-scale T_s , can only occur mediated by an exchange antisymmetric mechanism [76].

The main reason why T_s happens to be much longer than T_1 relies on the fact that many strong relaxation mechanisms, such as the dipole-dipole coupling between the nuclei, are in fact symmetric, and even though they may be the dominant relaxation mechanism for T_1 , they will not contribute to T_s . Usually, a relaxation mechanism can only promote singlet – triplet transitions if it acts differently in each nuclear spin. This logic holds to any molecule that contains a pair of magnetic nuclei. Since the singlet state does not give rise to an NMR signal, the secret for one to exploit such state is in magnetic inequivalence.

5.1.3 Singlets in Magnetically Inequivalent Environments

Let us consider now the case wherein each spin in the coupled spin pair is in a different chemical environment, *i.e.*, it experiences a different chemical shift. The new Hamiltonian in this case may be written as:

$$\mathcal{H} = \omega_0(1 + \delta_1)\mathbf{I}_{1z} + \omega_0(1 + \delta_2)\mathbf{I}_{2z} + 2\pi J\mathbf{I}_1 \cdot \mathbf{I}_2, \quad (5.6)$$

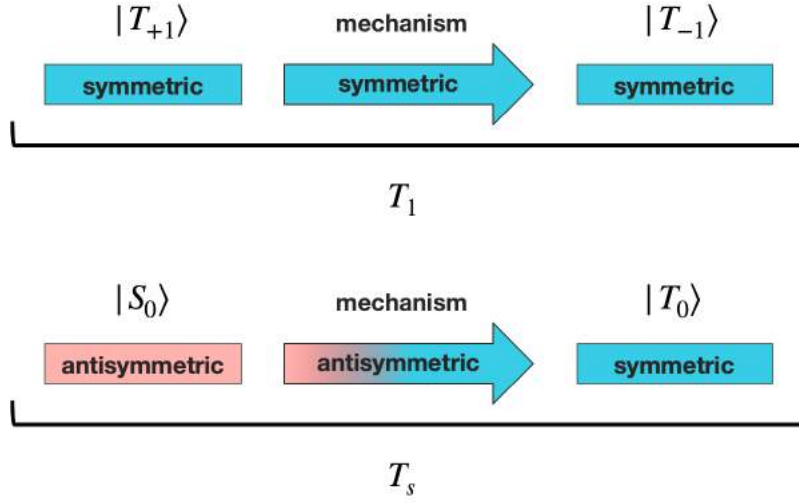


Figure 5.2: Illustration of the exchange mechanisms relating to transitions between two exchange symmetric spin states (upper scheme) and between an exchange antisymmetric and an exchange symmetric state (lower scheme).

wherein δ_1 and δ_2 denotes the chemical shifts of spins 1 and 2 respectively. The matrix representation of the new Hamiltonian, considering the same basis composed by the singlet and the triplet states, is expressed as:

$$\mathcal{H} = \begin{pmatrix}
 & |S_0\rangle & |T_{+1}\rangle & |T_0\rangle & |T_{-1}\rangle \\
 \begin{pmatrix} -\frac{3}{2}\pi J \\ 0 \\ \frac{1}{2}\omega_0\Delta\delta \\ 0 \end{pmatrix} & & \begin{pmatrix} 0 \\ \omega_0(1 + \frac{1}{2}\sum\delta) + \frac{1}{2}\pi J \\ 0 \\ 0 \end{pmatrix} & \begin{pmatrix} \frac{1}{2}\omega_0\Delta\delta \\ 0 \\ \frac{1}{2}\pi J \\ 0 \end{pmatrix} & \begin{pmatrix} 0 \\ 0 \\ 0 \\ -\omega_0(1 + \frac{1}{2}\sum\delta) + \frac{1}{2}\pi J \end{pmatrix} \\
 & & & &
 \end{pmatrix}, \quad (5.7)$$

in which,

$$\begin{aligned}
 \sum\delta &= \delta_1 + \delta_2, \\
 \Delta\delta &= \delta_1 - \delta_2.
 \end{aligned} \quad (5.8)$$

In a magnetically inequivalent environment the basis vector set $\{|S_0\rangle, |T_{+1}\rangle, |T_0\rangle, |T_{-1}\rangle\}$ is no longer the set of eigenvectors of the Hamiltonian. On what regards the relaxation of the spin system, the small difference in chemical environments on the case of a magnetically inequivalent spin pair it is not expected to strongly influence the fluctuation of microscopic fields, in a fair approximation [77]. This means that, on what concerns relaxation, the

singlet state $|S_0\rangle$ was expected to be long-lived independently of the system's magnetic equivalency, which is not observed in practice.

The explanation for such effect relies on the two off-diagonal terms $\frac{1}{2}\omega_0\Delta\delta$ on the right-side of Equation (5.7) connecting the singlet and the central triplet states. These terms actually represent that transitions occurring between the $|S_0\rangle$ and the $|T_0\rangle$ states are induced proportionally to the chemical shift difference $\omega_0\Delta\delta$ between both nuclei. Let us perform a quick estimate: consider a system composed by homonuclear coupled spin-1/2 pairs, in a magnetic inequivalent environment with a chemical shift difference of 1ppm, under the action of a 500 MHz static magnetic field, as the one used in the works presented in this thesis. Even though for this system the singlet state $|S_0\rangle$ is expected to be long-lived, transitions between the singlet and the central triplet state $|T_0\rangle$ are complete within 2 ms, after which the relaxation proceeds as usual, with the balancing between triplet states populations, governed by T_1 . In this case the immunity of singlet states to strong relaxation mechanisms is not observed simply due to the fast transitions induced by the chemical shift difference in inequivalent sites.

That is to say, the singlet state long-lived order can not be observed in magnetically equivalent environments because it does not give rise to an NMR signal and is obscured in magnetically inequivalent environments due to fast transitions induced by the chemical shift difference. The success on the application of singlet-assisted NMR techniques in fact relies on the use of experimental approaches for the suppression of the chemical shift difference term, by “switching” the magnetic inequivalence on and off. Two of the most common procedures adopted are:

- *Field cycling or low-field evolution:* in this approach the static magnetic field is reduced to a sufficiently low value after the preparation of singlet states in high-field conditions, in order to suppress the chemical shift difference between nuclei. Considering that high magnetic fields are often produced by superconducting magnets, which can not be switched on and off, this procedure requires an instrumental setup allowing a sufficiently fast transportation of the sample through high- and low-field conditions, on demand.
- *Radiofrequency spin-locking:* a resonant RF field is applied to temporally suppress the chemical shift difference between the nuclei after the singlet state is populated. This procedure has the practical advantage that RF pulses can be rapidly switched on and off in high-field spectrometers and does not require the transportation of the sample to low-field conditions.

Other not so common chemical shift suppression methods relate to the use of heteronuclear symmetry switching techniques or chemical reactions [77].

Generally, singlet-assisted NMR sequences can also be divided into 3 steps: initially, it is necessary to create and overpopulate the singlet state, starting from the initial Zeeman states (Equation (5.1)). This stage is usually referred to as the magnetization-to-singlet (M2S) or preparation stage. After the singlet state energy level is overpopulated it is necessary to prevent the transitions between the singlet and the central triplet states in order for the long-lived character of singlet states to be observed. The last step is responsible for converting singlet states back to observable magnetization (Zeeman states), usually referred to as the singlet-to-magnetization (S2M) or reading stage.

Depending on the technique chosen to suppress the singlet-triplet transitions, several distinct experimental setups and pulse sequences for the preparation, storage and observation of singlet long-lived spin order may be employed. Our initial developments with singlet-assisted NMR were based in the radiofrequency spin-locking technique, whose details are presented in the following Sections.

5.1.4 High-Field Radiofrequency Spin-Locking

Singlet State Preparation by Zero-Quantum Coherence

The first stage of singlet-assisted NMR, right before the application of a spin-locking technique, relates to the preparation of a density operator ρ containing a singlet population $|S_0\rangle\langle S_0|$, which may be expressed using Cartesian operators as [76]:

$$\begin{aligned} |S_0\rangle\langle S_0| &= \frac{1}{2}(|\alpha\beta\rangle - |\beta\alpha\rangle)(\langle\alpha\beta| - \langle\beta\alpha|) \\ &= \frac{1}{2}(|\alpha\beta\rangle\langle\alpha\beta| - |\beta\alpha\rangle\langle\alpha\beta| - |\alpha\beta\rangle\langle\beta\alpha| + |\beta\alpha\rangle\langle\beta\alpha|), \end{aligned} \quad (5.9)$$

wherein using the definition of raising and lowering operators:

$$\begin{aligned} \mathbf{I}^+ &= \mathbf{I}_x + i\mathbf{I}_y \\ \mathbf{I}^- &= \mathbf{I}_x - i\mathbf{I}_y, \end{aligned} \quad (5.10)$$

leads to:

$$\begin{aligned} |S_0\rangle\langle S_0| &= \frac{1}{2}(\mathbf{I}_1^\alpha \mathbf{I}_2^\beta - \mathbf{I}_1^+ \mathbf{I}_2^- - \mathbf{I}_1^- \mathbf{I}_2^+ + \mathbf{I}_1^\beta \mathbf{I}_2^\alpha) \\ &= -\frac{1}{2}(\mathbf{I}_1^+ \mathbf{I}_2^- + \mathbf{I}_1^- \mathbf{I}_2^+) - \mathbf{I}_{1z} \mathbf{I}_{2z} + \frac{1}{4} \mathbf{1}. \end{aligned} \quad (5.11)$$

The projection (or polarization) operators \mathbf{I}^α and \mathbf{I}^β are defined as [76]:

$$\begin{aligned} \mathbf{I}^\alpha &= \frac{1}{2} \mathbf{1} + \mathbf{I}_z \\ \mathbf{I}^\beta &= \frac{1}{2} \mathbf{1} - \mathbf{I}_z \end{aligned} \quad (5.12)$$

with,

$$\begin{aligned} \mathbf{I}^\alpha|\alpha\rangle &= |\alpha\rangle, & \mathbf{I}^\beta|\alpha\rangle &= 0, \\ \mathbf{I}^\alpha|\beta\rangle &= 0, & \mathbf{I}^\beta|\beta\rangle &= |\beta\rangle. \end{aligned} \quad (5.13)$$

In order to evaluate the result expressed in Equation (5.11) it is important to recall the meaning of multiple-quantum (MQ) coherence in NMR. The coherence definition is based on the expression of the time-dependent wave function $|\Psi(t)\rangle$ of the system as a summation of stationary basis function $|i\rangle$:

$$|\Psi(t)\rangle = \sum_{i=1}^n c_i(t)|i\rangle, \quad (5.14)$$

wherein $c_i(t)$ denotes the time-dependent coefficients and n is the dimension of the considered Hilbert space. There will be a coherence between any two states $|p\rangle$ and $|q\rangle$ when the ensemble average of the product of coefficients $\rho_{pq}(t)$, defined as the density matrix element:

$$\rho_{pq}(t) = \overline{c_p(t)c_q^*(t)}, \quad (5.15)$$

is non-vanishing [3, 76].

The order of the coherence is determined by the difference between the magnetic quantum numbers $\Delta m_{pq} = m_p - m_q$, according to the split in energy levels due to the Zeeman interaction in the presence of a polarizing magnetic field (Figure 2.1). An important coherence is the single-quantum (SQ) coherence ($\Delta m_{pq} = \pm 1$) - which can be excited by a simple $\pi/2$ pulse - as it corresponds to the observable NMR signal (or transverse magnetization) induced into the detection coil. A coherence which can be directly detected as a NMR signal, such as the SQ coherence, is often referred to as an “allowed” coherence and the ones which can not be directly detected are referred to as “forbidden”. For the case of an isolated spin $I = 1/2$ this “allowed” coherence relates to the transitions between the $|\alpha\rangle$ and $|\beta\rangle$ (up and down) spin states.

Let us consider once more the case of a system composed by two homonuclear spin-1/2 coupled nuclei, whose energy split between the singlet and the triplet manifold states is represented in Figure 5.1. In this case, the density operator ρ , depending on the wave function $|\Psi(t)\rangle$, can be expressed as a summation of several product operator terms, such as the one expressed in Equation (5.15). Consider the following random density operator:

$$\rho = c_1 \mathbf{1} + c_2 \mathbf{I}_{1z} + c_3 2\mathbf{I}_{1x}\mathbf{I}_{2y} + \dots, \quad (5.16)$$

wherein c_1 , c_2 and c_3 are real numbers. Each term composing the density operator implies

a certain configuration for the populations and coherences. Let us assume, as an example, the matrix form of the operator \mathbf{I}_{1z} :

$$\mathbf{I}_{1z} = \frac{1}{2} \begin{pmatrix} & |\alpha\alpha\rangle & |\alpha\beta\rangle & |\beta\alpha\rangle & |\beta\beta\rangle \\ \begin{pmatrix} 1 & 0 & 0 & 0 \\ 0 & 1 & 0 & 0 \\ 0 & 0 & -1 & 0 \\ 0 & 0 & 0 & -1 \end{pmatrix} \end{pmatrix}. \quad (5.17)$$

If the density operator ρ contains a positive \mathbf{I}_{1z} term it means that the populations of $|\beta\alpha\rangle$ and $|\beta\beta\rangle$ states are depleted with respect to the populations of the $|\alpha\alpha\rangle$ and the $|\alpha\beta\rangle$ states, indicating a population differential across the single-quantum transitions ($\Delta m_{pq} = \pm 1$) of spin \mathbf{I}_1 .

The operator $2\mathbf{I}_{1x}\mathbf{I}_{2y}$ is represented in its matrix form as:

$$2\mathbf{I}_{1x}\mathbf{I}_{2y} = \frac{1}{2i} \begin{pmatrix} & |\alpha\alpha\rangle & |\alpha\beta\rangle & |\beta\alpha\rangle & |\beta\beta\rangle \\ \begin{pmatrix} 0 & 0 & 0 & 1 \\ 0 & 0 & -1 & 0 \\ 0 & 1 & 0 & 0 \\ -1 & 0 & 0 & 0 \end{pmatrix} \end{pmatrix}. \quad (5.18)$$

The presence of a $2\mathbf{I}_{1x}\mathbf{I}_{2y}$ term in the expression of ρ indicates that there are zero- (ZQ) and double-quantum (DQ) coherences in the spin ensemble. Differently from the single-quantum coherence, the double- and the zero-quantum coherences do not induce a NMR signal. Notwithstanding, as discussed previously, these coherences are very important as both can be converted into single-quantum coherence, which do induce a NMR signal, through the application of suitable RF pulse sequences, which will be detailed in the following Sections.

Analyzing the expression obtained for the $|S_0\rangle\langle S_0|$ term in the last line of Equation (5.11) it is possible to notice that a singlet population may be constructed by the excitation of zero-quantum coherence (first term on the right-side) and/or longitudinal spin order (second term on the right-side). The search for optimized protocols for the conversion of Zeeman states into singlet states, on what regards the conversion efficiency, was addressed in the work of Sørensen and Levitt [154, 155]. In this work, the zero-quantum method

applied by Carravetta [75] was chosen for the creation of singlet states, whose pulse sequence goes as follows:

$$90_0 - \tau_1 - 180_0 - (\tau_1 + \tau_2) - 90_{90} - \tau_2, \quad (5.19)$$

in which the carrier frequency is set to the mean of the two chemical shifts and the notation β_ϕ indicates a strong, non-selective pulse, with flip angle β and phase ϕ . The delays τ_1 and τ_2 are given by:

$$\begin{aligned} \tau_1 &= \frac{1}{4J} \\ \tau_2 &= \frac{\pi}{2|\gamma B \Delta \delta|}, \end{aligned} \quad (5.20)$$

wherein $\Delta\delta$ denotes the chemical shift difference expressed in Equation (5.8).

Assuming that the investigated 2-spin-1/2 system is weakly coupled, *i.e.* the chemical shift difference is much greater than the coupling constant J :

$$|\gamma B \Delta \delta| \gg |\pi J|, \quad (5.21)$$

the effect of the pulse sequence in Equation (5.19) goes as follows: the first $\pi/2$ pulse transforms \mathbf{I}_z into $-\mathbf{I}_y$. The subsequent spin echo interval $\tau_1 - 180_0 - \tau_1$ performs the following transformation:

$$-\mathbf{I}_y \xrightarrow{\tau_1 - 180_0 - \tau_1} -2\mathbf{I}_{1x}\mathbf{I}_{2z} - 2\mathbf{I}_{1z}\mathbf{I}_{2x}. \quad (5.22)$$

After the spin echo step an isotropic evolution takes place during the time interval τ_2 . Considering that τ_2 is usually a relatively short period the simultaneous J -coupling evolution may be ignored [76, 77], and for a positive gyromagnetic ratio the components of the density operator evolve as:

$$-2\mathbf{I}_{1x}\mathbf{I}_{2z} - 2\mathbf{I}_{1z}\mathbf{I}_{2x} \xrightarrow{\tau_2} 2\mathbf{I}_{1y}\mathbf{I}_{2z} - 2\mathbf{I}_{1z}\mathbf{I}_{2y}, \quad (5.23)$$

and the zero-quantum coherence can be finally obtained after the last $\pi/2$ pulse:

$$2\mathbf{I}_{1y}\mathbf{I}_{2z} - 2\mathbf{I}_{1z}\mathbf{I}_{2y} \xrightarrow{90_0} 2\mathbf{I}_{1y}\mathbf{I}_{2x} - 2\mathbf{I}_{1x}\mathbf{I}_{2y} = -i(\mathbf{I}_1^+\mathbf{I}_2^- - \mathbf{I}_1^-\mathbf{I}_2^+), \quad (5.24)$$

even though the phase of the coherence is still not right. After the last time interval τ_2 the correct phase is obtained:

$$-i(\mathbf{I}_1^+\mathbf{I}_2^- - \mathbf{I}_1^-\mathbf{I}_2^+) \xrightarrow{\tau_2} -(\mathbf{I}_1^+\mathbf{I}_2^- + \mathbf{I}_1^-\mathbf{I}_2^+), \quad (5.25)$$

which can be rewritten as:

$$-(\mathbf{I}_1^+ \mathbf{I}_2^- + \mathbf{I}_1^- \mathbf{I}_2^+) = -|\alpha\beta\rangle\langle\beta\alpha| - |\beta\alpha\rangle\langle\alpha\beta| = |S_0\rangle\langle S_0| - |T_0\rangle\langle T_0|. \quad (5.26)$$

It is worth noticing that the result obtained in Equation (5.26) depends directly on the carrier frequency to be centered at the mean of the two chemical-shifts, which implies that both chemical shifts must be known.

Radio-frequency Spin-Locking

The next step following the population of the singlet state comprises a spin-locking method for the suppression of the chemical shift difference, according to the average Hamiltonian theory ¹ [156]. The role of the spin-locking is to sustain the singlet state during the entire storage period, which depending on the molecule employed and the desired application can be a time of the order of minutes. This brings up an immediate concern regarding the application of a continuous radiofrequency pulse, or a set of them, during a long period of time. In this case not only the amplifier's and probe's capabilities can easily be pushed further their limits on what regards operation power and duty cycle, but also during large pulsing cycles the sample is irradiated with a considerable large amount of power, which may lead to undesirable heating effects.

The characteristics of the spin-locking RF actually depend on both the chemical shifts of the coupled nuclei and the modulation scheme chosen for the spin-locking field. An *unmodulated* spin-locking scheme comprises the application of a continuous-wave field. Considering the RF frequency denoted by δ_{ref} , the resonance offset frequencies will be given by:

$$\begin{aligned} \Omega_1 &= 2\pi\gamma B(\delta_1 - \delta_{\text{ref}}), \\ \Omega_2 &= 2\pi\gamma B(\delta_2 - \delta_{\text{ref}}). \end{aligned} \quad (5.27)$$

Generally, a successful spin-locking using a CW field requires the condition:

$$|\omega_{\text{nut}}| \gg |\Omega_1|, |\Omega_2|, \quad (5.28)$$

wherein ω_{nut} represents the nutation frequency of the RF field.

In order to evaluate the effect of long spin-locking periods under the standpoint of the

¹The average Hamiltonian theory is a powerful tool for the analysis of the dynamics of nuclear spins in magnetic resonance experiments. The explicit form of such dynamics would require the solution of the Schrödinger equation for the spin system considering all contributions to the Hamiltonian from interactions of the spins with each other and their chemical environment, which are commonly both time-dependent and might not commute with each other. In average Hamiltonian theory the explicit time-dependent Hamiltonian is replaced by a time-independent effective Hamiltonian, which can be calculated up to a certain order by the use of proper expansion methods [156].

NMR instrument, let us consider once more the example of two coupled spin-1/2 nuclei with a chemical shift difference of 1 ppm in a 500 MHz polarizing field. In this case, assuming that the carrier frequency is set to the mean of the two chemical shifts, the offset frequencies will be $|\Omega_1/2\pi| = |\Omega_2/2\pi| = 250\text{Hz}$, and a reasonable spin-locking can be achieved using a nutation frequency of $\approx 1\text{kHz}$, which can be applied for times as large as one or two minutes without risk of hardware damage. Suppose now that the coupled spins at the extremities of the spectrum are separated by 10 ppm. In this case the offset frequencies will be ten times larger $\approx 2.5\text{kHz}$ and no effective spin-locking can be achieved without the application of a considerably large RF field and most probably some hardware damage and heating effects as well.

Another alternative for spin-locking schemes is the application of trains of broadband refocusing pulses, known as *modulated* or *decoupling* methods. During the initial tests with singlet spin-locking presented in this thesis the WALTZ-16 [157, 158] and the XY-16 [159] protocols were tested, and will be presented in details in Section 5.1.5. Assuming that after the preparation interval the singlet state is overpopulated with respect to the central triplet state, and that $\text{sign}(J) = \text{sign}(\gamma)$, the density operator before the spin-locking application may be approximated by [77]:

$$\mathcal{H} = \begin{array}{c} \begin{array}{cccc} |S_0\rangle & |T_{+1}\rangle & |T_0\rangle & |T_{-1}\rangle \end{array} \\ \left(\begin{array}{cccc} 1 + \mathcal{B} & 0 & 0 & 0 \\ 0 & 0 & 0 & 0 \\ 0 & 0 & 1 - \mathcal{B} & 0 \\ 0 & 0 & 0 & 0 \end{array} \right), \end{array} \quad (5.29)$$

wherein \mathcal{B} denotes the Boltzmann factor:

$$\mathcal{B} = \frac{\hbar\gamma B}{k_B T}. \quad (5.30)$$

During the spin-locking procedure, at short-times, the density operator evolves so that the populations of the triplet manifold states are balanced:

$$\mathcal{H} = \begin{array}{c} \begin{array}{cccc} |S_0\rangle & |T_{+1}\rangle & |T_0\rangle & |T_{-1}\rangle \end{array} \\ \left(\begin{array}{cccc} 1 + \mathcal{B} & 0 & 0 & 0 \\ 0 & 1 - \frac{1}{3}\mathcal{B} & 0 & 0 \\ 0 & 0 & 1 - \frac{1}{3}\mathcal{B} & 0 \\ 0 & 0 & 0 & 1 - \frac{1}{3}\mathcal{B} \end{array} \right). \end{array} \quad (5.31)$$

Over long times the singlet and triplet populations will be equalized due to the relaxation process associated with T_s , proportional to $\varepsilon = \exp(-t/T_s)$. At the end of the spin-locking stage the density operator may be described as:

$$\mathcal{H} = \begin{pmatrix} & |S_0\rangle & |T_{+1}\rangle & |T_0\rangle & |T_{-1}\rangle \\ \begin{matrix} 1 + \mathcal{B}\varepsilon \\ 0 \\ 0 \\ 0 \end{matrix} & & 0 & 0 & 0 \\ 0 & 1 - \frac{1}{3}\mathcal{B}\varepsilon & 0 & 0 & 0 \\ 0 & 0 & 1 - \frac{1}{3}\mathcal{B}\varepsilon & 0 & 0 \\ 0 & 0 & 0 & 0 & 1 - \frac{1}{3}\mathcal{B}\varepsilon \end{pmatrix}. \quad (5.32)$$

Singlet Detection

The observation of singlet states after the storage interval requires the conversion of singlet populations back to the observable Zeeman states, which can also be performed by distinct methods. The simplest one regards the application of a strong 90_0 pulse after a period τ_2 following the end of the spin-locking interval [77]. Most elaborate protocols were developed with the intention of suppressing undesirable T_1 relaxation artifacts at the detection stage, such as the one employed by Carravetta et al. [74]:

$$90_0 - (\tau_2 + \tau_1) - 180_{90} - \tau_1 - 90_{45}. \quad (5.33)$$

The calculation for the conversion of singlet state population into observable Zeeman states can be performed in a similar way as in Equations (5.22) to (5.26). Notwithstanding, the interesting feature about the protocol expressed in (5.33) regards the combined effect of the two $\pi/2$ pulses, considering that the interval $\tau_1 - 180_{90} - \tau_1$ relates solely to a spin echo step.

The relative 45 degree phase between two $\pi/2$ non-selective pulses separated by a τ_2 interval act as a single frequency-selective $\pi/2$ pulse. The resulting NMR spectra after the Fourier transform of the time-domain signal exhibits a characteristic anti-phase spectra at the position of the chemical shift δ_2 , while the NMR signals deriving from T_1 relaxation are seen separated at the chemical shift δ_1 [74]. The two separated doublets are typical from spin systems of the *AX* kind, in which the two protons are weakly coupled according to the condition expressed in Equation (5.21).

5.1.5 Sample Preparation and Experimental Setup

Experiments of ^1H inversion recovery (T_1), singlet-assisted relaxation (T_s) and singlet-assisted NMR spectroscopy were performed using a sample of 2,3-dibromothiophene diluted in dimethylsulfoxide- d_6 (DMSO- d_6) at a concentration of 20 mM. Figure 5.3 shows the molecular representation of the 2,3-dibromothiophene with the two weakly-coupled ^1H nuclei to compose the desired AX system. Singlet relaxation experiments were performed using the pulse sequence illustrated in Figure 5.4, for two distinct spin-locking protocols. All the experiments were performed in a Varian (Agilent) 500 MHz spectrometer using a 5mm probe.

The WALTZ-16 and the XY16 spin-locking pulse schemes are illustrated in Figure 5.5. The WALTZ-16 protocol can be understood as an evolution of the primitive dynamic decoupling protocol WALTZ-4. A curiosity for the music affectionate: the name is a direct reference to the waltz music, a form of classical dance music based on the $3/4$ time signature. In the original WALTZ-4 scheme a sequence of 3 pulses, 90° , 180° and 270° , also denoted 123 , is repeated 4 times (with the appropriate phase for each pulse), exactly as in the $3/4$ waltz time signature. The WALTZ-16 is a highly effective dynamic decoupling protocol which can also be employed as a spin-locking procedure [158].

The XY16 is also a dynamic decoupling protocol with high efficiency in correcting effects of pulse miscalibration [159]. It consists in a train of 16 π pulses with alternating phases, denoted by x , y , $-x$ and $-y$.

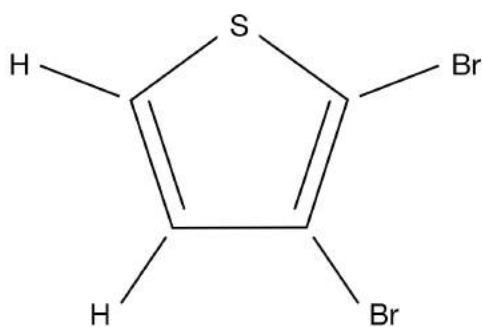


Figure 5.3: Representation of the 2,3-dibromothiophene molecule showing the two protons considered for the singlet-assisted NMR experiments to fulfill the homonuclear weak coupling condition of a spin- $1/2$ pair in a magnetically inequivalent environment.

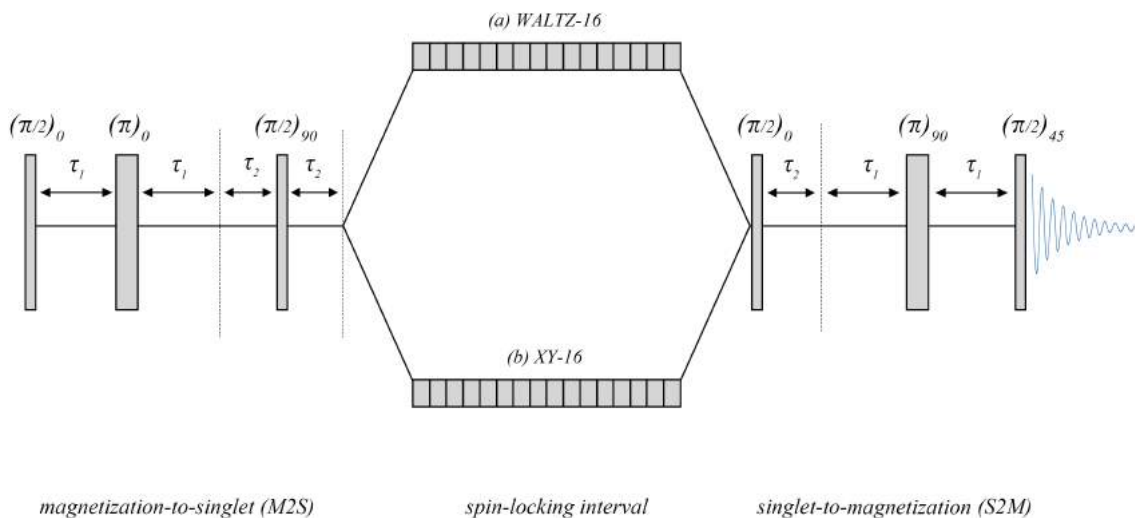


Figure 5.4: Illustration of the singlet-assisted NMR pulse sequence using the (a) WALTZ-16 and the (b) XY-16 spin-locking scheme. The conversion of Zeeman states into singlet states and back are illustrated in the M2S and S2M blocks, respectively. The storage interval, during which the T_s relaxation takes place, is denoted as the spin-locking interval.

5.1.6 Preliminary Results and Discussion

Figure 5.6 shows the characteristic anti-phase spectrum obtained for the sample of 2,3-dibromothiophene 20 mM, using the pulse sequence illustrated in Figure 5.4, with a single loop of the XY16 spin-locking scheme. The obtained spectra is in agreement with the results presented in Ref. [74], showing the anti-phase singlet peaks at the site of the δ_2 chemical shift and the peaks related to the signal from T_1 relaxation at the site of δ_1 . Figure 5.7 shows the inversion-recovery results for the 2,3-dibromothiophene sample and the T_1 values obtained considering the peaks of each chemical shift site. The values obtained for each chemical shift were $T_1(\delta_1) = 8.1 \pm 0.2$ s and $T_1(\delta_2) = 8.9 \pm 0.2$ s. Both values were considerably smaller than the T_1 values reported by Carravetta et al. [74] for this sample ($T_1 \approx 17$ s).

One possible reason for such discrepancy was the absence of a degassing step in the preparation stage in order to remove dissolved gas from the solution before the NMR measurements. The presence of dissolved oxygen is known as a strong relaxation mechanism in liquid state NMR [160]. Generally, the main mechanisms promoting proton T_1 relaxation are dipole-dipole interactions between protons, or between a proton and unpaired electrons. Dissolved molecular oxygen is a paramagnetic material which greatly contributes to increase relaxation. The freeze-pump-thawing method and sample bubbling with nitrogen are examples of procedures that can be performed to significantly reduce the dissolved content

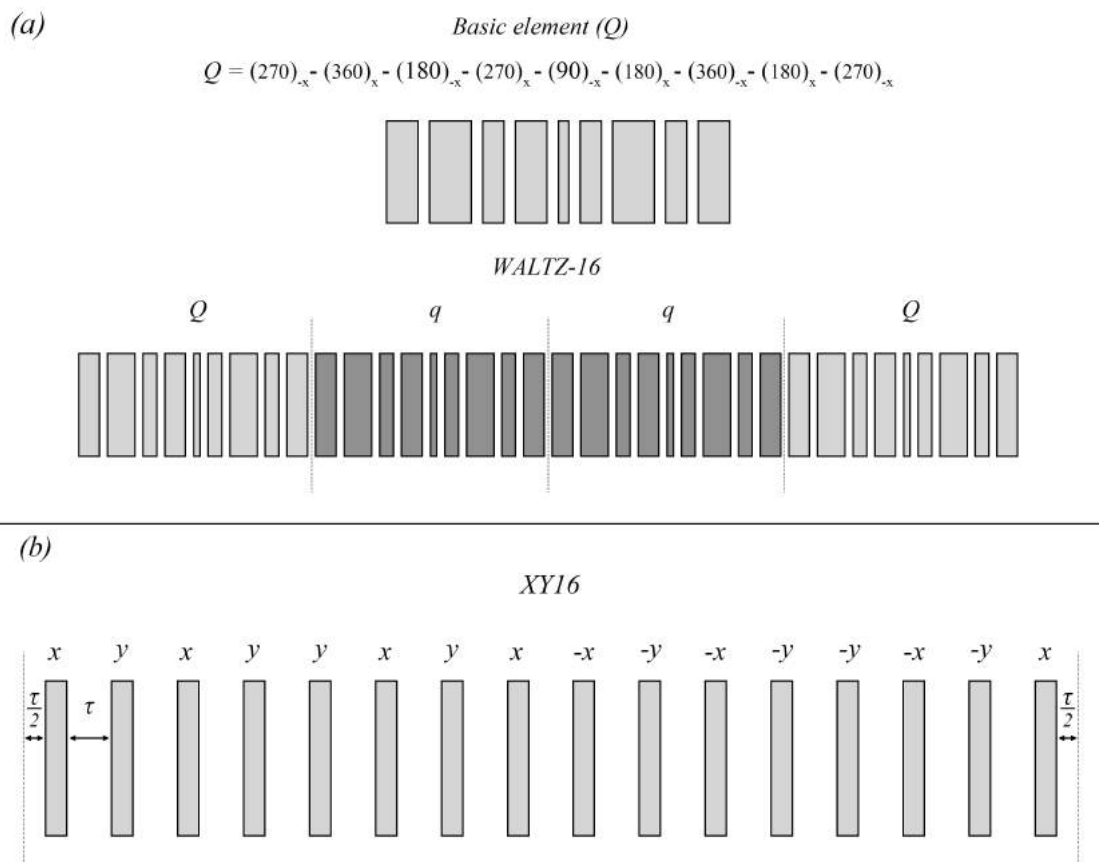


Figure 5.5: Illustration of the WALTZ-16 (a) and the XY-16 (b) spin-locking scheme. In the WALTZ-16 pulse sequence the pulse phases are denoted by x , y , $-x$ and $-y$. The lower case q denotes the same pulse block as in Q , but with the inverted pulse phases. In the XY16 sequence all the pulses have a 180° flip angle (π), with the respective phases also denoted by x , y , $-x$ and $-y$.

of oxygen in liquid samples, both of which are yet to be tested.

Figure 5.8 shows the singlet relaxation (T_s) results using the sequence illustrated in Figure 5.4 for five different storage times during the spin-locking interval. Both peaks of the anti-phase spectra were processed separately considering the exponential decay described in Equation (5.32). The peaks pertaining to the first spectra were discarded from the fit procedure in order to avoid the signal attenuation due to the balancing of triplet manifold populations over the short-time regime (Equation 5.31) on the analysis of the singlet relaxation [75].

Although the characteristic anti-phase peak was observed in all the acquisitions - a signature of weakly-coupled AX systems following the singlet detection sequence [74] - the measured time constant T_s for both peaks was no greater than the measured T_1 value

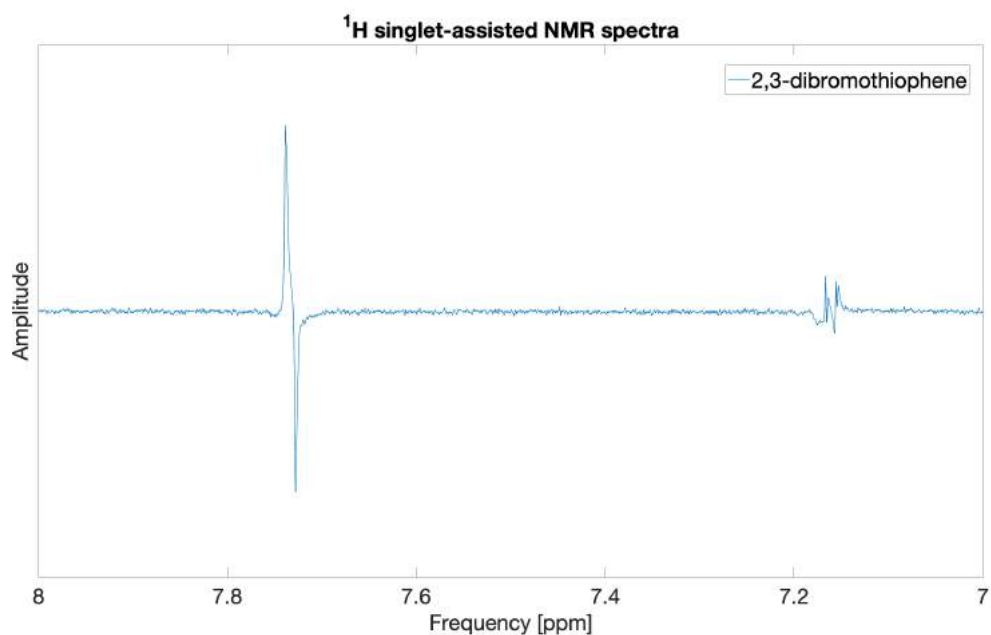


Figure 5.6: ¹H singlet-assisted NMR spectra of the 2,3-dibromothiophene solution (20mM in DMSO-d⁶). The characteristic anti-phase peak can be seen at the site of the chemical shift $\delta_2 \approx 7.72$ ppm.

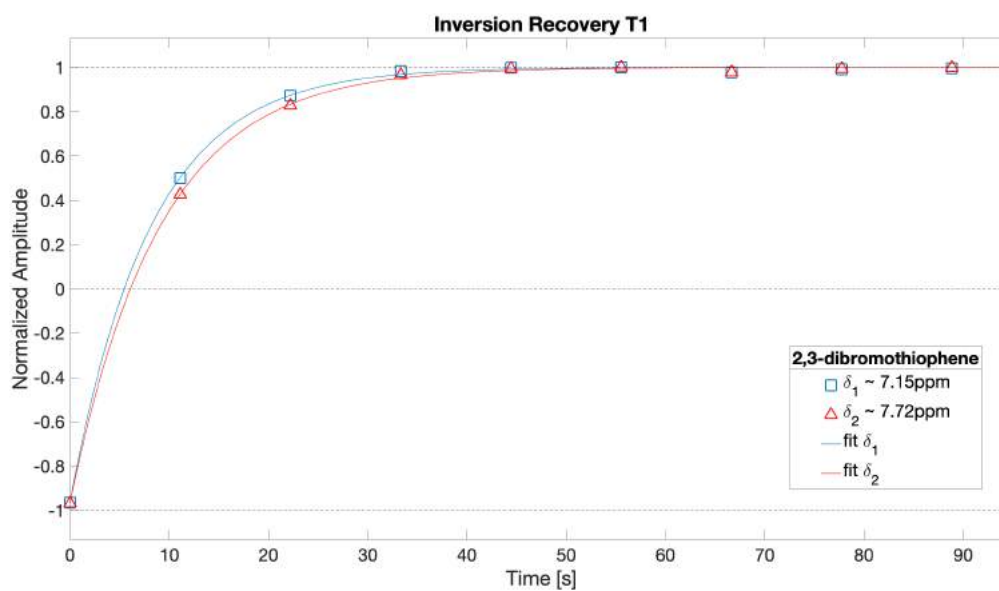


Figure 5.7: Inversion-recovery T_1 measurement of the 2,3-dibromothiophene solution (20mM in DMSO-d⁶). The values obtained for each chemical shift were $T_1(\delta_1) = 8.1 \pm 0.2$ s and $T_1(\delta_2) = 8.9 \pm 0.2$ s.

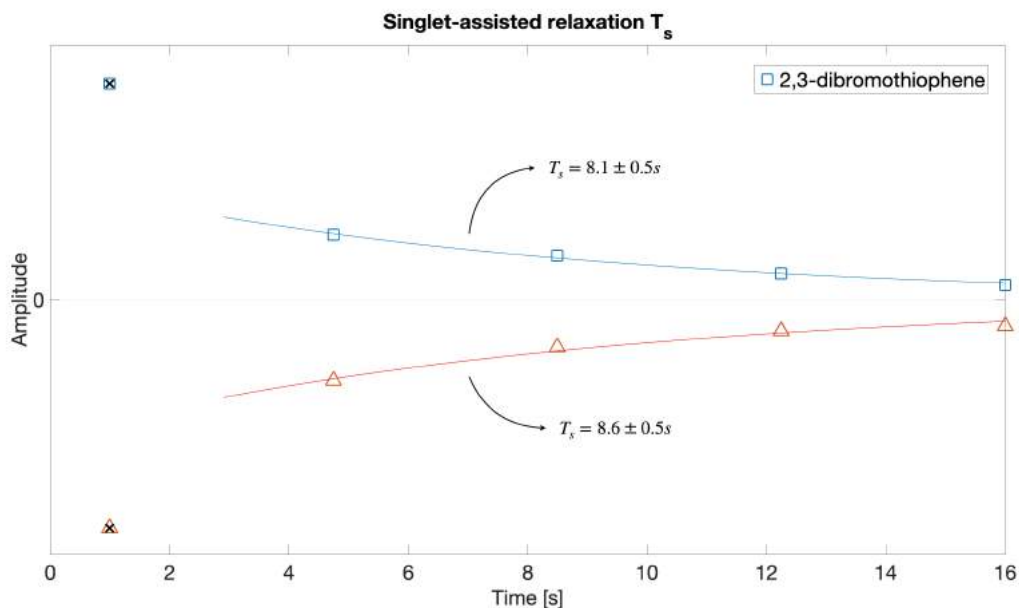


Figure 5.8: Singlet relaxation T_s of the 2,3-dibromothiophene solution (20mM in DMSO- d^6) obtained with the sequence illustrated in Figure 5.4, using the XY16 spin-locking protocol. The singlet relaxation time-constant T_s values obtained for each peak of the anti-phase spectra were $T_s = 8.1 \pm 0.5$ s and $T_s = 8.6 \pm 0.5$ s for the positive and the negative peaks, respectively. The cross markers denote the peaks which were excluded from the fit procedure (see text).

using a standard saturation recovery protocol, despite the spin-locking method adopted. The reasons why the long-lived behavior of singlet states could not be observed are still under investigation.

It is possible that the lack of a degassing stage in samples preparation somehow affected these initial results, as observed for the longitudinal relaxation measurements, even though it was reported that singlet states are between two to three times less sensitive to relaxation due to paramagnetic dissolved gas than conventional nuclear magnetization [160]. On what regards the storage interval, different power values were tested for both spin-locking methods within the safe duty cycle range of the employed instrument, with no success in surpassing the longitudinal relaxation time.

Nevertheless, it should be noticed that the initial decay observed in the singlet relaxation measurements, *i.e.*, the signal loss between the first and the second pairs of peaks, associated with the balancing between the populations of the triplet manifold states in short times, shows a significantly larger signal attenuation in comparison with previously reported results using [74, 75, 161, 162]. Such discrepancy could indicate two things: an inefficacy of the preparation stage, responsible for the overpopulation of singlet states with respect

to the central triplet state, or an inefficacy of the spin-locking procedure in suppressing the chemical shift difference between the coupled proton pair in a magnetically inequivalent environment, and consequently not preventing the transitions between the singlet and the triplet states from occurring over the short-time regime. This hypothesis would explain why the singlet relaxation times T_s observed are quite similar to the T_1 relaxation times measured in the usual longitudinal relaxation experiments. Notwithstanding, new experiments are yet to be performed in order to investigate this behavior. Different singlet preparation methods, as well as new spin-locking techniques will be tested.

5.2 Singlet-Assisted Diffusion NMR (SAD-NMR)

One important application of long-lived singlet states is the study of restricted molecular self-diffusion in the long-time regime. Although the use of time-independent acquisition PFG protocols, employed under a proper framework, allows the analysis of time-dependent diffusion coefficients disregards the effects of signal attenuation due to relaxation, most of the observable magnetization is lost due to relaxation effects much before the long-time diffusion regime can be achieved, especially for fluid molecules diffusing within porous media. In 2005, only one year after the first results with singlet relaxation experiments, Cavadini et al. [163] reported the method which would later be known as *Singlet-Assisted Diffusion NMR*, wherein the long-lived behavior of singlet states were combined with the pulsed-gradient encoding and decoding steps of a pulsed-field gradient (PFG) NMR diffusion experiment, allowing the observation of the behavior of molecules under restricted diffusion during the long-time regime.

In the years following the presentation of the technique several relevant works were published relating to the analysis of time-dependent self-diffusion coefficients of fluids undergoing restricted diffusion over the long-time regime, obtained with singlet-assisted diffusion techniques. Distinct applications can be cited such as the study of large molecules with slow diffusion coefficients [163–166], the analysis of diffusion-diffraction patterns in porous structures with larger characteristic distances [167, 168], magnetic resonance imaging with singlet-tagging localization [169, 170] or the determination of diffusive tortuosity in porous materials [79].

5.2.1 Diffusive Tortuosity and The Long-Time Diffusion Regime

Tortuosity can be seen as a tool on the onerous task of modeling fluid flow and transport properties in complex porous media, such as natural rocks. In these porous systems the path available for fluid flow is most often complex and tortuous, which prevents an exact

pore-scale modeling and forces the averaging of the microscopic conservation laws over a portion of the pore space which can be considered homogeneous. This approach inevitably rely on a set of coefficients - or parameters - which summarize an specific property of the porous geometry, such as permeability, diffusivity and electrical conductivity, and whose values can be determined experimentally.

The definition of tortuosity was proposed by Carman [171] as an attempt to match measured permeability values with theoretical predictions in a system composed by a bundle of capillary tubes. Tortuosity would later acquire distinct formulations depending on the physical property investigated [73], most often being defined as a geometry-related parameter, associated with hydraulic, electric or diffusive conductivity properties. Generally, tortuosity can be expressed as the ratio of the effective path length to the shortest path length in a porous medium. The relation between molecular self-diffusion and tortuosity comes from the association between molecular-self diffusion and the mean-squared displacement of diffusing molecules, discussed in Chapter 4 and expressed for the one-dimensional case by Equation (4.20):

$$\frac{d\mathcal{R}\{\Psi_s(G\delta, \Delta)\}}{d(\gamma G\delta)^2} = \frac{\langle z^2(\Delta) \rangle}{2} = \Delta D_{\text{eff}}(\Delta). \quad (5.34)$$

The mean squared displacement $\langle \vec{r}^2(t) \rangle$ can be defined as the second moment of the average propagator $\bar{P}(\vec{r}, t)$:

$$\langle \vec{r}^2(t) \rangle = \int_V \bar{P}(\vec{r}, t) \vec{r}^2 d\vec{r}. \quad (5.35)$$

Assuming the case wherein diffusion goes unrestricted, the averaged propagator is given by the 3D Gaussian function:

$$\bar{P}(\vec{r}, t) = \frac{1}{(\sqrt{4\pi Dt})^3} \exp\left(-\frac{(\vec{r}(t))^2}{4Dt}\right). \quad (5.36)$$

Solving Equation (5.35) for the 3D Gaussian propagator leads to the known Einstein relation:

$$\langle \vec{r}^2(t) \rangle = 6Dt. \quad (5.37)$$

which can be understood as an alternative definition for the self-diffusion coefficient [4, 96].

Nevertheless, as discussed in Chapter 4, when molecules experience restricted motion the diffusion coefficient exhibits a time dependence, and the relation between the mean-squared displacement and the effective diffusion coefficient becomes:

$$\langle \vec{r}^2(t) \rangle = 6D(t)t. \quad (5.38)$$

wherein $D(t)$ now represents an effective ($D_{\text{eff}}(\Delta)$) or apparent diffusion coefficient.

Due to restrictions imposed by the porous interface to molecular motion, $D(t)$ decreases in time from its initial (bulk) value D_0 , and molecular diffusion must be analyzed according to the specific diffusion regime, depending on the relation between the characteristic diffusion length and the confinement scale. The long-time diffusion regime may be expressed by the condition $\sqrt{D_0\Delta} \gg R_p$, wherein D_0 denotes the molecular (bulk) self-diffusion coefficient, Δ represents the diffusion time and R_p is a characteristic pore confinement scale.

Here, it is important to make a distinction between two different scenarios for the case of restricted diffusion in the long time asymptotics. The first one relates to porous systems composed by isolated pores. In this case, on the long time asymptotic, molecules will probe the available pore space as a whole and the magnetic field gradient will be averaged out. During this diffusion regime, referred to as a motional narrowing or averaging regime [131], the acquired magnetization phase of diffusing particles was also found to be approximately Gaussian [69]. As molecules probe the entire pore space the mean-squared displacement $\langle \bar{r}^2(t) \rangle$ is expected to saturate while the diffusion time Δ is increased. In this case the signal attenuation due to diffusion in the long time asymptotic can be used to estimate the characteristic confinement scale, as employed in the determination of a size distribution of oil droplets in Section 4.5.3.

For the case of systems where pores are well connected, or isolated pores are composed by permeable membranes, the porous geometry imposes barriers to molecular diffusion, but do not prevent molecules to reach new regions of the porous space. In this case, at long times, the time-dependent (or effective) diffusion coefficient D_{eff} is expected to reach a lower asymptotic value² D_∞ (or $D(\Delta \rightarrow \infty)$). [4, 33, 96, 135]. The ratio between the asymptotic effective diffusion coefficient at long times and its bulk value defines the property known as diffusive tortuosity τ_D :

$$\lim_{t \rightarrow \infty} \frac{D(t)}{D_0} = \frac{1}{\tau_D}. \quad (5.39)$$

The determination of diffusive tortuosity depends directly on the long-time condition for diffusion to be fulfilled, which requires in practice a porous media with small confinement scales, such as nanoporous materials [172, 173], and/or long diffusion times. The latter cannot be easily achieved in NMR experiments with confined fluids simply due to the fact that relaxation effects often destroy the observable magnetization much before the long time regime can be reached.

²Here, the cases of anomalous diffusion processes are not being considered.

Let us take as an example the samples described in Chapter 3, fabricated by sintering of glass microspheres. The pore size scale for these samples, considering the average pore radius estimated by the processing of microtomography images, ranges from approximately 100 to 200 μm . In this case, the long-time condition, assuming the diffusion of water molecules ($D_0 = 2.29\text{m}^2/\text{s}$ at 25°C), would be fulfilled for diffusion times $\Delta \gg 17\text{s}$, which in this case can be considered inaccessible since T_2 and T_1 relaxation times for water protons under such confinement scale range between tenths and hundreds of milliseconds [147].

5.2.2 Time-Dependent Diffusion Coefficients in Packed Glass Beads

To illustrate the relation between time-dependent diffusion coefficients and pore size scale five model porous samples were prepared using loose packs of soda lime glass microspheres (Cospheric) from five narrow size ranges: A: 45-53 μm ; B: 106-125 μm ; C: 212-250 μm ; D: 425-500 μm and E: 710-850 μm . All the samples were prepared in 5mm NMR tubes and saturated with 100% distilled water. Signal attenuation due to diffusion was measured for all samples using 18 different values for the diffusion time Δ varying from 4ms up to 1s.

All measurements were performed using the 13-interval APFG sequence proposed by Cotts (Figure 4.4) with time-independent acquisition, *i.e.*, fixing the storage time Δ and varying the gradient strength G for the observation of signal attenuation due to diffusion. Measurements were performed in a 500 MHz (VARIAN) spectrometer, in a 5 mm probe. Figures 5.9 to 5.13 show the signal attenuation due to diffusion as a function of the gradient field strength for all the 5 samples and the 18 storage times employed.

Time-dependent diffusion coefficients were extracted for all the 5 samples using a simple Gaussian model (Equations (4.24) and (4.31)), considering only the data sets (Δ values) wherein the Gaussian approximation for the diffusion propagator was considered valid. As in the analysis of the results presented in Chapter 4, the linearity of each data set in the logarithmic plot of Ψ versus G^2 was used to validate such approximation. The loss of linearity with increasing diffusion time Δ can easily be verified in Figures from 5.9 to 5.13. It is also possible to notice the expansion of the time range of Δ values during which the Gaussian approximation is valid as the pore size scale (\propto microspheres size range) is increased.

Figure 5.14 shows the extracted time-dependent diffusion coefficients for the 5 samples as a function of diffusion time. The plot in Figure 5.14 shows only the values of D_{eff} extracted from data sets with a linear Ψ versus G^2 decay, even though measurements were performed for diffusion times up to 1 s for all samples. The effect of signal loss due to relaxation can be verified by the increasing error bar in D_{eff} values as the diffusion time

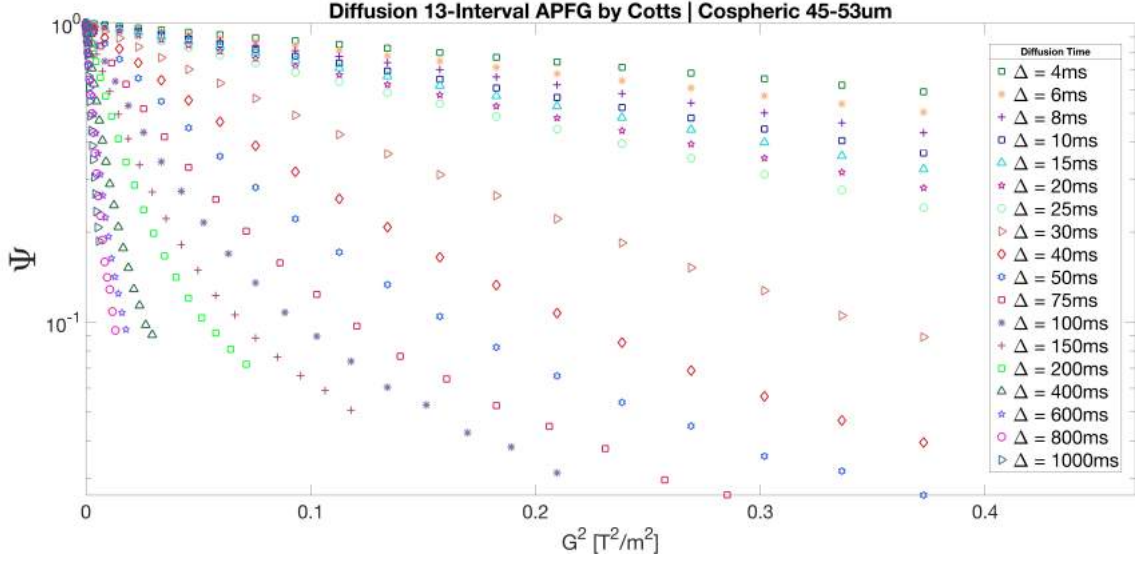


Figure 5.9: Signal attenuation due to diffusion Ψ as a function of gradient field strength G^2 for the water-saturated microsphere packing A: 45-53 μm , using the 13-interval APFG sequence (Figure 4.4). Diffusion was measured for 18 different diffusion time Δ values, ranging from 4ms up to 1s.

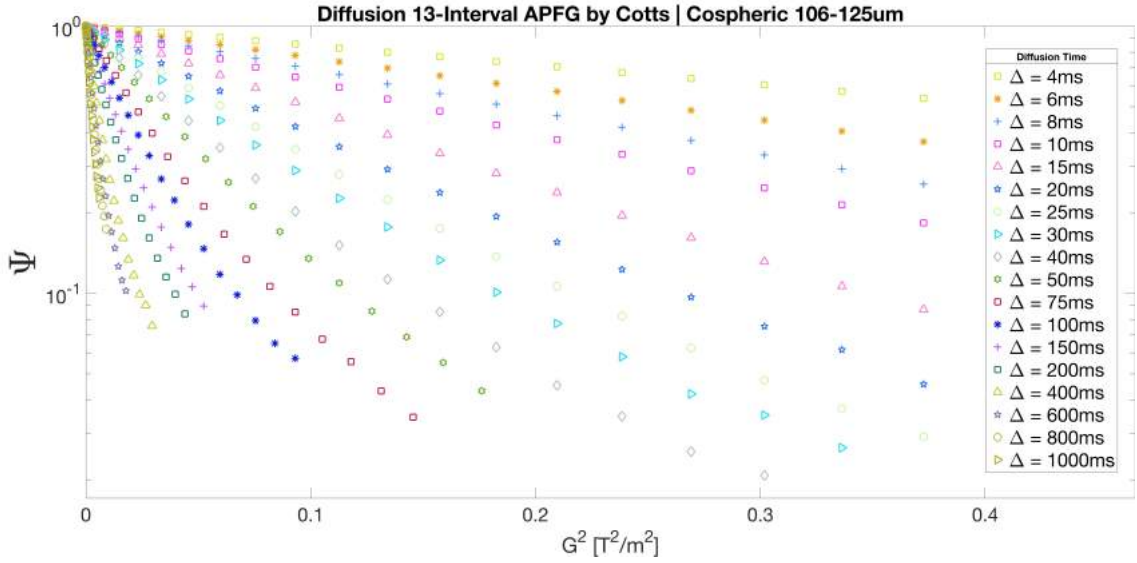


Figure 5.10: Signal attenuation due to diffusion Ψ as a function of gradient field strength G^2 for the water-saturated microsphere packing B: 106-125 μm using the 13-interval APFG sequence (Figure 4.4). Diffusion was measured for 18 different diffusion time Δ values, ranging from 4ms up to 1s.

is increased. One should notice that even the largest diffusion time employed ($\Delta = 1s$) would not satisfy the long-time condition $\sqrt{D_0\Delta} \gg R_p$ for these samples, which in this

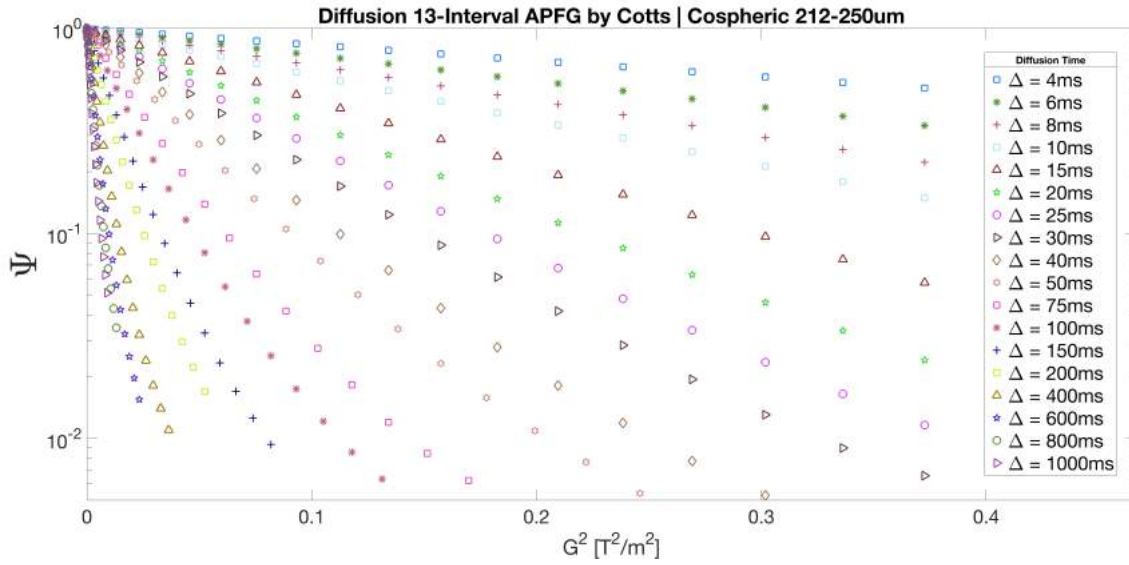


Figure 5.11: Signal attenuation due to diffusion Ψ as a function of gradient field strength G^2 for the water-saturated microsphere packing C: 212-250 μm using the 13-interval APFG sequence (Figure 4.4). Diffusion was measured for 18 different diffusion time Δ values, ranging from 4ms up to 1s.

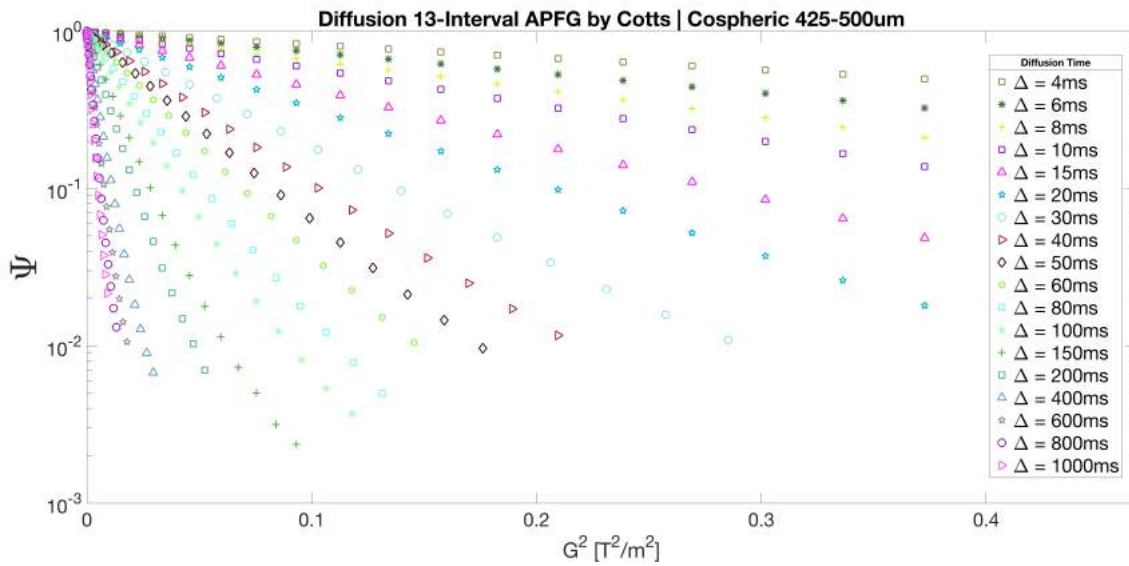


Figure 5.12: Signal attenuation due to diffusion Ψ as a function of gradient field strength G^2 for the water-saturated microsphere packing D: 425-500 μm using the 13-interval APFG sequence (Figure 4.4). Diffusion was measured for 18 different diffusion time Δ values, ranging from 4ms up to 1s.

case ranges from approximately $\Delta \gg 1$ s, for the smallest microspheres (45 – 53 μm), up to $\Delta \gg 5$ min, for the largest microspheres (710 – 850 μm).

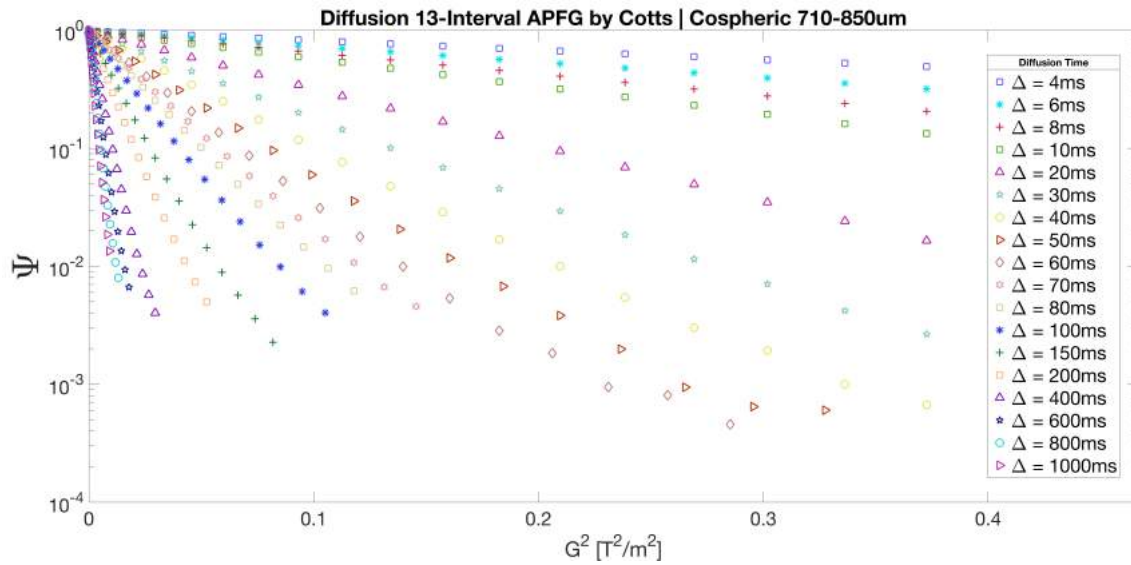


Figure 5.13: Signal attenuation due to diffusion Ψ as a function of gradient field strength G^2 for the water-saturated microsphere packing E: 710-850 μm using the 13-interval APFG sequence (Figure 4.4). Diffusion was measured for 18 different diffusion time Δ values, ranging from 4ms up to 1s.

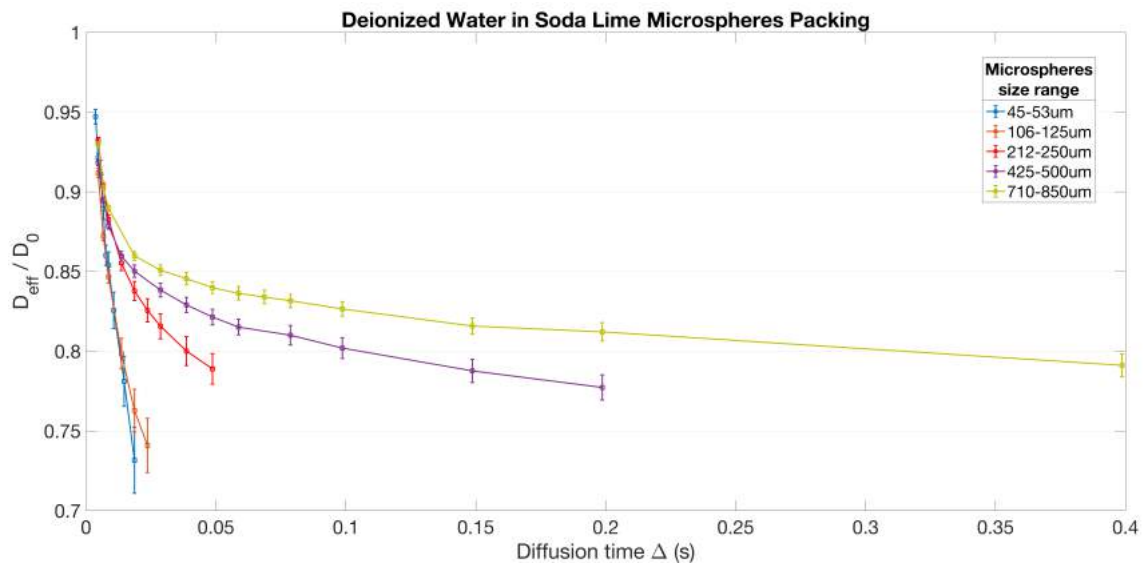


Figure 5.14: Effective diffusion coefficients extracted from the data sets in Figures from 5.9 to 5.13 using a standard 13-interval PGSTE sequence. Only the data sets with diffusion times Δ wherein the Gaussian approximation for the diffusion propagator was taken as valid were considered for the analysis. The error bar for the determination of D_{eff} values increases with the diffusion time as an effect of signal loss due to relaxation.

Tourell et al. [79] reported a set of results from a singlet-assisted diffusion study using two different home-synthesized molecular systems for singlet preparation and a variety of microsphere packages, including the same soda-lime glass package sample E (710 – 850 μm) employed in our previous example. On the reported results, using a singlet-assisted diffusion protocol, diffusion coefficients were obtained from data sets with diffusion times up to 240s.

5.2.3 SAD-NMR Pulse Sequences

The pulsed-field gradients of a regular stimulated echo PFG (PGSTE) sequence employed for encoding and decoding of a magnetization phase in diffusion experiments can be combined with the preparation and reading stages of singlet states to produce a singlet-assisted PGSTE protocol. Figure 5.15 shows the protocol proposed by Yadav et al. [167, 174].

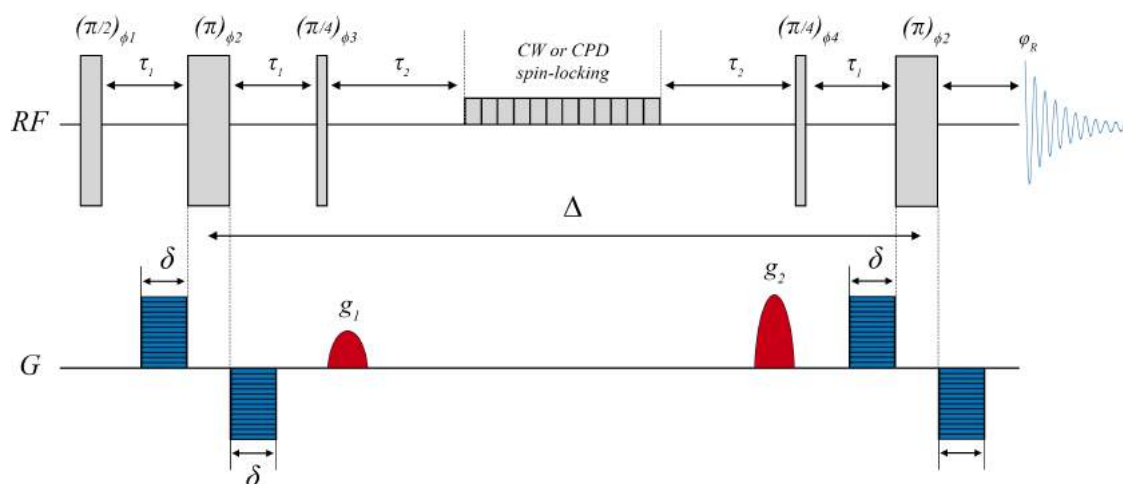


Figure 5.15: Singlet-assisted pulsed-field gradient stimulated echo (Singlet-PGSTE) sequence proposed by Yadav et al. [167, 174]. The upper scheme (RF) represents the radio-frequency pulses and the lower scheme (G) the pulsed gradients. At the lower scheme the encoding and decoding pulsed-gradient pairs are illustrated in blue and the spoiler gradients g_1 and g_2 are illustrated in red. The phase cycling schemes are: $\phi_1 = x$; $\phi_2 = x$; $\phi_3 = x, y, x, y, -x, y, x, y$; $\phi_4 = x, y, x, y, x, y, x, y$ and $\varphi_R = x, x, x, x, -x, -x, -x, -x$.

The singlet preparation stage is similar to the protocol described in Figure 5.4. The first pair of encoding gradient pulses are applied during the first spin echo interval $\tau_1 - 180 - \tau_1$, immediately before and after the refocusing π pulse. Singlet detection is performed with $\pi/4$ pulse followed by another spin echo interval $\tau_1 - 180 - \tau_1$, wherein both gradient pulses

for phase decoding are also placed right before and after the π pulse. The delays τ_1 and τ_2 are the same described in Equation (5.20). Two additional spoiling gradient pulses g_1 and g_2 (illustrated in red), as the ones employed in magnetic resonance imaging techniques [175, 176], are used to filter unwanted coherences. The suppression of singlet-triplet transitions can be achieved by a continuous wave (CW) or a composed pulse decoupling (CPD) spin-locking method. The phase cycling scheme for each pulse (ϕ_1 to ϕ_4) and the receiver (φ_R) can be found detailed at the caption of the figure.

Different examples of singlet-assisted diffusion sequences can be found in References [79, 167, 168, 170], even though they are based on the same principle, merging singlet preparation and reading stages with pulsed-gradients for phase encoding and decoding. The SAD-NMR experiments are yet to be performed, after a proper investigation on the preliminary results presented in Section 5.1.6 and a refinement on the experimental methodology, in order for the the long-lived behavior of singlet states to be properly exploited.

Chapter 6

Conclusion

Relaxation and diffusion NMR techniques can be widely employed for the characterization of confined fluids, providing insightful information on both saturating fluids and confining space. Particularly, three distinct applications, performed under high-field conditions, were presented and discussed in this thesis. In all of them, a special attention was brought to the establishment of a suitable framework for data analysis, in order to ensure a proper interpretation of parameters extracted from NMR data sets and their correlation with physical properties of fluids and geometrical features of porous structures. One of the main advantages of high-field NMR, associated with high resolutions for the determination of chemical-shifts and spectroscopy applications, is lost when fluids are under confinement in porous geometry, wherein magnetic fields become grossly inhomogeneous. Therefore, distinct applications of the time-domain analysis of relaxation rates and effective diffusion coefficients, performed in data sets obtained from controlled experiments using model porous samples, were discussed.

The problem of multi-exponential analysis and the direct association between relaxation rates and pore size distributions was addressed in Chapter 3, through a controlled study of water transverse relaxation rates obtained in a set of home-fabricated synthetic porous structures, designed to exhibit homogeneous pore size distributions and mineralogy, in different confinement scales, yet keeping close levels of porosity, which from the standpoint of data analysis upholds a fair comparison among data sets obtained from different samples on what regards the water content, *i.e.*, signal-to-noise ratio. The pore size distribution of the fabricated samples was determined by the processing micro tomography images. Even though the smallest observable pore size is known to be limited, in this case, by the image resolution, there were no signs nonetheless of the presence of two different size scales in pore size distributions, in opposition to the bi-exponential transverse relaxation profiles obtained for all samples.

The problem of magnetization loss due to diffusion of molecules through strong internal magnetic field gradients, originated from the enhanced magnetic susceptibility contrast between the porous and the fluid space in high-field NMR was also evaluated. Even though it was verified that this effect indeed affects the observed relaxation rates, the bi-exponential behavior of transverse relaxation was also observed in low-field measurements, wherein this effect is significantly reduced (and sometimes neglected), as it is proportional to the magnetic field strength. It is worth mentioning that despite the effort in producing model porous media for a fair investigation of surface effects on relaxation rates, pore size scale and connectivity in all samples were nevertheless high, indicating points wherein the methodology could be improved. Notwithstanding, the results obtained in this set of controlled experiments illustrate the problems related to the often unwary assumption of a fast diffusion regime and the establishment of a direct relation between relaxation time distributions and pore sizes, especially on what concerns NMR of porous rocks in oil industry.

An NMR diffusion-based methodology was proposed as a tool for the characterization of distinct fluid phases, as well as to the evaluation of conformation features, in bi-saturated porous media, with potential applications for the study of fluids in porous materials not only in oil, but also food or pharmaceutical industries. It was shown that through the analysis of time-dependent diffusion coefficients extracted with simple bi-Gaussian models from PFG NMR data sets it is possible to obtain valuable information on both wetting and non-wetting phases and conformation features. The short-time analysis of time-dependent diffusion coefficients was used to characterize the porous samples in pre-drainage experiments and it was shown to be sensitive to the enhancement in the surface-to-volume ratio probed by the wetting phase, in post drainage experiments, *i.e.*, after the injection of a second non-wetting fluid. It was discussed how the behavior of time-dependent diffusion coefficients of the non-wetting phase can be analyzed in order for one to draw possible conformation scenarios for both phases. Next steps for this work are already under development regarding the analysis time-dependent diffusion coefficients obtained from 2-dimensional D - T_2 experiments in low-field conditions with multi-saturated porous media, under the framework of restricted diffusion.

The influence of molecular diffusion through internal field gradients in the presence high magnetic fields was once more addressed in Chapter 4. In this case it was demonstrated that, under the choice of a proper framework, it is possible to evaluate the validity of the set of approximations regarding the analysis of time-dependent coefficients in the short-time diffusion regime, even in high-field conditions. It is worth mentioning that, particularly for the case of diffusion studies, high-field equipment bring some practical advantages. The often robust hardware electronic present in high-field NMR spectrometers allows the application of relatively strong and short gradient pulses, which can be rapidly

switched on and off. This is important not only for the observation of diffusion during short times, but also to create an experimental setup wherein the validity of fundamental approximations in diffusion theory such as the narrow pulse (NPA) and the Gaussian phase (GPA) approximations can be ensured, yet producing a sufficiently large signal attenuation for the analysis of molecular diffusion.

Initial experiments with the singlet-assisted NMR technique were reported, although some further investigation is yet to be performed in order for the long-lived behavior of singlet states to be better exploited. Among several possible applications, the long-lived spin order of singlet states can be employed to the observation of restricted molecular diffusion in the long-time regime. For the case of connected porous media, the asymptotic value of the effective diffusion coefficient in the long-time regime can be directly associated with porous media tortuosity, an important geometry-related parameter for the study of flow and transport properties of confined fluids.

Bibliography

- [1] F. Bloch. “Nuclear Induction”. In: *Phys. Rev.* 70 (7-8 1946), pp. 460–474. DOI: 10.1103/PhysRev.70.460. URL: <https://link.aps.org/doi/10.1103/PhysRev.70.460>.
- [2] Brian Cowan. *Nuclear magnetic resonance and relaxation*. Cambridge University Press, 2005.
- [3] Charles P Slichter. *Principles of magnetic resonance*. Vol. 1. Springer Science & Business Media, 2013.
- [4] R. Valiullin, ed. *Diffusion NMR of Confined Systems. Fluid Transport in Porous Solids and Heterogeneous Materials*. New Developments in NMR. The Royal Society of Chemistry, 2017, P001–576. ISBN: 978-1-78262-190-4. DOI: 10.1039/9781782623779. URL: <http://dx.doi.org/10.1039/9781782623779>.
- [5] G.R. Coates, L. Xiao, and Prammer M.G. *NMR Logging Principles and Applications*. Halliburton Energy Services, 1999.
- [6] K.J. Dunn, D. J. Bergman, and G. A. LaTorraca. *Nuclear magnetic resonance: Petrophysical and logging applications*. Vol. 32. Elsevier, 2002.
- [7] N. Bloembergen, E. M. Purcell, and R. V. Pound. “Relaxation Effects in Nuclear Magnetic Resonance Absorption”. In: *Phys. Rev.* 73 (7 1948), pp. 679–712. DOI: 10.1103/PhysRev.73.679. URL: <https://link.aps.org/doi/10.1103/PhysRev.73.679>.
- [8] F. Bloch. “Nuclear relaxation in gases by surface catalysis”. In: *Physical Review* 83.5 (1951), p. 1062.
- [9] E. L. Hahn. “Spin Echoes”. In: *Phys. Rev.* 80 (4 1950), pp. 580–594. DOI: 10.1103/PhysRev.80.580. URL: <https://link.aps.org/doi/10.1103/PhysRev.80.580>.
- [10] H. Y. Carr and E. M. Purcell. “Effects of Diffusion on Free Precession in Nuclear Magnetic Resonance Experiments”. In: *Phys. Rev.* 94 (3 1954), pp. 630–638. DOI: 10.1103/PhysRev.94.630. URL: <https://link.aps.org/doi/10.1103/PhysRev.94.630>.

- [11] S. Meiboom and D. Gill. “Modified Spin-Echo Method for Measuring Nuclear Relaxation Times”. In: *Review of Scientific Instruments* 29.8 (1958), pp. 688–691. DOI: 10.1063/1.1716296. eprint: <https://doi.org/10.1063/1.1716296>. URL: <https://doi.org/10.1063/1.1716296>.
- [12] J. E. Tanner. “Pulsed Field Gradients for NMR Spin-Echo Diffusion Measurements”. In: *Review of Scientific Instruments* 36.8 (1965), pp. 1086–1087. DOI: 10.1063/1.1719808. eprint: <https://doi.org/10.1063/1.1719808>. URL: <https://doi.org/10.1063/1.1719808>.
- [13] R. J. S. Brown and I. Fatt. “Measurements Of Fractional Wettability Of Oil Fields’ Rocks By The Nuclear Magnetic Relaxation Method”. In: (1956). DOI: 10.2118/743-G.
- [14] H. C. Torrey. “Bloch equations with diffusion terms”. In: *Physical review* 104.3 (1956), p. 563.
- [15] H. C. Torrey. “Theory of nuclear spin relaxation of liquids for large surface-to-volume ratios”. In: 1 (1956), p. 256.
- [16] Yi-Qiao Song et al. “Magnetic resonance in porous media: Recent progress”. In: *The Journal of Chemical Physics* 128.5 (2008), p. 052212. DOI: 10.1063/1.2833581. eprint: <https://doi.org/10.1063/1.2833581>. URL: <https://doi.org/10.1063/1.2833581>.
- [17] R. L. Kleinberg and J. A. Jackson. “An introduction to the history of NMR well logging”. In: *Concepts in Magnetic Resonance* 13.6 (2001), pp. 340–342. DOI: 10.1002/cmr.1018. eprint: <https://onlinelibrary.wiley.com/doi/pdf/10.1002/cmr.1018>. URL: <https://onlinelibrary.wiley.com/doi/abs/10.1002/cmr.1018>.
- [18] R. H. Varian. “Apparatus and method for identifying substances”. Pat. US3395337A. 1952.
- [19] R. J. S. Brown, H. C. Torrey, and J. Korringa. “Methods for investigating the properties of fluid (materials) within porous media”. Pat. US3213356A. 1956.
- [20] D. O. Seevers. “A Nuclear Magnetic Method For Determining The Permeability Of Sandstones”. In: (1966), p. 14.
- [21] A. Timur. “Pulsed Nuclear Magnetic Resonance Studies of Porosity, Movable Fluid, and Permeability of Sandstones”. In: *Journal of Petroleum Technology* 21 (1969), pp. 775–786. DOI: 10.2118/2045-PA.

- [22] Raymond Damadian. “Tumor Detection by Nuclear Magnetic Resonance”. In: *Science* 171.3976 (1971), pp. 1151–1153. ISSN: 0036-8075. DOI: 10.1126/science.171.3976.1151. eprint: <https://science.sciencemag.org/content/171/3976/1151.full.pdf>. URL: <https://science.sciencemag.org/content/171/3976/1151>.
- [23] D. C. Chang et al. “Spin Echo Studies on Cellular Water”. In: *Nature* 235 (1972), pp. 170–171. URL: <https://doi.org/10.1038/235170a0>.
- [24] K. R. Brownstein and C. E. Tarr. “Importance of classical diffusion in NMR studies of water in biological cells”. In: *Physical Review A* 19.6 (1979), p. 2446.
- [25] K. R. Brownstein and C. E. Tarr. “Spin-lattice relaxation in a system governed by diffusion”. In: *Journal of Magnetic Resonance (1969)* 26.1 (1977), pp. 17–24.
- [26] Max Lipsicas, Jayanth R. Banavar, and Jorge Willemsen. “Surface relaxation and pore sizes in rocks—a nuclear magnetic resonance analysis”. In: *Applied Physics Letters* 48.22 (1986), pp. 1544–1546. DOI: 10.1063/1.96864. eprint: <https://doi.org/10.1063/1.96864>. URL: <https://doi.org/10.1063/1.96864>.
- [27] Elliot Grunewald and Rosemary Knight. “A laboratory study of NMR relaxation times and pore coupling in heterogeneous media”. In: *Geophysics* 74.6 (2009), E215–E221.
- [28] Moacyr Nascimento. “Studies in NMR relaxation and diffusion: High-field applications to Petrophysics”. PhD thesis. Centro Brasileiro de Pesquisas Físicas, 2020.
- [29] M. Nascimento et al. “Enhanced NMR relaxation of fluids confined to porous media: A proposed theory and experimental tests”. In: *Phys. Rev. E* 99 (4 2019), p. 042901. DOI: 10.1103/PhysRevE.99.042901. URL: <https://link.aps.org/doi/10.1103/PhysRevE.99.042901>.
- [30] Martin D. Hürlimann, Lawrence L. Latour, and Christopher H. Sotak. “Diffusion measurement in sandstone core: NMR determination of surface-to-volume ratio and surface relaxivity”. In: *Magnetic Resonance Imaging* 12.2 (1994). Proceedings of the Second International Meeting on Recent Advances in MR Applications to Porous Media, pp. 325–327. ISSN: 0730-725X. DOI: [https://doi.org/10.1016/0730-725X\(94\)91548-2](https://doi.org/10.1016/0730-725X(94)91548-2). URL: <http://www.sciencedirect.com/science/article/pii/0730725X94915482>.
- [31] Zhi-Xiang Luo, Jeffrey Paulsen, and Yi-Qiao Song. “Robust determination of surface relaxivity from nuclear magnetic resonance DT2 measurements”. In: *Journal of Magnetic Resonance* 259 (2015), pp. 146–152. ISSN: 1090-7807. DOI: <https://doi.org/10.1016/j.jmr.2015.08.002>. URL: <http://www.sciencedirect.com/science/article/pii/S1090780715001676>.

- [32] E. Lucas-Oliveira et al. “Sandstone surface relaxivity determined by NMR T2 distribution and digital rock simulation for permeability evaluation”. In: *Journal of Petroleum Science and Engineering* 193 (2020), p. 107400. ISSN: 0920-4105. DOI: <https://doi.org/10.1016/j.petrol.2020.107400>. URL: <http://www.sciencedirect.com/science/article/pii/S0920410520304721>.
- [33] E. O. Stejskal and J. E. Tanner. “Spin Diffusion Measurements: Spin Echoes in the Presence of a Time-Dependent Field Gradient”. In: *The Journal of Chemical Physics* 42.1 (1965), pp. 288–292. DOI: 10.1063/1.1695690. eprint: <https://doi.org/10.1063/1.1695690>. URL: <https://doi.org/10.1063/1.1695690>.
- [34] J. H. Simpson and H. Y. Carr. “Diffusion and Nuclear Spin Relaxation in Water”. In: *Phys. Rev.* 111 (5 1958), pp. 1201–1202. DOI: 10.1103/PhysRev.111.1201. URL: <https://link.aps.org/doi/10.1103/PhysRev.111.1201>.
- [35] D. W. McCall, D. C. Douglass, and E. W. Anderson. “Diffusion in Liquids”. In: *The Journal of Chemical Physics* 31.6 (1959), pp. 1555–1557. DOI: 10.1063/1.1730651. eprint: <https://doi.org/10.1063/1.1730651>. URL: <https://doi.org/10.1063/1.1730651>.
- [36] D. E. Woessner. “NMR spin-echo self-diffusion measurements on fluids undergoing restricted diffusion”. In: *The Journal of Physical Chemistry* 67 (1963), pp. 1365–1367. DOI: 10.1021/j100800a509.
- [37] D. Guzey and D.J. McClements. “Formation, stability and properties of multilayer emulsions for application in the food industry”. In: *Advances in Colloid and Interface Science* 128-130 (2006). In Honor of Professor Nissim Garti’s 60th Birthday, pp. 227–248. ISSN: 0001-8686. DOI: <https://doi.org/10.1016/j.cis.2006.11.021>. URL: <http://www.sciencedirect.com/science/article/pii/S0001868606002004>.
- [38] E. von Meerwall et al. “Diffusion in binary liquid n-alkane and alkane-polyethylene blends”. In: *The Journal of Chemical Physics* 111.2 (1999), pp. 750–757. DOI: 10.1063/1.479354. eprint: <https://doi.org/10.1063/1.479354>. URL: <https://doi.org/10.1063/1.479354>.
- [39] David W. McCall, Dean C. Douglass, and Ernest W. Anderson. “Diffusion in Ethylene Polymers. IV”. In: *The Journal of Chemical Physics* 30.3 (1959), pp. 771–773. DOI: 10.1063/1.1730042. eprint: <https://doi.org/10.1063/1.1730042>. URL: <https://doi.org/10.1063/1.1730042>.
- [40] Sho-Wei Lo et al. “Mixing Rules and Correlations of NMR Relaxation Time With Viscosity, Diffusivity, and Gas/Oil Ratio of Methane/Hydrocarbon Mixtures”. In: *SPE Journal* 7 (2002), pp. 24–34. DOI: 10.2118/77264-PA.

- [41] Dan E Demco and Bernhard Blümich. “NMR imaging of materials”. In: *Current Opinion in Solid State and Materials Science* 5.2 (2001), pp. 195–202. ISSN: 1359-0286. DOI: [https://doi.org/10.1016/S1359-0286\(00\)00044-9](https://doi.org/10.1016/S1359-0286(00)00044-9). URL: <http://www.sciencedirect.com/science/article/pii/S1359028600000449>.
- [42] Harald Schwalbe. “Editorial: New 1.2 GHz NMR Spectrometers— New Horizons?” In: *Angewandte Chemie International Edition* 56.35 (2017), pp. 10252–10253. DOI: 10.1002/anie.201705936. eprint: <https://onlinelibrary.wiley.com/doi/pdf/10.1002/anie.201705936>. URL: <https://onlinelibrary.wiley.com/doi/abs/10.1002/anie.201705936>.
- [43] Y.-Q. Song et al. “T₁–T₂ Correlation Spectra Obtained Using a Fast Two-Dimensional Laplace Inversion”. In: *Journal of Magnetic Resonance* 154.2 (2002), pp. 261–268. ISSN: 1090-7807. DOI: <https://doi.org/10.1006/jmre.2001.2474>. URL: <http://www.sciencedirect.com/science/article/pii/S1090780701924747>.
- [44] Yi-Qiao Song, Lukasz Zielinski, and Seungoh Ryu. “Two-Dimensional NMR of Diffusion Systems”. In: *Phys. Rev. Lett.* 100 (24 2008), p. 248002. DOI: 10.1103/PhysRevLett.100.248002. URL: <https://link.aps.org/doi/10.1103/PhysRevLett.100.248002>.
- [45] Marcel Nogueira d’Eurydice et al. “T₂-Filtered T₂ - T₂ Exchange NMR”. In: *The Journal of Chemical Physics* 144.20 (2016), p. 204201. DOI: 10.1063/1.4951712. eprint: <https://doi.org/10.1063/1.4951712>. URL: <https://doi.org/10.1063/1.4951712>.
- [46] Y. Zhang and B. Blümich. “Spatially resolved D–T₂ correlation NMR of porous media”. In: *Journal of Magnetic Resonance* 242 (2014), pp. 41–48. ISSN: 1090-7807. DOI: <https://doi.org/10.1016/j.jmr.2014.01.017>. URL: <http://www.sciencedirect.com/science/article/pii/S1090780714000391>.
- [47] P.T. Callaghan and I. Furó. “Diffusion-diffusion correlation and exchange as a signature for local order and dynamics”. In: *The Journal of Chemical Physics* 120.8 (2004), pp. 4032–4038. DOI: 10.1063/1.1642604. eprint: <https://doi.org/10.1063/1.1642604>. URL: <https://doi.org/10.1063/1.1642604>.
- [48] M. A. Golberg, ed. *Solution Methods for Integral Equations - Theory and Applications*. Springer, Boston, MA, 1979.
- [49] Andrei A. Istratov and Oleg F. Vyvenko. “Exponential analysis in physical phenomena”. In: *Review of Scientific Instruments* 70.2 (1999), pp. 1233–1257. DOI: 10.1063/1.1149581. eprint: <https://doi.org/10.1063/1.1149581>. URL: <https://doi.org/10.1063/1.1149581>.

- [50] David L. Phillips. “A Technique for the Numerical Solution of Certain Integral Equations of the First Kind”. In: *J. ACM* 9.1 (Jan. 1962), 84–97. ISSN: 0004-5411. DOI: 10.1145/321105.321114. URL: <https://doi.org/10.1145/321105.321114>.
- [51] A. N. Tikhonov. “On the solution of non-linear integral equations of the first kind”. In: *Dokl. Akad. Nauk SSSR* 156 (1964), 1296–1299.
- [52] Andrei A Istratov and Oleg F Vyvenko. “Exponential analysis in physical phenomena”. In: *Review of Scientific Instruments* 70.2 (1999), pp. 1233–1257.
- [53] P. T. Callaghan. *Principles of nuclear magnetic resonance microscopy*. Oxford Clarendon Press, 2011.
- [54] R. S. Likes. “Moving gradient zeugmatography”. Pat. US4307343 (A). 1981.
- [55] Stig Ljunggren. “A simple graphical representation of fourier-based imaging methods”. In: *Journal of Magnetic Resonance (1969)* 54.2 (1983), pp. 338–343. ISSN: 0022-2364. DOI: [https://doi.org/10.1016/0022-2364\(83\)90060-4](https://doi.org/10.1016/0022-2364(83)90060-4). URL: <http://www.sciencedirect.com/science/article/pii/0022236483900604>.
- [56] Donald B. Twieg. “The k-trajectory formulation of the NMR imaging process with applications in analysis and synthesis of imaging methods”. In: *Medical Physics* 10.5 (1983), pp. 610–621. DOI: 10.1118/1.595331.
- [57] R. Kimmich et al. “Geometrical restrictions of water diffusion in aqueous protein systems. A study using NMR field-gradient techniques”. In: *Applied Magnetic Resonance* 4 (1993), pp. 425–440. DOI: 10.1007/BF03162458.
- [58] R. Kimmich et al. “Self-diffusion in fluids in porous glass: confinement by pores and liquid adsorption layers”. In: *Magn Reson Imaging* 14 (1996), pp. 793–797. DOI: 10.1016/S0730-725x(96)00165-8.
- [59] D.W.G. Smith and J.G. Powles. “Proton spin-lattice relaxation in liquid water and liquid ammonia”. In: *Molecular Physics* 10.5 (1966), pp. 451–463. DOI: 10.1080/00268976600100571. eprint: <https://doi.org/10.1080/00268976600100571>. URL: <https://doi.org/10.1080/00268976600100571>.
- [60] T. Keyes and D. Kivelson. “Light Scattering and the Coupling of Molecular Reorientation and Hydrodynamic Modes”. In: *The Journal of Chemical Physics* 54.4 (1971), pp. 1786–1798. DOI: 10.1063/1.1675086. eprint: <https://doi.org/10.1063/1.1675086>. URL: <https://doi.org/10.1063/1.1675086>.
- [61] D. P. Shelton. “Collective molecular rotation in water and other simple liquids”. In: *Chemical Physics Letters* 325.5 (2000), pp. 513–516. ISSN: 0009-2614. DOI: [https://doi.org/10.1016/S0009-2614\(00\)00734-X](https://doi.org/10.1016/S0009-2614(00)00734-X). URL: <http://www.sciencedirect.com/science/article/pii/S000926140000734X>.

- [62] H. J. Bakker, Y. L. A. Rezus, and R. L. A. Timmer. “Molecular Reorientation of Liquid Water Studied with Femtosecond Midinfrared Spectroscopy”. In: *The Journal of Physical Chemistry A* 112.46 (2008), pp. 11523–11534. DOI: 10.1021/jp8012943. eprint: <https://doi.org/10.1021/jp8012943>. URL: <https://doi.org/10.1021/jp8012943>.
- [63] Oleg V. Bychuk and Ben O’Shaughnessy. “Anomalous surface diffusion: A numerical study”. In: *The Journal of Chemical Physics* 101.1 (1994), pp. 772–780. DOI: 10.1063/1.468132. eprint: <https://doi.org/10.1063/1.468132>. URL: <https://doi.org/10.1063/1.468132>.
- [64] R. Valiullin, R. Kimmich, and N. Fatkullin. “Lévy walks of strong adsorbates on surfaces: Computer simulation and spin-lattice relaxation”. In: *Phys. Rev. E* 56 (4 1997), pp. 4371–4375. DOI: 10.1103/PhysRevE.56.4371. URL: <https://link.aps.org/doi/10.1103/PhysRevE.56.4371>.
- [65] J-P Korb, M Whaley-Hodges, and RG Bryant. “Translational diffusion of liquids at surfaces of microporous materials: Theoretical analysis of field-cycling magnetic relaxation measurements”. In: *Physical Review E* 56.2 (1997), p. 1934.
- [66] JP Korb. “Nuclear magnetic relaxation of liquids in porous media”. In: *New Journal of Physics* 13.3 (2011), p. 035016.
- [67] F. Barberon et al. “Probing the Surface Area of a Cement-Based Material by Nuclear Magnetic Relaxation Dispersion”. In: *Phys. Rev. Lett.* 90 (11 2003), p. 116103. DOI: 10.1103/PhysRevLett.90.116103. URL: <https://link.aps.org/doi/10.1103/PhysRevLett.90.116103>.
- [68] J.-P. Korb et al. “Microstructure and texture of hydrated cement-based materials: A proton field cycling relaxometry approach”. In: *Cement and Concrete Research* 37.3 (2007). Cementitious Materials as model porous media: Nanostructure and Transport processes, pp. 295–302. ISSN: 0008-8846. DOI: <https://doi.org/10.1016/j.cemconres.2006.08.002>. URL: <http://www.sciencedirect.com/science/article/pii/S0008884606001967>.
- [69] C. H. Neuman. “Spin echo of spins diffusing in a bounded medium”. In: *The Journal of Chemical Physics* 60.11 (1974), pp. 4508–4511. DOI: 10.1063/1.1680931. eprint: <https://doi.org/10.1063/1.1680931>. URL: <https://doi.org/10.1063/1.1680931>.
- [70] J.S. Murday and R.M. Cotts. “Self-Diffusion Coefficient of Liquid Lithium”. In: *The Journal of Chemical Physics* 48.11 (1968), pp. 4938–4945. DOI: 10.1063/1.1668160. eprint: <https://doi.org/10.1063/1.1668160>. URL: <https://doi.org/10.1063/1.1668160>.

- [71] P.T. Callaghan, K.W. Jolley, and R.S. Humphrey. “Diffusion of fat and water in cheese as studied by pulsed field gradient nuclear magnetic resonance”. In: *Journal of Colloid and Interface Science* 93.2 (1983), pp. 521–529. ISSN: 0021-9797. DOI: [https://doi.org/10.1016/0021-9797\(83\)90436-8](https://doi.org/10.1016/0021-9797(83)90436-8). URL: <http://www.sciencedirect.com/science/article/pii/0021979783904368>.
- [72] P.P. Mitra, P. N. Sen, and L. M. Schwartz. “Short-time behavior of the diffusion coefficient as a geometrical probe of porous media”. In: *Phys. Rev. B* 47 (14 1993), pp. 8565–8574. DOI: 10.1103/PhysRevB.47.8565. URL: <https://link.aps.org/doi/10.1103/PhysRevB.47.8565>.
- [73] B. Ghanbarian et al. “Tortuosity in Porous Media: A Critical Review”. In: *Soil Science Society of America Journal* 77.5 (2013), pp. 1461–1477. DOI: 10.2136/sssaj2012.0435. eprint: <https://access.onlinelibrary.wiley.com/doi/pdf/10.2136/sssaj2012.0435>. URL: <https://access.onlinelibrary.wiley.com/doi/abs/10.2136/sssaj2012.0435>.
- [74] Marina Carravetta, Ole G. Johannessen, and Malcolm H. Levitt. “Beyond the T_1 Limit: Singlet Nuclear Spin States in Low Magnetic Fields”. In: *Phys. Rev. Lett.* 92 (15 2004), p. 153003. DOI: 10.1103/PhysRevLett.92.153003. URL: <https://link.aps.org/doi/10.1103/PhysRevLett.92.153003>.
- [75] Marina Carravetta and Malcolm H. Levitt. “Long-Lived Nuclear Spin States in High-Field Solution NMR”. In: *Journal of the American Chemical Society* 126.20 (2004). PMID: 15149209, pp. 6228–6229. DOI: 10.1021/ja0490931. eprint: <https://doi.org/10.1021/ja0490931>. URL: <https://doi.org/10.1021/ja0490931>.
- [76] M. H. Levitt. *Spin Dynamics: Basics of Nuclear Magnetic Resonance, 2nd Edition*. Wiley, 2008.
- [77] Malcolm H. Levitt. “Singlet and Other States with Extended Lifetimes”. In: *eMagRes*. American Cancer Society, 2010. ISBN: 9780470034590. DOI: 10.1002/9780470034590.emrstm1036. eprint: <https://onlinelibrary.wiley.com/doi/pdf/10.1002/9780470034590.emrstm1036>. URL: <https://onlinelibrary.wiley.com/doi/abs/10.1002/9780470034590.emrstm1036>.
- [78] Malcolm H. Levitt. “Singlet Nuclear Magnetic Resonance”. In: *Annual Review of Physical Chemistry* 63.1 (2012). PMID: 22224703, pp. 89–105. DOI: 10.1146/annurev-physchem-032511-143724. eprint: <https://doi.org/10.1146/annurev-physchem-032511-143724>. URL: <https://doi.org/10.1146/annurev-physchem-032511-143724>.
- [79] M.C. Tourell et al. “Singlet-assisted diffusion-NMR (SAD-NMR): redefining the limits when measuring tortuosity in porous media”. In: *Phys. Chem. Chem. Phys.*

- 20 (20 2018), pp. 13705–13713. DOI: 10.1039/C8CP00145F. URL: <http://dx.doi.org/10.1039/C8CP00145F>.
- [80] Walther Gerlach and Otto Stern. “Über die Richtungsquantelung im Magnetfeld”. In: *Annalen der Physik* 379.16 (1924), pp. 673–699. DOI: <https://doi.org/10.1002/andp.19243791602>. eprint: <https://onlinelibrary.wiley.com/doi/pdf/10.1002/andp.19243791602>. URL: <https://onlinelibrary.wiley.com/doi/abs/10.1002/andp.19243791602>.
- [81] I. S. Oliveira. *Física Quântica: Fundamentos, Formalismo e Aplicações*. Livraria da Física, 2020.
- [82] I Foley, SA Farooqui, and RL Kleinberg. “Effect of paramagnetic ions on NMR relaxation of fluids at solid surfaces”. In: *Journal of Magnetic Resonance, Series A* 123.1 (1996), pp. 95–104.
- [83] Martin D. Hürlimann. “Effective Gradients in Porous Media Due to Susceptibility Differences”. In: *Journal of Magnetic Resonance* 131.2 (1998), pp. 232–240.
- [84] T. R. Bryar, C. J. Daughney, and R. J. Knight. “Paramagnetic effects of iron (III) species on nuclear magnetic relaxation of fluid protons in porous media”. In: *Journal of magnetic resonance* 142.1 (2000), pp. 74–85.
- [85] Yi-Qiao Song. “Pore sizes and pore connectivity in rocks using the effect of internal field”. In: *Magnetic Resonance Imaging* 19.3 (2001), pp. 417–421. ISSN: 0730-725X. DOI: [https://doi.org/10.1016/S0730-725X\(01\)00259-4](https://doi.org/10.1016/S0730-725X(01)00259-4). URL: <http://www.sciencedirect.com/science/article/pii/S0730725X01002594>.
- [86] R. Böhmer et al. “Nature of the non-exponential primary relaxation in structural glass-formers probed by dynamically selective experiments”. In: *Journal of Non-Crystalline Solids* 235-237 (1998), pp. 1–9. ISSN: 0022-3093. DOI: [https://doi.org/10.1016/S0022-3093\(98\)00581-X](https://doi.org/10.1016/S0022-3093(98)00581-X). URL: <http://www.sciencedirect.com/science/article/pii/S002230939800581X>.
- [87] Oleg V. Petrov and Siegfried Stapf. “Parameterization of NMR relaxation curves in terms of logarithmic moments of the relaxation time distribution”. In: *Journal of Magnetic Resonance* 279 (2017), pp. 29–38. ISSN: 1090-7807. DOI: <https://doi.org/10.1016/j.jmr.2017.04.009>. URL: <http://www.sciencedirect.com/science/article/pii/S109078071730099X>.
- [88] D. W. Preston and E. R. Dietz. *The Art of Experimental Physics*. Wiley, 1991. ISBN: I978-0-471-84748-9.
- [89] P. W. Anderson and P. R. Weiss. “Exchange Narrowing in Paramagnetic Resonance”. In: *Rev. Mod. Phys.* 25 (1 1953), pp. 269–276. DOI: 10.1103/RevModPhys.25.269. URL: <https://link.aps.org/doi/10.1103/RevModPhys.25.269>.

- [90] Ekaterina Nikolskaya and Yrjö Hiltunen. “Time-Domain NMR in Characterization of Liquid Fuels: A Mini-Review”. In: *Energy & Fuels* 34.7 (2020), pp. 7929–7934. DOI: [10.1021/acs.energyfuels.0c01464](https://doi.org/10.1021/acs.energyfuels.0c01464). eprint: <https://doi.org/10.1021/acs.energyfuels.0c01464>. URL: <https://doi.org/10.1021/acs.energyfuels.0c01464>.
- [91] J. van Duynhoven et al. “Chapter 3 - Time-Domain NMR Applied to Food Products”. In: vol. 69. Annual Reports on NMR Spectroscopy. Academic Press, 2010, pp. 145–197. DOI: [https://doi.org/10.1016/S0066-4103\(10\)69003-5](https://doi.org/10.1016/S0066-4103(10)69003-5). URL: <http://www.sciencedirect.com/science/article/pii/S0066410310690035>.
- [92] D. Besghini and R. Mauri M.and Simonutti. “Time Domain NMR in Polymer Science: From the Laboratory to the Industry”. In: *Appl. Sci.* 9 (2019), p. 1801.
- [93] M. C. Wang and G. E. Uhlenbeck. “On the Theory of the Brownian Motion II”. In: *Rev. Mod. Phys.* 17 (2-3 1945), pp. 323–342. DOI: [10.1103/RevModPhys.17.323](https://doi.org/10.1103/RevModPhys.17.323). URL: <https://link.aps.org/doi/10.1103/RevModPhys.17.323>.
- [94] F. Reif. *Fundamentals of Statistical and Thermal Physics*. Waveland Press, Inc, 1965.
- [95] L. Venkataramanan, Y.-Q. Song, and M.D. Hürlimann. “Solving Fredholm integrals of the first kind with tensor product structure in 2 and 2.5 dimensions”. In: *IEEE Transactions on Signal Processing* 50.5 (2002). cited By 424, pp. 1017–1026. DOI: [10.1109/78.995059](https://doi.org/10.1109/78.995059). URL: <https://www.scopus.com/inward/record.uri?eid=2-s2.0-0036571437&doi=10.1109%2f78.995059&partnerID=40&md5=03c97bfd30c5bc74ff683bc44e8df450>.
- [96] F. Stallmach and P. Galvosas. “Spin Echo NMR Diffusion Studies”. In: ed. by G.A. Webb. Vol. 61. Annual Reports on NMR Spectroscopy. Academic Press, 2007, pp. 51–131. DOI: [https://doi.org/10.1016/S0066-4103\(07\)61102-8](https://doi.org/10.1016/S0066-4103(07)61102-8). URL: <http://www.sciencedirect.com/science/article/pii/S0066410307611028>.
- [97] A. Simpson. “Multidimensional solution state NMR of humic substances: a practical guide and review”. In: *Soil Science* 166 (2001).
- [98] M. Mobli and J. C. Hoch. “Nonuniform sampling and non-Fourier signal processing methods in multidimensional NMR”. In: *Progress in Nuclear Magnetic Resonance Spectroscopy* 83 (2014), pp. 21–41. ISSN: 0079-6565. DOI: <https://doi.org/10.1016/j.pnmrs.2014.09.002>.
- [99] S. W. Provencher. “A constrained regularization method for inverting data represented by linear algebraic or integral equations”. In: *Computer Physics Communications* 27.3 (1982), pp. 213–227. ISSN: 0010-4655. DOI: [https://doi.org/10.1016/0010-4655\(82\)90173-4](https://doi.org/10.1016/0010-4655(82)90173-4).

- [100] G.C. Borgia, R.J.S. Brown, and P. Fantazzini. “Uniform-Penalty Inversion of Multiexponential Decay Data”. In: *Journal of Magnetic Resonance* 132.1 (1998), pp. 65–77. ISSN: 1090-7807. DOI: <https://doi.org/10.1006/jmre.1998.1387>.
- [101] L. Venkataramanan, Y.-Q. Song, and M.D. Hürlimann. “Nuclear magnetic resonance measurements and methods of analyzing nuclear magnetic resonance data”. Pat. US6462542B1. 2001.
- [102] O. Serra and L. Serra. *Well Logging. Data Acquisitions and Applications*. 2004.
- [103] M. Jonathan. “Chapter 11 Industrial Applications of Magnetic Resonance Diffusion and Relaxation Time Measurements”. In: *Diffusion NMR of Confined Systems: Fluid Transport in Porous Solids and Heterogeneous Materials*. The Royal Society of Chemistry, 2017, pp. 353–389. ISBN: 978-1-78262-190-4. DOI: 10.1039/9781782623779-00353. URL: <http://dx.doi.org/10.1039/9781782623779-00353>.
- [104] P. N. Sen et al. “Surface-to-volume ratio, charge density, nuclear magnetic relaxation, and permeability in clay-bearing sandstones”. In: *GEOPHYSICS* 55.1 (1990), pp. 61–69. DOI: 10.1190/1.1442772. eprint: "<https://doi.org/10.1190/1.1442772>". URL: <https://doi.org/10.1190/1.1442772>.
- [105] A. Afrough et al. “Magnetic-Resonance Imaging of High-Pressure Carbon Dioxide Displacement: Fluid/Surface Interaction and Fluid Behavior”. In: *SPE Journal* 23 (2018), pp. 772–787.
- [106] S. Stapf, R. Kimmich, and R.-O. Seitter. “Proton and Deuteron Field-Cycling NMR Relaxometry of Liquids in Porous Glasses: Evidence for Lévy-Walk Statistics”. In: *Phys. Rev. Lett.* 75 (15 1995), pp. 2855–2858. DOI: 10.1103/PhysRevLett.75.2855. URL: <https://link.aps.org/doi/10.1103/PhysRevLett.75.2855>.
- [107] S. Godefroy et al. “Surface nuclear magnetic relaxation and dynamics of water and oil in macroporous media”. In: *Phys. Rev. E* 64 (2 2001), p. 021605. DOI: 10.1103/PhysRevE.64.021605. URL: <https://link.aps.org/doi/10.1103/PhysRevE.64.021605>.
- [108] R. Kimmich, ed. *Field-cycling NMR Relaxometry. Instrumentation, Model Theories and Applications*. New Developments in NMR. The Royal Society of Chemistry, 2019, P001–571. ISBN: 978-1-78801-154-9. DOI: 10.1039/9781788012966. URL: <http://dx.doi.org/10.1039/9781788012966>.
- [109] Hiroshi Shimizu. “Effect of Molecular Shape on Nuclear Magnetic Relaxation. II. Quadrupole Relaxation”. In: *The Journal of Chemical Physics* 40.3 (1964), pp. 754–761. DOI: 10.1063/1.1725202. eprint: <https://doi.org/10.1063/1.1725202>. URL: <https://doi.org/10.1063/1.1725202>.

- [110] J.-P. Korb et al. “Relative role of surface interactions and topological effects in nuclear magnetic resonance of confined liquids”. In: *The Journal of Chemical Physics* 101.8 (1994), pp. 7074–7081. DOI: 10.1063/1.468333. eprint: <https://doi.org/10.1063/1.468333>. URL: <https://doi.org/10.1063/1.468333>.
- [111] Frank Bauer, Martin Gutting, and Mark A. Lukas. “Evaluation of Parameter Choice Methods for Regularization of Ill-Posed Problems in Geomathematics”. In: *Handbook of Geomathematics*. Ed. by Willi Freeden, M. Zuhair Nashed, and Thomas Sonar. Berlin, Heidelberg: Springer Berlin Heidelberg, 2015, pp. 1713–1774. ISBN: 978-3-642-54551-1. DOI: 10.1007/978-3-642-54551-1_99. URL: https://doi.org/10.1007/978-3-642-54551-1_99.
- [112] N. P. Galatsanos and A. K. Katsaggelos. “Methods for choosing the regularization parameter and estimating the noise variance in image restoration and their relation”. In: *IEEE Transactions on Image Processing* 1.3 (1992), pp. 322–336.
- [113] Daniela Calvetti et al. “Tikhonov regularization with nonnegativity constraint”. In: *Electronic Transactions on Numerical Analysis* 18 (Jan. 2004), pp. 153–173.
- [114] M Bertero, C De Mol, and El R Pike. “Linear inverse problems with discrete data. I. General formulation and singular system analysis”. In: *Inverse problems* 1.4 (1985), p. 301.
- [115] M. Sergiu et al. “Frequency-dependent NMR relaxation of liquids confined inside porous media containing an increased amount of magnetic impurities”. In: *Magnetic Resonance in Chemistry* 51.2 (2013), pp. 123–128. DOI: 10.1002/mrc.3924. eprint: <https://onlinelibrary.wiley.com/doi/pdf/10.1002/mrc.3924>. URL: <https://onlinelibrary.wiley.com/doi/abs/10.1002/mrc.3924>.
- [116] S. D. Senturia, J. D. Robinson, et al. “Nuclear spin-lattice relaxation of liquids confined in porous solids”. In: *Society of Petroleum Engineers Journal* 10.03 (1970), pp. 237–244.
- [117] H.C. Torrey et al. “Magnetic spin pumping in fluids contained in porous media”. In: *Physical Review Letters* 3.9 (1959), p. 418.
- [118] Morrel H Cohen and Kenneth S Mendelson. “Nuclear magnetic relaxation and the internal geometry of sedimentary rocks”. In: *Journal of Applied Physics* 53.2 (1982), pp. 1127–1135.
- [119] M. D. Correia et al. “Superstatistics model for T2 distribution in NMR experiments on porous media”. In: *Journal of Magnetic Resonance* 244 (2014), pp. 12–17.
- [120] W. E. Kenyon et al. “A three-part study of NMR longitudinal relaxation properties of water-saturated sandstones”. In: *SPE formation evaluation* 3.03 (1988), pp. 622–636.

- [121] Mohammad Mahdi Labani et al. “Evaluation of pore size spectrum of gas shale reservoirs using low pressure nitrogen adsorption, gas expansion and mercury porosimetry A case study from the Perth and Canning Basins, Western Australia”. In: *Journal of Petroleum Science and Engineering* 112 (2013), pp. 7–16.
- [122] Usman Ahmed, SF Crary, GR Coates, et al. “Permeability estimation: the various sources and their interrelationships”. In: *Journal of Petroleum Technology* 43.05 (1991), pp. 578–587.
- [123] A. Rabbani, S. Jamshidi, and S. Salehi. “An automated simple algorithm for realistic pore network extraction from micro-tomography images”. In: *Journal of Petroleum Science and Engineering* 123 (2014). Neural network applications to reservoirs: Physics-based models and data models, pp. 164–171. ISSN: 0920-4105. DOI: <https://doi.org/10.1016/j.petrol.2014.08.020>.
- [124] S. Beucher and C. Lantuéj. “Use of watersheds in contour detection”. In: *Proceedings of the International Workshop on Image Processing* (1979). URL: <https://ci.nii.ac.jp/naid/10008961959/en/>.
- [125] R. Romero-Zaliz and J. F. Reinoso-Gordo. “An Updated Review on Watershed Algorithms”. In: *Soft Computing for Sustainability Science*. Ed. by C. Cruz Corona. Cham: Springer International Publishing, 2018, pp. 235–258. ISBN: 978-3-319-62359-7. DOI: 10.1007/978-3-319-62359-7_12. URL: https://doi.org/10.1007/978-3-319-62359-7_12.
- [126] S. Rémond, J. L. Gallias, and A. Mizrahi. “Characterization of voids in spherical particle systems by Delaunay empty spheres”. In: *Granular Matter* 10 (2008), pp. 329–334. ISSN: 1434-7636. DOI: 10.1007/s10035-008-0092-4. URL: <https://doi.org/10.1007/s10035-008-0092-4>.
- [127] Mario Bertero, Christine De Mol, and Edward Roy Pike. “Linear inverse problems with discrete data: II. Stability and regularisation”. In: *Inverse problems* 4.3 (1988), p. 573.
- [128] Stingaciu L. R. et al. “Characterization of unsaturated porous media by high-field and low-field NMR relaxometry”. In: *Water Resources Research* 45.8 (2009).
- [129] S. Muncaci and I. Ardelean. “Probing the Pore Size of Porous Ceramics with Controlled Amount of Magnetic Impurities via Diffusion Effects on the CPMG Technique”. In: *Applied Magnetic Resonance* 44.7 (2013), pp. 837–848.
- [130] R. J. S. Brown and P. Fantazzini. “Conditions for initial quasilinear T_2^{-1} versus τ for Carr-Purcell-Meiboom-Gill NMR with diffusion and susceptibility differences in porous media and tissues”. In: *Phys. Rev. B* 47 (22 1993), pp. 14823–14834. DOI: 10.1103/PhysRevB.47.14823. URL: <https://link.aps.org/doi/10.1103/PhysRevB.47.14823>.

- [131] Denis S. Grebenkov. “Chapter 3 From the Microstructure to Diffusion NMR, and Back”. In: *Diffusion NMR of Confined Systems: Fluid Transport in Porous Solids and Heterogeneous Materials*. The Royal Society of Chemistry, 2017, pp. 52–110. ISBN: 978-1-78262-190-4. DOI: 10.1039/9781782623779-00052. URL: <http://dx.doi.org/10.1039/9781782623779-00052>.
- [132] R.F. Karlicek and I.J. Lowe. “A modified pulsed gradient technique for measuring diffusion in the presence of large background gradients”. In: *Journal of Magnetic Resonance (1969)* 37.1 (1980), pp. 75–91. ISSN: 0022-2364. DOI: [https://doi.org/10.1016/0022-2364\(80\)90095-5](https://doi.org/10.1016/0022-2364(80)90095-5). URL: <http://www.sciencedirect.com/science/article/pii/0022236480900955>.
- [133] R.M. Cotts et al. “Pulsed field gradient stimulated echo methods for improved NMR diffusion measurements in heterogeneous systems”. In: *Journal of Magnetic Resonance (1969)* 83.2 (1989), pp. 252–266. ISSN: 0022-2364. DOI: [https://doi.org/10.1016/0022-2364\(89\)90189-3](https://doi.org/10.1016/0022-2364(89)90189-3). URL: <http://www.sciencedirect.com/science/article/pii/0022236489901893>.
- [134] L.L. Latour et al. “Time-Dependent Diffusion Coefficient of Fluids in Porous Media as a Probe of Surface-to-Volume Ratio”. In: *Journal of Magnetic Resonance, Series A* 101.3 (1993), pp. 342–346. ISSN: 1064-1858. DOI: <https://doi.org/10.1006/jmra.1993.1056>. URL: <http://www.sciencedirect.com/science/article/pii/S1064185883710569>.
- [135] M.D. Hurlimann et al. “Restricted Diffusion in Sedimentary Rocks. Determination of Surface-Area-to-Volume Ratio and Surface Relaxivity”. In: *Journal of Magnetic Resonance, Series A* 111.2 (1994), pp. 169–178. ISSN: 1064-1858. DOI: <https://doi.org/10.1006/jmra.1994.1243>. URL: <http://www.sciencedirect.com/science/article/pii/S1064185884712435>.
- [136] B.A. Khan et al. “Basics of pharmaceutical emulsions: A review”. In: *African Journal of Pharmacy and Pharmacology* 5(25) (2011), pp. 2715–2725. ISSN: 1996-0816. DOI: <https://doi.org/10.5897/AJPP11.698>. URL: <http://www.academicjournals.org/AJPP>.
- [137] M.J. Lawrence and G.D. Rees. “Microemulsion-based media as novel drug delivery systems”. In: *Advanced Drug Delivery Reviews* 45.1 (2000). Emulsions for Drug Delivery, pp. 89–121. ISSN: 0169-409X. DOI: [https://doi.org/10.1016/S0169-409X\(00\)00103-4](https://doi.org/10.1016/S0169-409X(00)00103-4). URL: <http://www.sciencedirect.com/science/article/pii/S0169409X00001034>.
- [138] J.G. Speight. “A review of: “Emulsions Fundamentals and Applications In the Petroleum Industry” By Laurier L. Schramm, Editor”. In: *Fuel Science and Technology International* 10.7 (1992), pp. 1237–1237. DOI: 10.1080/08843759208916047.

- [139] A. Perazzo et al. “Emulsions in porous media: From single droplet behavior to applications for oil recovery”. In: *Advances in Colloid and Interface Science* 256 (2018), pp. 305–325. ISSN: 0001-8686. DOI: <https://doi.org/10.1016/j.cis.2018.03.002>. URL: <http://www.sciencedirect.com/science/article/pii/S0001868618300174>.
- [140] C.D. McAuliffe. “Oil and Gas Migration—Chemical and Physical Constraints”. In: *AAPG Bulletin* 63.5 (May 1979), pp. 761–781. ISSN: 0149-1423. DOI: 10.1306/2F9182CF-16CE-11D7-8645000102C1865D.
- [141] H. M. McConnell. “Reaction Rates by Nuclear Magnetic Resonance”. In: *The Journal of Chemical Physics* 28.3 (1958), pp. 430–431. DOI: 10.1063/1.1744152. eprint: <https://doi.org/10.1063/1.1744152>. URL: <https://doi.org/10.1063/1.1744152>.
- [142] K.J. Packer and C. Rees. “Pulsed NMR studies of restricted diffusion. I. Droplet size distributions in emulsions”. In: *Journal of Colloid and Interface Science* 40.2 (1972), pp. 206–218. ISSN: 0021-9797. DOI: [https://doi.org/10.1016/0021-9797\(72\)90010-0](https://doi.org/10.1016/0021-9797(72)90010-0). URL: <http://www.sciencedirect.com/science/article/pii/0021979772900100>.
- [143] K.G. Hollingsworth and M.L. Johns. “Measurement of emulsion droplet sizes using PFG NMR and regularization methods”. In: *Journal of Colloid and Interface Science* 258.2 (2003), pp. 383–389. ISSN: 0021-9797. DOI: [https://doi.org/10.1016/S0021-9797\(02\)00131-5](https://doi.org/10.1016/S0021-9797(02)00131-5). URL: <http://www.sciencedirect.com/science/article/pii/S0021979702001315>.
- [144] R. Valiulin, ed. *Diffusion NMR of Confined Systems. Fluid Transport in Porous Solids and Heterogeneous Materials*. Royal Society of Chemistry, 2017.
- [145] G.J. Hirasaki. “Wettability: Fundamentals and Surface Forces”. In: 6 (02 1991). DOI: 10.2118/17367-PA.
- [146] Schlumberger. *Oil Field Glossary - Drainage*. 2020. URL: <https://www.glossary.oilfield.slb.com/en/Terms/d/drainage.aspx>.
- [147] B. Chencarek et al. “Multi-exponential Analysis of Water NMR Spin–Spin Relaxation in Porosity/Permeability-Controlled Sintered Glass”. In: *Applied Magnetic Resonance* 50 (2019), pp. 211–225. DOI: 10.1007/s00723-018-1050-x. URL: <https://doi.org/10.1007/s00723-018-1050-x>.
- [148] R. Mills. “Self-diffusion in normal and heavy water in the range 1-45.deg.” In: *The Journal of Physical Chemistry* 77.5 (1973), pp. 685–688. DOI: 10.1021/j100624a025. eprint: <https://doi.org/10.1021/j100624a025>. URL: <https://doi.org/10.1021/j100624a025>.

- [149] H.L. Weissberg. “Effective Diffusion Coefficient in Porous Media”. In: *Journal of Applied Physics* 34.9 (1963), pp. 2636–2639. DOI: 10.1063/1.1729783. eprint: <https://doi.org/10.1063/1.1729783>. URL: <https://doi.org/10.1063/1.1729783>.
- [150] L.M. Schwartz et al. “Cross-property relations and permeability estimation in model porous media”. In: *Phys. Rev. E* 48 (6 1993), pp. 4584–4591. DOI: 10.1103/PhysRevE.48.4584. URL: <https://link.aps.org/doi/10.1103/PhysRevE.48.4584>.
- [151] F. Stallmach and H. Thomann. “Producible fluid volumes in porous media determined by pulsed field gradient nuclear magnetic resonance”. Pat. US5565775A. 1995.
- [152] P.J. McDonald et al. “Magnetic-resonance determination of the spatial dependence of the droplet size distribution in the cream layer of oil-in-water emulsions: Evidence for the effects of depletion flocculation”. In: *Phys. Rev. E* 59 (1 1999), pp. 874–884. DOI: 10.1103/PhysRevE.59.874. URL: <https://link.aps.org/doi/10.1103/PhysRevE.59.874>.
- [153] C. Russell Bowers and Daniel P. Weitekamp. “Transformation of Symmetrization Order to Nuclear-Spin Magnetization by Chemical Reaction and Nuclear Magnetic Resonance”. In: *Phys. Rev. Lett.* 57 (21 1986), pp. 2645–2648. DOI: 10.1103/PhysRevLett.57.2645. URL: <https://link.aps.org/doi/10.1103/PhysRevLett.57.2645>.
- [154] O. W. Sørensen. “A universal bound on spin dynamics”. In: *Journal of Magnetic Resonance (1969)* 86.2 (1990), pp. 435–440. ISSN: 0022-2364. DOI: [https://doi.org/10.1016/0022-2364\(90\)90278-H](https://doi.org/10.1016/0022-2364(90)90278-H). URL: <http://www.sciencedirect.com/science/article/pii/002223649090278H>.
- [155] M. H. Levitt. “Unitary evolution, Liouville space, and local spin thermodynamics”. In: *Journal of Magnetic Resonance (1969)* 99.1 (1992), pp. 1–17. ISSN: 0022-2364. DOI: [https://doi.org/10.1016/0022-2364\(92\)90151-V](https://doi.org/10.1016/0022-2364(92)90151-V). URL: <http://www.sciencedirect.com/science/article/pii/002223649290151V>.
- [156] B. Andreas. “Introduction to average Hamiltonian theory. I. Basics”. In: *Concepts in Magnetic Resonance Part A* 45A.6 (2016), e21414. DOI: <https://doi.org/10.1002/cmr.a.21414>. eprint: <https://onlinelibrary.wiley.com/doi/pdf/10.1002/cmr.a.21414>. URL: <https://onlinelibrary.wiley.com/doi/abs/10.1002/cmr.a.21414>.
- [157] A.J. Shaka et al. “An improved sequence for broadband decoupling: WALTZ-16”. In: *Journal of Magnetic Resonance (1969)* 52.2 (1983), pp. 335–338. ISSN: 0022-2364. DOI: [https://doi.org/10.1016/0022-2364\(83\)90207-X](https://doi.org/10.1016/0022-2364(83)90207-X). URL: <http://www.sciencedirect.com/science/article/pii/002223648390207X>.

- [158] G. Pileio and M. H. Levitt. “Theory of long-lived nuclear spin states in solution nuclear magnetic resonance. II. Singlet spin locking”. In: *The Journal of Chemical Physics* 130.21 (2009), p. 214501. DOI: 10.1063/1.3139064. eprint: <https://doi.org/10.1063/1.3139064>. URL: <https://doi.org/10.1063/1.3139064>.
- [159] Alexandre M. Souza, Gonzalo A. Álvarez, and Dieter Suter. “Robust Dynamical Decoupling for Quantum Computing and Quantum Memory”. In: *Phys. Rev. Lett.* 106 (24 2011), p. 240501. DOI: 10.1103/PhysRevLett.106.240501. URL: <https://link.aps.org/doi/10.1103/PhysRevLett.106.240501>.
- [160] M. C. D. Tayler and M. H. Levitt. “Paramagnetic relaxation of nuclear singlet states”. In: *Phys. Chem. Chem. Phys.* 13 (20 2011), pp. 9128–9130. DOI: 10.1039/C1CP20471H. URL: <http://dx.doi.org/10.1039/C1CP20471H>.
- [161] G. Pileio et al. “The Long-Lived Nuclear Singlet State of ¹⁵N-Nitrous Oxide in Solution”. In: *Journal of the American Chemical Society* 130.38 (2008). PMID: 18729363, pp. 12582–12583. DOI: 10.1021/ja803601d. eprint: <https://doi.org/10.1021/ja803601d>. URL: <https://doi.org/10.1021/ja803601d>.
- [162] G. Pileio, M. Carravetta, and M. H. Levitt. “Storage of nuclear magnetization as long-lived singlet order in low magnetic field”. In: *Proceedings of the National Academy of Sciences* 107.40 (2010), pp. 17135–17139. ISSN: 0027-8424. DOI: 10.1073/pnas.1010570107. eprint: <https://www.pnas.org/content/107/40/17135.full.pdf>. URL: <https://www.pnas.org/content/107/40/17135>.
- [163] Simone Cavadini et al. “Slow Diffusion by Singlet State NMR Spectroscopy”. In: *Journal of the American Chemical Society* 127.45 (2005). PMID: 16277516, pp. 15744–15748. DOI: 10.1021/ja052897b. eprint: <https://doi.org/10.1021/ja052897b>. URL: <https://doi.org/10.1021/ja052897b>.
- [164] S. Cavadini and P. R. Vasos. “Singlet states open the way to longer time-scales in the measurement of diffusion by NMR spectroscopy”. In: *Concepts in Magnetic Resonance Part A* 32A.1 (2008), pp. 68–78. DOI: <https://doi.org/10.1002/cmra.20100>. eprint: <https://onlinelibrary.wiley.com/doi/pdf/10.1002/cmra.20100>. URL: <https://onlinelibrary.wiley.com/doi/abs/10.1002/cmra.20100>.
- [165] R. Sarkar et al. “Measurement of Slow Diffusion Coefficients of Molecules with Arbitrary Scalar Couplings via Long-Lived Spin States”. In: *ChemPhysChem* 9.16 (2008), pp. 2414–2419. DOI: <https://doi.org/10.1002/cphc.200800476>. eprint: <https://chemistry-europe.onlinelibrary.wiley.com/doi/pdf/10.1002/cphc.200800476>. URL: <https://chemistry-europe.onlinelibrary.wiley.com/doi/abs/10.1002/cphc.200800476>.

- [166] P. Ahuja et al. “Diffusion Coefficients of Biomolecules Using Long-Lived Spin States”. In: *Journal of the American Chemical Society* 131.22 (2009). PMID: 19441812, pp. 7498–7499. DOI: 10.1021/ja902030k. eprint: <https://doi.org/10.1021/ja902030k>. URL: <https://doi.org/10.1021/ja902030k>.
- [167] A. M. Torres, B. Ghadirian, and W. S. Price. “Diffusion–diffraction using singlet spin states and various NMR coherences in a J-coupled AX spin system”. In: *RSC Adv.* 2 (8 2012), pp. 3352–3360. DOI: 10.1039/C2RA20063E. URL: <http://dx.doi.org/10.1039/C2RA20063E>.
- [168] Giuseppe Pileio and Sylwia Ostrowska. “Accessing the long-time limit in diffusion NMR: The case of singlet assisted diffusive diffraction q-space”. In: *Journal of Magnetic Resonance* 285 (2017), pp. 1–7. ISSN: 1090-7807. DOI: <https://doi.org/10.1016/j.jmr.2017.10.003>. URL: <http://www.sciencedirect.com/science/article/pii/S1090780717302495>.
- [169] J. N. Dumez et al. “Long-lived localization in magnetic resonance imaging”. In: *Journal of Magnetic Resonance* 246 (2014), pp. 27–30. ISSN: 1090-7807. DOI: <https://doi.org/10.1016/j.jmr.2014.06.008>. URL: <http://www.sciencedirect.com/science/article/pii/S1090780714001773>.
- [170] Giuseppe Pileio et al. “Real-space imaging of macroscopic diffusion and slow flow by singlet tagging MRI”. In: *Journal of Magnetic Resonance* 252 (2015), pp. 130–134. ISSN: 1090-7807. DOI: <https://doi.org/10.1016/j.jmr.2015.01.016>. URL: <http://www.sciencedirect.com/science/article/pii/S1090780715000178>.
- [171] P. C. Carman. “Fluid Flow Through Granular Beds”. In: *Trans. Inst. Chem. Engr.* 15 (1937), pp. 150–166.
- [172] X.-H. Ren et al. “Deactivation and regeneration of a naphtha reforming catalyst”. In: *Applied Catalysis A: General* 228.1 (2002), pp. 39–52. ISSN: 0926-860X. DOI: [https://doi.org/10.1016/S0926-860X\(01\)00958-9](https://doi.org/10.1016/S0926-860X(01)00958-9). URL: <http://www.sciencedirect.com/science/article/pii/S0926860X01009589>.
- [173] J. Wood and L. F. Gladden. “Effect of coke deposition upon pore structure and self-diffusion in deactivated industrial hydroprocessing catalysts”. In: *Applied Catalysis A: General* 249.2 (2003), pp. 241–253. ISSN: 0926-860X. DOI: [https://doi.org/10.1016/S0926-860X\(03\)00200-X](https://doi.org/10.1016/S0926-860X(03)00200-X). URL: <http://www.sciencedirect.com/science/article/pii/S0926860X0300200X>.
- [174] N. N. Yadav, A. M. Torres, and W. S. Price. “NMR q-space imaging of macroscopic pores using singlet spin states”. In: *Journal of Magnetic Resonance* 204.2 (2010), pp. 346–348. ISSN: 1090-7807. DOI: <https://doi.org/10.1016/j.jmr.2010.03.010>. URL: <http://www.sciencedirect.com/science/article/pii/S1090780710000807>.

- [175] Y. Zur, M. L. Wood, and L. J. Neuringer. “Spoiling of transverse magnetization in steady-state sequences”. In: *Magnetic Resonance in Medicine* 21.2 (1991), pp. 251–263. DOI: <https://doi.org/10.1002/mrm.1910210210>. eprint: <https://onlinelibrary.wiley.com/doi/pdf/10.1002/mrm.1910210210>. URL: <https://onlinelibrary.wiley.com/doi/abs/10.1002/mrm.1910210210>.
- [176] Frederick H. Epstein, John P. Mugler III, and James R. Brookeman. “Spoiling of transverse magnetization in gradient-echo (GRE) imaging during the approach to steady state”. In: *Magnetic Resonance in Medicine* 35.2 (1996), pp. 237–245. DOI: <https://doi.org/10.1002/mrm.1910350216>. eprint: <https://onlinelibrary.wiley.com/doi/pdf/10.1002/mrm.1910350216>. URL: <https://onlinelibrary.wiley.com/doi/abs/10.1002/mrm.1910350216>.